Phase Behavior, Filling Dynamics, and Packing of Fluids inside Isolated Carbon Nanotubes

by

Samuel James Faucher

B.S. Chemical Engineering
Yale University, 2016

M.S. Chemical Engineering Practice
Massachusetts Institute of Technology, 2018

SUBMITTED TO THE DEPARTMENT OF CHEMICAL ENGINEERING IN PARTIAL FULFILLMENT OF THE REQUIREMENTS FOR THE DEGREE OF

DOCTOR OF PHILOSOPHY IN CHEMICAL ENGINEERING
AT THE
MASSACHUSETTS INSTITUTE OF TECHNOLOGY

MAY 2022

Signature of Author……
Department of Chemical Engineering
May 9, 2022

Certified by:……...……
Michael S. Strano
Carbon P. Dubbs Professor of Chemical Engineering
Thesis Supervisor

Accepted by:……...……
Patrick S. Doyle
Chair, Department Committee on Graduate Students

Abstract

Fluids behave differently inside nanoscale pores than they do in bulk solution. When confined inside so-called single digit nanopores – pores with diameters smaller than 10 nm – the atomic configuration, phase behavior, and dynamics of fluids vary markedly from their bulk behavior and depend sensitively on the confining diameter. Understanding fluid behavior at these scales is critical to the design of a wide variety of engineering systems, such as membranes for chemical separations and batteries for energy storage. The study of nanofluidics also informs our understanding of natural phenomena, including the single-file transport of water into biological cells and flow through nanoporous geologic media.

In this thesis, we develop experimental platforms to study confinement effects on fluid packing, filling, and phase behavior inside isolated, substrate-bound carbon nanotubes with diameters ranging from 0.8 nm to 3 nm. Carbon nanotubes are grown by chemical vapor deposition on marked silicon substrates and segmented by photolithography or use of a focused ion beam, producing multiple, identical segments of the same diameter and chirality carbon nanotube. By Raman spectroscopy, it is possible to determine on the micrometer length scale and second time scale whether an isolated carbon nanotube is empty, fluid-filled, or partially fluid-filled as a function of location, time, temperature, and nanotube diameter.

After building precision nanopore systems and developing techniques to characterize nanopore filling, we address several topics of interest to the field of nanofluidics, as explored in the chapters of this thesis. First, we explore knowledge gaps in nanofluidics, including gaps in our understanding of phase behavior and dynamics of fluids under conditions of extreme confinement. Second, we study the diameter dependence of fluid packing and filling inside carbon nanotubes, showing that the variation in the change of the Raman radial breathing mode upon fluid filling is indicative of configurational changes in water inside nanotubes of different sizes. Third, we develop continuum elastic shell theories to explain why double-walled nanotubes, but not single-walled nanotubes, can distinguish between interior fluid filling and exterior fluid adsorption by changes in radial vibrations alone. Fourth, we perform a thermodynamic analysis of water-filled, closed carbon nanotubes, calculating enthalpies of phase change from a Clausius-Clapeyron type expression for nanoconfined water. Fifth, we perform a thermodynamic analysis of water-filled carbon nanotubes in a thermodynamically open system, observing a phase change driven by variable laser heating and calculating enthalpies of adsorption by comparison to a Langmuir-type adsorption model. Sixth, we observe dynamic changes in filling state with time, calculating diffusion coefficients of vapor-like and liquid-like water inside carbon nanotubes as a function of diameter. Finally, as an aside, we perform a computational analysis of a heated mask.

Measurement of water inside carbon nanotubes, as explored in this thesis, expands our view of the thermodynamic and kinetic properties of fluids under confinement and addresses key knowledge gaps in nanofluidics. These measurements can inform new theories, force fields, and mechanisms for fluids in nanoconfined environments.

Thesis Supervisor: Michael S. Strano
Title: Carbon P. Dubbs Professor in Chemical Engineering

Acknowledgements

I have felt fortunate to be surrounded by so many supportive colleagues, friends, and family in the Boston area and elsewhere during these last six years at MIT.

To my advisor, Michael Strano – thank you for your wide range of scientific insight on countless topics, and for your constant vision for the next big idea. You have taught me a lot about where to look for scientific breakthroughs, and how to pursue and present them. Thank you for your generosity in sharing your time and ideas with me.

To my committee – Daniel Blankschtein, Alex Noy, and Rohit Karnik – thank you for your scientific guidance, and for your kind mentorship and life advice. I have felt constantly that I'm in good hands.

To Matthias Kuehne, the postdoc with whom I've worked most closely, thank you for being my colleague and confidant these last several years in the lab, and for sharing your outstanding experimental insight, enthusiasm, and patience with me. I could not have done it without you, and not just in the literal sense that we've cowritten much of this work.

To other Strano group members, and there have been a lot over the course of the last six years, thanks to all of you for your diverse talents and abilities. To those who trained and mentored me (Volodymyr Koman, Daichi Kozawa, Ananth Govind Rajan), to those who joined with me and have now flown the nest (Kevin Silmore and Cache Hamilton), to the rest of my lab colleagues and friends (Xun Gong, Allan Brooks, Sylvia Li, Naveed Bakh, Dan Salem, Anton Cottrill, Minkyung Park, Mike Lee, Jingfan Yang, Ge Zhang, Cindy Jin, Dan Lundberg, Sungyun Yang, Leslie Cui, Michelle Quien, Thomas Porter), and to Brenda Pelletier, thank you for your words of wisdom and support. And to the MIT undergraduates I've had the privilege to work with (Natalie Northrup and Evie Mayner), thanks for sharing your enthusiasm and talents.

To my collaborators, including Daniel Blankschtein, Rahul Misra, Narayana Aluru, Hananeh Oliaei, Jacopo Buongiorno, Arun Majumdar, and others, thank you for the opportunities to work together. To Rahul, in particular – thank you for working closely with me, and sharing your encyclopedic knowledge of molecular simulation.

To other colleagues in the Center for Enhanced Nanofluidic Transport – I feel fortunate to have had a scientific home in this center for the last four years. Thank you for making it so.

To my Practice School group and mentors, thank you for making our work in Ireland and Australia one of the highlights of my time at MIT.

To my friends in Cambridge, many in chemical engineering and EAPS at MIT – Cynthia Ni, Neil Dalvie, Juliet Barker, Nika Stone, Mickey Stone, Karla de Souza, Pedro de Souza, Kevin Silmore, Cache Hamilton, Julia Wilcots, Tristan Abbott, Lyssa Freese, Henri Drake, Genia Prikhodko, Santi Benavides, Florence Bergeron, Raphael Rousseau-Rizzi, and others – thank you for sharing this long and tumultuous grad school journey with me.

To the friends from other periods of my life, and in particular my friends from Yale and Boise High, I feel lucky to have such rewarding and long-lasting friendships, and lucky that we've maintained them during my time at MIT. Thanks to those who have come to see me, and to those who I've visited in New York, New Haven, Boise, the Bay Area, the Berkshires, and elsewhere.

To Stefano, Alexandra, and Bernardo – thank you for your generosity and warmth in inviting me into your home.

To my family – I was very fortunate that two of my siblings lived in Boston for many of the years of my PhD. To Madeleine (and Gaelen), and Ian (and Megan), thank you for the endless support, the hundreds to possibly thousands of miles biked, and the meals shared. And to Paul, thank you for stopping by and for the support from afar. To my mom and Don, my dad and Cherie, JD, GB: thank you for raising and teaching me. I could not have done it without you.

To Astrid – thank you for your support, your sense of adventure, and for letting me share the highs and lows of grad school with such a caring person. I'm thankful for you every day.

Working toward a PhD means pursuing knowledge in some domain, but it's also a vote of confidence in learning itself. For me, evidently, education has taken a long time. Thank you to all of my teachers in Boise, New Haven, Cambridge, and elsewhere who have helped me get started.

Contents

1. Introduction

When confined in single-digit nanopores,[1] or pores with a characteristic dimension less than 10 nm, water displays physical properties that deviate substantially from those in larger nanopores.[2] Examples include slip flow of water inside carbon nanotubes less than 50 nm in diameter that results in flow rates that are orders of magnitude higher than those encountered in larger nanopores.[3–7] Similarly, the melting points of confined water and other fluids deviate from their values in the bulk in a diameter-dependent way described by the Gibbs Thomson effect,[8] but diverge substantially from them under extreme confinement.[9] The dielectric constant of water in graphene slit pores, too, varies widely with pore width.[10,11] Experimental observations in these exceptionally narrow nanopores have renewed interest in the study of fluids under confinement, and reveal knowledge gaps in the study of single-digit nanopore nanofluidics[1] that anticipate the development of nanofluidic devices for fundamental measurements and diverse applications. The interior of opened carbon nanotubes can serve as an experimental platform to answer these questions. However, methods do not yet exist for generating repeated and reliable comparisons of fluid filling for identical diameter single-digit nanopores of any kind. In this thesis, we create a platform that consists of precision nanopores in the critical diameter regime (< 10 nm) formed from cut and opened ultralong CNTs. By examining spatially dependent fluid filling repeatedly in identical systems, we can overcome impediments like pore blocking and closed CNT ends to learn fundamental aspects of confined fluid properties. This platform is relevant not only to carbon nanotube nanofluidics, but in addressing topics including nanoscale slip flow, fluid diffusion, phase behavior, and interfacial transport that span nanofluidic device geometries and fluid types.

The fabrication of precision nanopores in the range of extreme confinement has proven difficult, limiting the number of replicates and control of pore dimensions. Two-dimensional nanochannel arrays, produced both by top-down etching of silicon and other materials and bottom-up assembly of 2D materials to form van der Waals heterostructures, comprise one class of experimental system. Enhanced water transport in hybrid nanochannels[12] and modified interfacial behavior of water under nanoconfinement, including evaporation,[13] cavitation,[14] and vapor transport selectivity,[15] have been observed in etched Si nanochannels, though channel dimensions do not typically reach the single-digit nanometer regime. Van der Waals heterostructures with graphene and other 2D materials[16,17] have addressed fundamental questions about water properties, including dielectric constant[11] and capillary condensation[18] under extreme 2D confinement, but cannot mimic the 1D confinement of nanotubes. Another class of experimental systems are multi-pore nanotube membranes. Carbon nanotubes membranes have been studied for close to two decades,[6,19–21] with permeation measurements showing significant flow enhancement and high slip length for membranes containing ensembles of pores with diameters in the single-digit range. CNT porins, which contain short carbon nanotubes embedded in a lipid bilayer, provide another platform for the study of water and ions through ensembles of carbon nanotubes, and also show flow enhancements that vary dramatically with nanotube diameter.[5,22] This allows for precision and many replicates, but the pore length itself is extremely small (around 10 nm), causing the CNT entrance region to dominate fluid behavior. Research groups have studied water structure and phase behavior in carbon nanotube ensembles using techniques like x-ray diffraction,[23,24] allowing the proposal of a temperature-diameter phase

diagram for the water-SWNT system; NMR;[25] and neutron scattering.[26,27] Spectroscopies, including IR spectroscopy,[28,29] Raman,[30–32] and photoluminescence,[31] have been used to distinguish ensembles of empty and water-filled CNTs, confirming, in some cases, the separation of the two by centrifugation.[31,33]

Only in recent years have nanofabrication techniques allowed the study of fluids in isolated, single carbon nanotubes, but to date these experimental platforms have not allowed repeat measurements of identical CNT devices. One study by Secchi and co-workers[3] uses fluid entrainment in a Landau-Squire jet to measure flow enhancements for CNTs outside the single-digit regime from 15 to 50 nm in diameter, showing large slip lengths for CNTs and negligible slip lengths for boron nitride nanotubes. The difference in performance between CNTs and boron nitride nanotubes suggests that solid and interfacial properties beyond the confining diameter, like wettability and electronic structure, may affect hydrodynamics, but experimental observations of water behavior in other quasi-1D nanopores are even scarcer than those in CNTs. Additionally, the fabrication of trans-membrane single carbon nanotubes does not easily extend to diameters below 10 nm and replicates are difficult to realize.[34,35] Other studies use photoluminescence of individual solution-phase[36] or suspended CNTs,[37,38] and, from our research group, Raman spectroscopy of substrate-bound CNTs[9] to observe water inside single carbon nanotube pores. Yet none of these platforms provides multiple copies of identical, localizable nanopores for repeated measurement of nanofluidic filling. The limited number of replicates or the averaging together of multiple nanopores suggest that random atomic defects, variations in pore mouth chemistry, and strongly non-monotonic effects with confining diameter can obscure fundamental fluid properties.

In this thesis, we develop a nanofluidic platform consisting of lithographically segmented, isolated, substrate-bound CNTs to study water and other fluids under nanometer confinement. We show that external fluid adsorption and internal fluid filling of CNTs can be distinguished by Raman spectroscopy: internal water filling causes a blue shift in the Raman radial breathing mode (RBM), while under these conditions external water application does not, as shown by measurements of large numbers of isolated CNTs using air and water-immersion objectives. We use the Raman radial breathing mode as a probe of a fluid filling state which can change with temperature, location, or time. In so doing, we are able to advance several important knowledge gaps in carbon nanotube nanofluidics. Each of these topics has been published as a peer-reviewed publication or will be published as a peer-reviewed publication by the conclusion of this thesis work. They are as follows: (I) a critical review of knowledge gaps in nanofluidics of single-digit nanopores, (II) the diameter dependence of fluid filling and fluid packing inside isolated CNTs, (III) the vibrational signatures of interior fluid filling and exterior fluid adsorption in double-walled carbon nanotubes, (IV) observation of partial filling and thermodynamic analysis inside sealed carbon nanotube segments, (V) thermodynamics of interior fluid adsorption inside open carbon nanotubes by laser heating, and, (VI) dynamics of filling and emptying, and, while not entirely related to the theme of nanofluidic behavior inside carbon nanotubes, (VII) computational analysis of heat and mass transport inside a virucidal mask.

The remainder of this chapter, which outlines knowledge gaps in nanofluidics, has been adapted from “Critical Knowledge Gaps in Mass Transport through Single-Digit Nanopores: A

Review and Perspective," by Samuel Faucher, Narayana Aluru, Martin Z. Bazant, Daniel Blankschtein, Alexandra H. Brozena, John Cumings, J. Pedro de Souza, Menachem Elimelech, Razi Epsztein, John T. Fourkas, Ananth Govind Rajan, Heather J. Kulik, Amir Levy, Arun Majumdar, Charles Martin, Michael McEldrew, Rahul Prasanna Misra, Aleksandr Noy, Tuan Anh Pham, Mark Reed, Eric Schwegler, Zuzanna Siwy, YuHuang Wang, and Michael Strano, *The Journal of Physical Chemistry C* **2019** 123 (35), 21309-21326, DOI: 10.1021/acs.jpcc.9b02178.

1.1 Knowledge Gaps in Nanofluidics

Not all nanopores are created equal. By definition, nanopores have characteristic diameters or conduit widths between approximately 1 and 100 nm. However, the narrowest of such pores, perhaps best called Single Digit Nanopores (SDNs) and defined as those with regular diameters less than 10 nm, have only recently been accessible experimentally for precision transport measurements. This review summarizes recent experiments on pores in this size range that yield surprising results, pointing towards extraordinary transport efficiencies and selectivities for SDN systems. These studies have identified critical gaps in our understanding of nanoscale hydrodynamics, molecular sieving, fluidic structure and thermodynamics. These knowledge gaps are, in turn, an opportunity to discover and understand fundamentally new mechanisms of molecular and ionic transport at the nanometer scale that may inspire a host of new technologies, from novel membranes for separations and water purification to new gas-permeable materials and energy storage devices. Here we highlight seven critical knowledge gaps in the study of SDNs and identify the need for new approaches to address these topics.

Nanopores, broadly defined as pores with diameters or conduit widths smaller than 100 nm, underpin a large array of material systems and technological applications. For example, adsorbent technology for chemical and air separations employs activated carbon with pores as small as 0.6 nm in size,[1-3] while zeolites such as ZSM-5, with a pore diameter of 5.5 Å, have been used for a wide variety of catalysis, adsorption, and pollution abatement applications.[4, 5] Membrane technology for reverse osmosis and nanofiltration typically involves inorganic substrates with pores on the order of 0.5 nm and 1 to 5 nm, respectively.[6, 7] However, detailed studies of nanopore transport at the single pore level have only become possible recently with the advent of isolated pore systems combined with sophisticated readout mechanisms to probe fluidic motion and mass transport in pores that are geometrically and compositionally well-defined. Examples of such systems include short[8] and ultralong carbon nanotubes,[9, 10] boron nitride nanotubes,[11] graphene oxide laminates,[12, 13] polymer nanochannels, [14, 15] and silicon nanochannels.[16, 17] These systems have been probed with analytical techniques including fluorescence, Raman, non-linear,[18] and single defect spectroscopies,[19-22] *ab initio* density functional theory (DFT) simulations,[23-25] and multi-scale models[26-32] to elucidate solvation phenomena,[23, 25] correlative and dissipative behaviors,[29] and ionic and molecular selectivity mechanisms[33] that arise under extreme confinement.

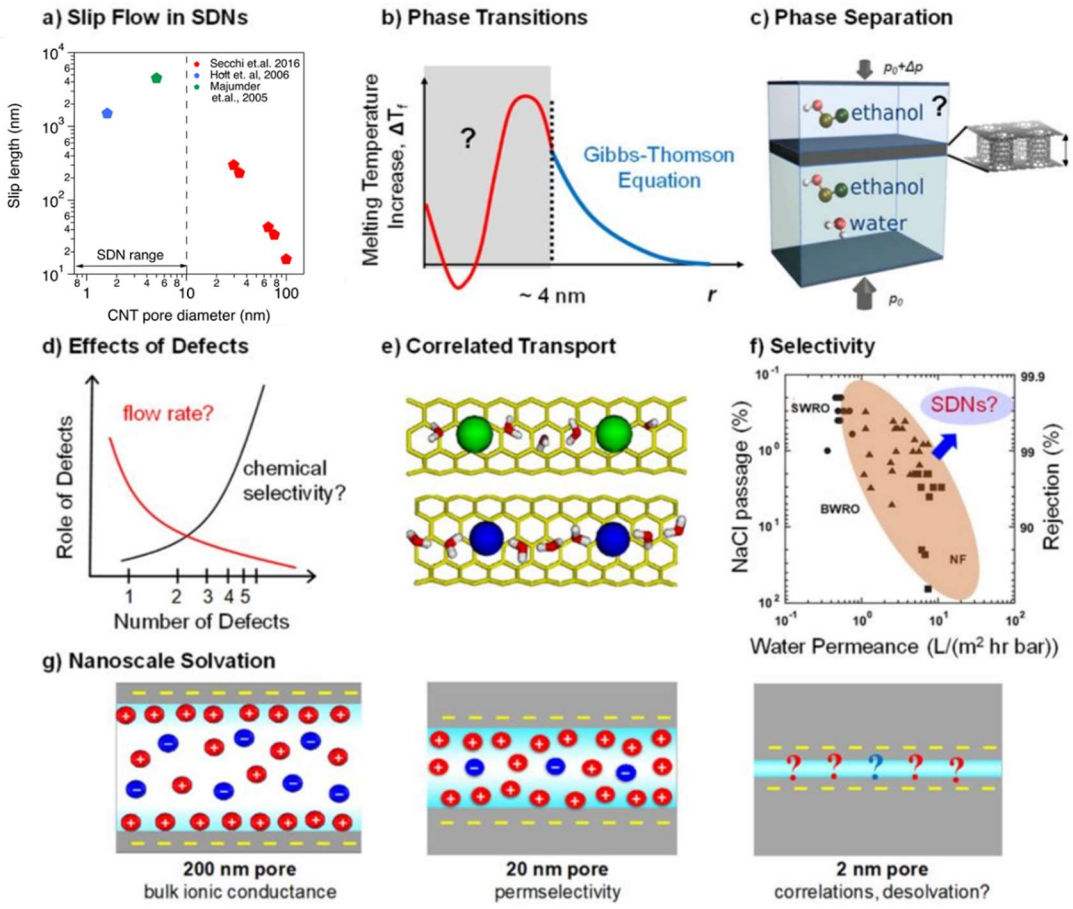

Figure 1-1 | Critical knowledge gaps in SDN nanofluidics. (a) The scaling of slip length with nanopore diameter is unknown and possibly non-monotonic in the single-digit range. Data taken from refs. 34-36 (b) The phase behavior of fluids inside SDNs cannot be predicted by existing theories. (c) Phase separation may be enhanced by nanoconfinement. (d) Defects may have an outsized effect on transport inside SDNs, but the magnitude of these effects is unknown. (e) Transport of ions in SDNs shows novel spatial and temporal correlations. (f) SDNs may form the basis for systems with enhanced molecular and ionic selectivity, surpassing that of membranes currently used for reverse osmosis. (g) Solvation in confinement differs from that in bulk, with profound effects on transport rates and selectivity.

In particular, recent studies of transport in single-digit nanopores (SDNs), i.e. pores with a diameter or conduit width smaller than 10 nm, reveal many counterintuitive behaviors that often defy continuum descriptions of fluid flow. These results expose critical knowledge gaps that motivate investigation and challenge existing theories. SDNs also provide exciting opportunities to advance fundamentally new technology in the form of membranes and fluidic platforms with unprecedented transport rates and selectivities, and a unique opportunity for the seamless integration of wet ionic devices with dry electronics, thus enabling long-sought bioelectronic interfaces.[37] Specifically, SDNs can be tailored to (i) sieve ions efficiently from seawater and serve as membranes for seawater desalination,[38] (ii) differentiate between polar and nonpolar fluids and serve as flow sensors,[39] (iii) enhance proton transport in fuel cell

applications,[40] and (iv) generate electricity from osmotic power harvesting.[11] Moreover, a deeper mechanistic understanding of water transport through SDNs may allow us to build robust synthetic analogs of transmembrane proteins, such as aquaporins,[41] for water treatment applications. This review discusses recent work and critical gaps in our understanding of nanoscale hydrodynamics, molecular sieving, fluidic structure and thermodynamics in SDNs. It also comments on the implications of these new molecular transport mechanisms. We refer the reader to other compelling reviews on other classes of nanopores,[42, 43] nanoporous materials for energy storage,[44, 45] and for water and gas purification.[46-48]

This brief literature survey identifies knowledge gaps that have recently emerged in the areas of nanofluidics and fluid confinement. Examples of these gaps include: the observation of slip-flow enhancement, in which the narrowest nanopores demonstrate the highest mass transport rates;[8, 35] non-Gibbs-Thomson phase behavior, in which fluid phase boundaries in SDNs are distorted relative to their bulk fluid counterparts; and non-linear, correlative effects[10, 49] in ion transport through SDNs that are not observed in larger nanopores (**Figure 1-1**). We define these and other observations as critical knowledge gaps because existing theories – whether continuum, atomistic, or molecular – fail to adequately describe the basis for these exotic effects. In this review, we identify seven such knowledge gaps, highlight recent progress, and suggest next steps for their exploration.

1.1.1 Slip Flow Enhancement

Flow enhancement by slip flow in SDNs is unexpectedly large. Slip flow[50] occurs when the fluid molecules in contact with the wall have a non-zero velocity and the no-slip boundary condition in fluid mechanics does not hold. This situation often occurs in nanopores with atomically smooth walls. The slip length is defined mathematically as the distance required beyond the wall for the fluid velocity to decrease linearly to zero. Large values of slip lengths for fluids confined inside SDNs can result in flow rates that greatly exceed the predictions of the Hagen-Poiseuille equation, thereby substantially lowering the pressure drop for narrow conduits.[8, 35, 50] Several recent studies[35, 36, 51-56] suggest that the narrowest pores demonstrate the largest slip-length enhancements. Mechanistic understanding of this scaling is in its infancy because theory and simulations[50, 57-63] have failed to match the results of recent measurements on pores that are wider than SDNs.

Carbon Nanotube and 2D Material Assemblies. Carbon nanotubes (CNTs), with their atomically smooth walls and constant diameters, are an ideal system for probing flow enhancement in SDNs. Following a landmark molecular dynamics prediction of fast flow in CNT pores,[64] there has been a long history of experimental investigations of water flow through membranes composed of arrays of vertically aligned CNTs.[35, 36, 55, 65] For example, Majumdar et al. studied fluid flow through membranes composed of vertically-aligned multiwalled CNTs of ~7 nm diameter and reported water slip lengths of 39 to 68 μm, which correspond to water flow rates that are 4 to 5 orders of magnitude faster than the predictions of the Hagen-Poiseuille equation with a no-slip boundary condition.[36] Holt et al. studied water and gas flow through membranes composed of double-walled CNTs (DWCNTs) with diameters less than 2 nm, and reported water slip lengths of 140 to 1500 nm.[35] These studies and others were also motivated by

earlier work showing selective ionic and molecular transport through synthetic membranes with nanopores in the single-digit range.[66-68]

These pioneering CNT studies revealed large slip lengths of water inside CNTs, but they were performed on CNT membranes and measurement of fluid flow through individual, isolated CNTs remained a technical challenge for many years. In a recent study, Secchi et al.[34] devised an experimental platform to measure pressure-driven water flow through isolated CNTs larger than the SDN range, and reported a large radius-dependent flow enhancement, with the slip length reaching 300 nm for CNTs with a diameter of 30 nm diameter. Furthermore, by measuring the flow rate of water inside 30 to 100 nm diameter CNTs, Secchi et al.[34] showed that the slip length of water increases monotonically with a decrease in the CNT diameter. This monotonicity, however, may not continue into the SDN range (**Figure 1-1a**). When the diameter of the CNT approaches the van der Waals diameter of water in the range of 0.8 to 2 nm, for instance, water molecules adopt a layered structure that can result in a non-monotonic variation of slip length with CNT diameter. Between 2 nm and 10 nm, experimental results are varied.

Recent experimental advances using CNT porins,[69] i.e., 10 nm-long nanotube segments inserted into lipid membranes (**Figure 1-2a-b**), complement experimental results using isolated CNTs. CNT porins occupy a unique place in the arsenal of nanofluidic tools, because these materials allow researchers to probe ensemble-scale transport in the important sub-1-nm size regime of nanotube pores that are inaccessible for conventional aligned CNT membrane platforms.[8] The osmotic water permeability of 0.8-nm-diameter CNT porins exceeds that of 1.5-nm-diameter CNTs by an order of magnitude (**Figure 1-2c**),[8] suggesting that a 1D arrangement of water molecules,[70, 71] which is only achievable at small diameters, introduces an additional enhancement mechanism besides the wall slip, and promotes ultrafast water transport in collective bursts.[64] The same 1D arrangement of water molecules appears to produce a significant enhancement of Grotthuss proton transport rates in narrow CNT pores.[40, 72] Transport through short CNT porins can be compared with the results from a complementary platform[9,10] that uses Raman spectroscopy to characterize transport in ultra-long CNTs (**Fig 2d-f**). A recent study with ultra-long CNTs reported highly non-monotonic freezing point elevation of confined water as a function of nanotube diameter.[10] Taken together, these results suggest that slip flow may be highly non-monotonic with diameter, especially for the smallest diameters and channel lengths. These intriguing findings highlight the need to develop structure/function relationships for SDNs that can predict exotic transport given specific confinement conditions.

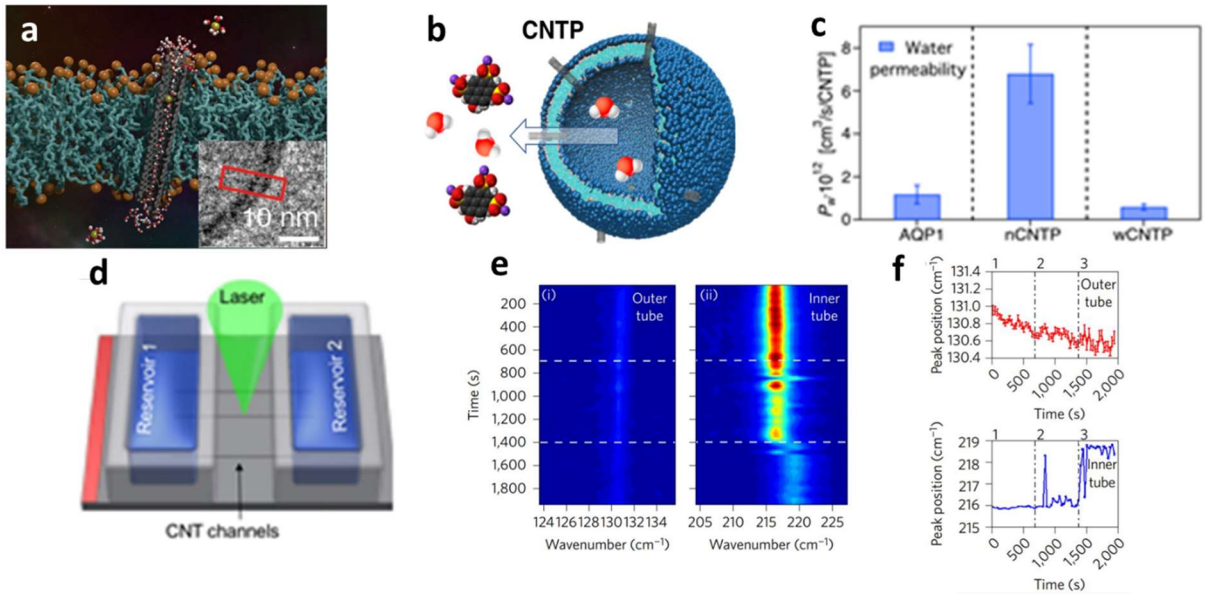

Figure 1-2 | Transport measurements in CNT porins and CNTs. (a) CNT porins (CNTP) in lipid membranes (inset shows a cryo-TEM image of a 0.8 nm diameter CNTP in a lipid membrane). From Tunuguntla, R. H.; Henley, R. Y.; Yao, Y.-C.; Pham, T. A.; Wanunu, M.; Noy, A., Enhanced water permeability and tunable ion selectivity in subnanometer carbon nanotube porins. *Science* **2017,** *357*, 792-796. Reprinted with permission from AAAS. (b) Osmotically-driven water transport through CNT porins. From Tunuguntla, R. H.; Henley, R. Y.; Yao, Y.-C.; Pham, T. A.; Wanunu, M.; Noy, A., Enhanced water permeability and tunable ion selectivity in subnanometer carbon nanotube porins. *Science* **2017,** *357*, 792-796. Reprinted with permission from AAAS. (c) Water permeability of aquaporin protein (AQP1) compared with that of 0.8 nm (nCNTP) and 1.5 nm (wCNTP) diameter CNT porins. From Tunuguntla, R. H.; Henley, R. Y.; Yao, Y.-C.; Pham, T. A.; Wanunu, M.; Noy, A., Enhanced water permeability and tunable ion selectivity in subnanometer carbon nanotube porins. *Science* **2017,** *357*, 792-796. Reprinted with permission from AAAS. (d) The CNT experimental platform, which comprises isolated CNTs connected to two reservoirs, enables monitoring by microRaman spectroscopy. Reprinted from ref. 10, Springer Nature. (e) Temporal study of the radial breathing mode (RBM) frequency. (i,ii) A time-map showing the evolution of the RBM frequency and intensities for a 1.15 nm double walled nanotube (DWCNT). Dotted lines indicate the time points at which water is added to the reservoirs. Reprinted from ref. 10, Springer Nature. (f) Filling is shown for the inner tube of a DWCNT but not the outer tube by an upshift in RBM frequency. Reprinted from ref. 10, Springer Nature.

The van der Waals assembly of 2D materials to form nanoconduits, pioneered by Andre Geim and coworkers, provides another avenue to study fluids under extreme confinement.[73] In this series of experiments, fluid flow was measured through nanocapillaries formed by sandwiching few-layer 2D materials like graphene, hBN, or MoS_2 between atomically smooth crystals of graphite, hBN, or MoS_2.[73-78] Gravimetric measurements of water permeation through channels formed by graphene spacers show extreme slip flow and suggest high capillary driving pressures.[74] The structure and properties of water under 2D confinement are quite different from

bulk, with unusually low dielectric constant,[75] changes in viscosity that arise from finite-size effects,[79] and the appearance of unusual phases like 2D square ice.[80] These slit pores with 2D material spacers also show remarkable ionic transport properties, including transport of protons with complete rejection of larger ions[77] and asymmetric transport between similarly sized cations and ions even in the absence of substantial surface charge.[78] While fluid structure and transport are likely different under 2D confinement than in the 1D systems discussed elsewhere in this article, the implications of these differences for slip flow and ion transport have not been fully established.

Slip Flow Simulations. Molecular dynamics (MD) simulations show wide disparities in slip flow inside carbon nanotubes. Snapshots and illustrations from several MD simulations are shown below (**Figure 1-3**). Slip lengths determined from MD simulation studies differ by about 3 orders of magnitude, varying between 1 nm and 1 μm for water flow through CNTs with diameters ranging from 0.81 nm to 7 nm.[63] The slip length of water can be estimated using both nonequilibrium and equilibrium MD simulations. In nonequilibrium MD (NEMD) simulations, a pressure-driven water flow is simulated by applying an external force on the water molecules. However, results from NEMD simulations can depend sensitively on: (i) the choice of the thermostat used to maintain the temperature of the water molecules and CNT;[81] (ii) the length of the CNT when considering finite-size CNTs due to entrance/exit effects;[82] and (iii) the type of fitting of the velocity profile used to obtain the slip length due to the nearly plug-like velocity profile of water inside CNTs.[63] In contrast, equilibrium MD simulations of water confined inside a periodic CNT can be carried out to obtain the slip length reliably based on the Green-Kubo relationship.[50]

Several factors have contributed to the large variation in the slip lengths of water reported in previous MD simulation studies, including: (i) the use of different methods (e.g., NEMD vs. equilibrium MD) to calculate the slip length; (ii) the nature and strength of the force field used to model water-carbon interactions; and (iii) the water model used to model water-water interactions inside the CNT.[83] The concept of slip length itself is ambiguous in the case of 0.8 to 1.6 nm diameter CNTs. In such small pores, water molecules arrange in separate chains connected through intra-chain and inter-chain hydrogen bonding, and so the water velocity profile is not well-defined. Therefore, it is more reasonable to describe the water flow rate in terms of the CNT permeability, which is expressed as a function of the water friction coefficient.[50] Additional studies are required to elucidate the dependence of the CNT permeability on water-CNT and water-water interactions.
It is noteworthy that previous MD simulation studies have used a simple pair-wise additive Lennard-Jones potential to model the interactions of water molecules with CNTs. However, water, as a polar solvent, can exert strong electric fields that can result in a significant polarization of the carbon atoms in CNTs. Polarizable force fields, which can self-consistently model the polarization and dispersion energy components of the water-CNT binding energy, can be used to obtain a more realistic modeling of the water-CNT interface at a modest increase in computational cost.[30] Additionally, hybrid quantum mechanical/molecular mechanics (QM/MM) and full *ab initio* molecular dynamics (AIMD) simulations can be carried out to obtain more accurate estimates of the friction coefficient of water inside some of the small-diameter CNTs, although the computational cost for carrying out these simulations will be significantly higher than that incurred using classical, force-field-based MD simulations.[84] Finally, the study of fluid

flow through nanotubes made of heteropolar nanomaterials, such as molybdenum disulfide and hexagonal boron nitride, will allow for decoupling the effects of electrostatic and London dispersion forces on nanofluidic phenomena.[31, 85, 86]

1.1.2 Phase Transitions in SDNs

Fluids confined in nanopores exhibit significant distortions of the temperature-pressure phase boundary. This has been shown experimentally in carbon nanotubes,[10, 49] and discussed at length for fluids in nanoporous silica.[87] These distorted phase transitions can be described by modifying the Gibbs-Thomson equation with the Turnbull coefficient.[49] This coefficient, which was originally proposed in metal nucleation theory, is the ratio of the nanopore-liquid interfacial tension γ_{SL} to the enthalpy of fusion ΔH_m of the liquid (which is also proportional to the molar volume to the two-thirds power, ${V_m}^{2/3}$),[88] and has been shown to be invariant with pore size for a given liquid. In this model, the change in freezing point is given by

$$\Delta T_f = T_{f,bulk} - T_{f,pore} = \frac{2T_{f,bulk}V_m\gamma_{SL}}{r_{pore}\Delta H_m} \quad [1.1]$$

where T_f is the freezing point and r_{pore} is the radius of the nanopore.

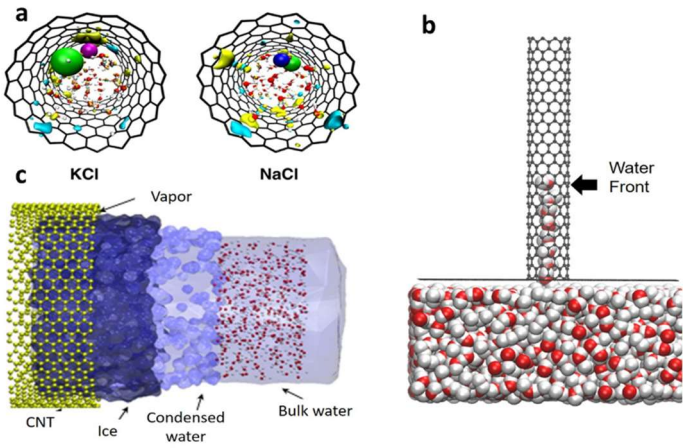

Figure 1-3 | Modeling confinement effects on transport and phase transitions in SDNs. (a) Simulations of NaCl and KCl solutions confined in 1.4 nm diameter CNTs. Reproduced from ref. 23, Journal of Physical Chemistry C, American Chemical Society. (b) MD simulation snapshot showing the capillary filling of a (10,0) chirality CNT by a single file of water molecules. (c) Multiphase structure of water near a CNT interface where the vapor phase, ice, condensed water, and the bulk phase of water co-exist. Reproduced from ref. 26, Journal of Physical Chemistry C, American Chemical Society.

However, no theory currently exists for describing phase transitions in the narrowest of pores.[10] Below approximately 4 nm, water structuring effects cause the Gibbs-Thomson equation to fail, with freezing points varying dramatically and changing non-monotonically with pore diameter. For example, recent simulations[89, 90] and experimental data[10] show water freezing above 100 °C in a narrow range of CNTs close to 1 nm in diameter, and confirm the non-

monotonic dependence on diameter of confined phase transitions predicted by simulation. Experimentally, phase transitions in CNT pores can be tracked by shifts of the radial breathing mode (RBM) using Raman spectroscopy.[10] MD studies have also shown that the phase transition temperature of polar fluids such as water inside CNTs can be strongly modulated by external electric fields.[91-94] However, because the results of force-field-based MD simulations can depend sensitively on the force field parameters used to model water-CNT interactions and on the choice of the water model, it is not yet clear how the complex interplay between water-CNT and water-water interactions determines the phase behavior of water inside CNTs. The thermodynamics and phase behavior of confined water represent a significant knowledge gap that needs to be understood with a new theory and modeling approaches supported by comprehensive experimental data. One promising technique is to incorporate chemically-specific emissive defects in CNTs. These defects can then be used as molecular rulers to resolve the state of the fluid at the single defect level.[19, 20, 95]

1.1.3 Phase Separation under Extreme Confinement

Phase separation, in which a single phase transitions into a two-phase or multiphase co-existence region, is also influenced under the extreme confinement of SDNs.[96-98] Of particular interest is the use of this phenomenon in new nanopore and membrane separation mechanisms.[98, 99] Gravelle et al. noted from MD simulations that CNT membranes may achieve selective transport by nanoconfinement-induced preferential adsorption of water over ethanol.[97] MD studies have shown that gases such as CO_2, O_2 and H_2 from gas-water mixtures exhibit selective physisorption into single-digit CNTs. Furthermore, the solubility difference of gases in water combined with phase separation using SDNs can be exploited for the separation of gases.[100] Nanoscale confinement has also been shown to change the phase diagram and azeotrope location of CCl_4/C_6H_{12} mixtures in activated carbon fibers, with implications for phase separation.[78] In water, it could also be important in future work to investigate the role of dissolved ions on phase transformations, such as freezing or evaporation, which would tend to reject and concentrate ions in the liquid phase after nucleation and potentially generate large disjoining pressures.

Even less is known about the behavior of non-aqueous fluids under similar conditions of extreme nanoconfinement inside SDNs. Solvent-solvent and solvent-solute interactions necessarily change as the fluid phase squeezes into molecularly-sized channels, but the nature of the change is not understood in detail.[96, 98, 101-104] Simulation studies have so far focused on understanding the fluidic structure of liquids, such as methanol[105] and ethanol,[97] confined inside CNTs. On the experimental front, Ellison et al. studied the transport of methanol, lithium ions, and various amino acid cations in the presence of water through a 2.25 nm CNT, and rationalized the different dwell times of the various species based on a simple model that took into account molecular and ionic sizes.[106, 107] Other relevant questions are whether and how confinement in a small nanopore changes the thermodynamics and kinetics of phase separation of ordinarily miscible fluids.[108] For example, de-mixing induced by confinement[97] could be used to control fluid transport or to achieve more efficient or selective separations. Examples could include separating alcohols from water, fractionating hydrocarbons, and separating other complex macromolecular mixtures. For example, Mao and Sinnott used classical MD simulations to investigate the use of CNTs for separation of light gases, such as methane, ethane, and butane, from one another.[109] In another study, Rodriguez et al. studied polar mixtures of water and

acetonitrile nanoconfined between silica surfaces, and found an almost equal reduction in the diffusion coefficients of confined water and acetonitrile molecules as compared to their respective bulk diffusion coefficients.[110] As the nanochannel diameter approaches 1 to 5 nm, surface tension starts to exert an outsized influence on the fluid inside the channel, potentially creating conditions for spontaneous phase separation via spinodal decomposition.[111-113]

1.1.4 The Outsized Impact of Defects

Defects are ubiquitous in nanopores, but their effects on nanofluidic transport are poorly understood. Structurally, defects are deviations within an otherwise continuous and regular conduit, manifesting as changes in diameter or CNT chirality, atomic vacancies or substitutions, dangling bonds, and point defects that can be as simple as the addition of a hydrogen atom or as complex as a charged organic functional group.

In large pores a fluid may flow around a defect site. However, the effect of defects can become increasingly pronounced as the size of the pore/channel decreases. The role of defects in molecular transport by SDNs can be as critical as it is in electrical transport, in which defects are known to dominate conductive pathways at the nanometer scale.[114, 115] In a spectacular example of the power of defects to influence molecular transport, a few strategically placed charges in aquaporin proteins block proton flow through the protein channel.[116] Comparing aquaporin to other protein channels, the elimination of hydrogen-bonding interactions increases the diffusion coefficient of single-file water by up to two orders of magnitude.[117, 118] Similarly, in an AIMD study of synthetic nanopores, Joly et al. found significantly larger friction of the liquid as water flowed past wall defects that caused the molecules to dissociate.[118] In extreme cases, fluid interactions with defects in SDNs, and the resultant pinning effects, could completely change the nature of transport through the pore.

There are two significant challenges to understanding the effects of defects on nanopore transport. First, most defects occur randomly, and it is difficult to locate and resolve them in a pore.[114, 119] Second, there is a lack of tools to resolve defects and quantify their impact on fluidic transport *in situ*. Although techniques such as transmission electron microscopy (TEM) can resolve defects at atomic resolution, such methods typically require ultrahigh vacuum and can cause significant beam damage to nanomaterials, prohibiting a direct correlation between defects and fluid transport.

SDN platforms provide a unique opportunity to quantify the effects of defects on molecular transport. With the development of new tools and synthetic methods to control and probe defects, the effect of defects on fluid transport may be observed unambiguously. Defects can be intentionally implanted to control various material properties, such as electrical conductivity and photoluminescence, and can thereby be used as experimental markers to understand better the system and the effects of molecular transport.[114, 120] When we control and intentionally add defects in a limited manner, their properties can be spatially localized, acting as perturbations rather than completely changing the structure of the host. In combination with advanced imaging techniques, controlled defects can therefore be used to understand behaviors like molecular transport in SDNs. In fact, recent theoretical work has enabled the prediction of the exact shapes of extended vacancy defects or nanopores in graphitic surfaces, thereby

allowing for direct linkages with experimental data through the simulation of realistic defect morphologies in nanofluidic systems.[121]

Single-defect spectroscopy may enable the understanding of how defects affect, and can be used to control, fluid transport.[122] Recent advances in super-resolved hyperspectral imaging[22, 122, 123] and our knowledge of defects in 1D and 2D systems[19, 20, 120, 124, 125] are rapidly making this prospect a reality. For instance, to quantify the effect of molecular defects on nanofluidic transport, single defects can be used as quantum light emitters.[95, 126-128] Such defects can be installed synthetically along single-walled CNTs by covalently attaching organic functional groups to the sidewall and pore mouth of the nanotube.[20, 21] A particularly exciting property is that these emissive defects create potential wells that trap excitons that can recombine to produce bright photoluminescence that is sensitive to the chemical environment.[19, 20, 95, 126, 128, 129] At the single-molecule level, ion pairs can cause much more substantial perturbation to the local environment of the trapped excitons than do individual ions. Thus, it also should be possible to perform spectral differentiation to count ion pairs. With advances in precision spectroscopic techniques, a more detailed understanding of defects in SDN transport is forthcoming.

1.1.5 Correlated Transport of Ions

Strong nanopore confinement, which is often accompanied by partial or complete de-solvation of solutes, gives rise to interesting physical phenomena in which ions and molecules exhibit unusual spatial and temporal correlations.[130, 131] A good theoretical description is currently available only for wide nanopores in dilute solutions (**Figure 1-4**). In these larger nanopores under dilute conditions, when the Debye screening (λ_D) length is larger than the average ionic distance, and the average ionic distance (r_{nn}) is smaller than the pore diameter (d), mean field theories can correctly predict the transport behavior of ionic channels, including interesting physical phenomena such as channel gating and a nonlinear diode-like behavior.[17, 28, 65, 132, 133] In concentrated electrolytes, ion-ion correlations lead to ordering of ions in nanopores, and even to charge inversion in highly charged pores. Ion-ion correlations require a departure from classical mean-field electrostatics models to describe charge inversion, leading to attractive pressures or bridging between like-charged pore walls.[134, 135] Charge inversion can also result in electroosmotic flow reversals and electrophoretic mobility reversals.[28, 136]

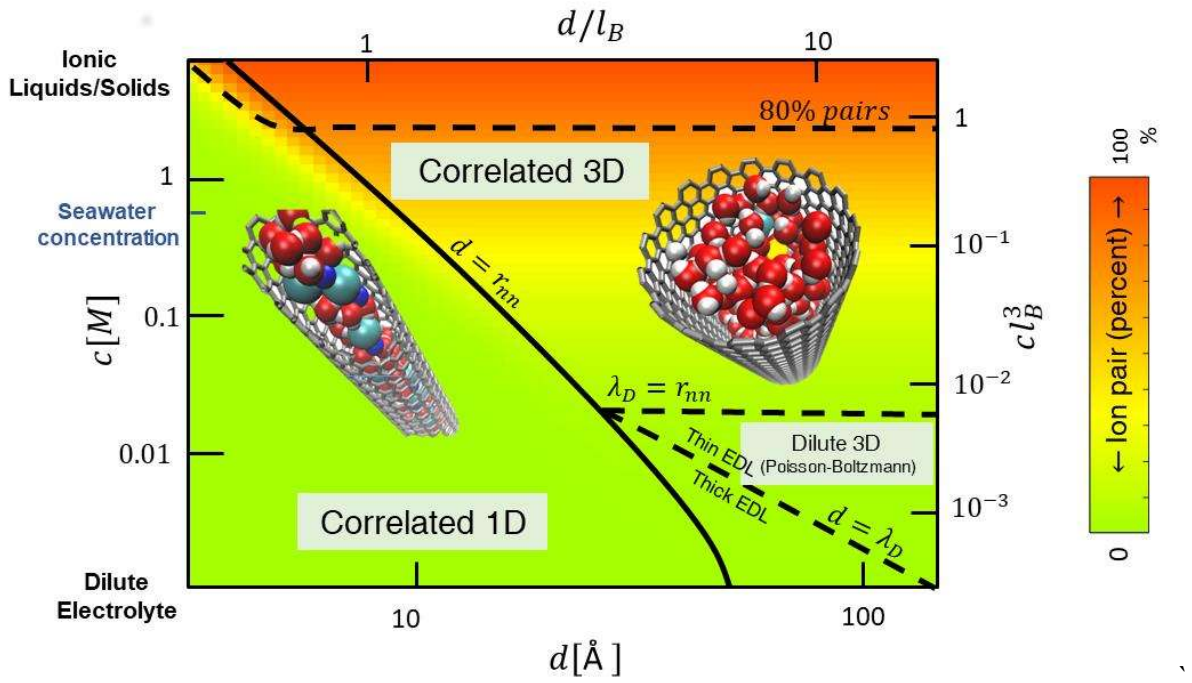

Figure 1-4 | Electrostatics under confinement. Different behavior expected for the electrostatic interactions in a nanopore as a function of ionic concentration (c) and pore radius (d). Classical theories (Poisson-Boltzmann) are only appropriate in the bottom right corner. New approaches are needed under extreme confinement and high concentrations. The Bjerrum length, or the characteristic length for electrostatic interactions, determines the extent of ion pairing relative to r_{nn}, Under extreme confinement, $d < r_{nn}$ or $d < \lambda_D$, 1D correlated transport is expected to dominate. At high concentrations, $\lambda_D < r_{nn}$, 3D correlations and ion pairing can play a bigger role.

The effect of confinement is most pronounced in small nanopores, in which the average ionic separation is larger than the pore diameter and ions effectively form a 1D chain for which 3D continuum models are therefore not relevant.[137] This configuration gives rise to exotic behavior. Extremely small channels can be modeled as discrete Ising chains of charges, giving rise to anomalous capacitance curves.[138, 139] Sub-2-nm pores also display ionic and protonic current fluctuations,[9, 140] as well as the formation of ion pairs and even larger aggregates.[65, 141, 142] Partial removal of ion solvation shells, which prevents those ions from forming long-term pairs in the bulk, leads to ion pairs with unusually long lifetimes in confinement, along with potentially enhanced reaction dynamics.[65, 141, 142] Spontaneous, long-scale ordering in nanopores can also create conditions for efficient and selective transport of particular molecular or ionic species; formation of the hydrogen-bonded single-file water chain in narrow CNTs, for example, gives rise to fast proton conduction via the Grotthuss mechanism.[8, 64] Confinement-induced effects lead to unusually strong correlative transport modes, dramatically enhancing mechanisms such as electroosmotic transport and ion concentration polarization.[143, 144] As hydrated ions become squeezed into narrow gaps with slippery wall surfaces, the distinction between ion solvation shells and the rest of the solution becomes increasingly blurred, increasing the probability of strong electroosmotic and diffusioosmotic coupling effects, which can become dominant in the narrowest of channels.[144, 145] Recent experimental and theoretical work also

highlights the importance of considering charge-regulation effects on nanofluidic transport, where the surface charge density in SDNs depends sensitively on the pH of the solution.[146] Even though these effects are not surprising on an intuitive level, their rigorous treatment has occurred only recently,[145] and experimental efforts are still sparse. The incorporation of these effects to enhance scaling of ionic flux and selectivity for SDNs points to operational realms for nanopore membranes that may circumvent flux-selectivity tradeoffs. Finally, future research also must address the behavior of ionic mixtures confined within nanopores. In one of the few examples to date, the anomalous mole fraction effect, in which permeation of ion mixtures is slower than permeation of either ion individually, was demonstrated inside synthetic nanopores.[147-149]

Modeling the coupling between driving forces under confinement, such as gradients in pressure and electric potential, is essential for our understanding of these unique transport phenomena. Pressure-driven flow through a nanopore will advect ions in the electric double layer, resulting in a streaming current, whereas electric fields conducting ions through a pore will also drive electroosmotic flow in the double layer.[28, 150] The interplay between Coulombic ordering and steric repulsion can influence the thermodynamic driving forces for ion transport.[135, 151, 152] A more general coupled flux model is necessary, especially at high concentrations within a nanopore, as pioneered by Stefan-Maxwell for dilute gases and Onsager for generalized linear irreversible thermodynamics.[153]

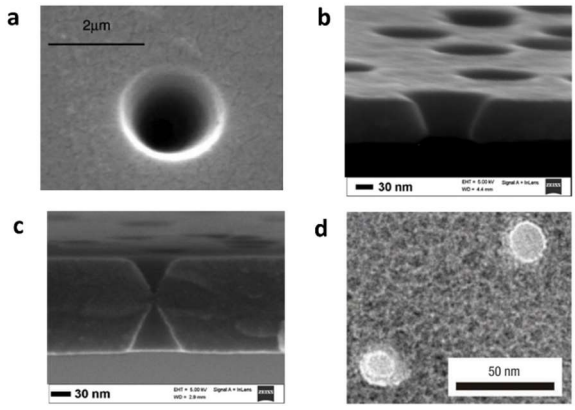

Figure 1-5 | Single-nanopore system construction. (a) Track-etched nanopores in polyimide. Reprinted by permission from Springer Nature: Applied Physics A; Siwy, Z., Dobrev, D., Neumann, R., Trautmann, C., Voss, K. J. A. P. A., Electro-responsive asymmetric nanopores in polyimide with stable ion-current signal, 2003. (b,c) Track-etched nanopores in silicon nitride. Reproduced from ref. 155, National Academy of Sciences. (d) A nanopore drilled by TEM. Reprinted by permission from Springer Nature: Nature Materials; Storm, A., Chen, J., Ling, X., Zandbergen, H., Dekker, C., Fabrication of solid-state nanopores with single-nanometre precision, 2003.

Experimentally, the study of correlated nanopore ion transport could benefit from new approaches to electrical manipulation, spectroscopic probing, and precise pore construction and modification (**Figure 1-5**). When pore geometrical and chemical properties are known and controlled, the presence of spatial and temporal correlations of ions will be made evident by examining the ion current. Ion current through a nanopore is extremely sensitive to the properties

of the pore walls and distributions of ions in the pore. As an example, the effect of charge inversion at a surface can be probed by recording current-voltage curves of asymmetric nanopores.[157] Structurally asymmetric and charged nanopores behave as rectifiers, transporting ions in one direction and hindering ionic transport in the opposite direction; the direction of preferential ion flow depends on the surface potential.[158-160] A nanopore that undergoes charge inversion can be therefore immediately identified by its flipped current-voltage curve (**Figure 1-6**).[157] The magnitude and polarity of effective surface potential can also be measured precisely in nanopores via the so-called reversal potential, i.e. an electrical potential difference established across a membrane in contact with a salt concentration gradient.[161] It is expected that nanoconfinement-induced ion correlation effects, such as the breakdown of electroneutrality,[130, 162] could be probed electrochemically with a nanopore whose geometry and surface chemistry were tuned to make it especially sensitive to the balance of positive and negative charges.

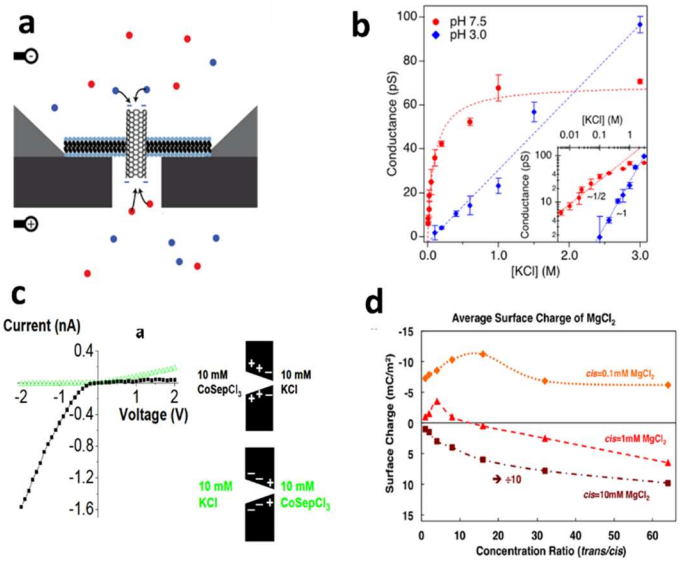

Figure 1-6 | Probing ion transport through SDNs. (a) A platform for single CNT porin ionic conductance measurements. (b) Ionic conductance of individual, 0.8-nm-diameter CNT porins. From Tunuguntla, R. H.; Henley, R. Y.; Yao, Y.-C.; Pham, T. A.; Wanunu, M.; Noy, A., Enhanced water permeability and tunable ion selectivity in subnanometer carbon nanotube porins. *Science* **2017,** *357*, 792-796. Reprinted with permission from AAAS. (c) Local charge inversion induced by trivalent cobalt ions (CoSep) causes the formation of positive surface charges and the appearance of diode-like behavior in individual conical nanopores. Reproduced from ref. 157, Journal of the American Chemical Society, American Chemical Society. (d) Measuring the reversal potential allows the surface charge to be calculated. Data shown are from silica nanochannels and charge inversion was obtained with Mg^{2+}. Reproduced from ref. 161, Nano Letters, American Chemical Society.

Ion correlations may influence the ion selectivity of nanopores.[163] Experiments with single nanopores could provide experimental guidance to such modeling, and help to design systems with new mechanisms of ionic and molecular selectivity. Probing ion correlation

systematically in nanopores of controlled chemical properties, using solvents that vary in dielectric constant and ions that differ in size and valence, would help build a universal description of how correlation of ions influences transport at the nanoscale.[164]

Another important direction of inquiry is the identification of current and electrokinetic fingerprints of ion pairs and aggregates. Extreme confinement can lead to the formation of pairs of ions of the same charge,[131] and that these pairs can be broken with an electric field. Formation of ion pairs of different charge (i.e. pairs containing both cations and anions) has also been reported[130, 142, 165] but it is not known how their presence influences electrokinetic transport. The possibility of tuning the formation of ion pairs by the properties of the pore wall has also been suggested.[142] Nanopores with tunable electrochemical properties could enable an understanding of the role of ion pairs in ionic transport, as well as how to incorporate ion pairs and aggregates into existing models.

1.1.6 Nanoscale Solvation Behavior

Protein ion channels routinely exploit minute differences in solvation behavior to act as exquisitely selective molecular gates (e.g., K^+ ion channels).[166, 167] As confinement approaches the levels seen in SDNs, solvation effects start to diverge from their bulk behavior, with profound effects on transport efficiency and selectivity.[168-173] The energetics of solvation under strong confinement affect nanopore entry and lead to ion-specific modulations of the double-layer structure inside the pore.[23, 24] As an example, in extreme confinement and under double-layer overlap, counter-ions with strong hydration shells, such as sodium ions, were found to create a layered structure close to the charged surfaces.[173-175] This effect was discovered experimentally with a surface-force apparatus (SFA), in which two mica surfaces were brought into close contact with distance controlled with sub-nm precision. Introducing the effects of solvent to solute-solute interactions leads to the prediction of an oscillatory force between two surfaces, an effect that has also been measured with the SFA.[176] These phenomena are only beginning to be probed.

Understanding and exploiting solvation phenomena in synthetic SDNs could lead to a new generation of membranes that are capable of manipulating hydration effects to achieve single-species selectivity in a manner that is virtually impossible with current technologies.[177] Recently, Zwolak and colleagues proposed that dehydration-based selectivity could be indeed the basis for a universal mechanism to achieve selectivity between ions of the same charge, e.g. Na^+ and K^+.[178] Interestingly, it was shown that to optimize ion selectivity, both pore diameter and pore length need to be tuned.[168] These concepts could potentially be extended to design systems that could effectively filter out pharmaceutical compounds that plague water supplies in industrialized nations,[179, 180] harvest Li^+ ions for batteries,[181] or provide efficient and thin exclusive proton-conducting membranes for fuel-cell technologies.[182, 183]

Probing chemistry and organization in SDNs requires a technique that can offer high spatial resolution, such as infrared spectroscopy, Raman spectroscopy,[10, 184, 185] UV/visible (electronic) spectroscopy, fluorescence spectroscopy, X-ray scattering,[186] X-ray photoelectron spectroscopy,[187] optical Kerr effect (OKE) spectroscopy, [18, 188, 189] or neutron diffraction.[190] These techniques can have sufficiently high depth resolution to study solid-liquid interfaces, but

their lateral resolution is typically limited by diffraction or spot size to something on the order of 1 □m. In SDNs, the width of a pore may provide the desired resolution in one lateral direction, but not along the pore axis. A lateral resolution on the nanometer scale would be ideal for understanding, for instance, the chemical bonding in the neighborhood of individual ions. An understanding of the complex interplay among steric, electrostatic, and van der Waals interactions, as well as solvent entropy, becomes possible only at this length scale. Although tip-enhanced Raman spectroscopy (TERS) and other scanning-probe techniques have found success in probing interfaces on this scale,[191,192-195] chemical mapping with roughly 1 nm resolution is not yet routine. Furthermore, the dielectric constants of polar solvents, like water, confined inside SDNs can be dramatically lower than those in the bulk. For example, in a recent experimental study of water confined between hexagonal boron nitride (h-BN) and graphite, Fumagalli et al. reported that the out-of-plane dielectric constant of water drops from 78.5 in the bulk to just 2 inside nanocapillaries.[75] Moreover, the dielectric constants of solvents can also vary with ion concentration.[196] In this regard, the classical Born equation of ion solvation predicts a higher free energy of solvation of an ion in a bulk medium with a higher dielectric constant.[197] However, the manner in which changes in the dielectric constants of solvents confined inside SDNs impacts the solvation of ions remains an open question.

Another issue with many of these techniques is that they are not compatible with every SDN material. Optical spectroscopies are useful for studying behavior in pores in transparent materials. There is a large literature, for instance, in the use of OKE, Raman, and NMR spectroscopies to probe liquid dynamics in silica pores that has led to important insights regarding the behavior of pure solvents. For instance, in OKE spectroscopy,[18, 188, 189] a linearly-polarized pump induces a small net alignment, and thereby a transient birefringence, in a transparent liquid composed of molecules with an anisotropic polarizability. The return to an isotropic orientational distribution is monitored via depolarization of a probe pulse as a function of time delay. This technique has provided a detailed picture of the spatial dependence of orientational relaxation in liquids confined in silica nanopores,[198] and could readily be applied to confined solutions. It is important to note that such studies probe behaviors that are averaged over large numbers of pores, rather than behavior in a single, well-characterized pore. Furthermore, other SDN materials with strong optical signatures, like carbon nanotubes, may present challenges for the use of optical spectroscopies to study confined fluid alone.

Spectroscopic techniques that have never been applied to SDNs may enhance our understanding of solvation behavior under nanoconfinement. Vibrational sum-frequency generation (VSFG) spectroscopy[199-204] is a surface-selective technique that can reveal chemically-specific information at solid/liquid interfaces. For instance, VSFG has been used to show that acetonitrile next to a silica surface forms an unexpected bilayer structure that has a profound influence on the properties of the interface.[198, 205] VSFG probes vibrational modes that are simultaneously IR and Raman active, and by collecting spectra under different polarization conditions, it is possible to obtain information on the structure of interfacial molecules.[201] VSFG has not been applied to fluids confined within SDNs to our knowledge, but has great potential for studying nanopores that are transparent to the relevant colors of light. SDN liquid-solid interfaces and ion-solvent interactions might also be probed with the addition of an electron beam in the form of ultrafast electron crystallography[206] or *in situ* TEM with applied electric fields[207] or magnetic fields,[208] or electron holography.[209]

1.1.7 Enhanced Ionic Selectivity

The translation of SDN physics to multipore membrane systems with precise ionic selectivity remains elusive. Membrane-based technologies have played an important role in separations, including water purification and seawater desalination, for many years.[47, 177, 210, 211] Most state-of-the-art solute-rejecting (e.g. reverse osmosis and nanofiltration) and ion-exchange membranes are polymer films with non-uniform pore characteristics, which hinder precise ion-ion selectivity. In these membranes, size- and charge-based separation are the main mechanisms that govern selectivity, rendering the membranes poorly selective when species with similar size or charge are present.[212-214] On top of the inherent challenge of separating similar species, engineering ultra-selective pores for separation of small ions (e.g., chloride, fluoride, and lithium) is technologically difficult due to the sub-nanometer precision required.[47, 215] Graphene oxide membranes, for instance, demonstrate remarkable molecular selectivity[216] but allow fast transport of small ions.[217] While ion selectivity can be achieved, framework defects and swelling of graphene oxide laminates in water remain issues.[12, 218] For CNT membranes, it is possible to achieve moderate charge- or size-selective transport,[219-221] but scaling is difficult and high selectivity between ions of similar size and charge has not been achieved. The major obstacles for aligned CNT membrane development are the difficulty of growing arrays of CNTs with uniform diameters, the difficulty of controlling the arrangement and quality of the nanotubes in those arrays, [222, 223] the low yield of the fabrication process,[224, 225] and the crude nature of the procedures used to remove the nanotube end caps. An added difficulty is that CNTs would likely need to have diameters less than 1 nm to effect truly selective ion transport. But despite these challenges, the exploration of enhanced ion-ion selectivity in SDNs is a promising area of research. It may assist the development of materials strategies for separating a target ion from multi-ion solutions more generally; example applications include separating Li^+ ions from Na^+ and K^+ ions in seawater and designing an exclusively proton-conducting membrane for fuel cells.[226]

Although major efforts have focused on studying size-based selectivity,[8, 12, 217, 227] emerging research suggests that enhanced ion-ion selectivity in SDNs may be based on differences in ion hydration, charge, or shape properties (**Figure 1-7**). The limited difference in selectivity observed for small ions in membranes with sub-nanometer pores, for instance, is often attributed to hydration and dehydration effects. Specifically, an ion with a smaller radius (e.g., F^- or Na^+) acquires a larger and stronger hydration shell and undergoes lower dehydration at the pore mouth compared to an ion with a larger ionic radius (e.g., Cl^- or K^+).[8, 171] Ion dehydration also underlies the precise selectivity observed in selective-ion biological channels. [228, 229] Here, specific sites within the channel create a cavity with a perfect match for a specific bare ion, compensating energetically for its loss of hydration shell and excluding the permeation of other ions (**Figure 1-7a**).

Knock-on mechanisms have recently been proposed[230] to explain how biological nanopores discriminate similarly sized ions (i.e., Na^+ vs. K^+). Here, fully dehydrated K^+ can pass through a potassium channel all without intervening water molecules, whereas Na^+ does not enter the channel without water. Long-time (i.e., multi-□s) MD simulation has played an essential role in elucidating this mechanism.[231] At the same time, computational predictions are

known to be sensitive not only to the sampling times, which are getting more and more straightforward, but also to the nature of the physics included in the force field. For instance, beyond scaling charges in non-polarizable force fields[232], polarizable force fields[233] have been suggested[234] to capture essential features of divalent cations (e.g., Ca^{2+} vs. Mg^{2+}). Furthermore, effects not captured in any conventional force field, such as charge transfer, have proven essential to describe ion-specific effects in some cases[235]. Thus, predictive modeling in this area requires both development of multi-scale approaches as well as careful consideration of the physics involved.

Experimentally, ion dehydration was recently proposed to explain the Arrhenius-type behavior observed for ion permeation through nanopores and membranes:[8, 12, 236-238]

$$J = A \exp\left(-\frac{E_a}{RT}\right) \qquad [1.2]$$

where J is the ion flux through the membrane, A is the pre-exponential factor, E_a is the activation energy, R is the gas constant, and T is the temperature in Kelvin. Differences in dehydration-based energy barriers have been shown to boost selectivity between ions permeating through nanopores.[12, 237-240] Experiments that quantify energy barriers as a function of pore diameter, or location-specific functionalization of the pore mouths or bodies of SDNs, may shed light on the physical and chemical effects that induce dehydration can lead to selective transport.

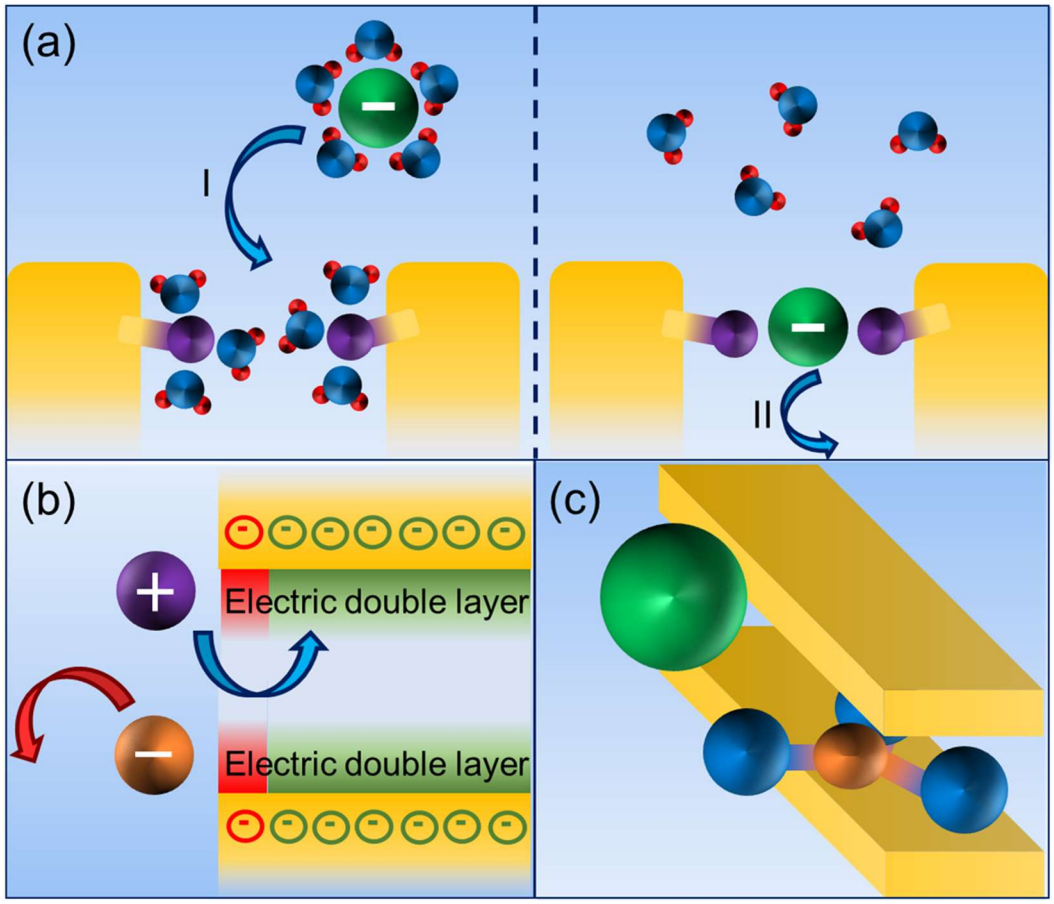

Figure 1-7 | Potential mechanisms for increasing ionic selectivity. These mechanisms include selectivity by (a) ion dehydration; (b) surface charge, in-pore charge, and electric double-layer effects; and (c) shape-related steric exclusion. By using a combination of these selectivity mechanisms, it may be possible to design SDN systems with unprecedented ionic selectivity.

Another aspect of SDNs that can be used for enhanced ionic selectivity is their electric interaction with ions (**Figure 1-7b**). In general, charged pores repel co-ions, and the extent of repulsion is correlated with the extent of ion charge. However, recent results show that even ions with the same charge (e.g., Cl^- and NO_3^-) are affected differently by a charged membrane,[33] a phenomenon that calls for fundamental investigation of charge-exclusion mechanisms. These results cannot be predicted by traditional models for transport and exclusion of ions in nanofiltration membranes, based on the extended Nernst-Planck equation,[241, 242] even when this equation is modified to include contributions from ion-specific effects in the electric double layer. Experimentally, state-of-the-art membranes are either neutral or contain charged groups on their surfaces and within their pores. As a result, surface and in-pore charge effects on ion selectivity cannot be distinguished. SDNs that have charges localized either in the pore mouth or pore body (e.g., CNTs with a functionalized and negatively charged pore mouth)[8] may provide an opportunity to highlight surface and/or in-pore charge effects. MD simulation studies have shown that the free-energy barrier for ion transport through CNTs can be enhanced significantly by chemical functionalization of the pore mouth, raising the possibility of practical applications of SDNs that are chemically functionalized at particular sites.[243, 244]

Finally, pore shape influences selectivity **(Figure 1-7c)**. This effect can occur, for example, between non-spherical polyatomic ions (e.g., NO_3^-, ClO_4^-, and AsO_4^-) and spherical monoatomic ions (e.g., Cl^- and F^-), as evidenced by discrepancies between experimental energy barriers and theoretical hydration free energies.[33, 238, 245, 246] Structural characterization and modeling techniques such as MD simulations can assess the effect of pore mouth and pore-body shape on permeant selectivity for monoatomic and polyatomic ions.[246] Overall, fundamental questions about the effect of pore geometry, charge-based selectivity, and dehydration on selective ionic transport will need to be addressed in future research, with the goal of creating rules for the rational design of selective SDN membranes.

1.1.8 Conclusions

In this Review we have highlighted seven knowledge gaps that are central to the study of molecular and ionic transport in single-digit nanopores. These gaps include the presence and magnitude of slip flow, phase behavior under nanoconfinement, nanoconfined phase separation, the impact of defects on transport, correlated ion transport inside SDNs, nanoscale solvation behavior, and the engineering of enhanced ionic selectivity. Although nanoporous materials with characteristic dimensions smaller than 10 nm have been studied for some time, the confluence within the last decade of precise model systems with well-characterized pores, new spectroscopic techniques, and improved simulations has subjected these knowledge gaps to studies at unprecedented new levels of detail. Although some knowledge gaps, such as the scaling of slip length with SDN diameter, have been posed but not resolved, other knowledge gaps, like the

impact of a single defect on molecular transport inside a SDN, are only now coming into focus. We expect that the study of molecular and ionic transport under extreme confinement will test the limits of bulk-scale fluid mechanics, provide opportunities for the exploration of new synthetic and spectroscopic techniques, and inform our understanding of transport at molecular interfaces. We also anticipate the development of fundamentally new technologies, as the dramatic effects of nanoconfinement give rise to adsorbents, membranes, and fluidic platforms with extraordinary transport efficiencies and selectivities.

1.2 References

1. Sircar, S.; Golden, T. C.; Rao, M. B. Activated carbon for gas separation and storage. *Carbon* **1996,** *34*, 1-12.
2. Drage, T. C.; Blackman, J. M.; Pevida, C.; Snape, C. E. Evaluation of activated carbon adsorbents for CO2 capture in gasification. *Energy Fuels* **2009,** *23*, 2790-2796.
3. Bansal, R. C.; Goyal, M. *Activated carbon adsorption*. CRC Press: Boca Raton, FL, 2005.
4. Auerbach, S. M.; Carrado, K. A.; Dutta, P. K. *Handbook of zeolite science and technology*. CRC Press: Boca Raton, FL, 2003.
5. Davis, M. E. Ordered porous materials for emerging applications. *Nature* **2002,** *417*, 813-821.
6. Lee, K. P.; Arnot, T. C.; Mattia, D. J. A review of reverse osmosis membrane materials for desalination—development to date and future potential. *J. Membr. Sci.* **2011,** *370*, 1-22.
7. Mohammad, A. W.; Teow, Y.; Ang, W.; Chung, Y.; Oatley-Radcliffe, D.; Hilal, N. Nanofiltration membranes review: Recent advances and future prospects. *Desalination* **2015,** *356*, 226-254.
8. Tunuguntla, R. H.; Henley, R. Y.; Yao, Y.-C.; Pham, T. A.; Wanunu, M.; Noy, A. Enhanced water permeability and tunable ion selectivity in subnanometer carbon nanotube porins. *Science* **2017,** *357*, 792-796.
9. Lee, C. Y.; Choi, W.; Han, J.-H.; Strano, M. S. Coherence Resonance in a Single-Walled Carbon Nanotube Ion Channel. *Science* **2010,** *329*, 1320-1324.
10. Agrawal, K. V.; Shimizu, S.; Drahushuk, L. W.; Kilcoyne, D.; Strano, M. S. Observation of extreme phase transition temperatures of water confined inside isolated carbon nanotubes. *Nat. Nanotechnol.* **2017,** *12*, 267-274.
11. Siria, A.; Poncharal, P.; Biance, A.-L.; Fulcrand, R.; Blase, X.; Purcell, S. T.; Bocquet, L. Giant osmotic energy conversion measured in a single transmembrane boron nitride nanotube. *Nature* **2013,** *494*, 455-458.
12. Abraham, J.; Vasu, K. S.; Williams, C. D.; Gopinadhan, K.; Su, Y.; Cherian, C. T.; Dix, J.; Prestat, E.; Haigh, S. J.; Grigorieva, I. V.; Carbone, P.; Geim, A. K.; Nair, R. R. Tunable sieving of ions using graphene oxide membranes. *Nat. Nanotechnol.* **2017,** *12*, 546-551.
13. Zhou, K.-G.; Vasu, K.; Cherian, C.; Neek-Amal, M.; Zhang, J. C.; Ghorbanfekr-Kalashami, H.; Huang, K.; Marshall, O.; Kravets, V.; Abraham, J. J. Electrically controlled water permeation through graphene oxide membranes. *Nature* **2018**, *559,* 236-240.
14. Siwy, Z.; Kosińska, I.; Fuliński, A.; Martin, C. Asymmetric diffusion through synthetic nanopores. *Phys. Rev. Lett.* **2005,** *94*, 048102.
15. Martin, C. R.; Siwy, Z. S. Learning Nature's Way: Biosensing with Synthetic Nanopores. *Science* **2007,** *317*, 331-332.
16. Guan, W.; Reed, M. A. Electric Field Modulation of the Membrane Potential in Solid-State Ion Channels. *Nano Lett.* **2012,** *12*, 6441-6447.
17. Daiguji, H.; Yang, P. D.; Majumdar, A. Ion transport in nanofluidic channels. *Nano Lett.* **2004,** *4*,

137-142.
18. Zhong, Q.; Fourkas, J. T. Optical Kerr Effect Spectroscopy of Simple Liquids. *J. Phys. Chem. B* **2008,** *112*, 15529-15539.
19. Kwon, H.; Furmanchuk, A. O.; Kim, M.; Meany, B.; Guo, Y.; Schatz, G. C.; Wang, Y. Molecularly Tunable Fluorescent Quantum Defects. *J. Am. Chem. Soc* **2016,** *138*, 6878-6885.
20. Piao, Y. M.; Meany, B.; Powell, L. R.; Valley, N.; Kwon, H.; Schatz, G. C.; Wang, Y. Brightening of carbon nanotube photoluminescence through the incoporation of sp3 defects. *Nat. Chem.* **2013,** *5*, 840-845.
21. Wu, X.; Kim, M.; Kwon, H.; Wang, Y. Photochemical Creation of Fluorescent Quantum Defects in Semiconducting Carbon Nanotube Hosts. *Angew. Chem., Int. Ed.* **2018,** *57*, 648-653.
22. Danné, N.; Kim, M.; Godin, A. G.; Kwon, H.; Gao, Z. H.; Wu, X.; Hartmann, N.; Doorn, S. K.; Lounis, B.; Wang, Y. H.; Cognet, L. Ultrashort carbon nanotubes that fluoresce brightly in the near infrared. *ACS Nano* **2018**, *12,* 6059-6065.
23. Pham, T. A.; Mortuza, S. G.; Wood, B. C.; Lau, E. Y.; Ogitsu, T.; Buchsbaum, S. F.; Siwy, Z. S.; Fornasiero, F.; Schwegler, E. Salt solutions in carbon nanotubes: The role of cation− π interactions. *J. Phys. Chem. C* **2016,** *120*, 7332-7338.
24. Kulik, H. J.; Schwegler, E.; Galli, G. Probing the structure of salt water under confinement with first-principles molecular dynamics and theoretical x-ray absorption spectroscopy. *J. Phys. Chem. Lett.* **2012,** *3*, 2653-2658.
25. Pham, T. A.; Ogitsu, T.; Lau, E. Y.; Schwegler, E. Structure and dynamics of aqueous solutions from PBE-based first-principles molecular dynamics simulations. *J. Chem. Phys.* **2016,** *145*, 154501.
26. Barati Farimani, A.; Aluru, N. R. Existence of multiple phases of water at nanotube interfaces. *J. Phys. Chem. C.* **2016,** *120*, 23763-23771.
27. Bhadauria, R.; Aluru, N. R. Multiscale modeling of electroosmotic flow: Effects of discrete ion, enhanced viscosity, and surface friction. *J. Chem. Phys.* **2017,** *146*, 184106.
28. Biesheuvel, P. M.; Bazant, M. Z. Analysis of ionic conductance of carbon nanotubes. *Phys. Rev. E* **2016,** *94*, 050601.
29. Storey, B. D.; Bazant, M. Z. Effects of electrostatic correlations on electrokinetic phenomena. *Phys. Rev. E* **2012,** *86*, 056303.
30. Misra, R. P.; Blankschtein, D. Insights on the Role of Many-Body Polarization Effects in the Wetting of Graphitic Surfaces by Water. *J. Phys. Chem. C* **2017,** *121*, 28166-28179.
31. Rajan, A. G.; Sresht, V.; Padua, A. A. H.; Strano, M. S.; Blankschtein, D. Dominance of Dispersion Interactions and Entropy over Electrostatics in Determining the Wettability and Friction of Two-Dimensional MoS_2 Surfaces. *ACS Nano* **2016,** *10*, 9145-9155.
32. Joseph, S.; Aluru, N. R. Hierarchical multiscale simulation of electrokinetic transport in silica nanochannels at the point of zero charge. *Langmuir* **2006,** *22*, 9041-9051.
33. Epsztein, R.; Shaulsky, E.; Dizge, N.; Warsinger, D. M.; Elimelech, M., Role of Ionic Charge Density in Donnan Exclusion of Monovalent Anions by Nanofiltration. *Environ. Sci. Technol.* **2018,** *52*, 4108-4116.
34. Secchi, E.; Marbach, S.; Niguès, A.; Stein, D.; Siria, A.; Bocquet, L., Massive radius-dependent flow slippage in carbon nanotubes. *Nature* **2016,** *537*, 210-213.
35. Holt, J. K.; Park, H. G.; Wang, Y.; Stadermann, M.; Artyukhin, A. B.; Grigoropoulos, C. P.; Noy, A.; Bakajin, O. Fast mass transport through sub-2-nanometer carbon nanotubes. *Science* **2006,** *312*, 1034-1037.
36. Majumder, M.; Chopra, N.; Andrews, R.; Hinds, B. J. Nanoscale hydrodynamics: Enhanced flow

in carbon nanotubes. *Nature* **2005,** *438*, 44-44.
37. Rassaei, L.; Mathwig, K.; Kang, S.; Heering, H. A.; Lemay, S. G. Integrated Biodetection in a Nanofluidic Device. *ACS Nano* **2014,** *8*, 8278-8284.
38. Das, R.; Ali, M. E.; Hamid, S. B. A.; Ramakrishna, S.; Chowdhury, Z. Z. Carbon nanotube membranes for water purification: A bright future in water desalination. *Desalination* **2014,** *336*, 97-109.
39. Ghosh, S.; Sood, A. K.; Kumar, N. Carbon Nanotube Flow Sensors. *Science* **2003,** *299*, 1042-1044.
40. Tunuguntla, R.; Allen, F.; Kim, K.; Bellivieau, A.; Noy, A. Ultrafast proton transport in sub-1-nm diameter carbon nanotube porins. *Nat. Nanotechnol.* **2016,** *11*, 639–644.
41. Agre, P.; King, L. S.; Yasui, M.; Guggino, W. B.; Ottersen, O. P.; Fujiyoshi, Y.; Engel, A.; Nielsen, S., Aquaporin water channels – from atomic structure to clinical medicine. *J. Physiol. (Oxford, U. K.)* **2002,** *542*, 3-16.
42. Zhao, Y.; Xie, Y.; Liu, Z.; Wang, X.; Chai, Y.; Yan, F. J. Two-Dimensional Material Membranes: An Emerging Platform for Controllable Mass Transport Applications. *Small* **2014,** *10*, 4521-4542.
43. Meek, S. T.; Greathouse, J. A.; Allendorf, M. D. Metal-organic frameworks: A rapidly growing class of versatile nanoporous materials. *Adv. Mater. (Weinheim, Ger.)* **2011,** *23*, 249-267.
44. Morris, R. E.; Wheatley, P. S. Gas storage in nanoporous materials. *Ang. Chem. Int. Ed.* **2008,** *47*, 4966-4981.
45. Zhai, Y.; Dou, Y.; Zhao, D.; Fulvio, P. F.; Mayes, R. T.; Dai, S. Carbon materials for chemical capacitive energy storage. *Adv. Mater. (Weinheim, Ger.)* **2011,** *23*, 4828-4850.
46. Gargiulo, N.; Pepe, F.; Caputo, D. J. CO_2 adsorption by functionalized nanoporous materials: A review. *J. Nanosci. Nanotechnol.* **2014,** *14*, 1811-1822.
47. Werber, J. R.; Osuji, C. O.; Elimelech, M., Materials for next-generation desalination and water purification membranes. *Nat. Rev. Mater.* **2016,** *1*, 16018.
48. Kar, S.; Bindal, R.; Tewari, P. J. Carbon nanotube membranes for desalination and water purification: Challenges and opportunities. *Nano Today* **2012,** *7*, 385-389.
49. Shimizu, S.; Agrawal, K. V.; O'Mahony, M.; Drahushuk, L. W.; Manohar, N.; Myerson, A. S.; Strano, M. S. Understanding and Analyzing Freezing-Point Transitions of Confined Fluids within Nanopores. *Langmuir* **2015,** *31*, 10113-10118.
50. Falk, K.; Sedlmeier, F.; Joly, L.; Netz, R. R.; Bocquet, L., Molecular origin of fast water transport in carbon nanotube membranes: superlubricity versus curvature dependent friction. *Nano Lett.* **2010,** *10*, 4067-4073.
51. Whitby, M.; Cagnon, L.; Thanou, M.; Quirke, N. Enhanced fluid flow through nanoscale carbon pipes. *Nano Lett.* **2008,** *8*, 2632-2637.
52. Sinha, S.; Pia Rossi, M.; Mattia, D.; Gogotsi, Y.; Bau, H. H., Induction and measurement of minute flow rates through nanopipes. *Phys. Fluids* **2007,** *19*, 013603.
53. Qin, X.; Yuan, Q.; Zhao, Y.; Xie, S.; Liu, Z., Measurement of the rate of water translocation through carbon nanotubes. *Nano Lett.* **2011,** *11*, 2173-2177.
54. Du, F.; Qu, L.; Xia, Z.; Feng, L.; Dai, L., Membranes of vertically aligned superlong carbon nanotubes. *Langmuir* **2011,** *27*, 8437-8443.
55. Majumder, M.; Chopra, N.; Hinds, B. J., Mass Transport through Carbon Nanotube Membranes in Three Different Regimes: Ionic Diffusion and Gas and Liquid Flow. *ACS Nano* **2011,** *5*, 3867-3877.
56. Majumder, M.; Corry, B., Anomalous decline of water transport in covalently modified carbon nanotube membranes. *Chem. Commun. (London)* **2011,** *47*, 7683-7685.

57. Kotsalis, E. M.; Walther, J. H.; Koumoutsakos, P. Multiphase water flow inside carbon nanotubes. *Int. J. Multiphase Flow* **2004,** *30*, 995-1010.
58. Thomas, J. A.; McGaughey, A. J. Reassessing fast water transport through carbon nanotubes. *Nano Lett.* **2008,** *8*, 2788-2793.
59. Joseph, S.; Aluru, N. R. Why are carbon nanotubes fast transporters of water? *Nano Lett.* **2008,** *8*, 452-458.
60. Thomas, J. A.; McGaughey, A. J. H.; Kuter-Arnebeck, O. Pressure-driven water flow through carbon nanotubes: Insights from molecular dynamics simulation. *Int. J. Therm. Sci.* **2010,** *49*, 281-289.
61. Babu, J. S.; Sathian, S. P. The role of activation energy and reduced viscosity on the enhancement of water flow through carbon nanotubes. *J. Chem. Phys.* **2011,** *134,* 194509.
62. Ma, M. D.; Shen, L. M.; Sheridan, J.; Liu, J. Z.; Chen, C. O.; Zheng, Q. S. Friction of water slipping in carbon nanotubes. *Phys. Rev. E* **2011,** *83*, 036316.
63. Kannam, S. K.; Todd, B. D.; Hansen, J. S.; Daivis, P. J. How fast does water flow in carbon nanotubes? *J. Chem. Phys.* **2013,** *138*, 094701.
64. Hummer, G.; Rasaiah, J. C.; Noworyta, J. P. Water conduction through the hydrophobic channel of a carbon nanotube. *Nature* **2001,** *414*, 188-190.
65. Wu, J.; Gerstandt, K.; Zhang, H.; Liu, J.; Hinds, B. J. Electrophoretically induced aqueous flow through single-walled carbon nanotube membranes. *Nat. Nanotechnol.* **2012,** *7*, 133-139.
66. Hulteen, J. C.; Jirage, K. B.; Martin, C. R. Introducing chemical transport selectivity into gold nanotubule membranes. *J. Am. Chem. Soc.* **1998,** *120*, 6603-6604.
67. Nishizawa, M.; Menon, V. P.; Martin, C. R. J. S., Metal nanotubule membranes with electrochemically switchable ion-transport selectivity. *Science* **1995,** *268*, 700-702.
68. Jirage, K. B.; Hulteen, J. C.; Martin, C. R. Nanotubule-based molecular-filtration membranes. *Science* **1997,** *278*, 655-658.
69. Geng, J.; Kim, K.; Zhang, J.; Tunuguntla, R.; Comolli, L.; Allen, F.; Cho, K.; Munoz, D.; Wang, Y.; Grigoropoulos, C. P.; Ajo-Franklin, C. M.; Noy, A. Stochastic transport through carbon nanotubes in lipid bilayers and live cell membranes. *Nature* **2014,** *514*, 612-615.
70. Cambré, S.; Schoeters, B.; Luyckx, S.; Goovaerts, E.; Wenseleers, W., Experimental Observation of Single-File Water Filling of Thin Single-Wall Carbon Nanotubes Down to Chiral Index (5,3). *Phys. Rev. Lett.* **2010,** *104*, 207401.
71. Kolesnikov, A. I.; Zanotti, J.-M.; Loong, C.-K.; Thiyagarajan, P.; Moravsky, A. P.; Loutfy, R. O.; Burnham, C. J., Anomalously Soft Dynamics of Water in a Nanotube: A Revelation of Nanoscale Confinement. *Phys. Rev. Lett.* **2004,** *93*, 035503.
72. Dellago, C.; Naor, M. M.; Hummer, G. Proton Transport through Water-Filled Carbon Nanotubes. *Phys. Rev. Lett.* **2003,** *90*, 105902.
73. Geim, A. K.; Grigorieva, I. V. Van der Waals heterostructures. *Nature,* **2013,** *499* (7459), 419.
74. Radha, B.; Esfandiar, A.; Wang, F.; Rooney, A.; Gopinadhan, K.; Keerthi, A.; Mishchenko, A.; Janardanan, A.; Blake, P.; Fumagalli, L. Molecular transport through capillaries made with atomic-scale precision. *Nature,* **2016,** *538*, 222-225.
75. Fumagalli, L.; Esfandiar, A.; Fabregas, R.; Hu, S.; Ares, P.; Janardanan, A.; Yang, Q.; Radha, M.; Taniguchi, T.; Watanabe, K. Anomalously low dielectric constant of confined water. *Science,* **2018,** *360*, 1339-1342.
76. Keerthi, A.; Geim, A.; Janardanan, A.; Rooney, A.; Esfandiar, A.; Hu, S.; Dar, S.; Grigorieva, I.; Haigh, S.; Wang, F. Ballistic molecular transport through two-dimensional channels. *Nature,* **2018,** *558*, 420-424.

77. Gopinadhan, K.; Hu, S.; Esfandiar, A.; Lozada-Hidalgo, M.; Wang, F.; Yang, Q.; Tyurnina, A.; Keerthi, A.; Radha, B.; Geim, A. Complete steric exclusion of ions and proton transport through confined monolayer water. *Science,* **2019,** *363*, 145-148.
78. Esfandiar, A.; Radha, B.; Wang, F.; Yang, Q.; Hu, S.; Garaj, S.; Nair, R.; Geim, A.; Gopinadhan, K. Size effect in ion transport through angstrom-scale slits. *Science,* **2017,** *358*, 511-513.
79. Neek-Amal, M.; Peeters, F. M.; Grigorieva, I. V.; Geim, A. K. Commensurability effects in viscosity of nanoconfined water. *ACS Nano* **2016,** *10*, 3685-3692.
80. Algara-Siller, G.; Lehtinen, O.; Wang, F.; Nair, R.; Kaiser, U.; Wu, H.; Geim, A.; Grigorieva, I. Square ice in graphene nanocapillaries. *Nature*, **2015,** *519* (7544), 443.
81. Sam, A.; Kannam, S. K.; Hartkamp, R.; Sathian, S. P., Water flow in carbon nanotubes: The effect of tube flexibility and thermostat. *J. Chem. Phys.* **2017,** *146*, 234701.
82. Walther, J. H.; Ritos, K.; Cruz-Chu, E. R.; Megaridis, C. M.; Koumoutsakos, P. Barriers to Superfast Water Transport in Carbon Nanotube Membranes. *Nano Lett.* **2013,** *13*, 1910-1914.
83. Berendsen, H. J. C.; Grigera, J. R.; Straatsma, T. P. The missing term in effective pair potentials. *J. Phys. Chem.* **1987,** *91*, 6269-6271.
84. Tocci, G.; Joly, L.; Michaelides, A. Friction of water on graphene and hexagonal boron nitride from ab initio methods: very different slippage despite very similar interface structures. *Nano Lett.* **2014,** *14*, 6872-6877.
85. Govind Rajan, A.; Strano, M. S.; Blankschtein, D. J. Liquids with Lower Wettability can Exhibit Higher Friction on Hexagonal Boron Nitride: The Intriguing Role of Solid-Liquid Electrostatic Interactions. *Nano Lett.* **2019,** *19,* 1539-1551.
86. Wei, X.; Luo, T. J. Effects of electrostatic interaction and chirality on the friction coefficient of water flow inside single-walled carbon nanotubes and boron nitride nanotubes. *J. Phys. Chem. C* **2018,** *122*, 5131-5140.
87. Coasne, B.; Galarneau, A.; Pellenq, R. J.; Di Renzo, F. Adsorption, intrusion and freezing in porous silica: the view from the nanoscale. *Chem. Soc. Rev.* **2013,** *42*, 4141-4171.
88. Laird, B. B., The solid–liquid interfacial free energy of close-packed metals: Hard-spheres and the Turnbull coefficient. *J. Chem. Phys.* **2001,** *115*, 2887-2888.
89. Pugliese, P.; Conde, M. M.; Rovere, M.; Gallo, P. Freezing Temperatures, Ice Nanotubes Structures, and Proton Ordering of TIP4P/ICE Water inside Single Wall Carbon Nanotubes. *J. Phys. Chem. B* **2017,** *121*, 10371-10381.
90. Raju, M.; van Duin, A.; Ihme, M. Phase transitions of ordered ice in graphene nanocapillaries and carbon nanotubes. *Sci. Rep.* **2018,** *8,* 3851.
91. Fu, Z.; Luo, Y.; Ma, J.; Wei, G. Phase transition of nanotube-confined water driven by electric field. *J. Chem. Phys.* **2011,** *134*, 154507.
92. Wu, X.; Lu, L.; Zhu, Y.; Wei, M.; Guo, X.; Lu, X. Changes in CNT-confined water structural properties induced by the variation in water molecule orientation. *Mol. Simul.* **2012,** *38*, 1094-1102.
93. Qian, Z.; Fu, Z.; Wei, G. Influence of electric fields on the structure and structure transition of water confined in a carbon nanotube. *J. Chem Phys.* **2014,** *140*, 154508.
94. He, Y.; Sun, G.; Koga, K.; Xu, L. Electrostatic field-exposed water in nanotube at constant axial pressure. *Sci. Rep.* **2014,** *4*, 6596.
95. Kwon, H.; Kim, M.; Meany, B.; Piao, Y.; Powell, L. R.; Wang, Y. Optical Probing of Local pH and Temperature in Complex Fluids with Covalently Functionalized, Semiconducting Carbon Nanotubes. *J. Phys. Chem. C* **2015,** *119*, 3733-3739.
96. Le, T. T. B.; Striolo, A.; Gautam, S. S.; Cole, D. R. Propane-Water Mixtures Confined within

Cylindrical Silica Nanopores: Structural and Dynamical Properties Probed by Molecular Dynamics. *Langmuir* **2017,** *33*, 11310-11320.
97. Gravelle, S.; Yoshida, H.; Joly, L.; Ybert, C.; Bocquet, L. Carbon membranes for efficient water-ethanol separation. *J. Chem. Phys* **2016,** *145,* 124708.
98. Gelb, L. D.; Gubbins, K. E.; Radhakrishnan, R.; Sliwinska-Bartkowiak, M. Phase separation in confined systems. *Rep. Prog. Phys.* **1999,** *62*, 1573-1659.
99. Czwartos, J.; Coasne, B.; Gubbins, K. E.; Hung, F. R.; Sliwinska-Bartkowiak, M. Freezing and melting of azeotropic mixtures confined in nanopores: experiment and molecular simulation. *Mol. Phys.* **2005,** *103*, 3103-3113.
100. Lee, J.; Aluru, N. R. Water-solubility-driven separation of gases using graphene membrane. *J. Membr. Sci.* **2013,** *428*, 546-553.
101. Ganji, M. D.; Mirzaei, S.; Dalirandeh, Z. Molecular origin of drug release by water boiling inside carbon nanotubes from reactive molecular dynamics simulation and DFT perspectives. *Sci. Rep.* **2017,** *7,* 4669.
102. Luo, S.; Lutkenhaus, J. L.; Nasrabadi, H. Confinement-Induced Supercriticality and Phase Equilibria of Hydrocarbons in Nanopores. *Langmuir* **2016,** *32*, 11506-11513.
103. Shimizu, R.; Tanaka, H., Impact of complex topology of porous media on phase separation of binary mixtures. *Sci. Adv.* **2017,** *3*, 1-9.
104.Muthulakshmi, T.; Dutta, D.; Priya, M.; Pujari, P. K. Evidence for confinement induced phase separation in ethanol–water mixture: a positron annihilation study. *J. Phys. Cond. Matt.* **2018,** *30*, 025001.
105. Zhao, W.-H.; Shang, B.; Du, S.-P.; Yuan, L.-F.; Yang, J.; Cheng Zeng, X. J. Highly selective adsorption of methanol in carbon nanotubes immersed in methanol-water solution. *J. Chem. Phys.* **2012,** *137*, 034501.
106. Ellison, M. D.; Menges, S.; Nebel, L.; D'Arcangelo, G.; Kramer, A.; Drahushuk, L.; Benck, J.; Shimizu, S.; Strano, M. S. Electrokinetic Transport of Methanol and Lithium Ions Through a 2.25-nm-Diameter Carbon Nanotube Nanopore. *J. Phys. Chem. C* **2017,** *121*, 2005-2013.
107. Ellison, M. D.; Bricker, L.; Nebel, L.; Miller, J.; Menges, S.; D'Arcangelo, G.; Kramer, A.; Drahushuk, L.; Benck, J.; Shimizu, S. J. Transport of Amino Acid Cations through a 2.25-nm-Diameter Carbon Nanotube Nanopore: Electrokinetic Motion and Trapping/Desorption. *J. Phys. Chem. C* **2017,** *121*, 27709-27720.
108. Kanda, H.; Makino, H., Liquid-liquid phase separation of binary Lennard-Jones fluid in slit nanopores. *Adsorption* **2008,** *14*, 485-491.
109. Mao, Z.; Sinnott, S. B. Separation of organic molecular mixtures in carbon nanotubes and bundles: molecular dynamics simulations. *J. Phys. Chem. B* **2001,** *105*, 6916-6924.
110. Rodriguez, J.; Elola, M. D.; Laria, D. J. Polar mixtures under nanoconfinement. *J. Phys. Chem. B* **2009,** *113*, 12744-12749.
111. Koch, S.; Desai, R. C.; Abraham, F. F., Dynamics of phase separation in two-dimensional fluids: spinodal decomposition. *Phys. Rev. A* **1983,** *27*, 2152.
112. Cahn, J. W., Phase separation by spinodal decomposition in isotropic systems. *J. Chem. Phys.* **1965,** *42*, 93-99.
113. Jones, R. A.; Norton, L. J.; Kramer, E. J.; Bates, F. S.; Wiltzius, P. Surface-directed spinodal decomposition. *Phys. Rev. Lett.* **1991,** *66*, 1326.
114. Collins, P. G., Defects and disorder in carbon nanotubes. *Oxford Handbook of Nanoscience and Technology: Frontiers and Advances.* Oxford Unviersity Press: Oxford, U.K., 2010.
115. Goldsmith, B. R.; Coroneus, J. G.; Khalap, V. R.; Kane, A. A.; Weiss, G. A.; Collins, P. G.

Conductance-controlled point functionalization of single-walled carbon nanotubes. *Science* **2007,** *315*, 77-81.
116. Murata, K.; Mitsuoka, K.; Hirai, T.; Walz, T.; Agre, P.; Heymann, J. B.; Engel, A.; Fujiyoshi, Y., Structural determinants of water permeation through aquaporin-1. *Nature* **2000,** *407*, 599-605.
117. Horner, A.; Zocher, F.; Preiner, J.; Ollinger, N.; Siligan, C.; Akimov, S. A.; Pohl, P. The mobility of single-file water molecules is governed by the number of H-bonds they may form with channel-lining residues. *Sci. Adv.* **2015,** *1*, e1400083.
118. Joly, L.; Tocci, G.; Merabia, S.; Michaelides, A. Strong coupling between nanofluidic transport and interfacial chemistry: How defect reactivity controls liquid–solid friction through hydrogen bonding. *J. Phys. Chem. Lett.* **2016,** *7*, 1381-1386.
119. Deng, S.; Zhang, Y.; Brozena, A. H.; Mayes, M. L.; Banerjee, P.; Chiou, W.-A.; Rubloff, G. W.; Schatz, G. C.; Wang, Y. Confined propagation of covalent chemical reactions on single-walled carbon nanotubes. *Nat. Commun.* **2011,** *2*, 382.
120. Kim, M.; Wu, X.; Ao, G.; He, X.; Kwon, H.; Hartmann, N. F.; Zheng, M.; Doorn, S. K.; Wang, Y., Mapping Structure-Property Relationships of Organic Color Centers. *Chem* **2018,** *4*, 2180-2191.
121. Rajan, A. G.; Silmore, K. S.; Swett, J.; Robertson, A. W.; Warner, J. H.; Blankschtein, D.; Strano, M. S. Addressing the isomer cataloguing problem for nanopores in two-dimensional materials. *Nat. Mater.* **2019**, *18*, 129-135.
122. Wu, X. J. K., M.J.; Qu, H.; Wang, Y.H. Single-defect spectroscopy in the shortwave infrared. *Submitted.* **2018**.
123. Roxbury, D.; Jena, P. V.; Williams, R. M.; Enyedi, B.; Niethammer, P.; Marcet, S.; Verhaegen, M.; Blais-Ouellette, S.; Heller, D. A. Hyperspectral Microscopy of Near-Infrared Fluorescence Enables 17-Chirality Carbon Nanotube Imaging. *Sci. Rep.* **2015,** *5*, 14167.
124. Museur, L.; Feldbach, E.; Kanaev, A. Defect-related photoluminescence of hexagonal boron nitride. *Phys. Rev. B* **2008,** *78*, 155204.
125. Grosso, G.; Moon, H.; Lienhard, B.; Ali, S.; Efetov, D. K.; Furchi, M. M.; Jarillo-Herrero, P.; Ford, M. J.; Aharonovich, I.; Englund, D., Tunable and high-purity room temperature single-photon emission from atomic defects in hexagonal boron nitride. *Nat. Commun.* **2017,** *8* (1), 705.
126. Srinivasan, K.; Zheng, M. Quantum optics: Nanotube chemistry tunes light. *Nat. Photon.* **2017,** *11*, 535-537.
127. Hartmann, N. F.; Velizhanin, K. A.; Haroz, E. H.; Ma, X.; Htoon, H.; Doorn, S. K.; Kim, M.; Wang, Y. Photoluminescence Dynamics of Aryl sp^3 Defect States in Single-Walled Carbon Nanotubes. *ACS Nano* **2016,** *10*, 8355-65.
128. He, X.; Hartmann, N. F.; Ma, X.; Kim, Y.; Ihly, R.; Blackburn, J. L.; Gao, W.; Kono, J.; Yomogida, Y.; Hirano, A.; Tanaka, T.; Kataura, H.; Htoon, H.; Doorn, S. K. Tunable room-temperature single-photon emission at telecom wavelengths from sp3 defects in carbon nanotubes. *Nat. Photon.* **2017,** *11*, 577-582.
129. Wang, Q. H.; Strano, M. S., Carbon nanotubes: A bright future for defects. *Nat. Chem.* **2013,** *5*, 812-813.
130. Luo, Z.-X.; Xing, Y.-Z.; Ling, Y.-C.; Kleinhammes, A.; Wu, Y. Electroneutrality breakdown and specific ion effects in nanoconfined aqueous electrolytes observed by NMR. *Nat. Commun* **2015,** *6*, 6358.
131. Futamura, R.; Iiyama, T.; Takasaki, Y.; Gogotsi, Y.; Biggs, M. J.; Salanne, M.; Ségalini, J.; Simon, P.; Kaneko, K. Partial breaking of the Coulombic ordering of ionic liquids confined in carbon nanopores. *Nat. Mater.* **2017,** *16*, 1225.
132. Berg, P.; Ladipo, K. Exact solution of an electro-osmotic flow problem in a cylindrical channel of

polymer electrolyte membranes. *Proc. R. Soc. London, Ser. A* **2009**, *465,* 2663-2679.
133. Peters, P.; Van Roij, R.; Bazant, M. Z.; Biesheuvel, P. Analysis of electrolyte transport through charged nanopores. *Phys. Rev. E* **2016,** *93*, 053108.
134. Moreira, A.; Netz, R. Simulations of counterions at charged plates. *Eur. Phys. J. E* **2002,** *8*, 33-58.
135. Bazant, M. Z.; Storey, B. D.; Kornyshev, A. A., Double Layer in Ionic Liquids: Overscreening versus Crowding. *Phys. Rev. Lett.* **2011,** *106*, 046102.
136. Corry, B.; Kuyucak, S.; Chung, S.-H. Invalidity of continuum theories of electrolytes in nanopores. *Chem. Phys. Lett.* **2000,** *32*, 35-41.
137. Chmiola, J.; Yushin, G.; Gogotsi, Y.; Portet, C.; Simon, P.; Taberna, P.-L. Anomalous increase in carbon capacitance at pore sizes less than 1 nanometer. *Science,* **2006,** *313*, 1760-1763.
138. Kondrat, S.; Kornyshev, A. J. Superionic state in double-layer capacitors with nanoporous electrodes. *J. Phys. Cond. Matt.* **2010,** *23*, 022201.
139. Stout, R. F.; Khair, A. S. A continuum approach to predicting electrophoretic mobility reversals. *J. Fluid Mech.* **2014,** *752,* R1.
140. Powell, M. R.; Cleary, L.; Davenport, M.; Shea, K. J.; Siwy, Z. S. Electric-field-induced wetting and dewetting in single hydrophobic nanopores. *Nat. Nanotechnol.* **2011,** *6*, 798-802.
141. Kalra, A.; Garde, S.; Hummer, G. Osmotic water transport through carbon nanotube membranes. *Proc. Natl. Acad. Sci. U. S. A.* **2003,** *100*, 10175-10180.
142. Park, J. H.; Sinnott, S. B.; Aluru, N. R. Ion separation using a Y-junction carbon nanotube. *Nanotechnology* **2006,** *17*, 895-900.
143. Kim, S. J.; Wang, Y.-C.; Lee, J. H.; Jang, H.; Han, J. Concentration polarization and nonlinear electrokinetic flow near a nanofluidic channel. *Phys. Rev. Lett.* **2007,** *99*, 044501.
144. Bocquet, L.; Charlaix, E., Nanofluidics, from bulk to interfaces. *Chem. Soc. Rev.* **2010,** *3*, 1073-1095.
145. Manghi, M.; Palmeri, J.; Yazda, K.; Henn, F.; Jourdain, V. Role of charge regulation and flow slip in the ionic conductance of nanopores: An analytical approach. *Phys. Rev. E* **2018,** *98*, 012605.
146. Secchi, E.; Niguès, A.; Jubin, L.; Siria, A.; Bocquet, L. Scaling behavior for ionic transport and its fluctuations in individual carbon nanotubes. *Phys. Rev. Lett.* **2016,** *116*, 154501.
147. Gillespie, D.; Boda, D., The anomalous mole fraction effect in calcium channels: a measure of preferential selectivity. *Biophys. J.* **2008,** *9*, 2658-2672.
148. Nonner, W.; Chen, D. P.; Eisenberg, B. Anomalous mole fraction effect, electrostatics, and binding in ionic channels. *Biophys. J.* **1998,** *74*, 2327-2334.
149. Gillespie, D.; Boda, D.; He, Y.; Apel, P.; Siwy, Z. S. Synthetic nanopores as a test case for ion channel theories: the anomalous mole fraction effect without single filing. *Biophys. J.* **2008,** *95*, 609-619.
150. Mirzadeh, M.; Bazant, M. Z. Electrokinetic Control of Viscous Fingering. *Phys. Rev. Lett.* **2017,** *119*, 174501.
151. Bazant, M. Z.; Kilic, M. S.; Storey, B. D.; Ajdari, A. Towards an understanding of induced-charge electrokinetics at large applied voltages in concentrated solutions. *Adv. Colloid Interface Sci.* **2009,** *152*, 48-88.
152. Bazant, M. Z. Theory of chemical kinetics and charge transfer based on nonequilibrium thermodynamics. *Acc. Chem. Res.* **2013,** *46*, 1144-1160.
153. Bazant, M. Z. Thermodynamic stability of driven open systems and control of phase separation by electro-autocatalysis. *Faraday Discuss.* **2017,** *199*, 423-463.
154. Siwy, Z.; Dobrev, D.; Neumann, R.; Trautmann, C.; Voss, K. Electro-responsive asymmetric nanopores in polyimide with stable ion-current signal. *Appl. Phys. A* **2003,** *76*, 781-785.

155. Vlassiouk, I.; Apel, P. Y.; Dmitriev, S. N.; Healy, K.; Siwy, Z. S. Versatile ultrathin nanoporous silicon nitride membranes. *Proc. Natl. Acad. Sci. U. S. A.* **2009,** *106*, 21039-21044.
156. Storm, A.; Chen, J.; Ling, X.; Zandbergen, H.; Dekker, C., Fabrication of solid-state nanopores with single-nanometre precision. *Nat. Mater.* **2003,** *2*, 537.
157. He, Y.; Gillespie, D.; Boda, D.; Vlassiouk, I.; Eisenberg, R. S.; Siwy, Z. S. Tuning Transport Properties of Nanofluidic Devices with Local Charge Inversion. *J. Am. Chem.. Soc* **2009,** *131*, 5194-5202.
158. Siwy, Z. S.; Howorka, S. Engineered voltage-responsive nanopores. *Chem. Soc. Rev.* **2010,** *39*, 5067.
159. Wei, C.; Bard, A. J.; Feldberg, S. W. Current rectification at quartz nanopipet electrodes. *Anal. Chem.* **1997,** *69*, 4627-4633.
160. Siwy, Z. S. Ion-current rectification in nanopores and nanotubes with broken symmetry. *Adv. Funct. Mater.* **2006,** *16*, 735-746.
161. Li, S. X.; Guan, W.; Weiner, B.; Reed, M. A. Direct Observation of Charge Inversion in Divalent Nanofluidic Devices. *Nano Lett.* **2015,** *15*, 5046-5051.
162. Colla, T.; Girotto, M.; dos Santos, A. P.; Levin, Y., Charge neutrality breakdown in confined aqueous electrolytes: Theory and simulation. *J. Chem. Phys.* **2016,** *145,* 094704.
163. Buyukdagli, S.; Ala-Nissila, T., Electrostatic correlations on the ionic selectivity of cylindrical membrane nanopores. *J. Chem. Phys.* **2014,** 064701.
164. Laanait, N.; Mihaylov, M.; Hou, B. Y.; Yu, H.; Vanysek, P.; Meron, M.; Lin, B. H.; Benjamin, I.; Schlossman, M. L. Tuning ion correlations at an electrified soft interface. *P. Natl. Acad. Sci. U. S. A.* **2012,** *109*, 20326-20331.
165. Nicholson, D.; Quirke, N. Ion pairing in confined electrolytes. *Mol. Simulat.* **2003,** *29*, 287-290.
166. Khalili-Araghi, F.; Jogini, V.; Yarov-Yarovoy, V.; Tajkhorshid, E.; Roux, B.; Schulten, K. Calculation of the Gating Charge for the Kv1.2 Voltage-Activated Potassium Channel. *Biophys. J.* **2010,** *98*, 2189-2198.
167. Khalili-Araghi, F.; Tajkhorshid, E.; Roux, B.; Schulten, K. Molecular dynamics investigation of the omega-current in the Kv1.2 voltage sensor domains. *Biophys. J.* **2012,** *102*, 258-67.
168. Sahu, S.; Zwolak, M. Ionic selectivity and filtration from fragmented dehydration in multilayer graphene nanopores. *Nanoscale* **2017,** *9*, 11424-11428.
169. Luo, Z. X.; Xing, Y. Z.; Liu, S. B.; Ling, Y. C.; Kleinhammes, A.; Wu, Y. Dehydration of Ions in Voltage-Gated Carbon Nanopores Observed by in Situ NMR. *J. Phys. Chem. Lett.* **2015,** *6*, 5022-5026.
170. Raviv, U.; Laurat, P.; Klein, J. Time dependence of forces between mica surfaces in water and its relation to the release of surface ions. *J. Chem. Phys.* **2002,** *116*, 5167-5172.
171. Richards, L. A.; Schafer, A. I.; Richards, B. S.; Corry, B. The Importance of Dehydration in Determining Ion Transport in Narrow Pores. *Small* **2012,** *8*, 1701-1709.
172. Malani, A.; Murad, S.; Ayappa, K. G. Hydration of ions under confinement. *Mol. Simulat.* **2010,** *36*, 579-589.
173. Zachariah, Z.; Espinosa-Marzal, R. M.; Heuberger, M. P. Ion specific hydration in nano-confined electrical double layers. *J. Colloid Interface Sci.* **2017,** *506*, 263-270.
174. Baimpos, T.; Shrestha, B. R.; Raman, S.; Valtiner, M. Effect of Interfacial Ion Structuring on Range and Magnitude of Electric Double Layer, Hydration, and Adhesive Interactions between Mica Surfaces in 0.05-3 M Li^+ and Cs^+ Electrolyte Solutions. *Langmuir* **2014,** *30*, 4322-4332.
175. Kalcher, I.; Schulz, J. C. F.; Dzubiella, J., Electrolytes in a nanometer slab-confinement: Ion-specific structure and solvation forces. *J. Chem. Phys.* **2010,** *133*, 164511.

176. Kjellander, R. Focus Article: Oscillatory and long-range monotonic exponential decays of electrostatic interactions in ionic liquids and other electrolytes: The significance of dielectric permittivity and renormalized charges. *J. Chem. Phys.* **2018,** *148*, 193701.
177. Park, H. B.; Kamcev, J.; Robeson, L. M.; Elimelech, M.; Freeman, B. D., Maximizing the right stuff: The trade-off between membrane permeability and selectivity. *Science* **2017,** *356*, 1137.
178. Sahu, S.; Di Ventra, M.; Zwolak, M. Dehydration as a Universal Mechanism for Ion Selectivity in Graphene and Other Atomically Thin Pores. *Nano Lett.* **2017,** *17*, 4719-4724.
179. Chaban, V. V.; Savchenko, T. I.; Kovalenko, S. M.; Prezhdo, O. V. Heat-Driven Release of a Drug Molecule from Carbon Nanotubes: A Molecular Dynamics Study. *J. Phys. Chem. B* **2010,** *114*, 13481-13486.
180. Liu, Y. C.; Wang, Q. Dynamic behaviors on zadaxin getting into carbon nanotubes. *J. Chem. Phys.* **2007,** *126*, 124901.
181. Gao, B.; Kleinhammes, A.; Tang, X. P.; Bower, C.; Fleming, L.; Wu, Y.; Zhou, O. Electrochemical intercalation of single-walled carbon nanotubes with lithium. *Chem. Phys. Lett.* **1999,** *307*, 153-157.
182. Li, W.; Wang, X.; Chen, Z.; Waje, M.; Yan, Y. Carbon nanotube film by filtration as cathode catalyst support for proton-exchange membrane fuel cell. *Langmuir* **2005,** *21*, 9386-9389.
183. Mann, D. J.; Halls, M. D. Water alignment and proton conduction inside carbon nanotubes. *Phys. Rev. Lett.* **2003,** *90*, 195503.
184. Doorn, S. K.; Heller, D. A.; Barone, P. W.; Usrey, M. L.; Strano, M. S. Resonant Raman excitation profiles of individually dispersed single walled carbon nanotubes in solution. *Appl. Phys. A: Mater. Sci. Process.* **2004,** *78*, 1147-1155.
185. Barone, P. W.; Yoon, H.; Ortiz-Garcia, R.; Zhang, J. Q.; Ahn, J. H.; Kim, J. H.; Strano, M. S. Modulation of Single-Walled Carbon Nanotube Photoluminescence by Hydrogel Swelling. *ACS Nano* **2009,** *3*, 3869-3877.
186. Prehal, C.; Weingarth, D.; Perre, E.; Lechner, R. T.; Amenitsch, H.; Paris, O.; Presser, V. Tracking the structural arrangement of ions in carbon supercapacitor nanopores using in situ small-angle X-ray scattering. *Energy Environ. Sci.* **2015,** *8*, 1725-1735.
187. Favaro, M.; Jeong, B.; Ross, P. N.; Yano, J.; Hussain, Z.; Liu, Z.; Crumlin, E. J., Unravelling the electrochemical double layer by direct probing of the solid/liquid interface. *Nat.Commun.* **2016,** *7,* 12695.
188. Hunt, N. T.; Jaye, A. A.; Meech, S. R. Ultrafast Dynamics in Complex Fluids Observed Through the Ultrafast Optically-Heterodyne-Detected Optical-Kerr-Effect (OHD-OKE). *Phys. Chem. Chem. Phys.* **2007,** *9*, 2167-2180.
189. Righini, R., Ultrafast Optical Kerr-Effect in Liquids and Solids. *Science* **1993,** *262*, 1386-1390.
190. Williams, G. D.; Soper, A. K.; Skipper, N. T.; Smalley, M. V. High-resolution structural study of an electrical double layer by neutron diffraction. *J. Phys. Chem. B* **1998,** *102*, 8945-8949.
191. Stockle, R. M.; Suh, Y. D.; Deckert, V.; Zenobi, R., Nanoscale chemical analysis by tip-enhanced Raman spectroscopy. *Chem. Phys. Lett.* **2000,** *318*, 131-136.
192. Yeo, B. S.; Stadler, J.; Schmid, T.; Zenobi, R.; Zhang, W. H. Tip-enhanced Raman Spectroscopy - Its status, challenges and future directions. *Chem. Phys. Lett.* **2009,** *472*, 1-13.
193. Bailo, E.; Deckert, V. Tip-enhanced Raman scattering. *Chem. Soc. Rev.* **2008,** *37*, 921-930.
194. Pettinger, B.; Ren, B.; Picardi, G.; Schuster, R.; Ertl, G. Nanoscale probing of adsorbed species by tip-enhanced Raman spectroscopy. *Phys. Rev. Lett.* **2004,** *92*, 096101.
195. Steidtner, J.; Pettinger, B. Tip-enhanced Raman spectroscopy and microscopy on single dye molecules with 15 nm resolution. *Phys. Rev. Lett.* **2008,** *100*, 236101.

196. Hasted, J.; Ritson, D.; Collie, C. Dielectric properties of aqueous ionic solutions. Parts I and II. *J. Chem. Phys.* **1948,** *16*, 1-21.
197. Babu, C. S.; Lim, C. J. Theory of ionic hydration: Insights from molecular dynamics simulations and experiment. *J. Phys. Chem. B* **1999,** *103*, 7958-7968.
198. Farrer, R. A.; Fourkas, J. T., Orientational Dynamics of Liquids Confined in Nanoporous Sol-Gel Glasses Studied by Optical Kerr Effect Spectroscopy. *Acc. Chem. Res.* **2003,** *36*, 605-612.
199. Buck, M.; Himmelhaus, M. Vibrational Spectroscopy of Interfaces by Infrared-Visible Sum Frequency Generation. *J. Vac. Sci. Technol., A* **2001,** *19*, 2717-2736.
200. Eisenthal, K. B. Liquid Interfaces Probed by Second-Harmonic and Sum-Frequency Spectroscopy. *Chem. Rev.* **1996,** *96*, 1343-1360.
201. Richmond, G. L., Molecular Bonding and Interactions at Aqueous Surfaces as Probed by Vibrational Sum Frequency Spectroscopy. *Chem. Rev.* **2002,** *102*, 2693-2724.
202. Rivera, C. A.; Fourkas, J. T. Reexamining the Interpretation of Vibrational Sum-Frequency Generation Spectra. *Int. Rev. Phys. Chem* **2011,** *30*, 409-443.
203. Vidal, F.; Tadjeddine, A. Sum-Frequency Generation Spectroscopy of Interfaces. *Rep. Prog. Phys.* **2005,** *68*, 1095-1127.
204. Wang, H. F.; Gan, W.; Lu, R.; Rao, Y.; Wu, B. H. Quantitative Spectral and Orientational Analysis in Surface Sum Frequency Generation Vibrational Spectroscopy (SFG-VS). *Int. Rev. Phys. Chem.* **2005,** *24*, 191-256.
205. Berne, B. J.; Fourkas, J. T.; Walker, R. A.; Weeks, J. D. Nitriles at Silica Interfaces Resemble Supported Lipid Bilayers. *Acc. Chem. Res.* **2016,** *49*, 1605-1613.
206. Zewail, A. H. 4D ultrafast electron diffraction, crystallography, and microscopy. *Ann. Rev. Phys. Chem.* **2006,** *57*, 65-103.
207. Baloch, K. H.; Voskanian, N.; Bronsgeest, M.; Cumings, J. Remote Joule heating by a carbon nanotube. *Nat. Nanotechnol.* **2012,** *7*, 316-319.
208. Daunheimer, S. A.; Petrova, O.; Tchernyshyov, O.; Cumings, J. Reducing disorder in artificial kagome ice. *Phys. Rev. Lett.* **2011,** *107*, 167201.
209. Park, J. S.; Hirana, Y.; Mouri, S.; Miyauchi, Y.; Nakashima, N.; Matsuda, K. Observation of negative and positive trions in the electrochemically carrier-doped single-walled carbon nanotubes. *J. Am. Chem. Soc.* **2012,** *134*, 14461-14466.
210. Shenvi, S. S.; Isloor, A. M.; Ismail, A. A review on RO membrane technology: Developments and challenges. *Desalination* **2015,** *368*, 10-26.
211. Castel, C.; Favre, E. Membrane separations and energy efficiency. *J. Membr. Sci.* **2018,** *548*, 345-357.
212. Yaroshchuk, A. E. Non-steric mechanisms of nanofiltration: superposition of Donnan and dielectric exclusion. *Sep. Purif. Technol.* **2001,** *22-23*, 143-158.
213. Deen, W. M., Hindered transport of large molecules in liquid-filled pores. *AIChE J.* **1987,** *33*, 1409-1425.
214. Van der Bruggen, B.; Koninckx, A.; Vandecasteele, C. Separation of monovalent and divalent ions from aqueous solution by electrodialysis and nanofiltration. *Water Research* **2004,** *38*, 1347-1353.
215. Shannon, M. A.; Bohn, P. W.; Elimelech, M.; Georgiadis, J. G.; Mariñas, B. J.; Mayes, A. M. Science and technology for water purification in the coming decades. *Nature* **2008,** *452*, 301-310.
216. Yang, Q.; Su, Y.; Chi, C.; Cherian, C.; Huang, K.; Kravets, V.; Wang, F.; Zhang, J.; Pratt, A.; Grigorenko, A. Ultrathin graphene-based membrane with precise molecular sieving and ultrafast solvent permeation. *Nat. Mater.* **2017,** *16*, 1198-1202.
217. Joshi, R. K.; Carbone, P.; Wang, F. C.; Kravets, V. G.; Su, Y.; Grigorieva, I. V.; Wu, H. A.; Geim,

A. K.; Nair, R. R. Precise and Ultrafast Molecular Sieving Through Graphene Oxide Membranes. *Science* **2014,** *343*, 752-754.
218. Ritt, C.; Werber, J. R.; Deshmukh, A.; Elimelech, M. Monte Carlo Simulations of Framework Defects in Layered Two-Dimensional Nanomaterial Desalination Membranes: Implications for Permeability and Selectivity. *Environ. Sci. Technol.* **2019**.
219. Fornasiero, F.; Park, H. G.; Holt, J.; Stadermann, M.; Grigoropoulos, C.; Noy, A.; Bakajin, O. Ion exclusion by sub-2-nm carbon nanotube pores. *Proc. Natl. Acad. Sci. U. S. A.* **2008,** *105*, 17250-17255.
220. Majunder, M.; Zhan, X.; Andrews, R.; Hinds, B., Voltage Gated Carbon Nanotube Membranes. *Langmuir* **2007,** *23*, 8624-8631.
221. Choi, W.; Ulissi, Z.; Shimizu, S.; Bellisario, D.; Ellison, M.; Strano, M. Diameter-dependent ion transport through the interior of isolated single-walled carbon nanotubes. *Nature Commun.* **2013,** *4*, 1-8.
222. In, J. B.; Grigoropoulos, C. P.; Chernov, A. A.; Noy, A. Hidden role of trace gas impurities in chemical vapor deposition growth of vertically-aligned carbon nanotube arrays. *Appl. Phys. Lett.* **2011,** *98*, 153102.
223. Nessim, G. D.; Hart, A. J.; Kim, J. S.; Acquaviva, D.; Oh, J.; Morgan, C. D.; Seita, M.; Leib, J. S.; Thompson, C. V. Tuning of vertically-aligned carbon nanotube diameter and areal density through catalyst pre-treatment. *Nano Lett.* **2008,** *8*, 3587-3593.
224. Kim, S.; Fornasiero, F.; Park, H. G.; In, J. B.; Meshot, E.; Giraldo, G.; Stadermann, M.; Fireman, M.; Shan, J.; Grigoropoulos, C. P. Fabrication of flexible, aligned carbon nanotube/polymer composite membranes by in-situ polymerization. *J. Membr. Sci.* **2014,** *460*, 91-98.
225. Buchheim, J.; Park, H. G. Failure mechanism of the polymer infiltration of carbon nanotube forests. *Nanotechnology* **2016,** *27*, 464002.
226. Zhang, H.; Tian, Y.; Jiang, L. Fundamental studies and practical applications of bio-inspired smart solid-state nanopores and nanochannels. *Nano Today* **2016,** *11*, 61-81.
227. Chen, L.; Shi, G.; Shen, J.; Peng, B.; Zhang, B.; Wang, Y.; Bian, F.; Wang, J.; Li, D.; Qian, Z.; Xu, G.; Liu, G.; Zeng, J.; Zhang, L.; Yang, Y.; Zhou, G.; Wu, M.; Jin, W.; Li, J.; Fang, H. Ion sieving in graphene oxide membranes via cationic control of interlayer spacing. *Nature* **2017,** *550*, 380-383.
228. Gouaux, E.; MacKinnon, R. Principles of Selective Ion Transport in Channels and Pumps. *Science* **2005,** *310*, 1461-1465.
229. Doyle, D. A.; Cabral, J. M.; Pfuetzner, R. A.; Kuo, A.; Gulbis, J. M.; Cohen, S. L.; Chait, B. T.; MacKinnon, R. The Structure of the Potassium Channel: Molecular Basis of K^+ Conduction and Selectivity. *Science* **1998,** *280*, 69-77.
230. Köpfer, D. A.; Song, C.; Gruene, T.; Sheldrick, G. M.; Zachariae, U.; de Groot, B. L. Ion permeation in K^+ channels occurs by direct Coulomb knock-on. *Science* **2014,** *346*, 352-355.
231. Kopec, W.; Köpfer, D. A.; Vickery, O. N.; Bondarenko, A. S.; Jansen, T. L.; de Groot, B. L.; Zachariae, U. Direct knock-on of desolvated ions governs strict ion selectivity in K^+ channels. *Nat. Chem.* **2018,** *10*, 813-820.
232. Kohagen, M.; Pluhařová, E.; Mason, P. E.; Jungwirth, P. Exploring ion–ion interactions in aqueous solutions by a combination of molecular dynamics and neutron scattering. *J. Phys. Chem. Lett.* **2015,** *6*, 1563-1567.
233. Ponder, J. W.; Wu, C.; Ren, P.; Pande, V. S.; Chodera, J. D.; Schnieders, M. J.; Haque, I.; Mobley, D. L.; Lambrecht, D. S.; DiStasio Jr, R. A. Current status of the AMOEBA polarizable force field. *J. Phys. Chem. B* **2010,** *114*, 2549-2564.

234. Jing, Z.; Liu, C.; Qi, R.; Ren, P. Many-body effect determines the selectivity for Ca^{2+} and Mg^{2+} in proteins. *Proc. Natl. Acad. Sci. U. S. A.* **2018,** *115*, E7495-E7501.
235. Willow, S. Y.; Xantheas, S. S. Molecular-level insight of the effect of Hofmeister anions on the interfacial surface tension of a model protein. *J. Phys. Chem. Lett.* **2017,** *8*, 1574-1577.
236. Richards, L. A.; Richards, B. S.; Corry, B.; Schäfer, A. I. Experimental Energy Barriers to Anions Transporting through Nanofiltration Membranes. *Environ. Sci. Technol.* **2013,** *47*, 1968-1976.
237. Corry, B., Designing carbon nanotube membranes for efficient water desalination. *J. Phys. Chem. B* **2008,** *112*, 1427-1434.
238. Epsztein, R.; Shaulsky, E.; Qin, M.; Elimelech, M. Activation behavior for ion permeation in ion-exchange membranes: Role of ion dehydration in selective transport. *J. Membr. Sci.* **2019**, *580*, 316-326.
239. Richards, L. A.; Schäfer, A. I.; Richards, B. S.; Corry, B. Quantifying barriers to monovalent anion transport in narrow non-polar pores. *Phys. Chem. Chem. Phys.* **2012,** *14*, 11633-11638.
240. Song, C.; Corry, B. Intrinsic Ion Selectivity of Narrow Hydrophobic Pores. *J. Phys. Chem. B* **2009,** *113*, 7642-7649.
241. Brown, M. A.; Abbas, Z.; Kleibert, A.; Green, R. G.; Goel, A.; May, S.; Squires, T. M. Determination of Surface Potential and Electrical Double-Layer Structure at the Aqueous Electrolyte-Nanoparticle Interface. *Phys. Rev. X* **2016,** *6*, 011007.
242. Parsons, D. F.; Bostrom, M.; Nostro, P. L.; Ninham, B. W. Hofmeister effects: interplay of hydration, nonelectrostatic potentials, and ion size. *Phys. Chem. Chem. Phys.* **2011,** *13*, 12352-12367.
243. Corry, B. Water and ion transport through functionalised carbon nanotubes: implications for desalination technology. *Energy Environ. Sci.* **2011,** *4*, 751-759.
244. Chan, W.-F.; Chen, H.-Y.; Surapathi, A.; Taylor, M. G.; Shao, X.; Marand, E.; Johnson, J. K. Zwitterion functionalized carbon nanotube/polyamide nanocomposite membranes for water desalination. *ACS Nano,* **2013,** *7*, 5308-5319.
245. Epsztein, R.; Cheng, W.; Shaulsky, E.; Dizge, N.; Elimelech, M. Elucidating the mechanisms underlying the difference between chloride and nitrate rejection in nanofiltration. *J. Membr. Sci.* **2018,** *548*, 694-701.
246. Gravelle, S.; Joly, L.; Detcheverry, F.; Ybert, C.; Cottin-Bizonne, C.; Bocquet, L. Optimizing water permeability through the hourglass shape of aquaporins. *Proc. Natl. Acad. Sci. U. S. A.* **2013**, *110,* 16367-16372.

2. Diameter Dependence of Fluid Filling

This chapter has been adapted from "Diameter Dependence of Water Filling in Lithographically Segmented Isolated Carbon Nanotubes," Samuel Faucher, Matthias Kuehne, Volodymyr B. Koman, Natalie Northrup, Daichi Kozawa, Zhe Yuan, Sylvia Xin Li, Yuwen Zeng, Takeo Ichihara, Rahul Prasanna Misra, Narayana Aluru, Daniel Blankschtein, and Michael S. Strano, *ACS Nano* **2021** 15 (2), 2778-2790, DOI: 10.1021/acsnano.0c08634

Abstract

Although the structure and properties of water under conditions of extreme confinement are fundamentally important for a variety of applications, they remain poorly understood, especially for dimensions less than 2 nm. This problem is confounded by the difficulty in controlling surface roughness and dimensionality in fabricated nanochannels, contributing to a dearth of experimental platforms capable of carrying out the necessary precision measurements. In this work, we utilize an experimental platform based on the interior of lithographically segmented, isolated single-walled carbon nanotubes to study water under extreme nanoscale confinement. This platform generates multiple copies of nanotubes with identical chirality, of diameters from 0.8 to 2.5 nm and lengths spanning 6 μm to 160 μm, that can be studied individually in real time before and after opening, exposure to water, and subsequent water filling. We demonstrate that under controlled conditions, the diameter-dependent blue shift of the Raman radial breathing mode between 1 and 8 cm^{-1} measures an increase in the interior mechanical modulus associated with liquid water filling, with no response from exterior water exposure. The observed RBM shift with filling demonstrates a non-monotonic trend with diameter, supporting the assignment of a minimum of 1.81±0.09 cm^{-1} at 0.93±0.08 nm with a nearly linear increase at larger diameters. We find that a simple hard sphere model of water in the confined nanotube interior describes key features of the diameter-dependent modulus change of the CNT, and supports previous observations in the literature. Longer segments of 160 μm show partial filling from the ends of the segment that terminates along the length, consistent with pore clogging. These devices provide an opportunity to study fluid behavior under extreme confinement with high precision and repeatability.

2.1 Introduction

When confined in single-digit nanopores,[1] or pores with a characteristic dimension less than 10 nm, water displays physical properties that deviate substantially from those in larger nanopores.[2] Examples include slip flow of water inside carbon nanotubes less than 50 nm in diameter that results in flow rates that are orders of magnitude higher than those encountered in larger nanopores.[3–7] Similarly, the melting points of confined water and other fluids deviate from their values in the bulk in a diameter-dependent way described by the Gibbs Thomson effect,[8] but diverge substantially from them under extreme confinement.[9] The dielectric constant of water in graphene slit pores, too, varies widely with pore width.[10,11] Experimental observations in these exceptionally narrow nanopores have renewed interest in the study of fluids under confinement, and reveal knowledge gaps in the study of single-digit nanopore nanofluidics[1] that anticipate the development of nanofluidic devices for fundamental measurements and diverse applications. The interior of opened carbon nanotubes can serve as an experimental platform to answer these questions. However, methods do not yet exist for generating repeated and reliable comparisons of fluid filling for identical diameter single-digit nanopores of any kind. In this work, we create a platform that consists of precision nanopores in the critical diameter regime (< 10 nm) formed from cut and opened ultralong CNTs. By examining spatially dependent fluid filling repeatedly in identical systems, we can overcome impediments like pore blocking and closed CNT ends to learn fundamental aspects of confined fluid properties. This platform is relevant not only to carbon nanotube nanofluidics, but in addressing topics including nanoscale slip flow, fluid diffusion, phase behavior, and interfacial transport that span nanofluidic device geometries and fluid types.

The fabrication of precision nanopores in the range of extreme confinement has proven difficult, limiting the number of replicates and control of pore dimensions. Two-dimensional nanochannel arrays, produced both by top-down etching of silicon and other materials and bottom-up assembly of 2D materials to form van der Waals heterostructures, comprise one class of experimental system. Enhanced water transport in hybrid nanochannels[12] and modified interfacial behavior of water under nanoconfinement, including evaporation,[13] cavitation,[14] and vapor transport selectivity,[15] have been observed in etched Si nanochannels, though channel dimensions do not typically reach the single-digit nanometer regime. Van der Waals heterostructures with graphene and other 2D materials[16,17] have addressed fundamental questions about water properties, including dielectric constant[11] and capillary condensation[18] under extreme 2D confinement, but cannot mimic the 1D confinement of nanotubes. Another class of experimental systems are multi-pore nanotube membranes. Carbon nanotubes membranes have been studied for close to two decades,[6,19–21] with permeation measurements showing significant flow enhancement and high slip length for membranes containing ensembles of pores with diameters in the single-digit range. CNT porins, which contain short carbon nanotubes embedded in a lipid bilayer, provide another platform for the study of water and ions through ensembles of carbon nanotubes, and also show flow enhancements that vary dramatically with nanotube diameter.[5,22] This allows for precision and many replicates, but the pore length itself is extremely small (around 10 nm), causing the CNT entrance region to dominate fluid behavior. Research groups have studied water structure and phase behavior in carbon nanotube ensembles using techniques like x-ray diffraction,[23,24] allowing the proposal of a temperature-diameter phase diagram for the water-SWNT system; NMR;[25] and neutron scattering.[26,27] Spectroscopies,

including IR spectroscopy,[28,29] Raman,[30–32] and photoluminescence,[31] have been used to distinguish ensembles of empty and water-filled CNTs, confirming, in some cases, the separation of the two by centrifugation.[31,33]

Only in recent years have nanofabrication techniques allowed the study of fluids in isolated, single carbon nanotubes, but to date these experimental platforms have not allowed repeat measurements of identical CNT devices. One study by Secchi and co-workers[3] uses fluid entrainment in a Landau-Squire jet to measure flow enhancements for CNTs outside the single-digit regime from 15 to 50 nm in diameter, showing large slip lengths for CNTs and negligible slip lengths for boron nitride nanotubes. The difference in performance between CNTs and boron nitride nanotubes suggests that solid and interfacial properties beyond the confining diameter, like wettability and electronic structure, may affect hydrodynamics, but experimental observations of water behavior in other quasi-1D nanopores are even scarcer than those in CNTs. Additionally, the fabrication of trans-membrane single carbon nanotubes does not easily extend to diameters below 10 nm and replicates are difficult to realize.[34,35] Other studies use photoluminescence of individual solution-phase[36] or suspended CNTs,[37,38] and, from our research group, Raman spectroscopy of substrate-bound CNTs[9] to observe water inside single carbon nanotube pores. Yet none of these platforms provides multiple copies of identical, localizable nanopores for repeated measurement of nanofluidic filling. The limited number of replicates or the averaging together of multiple nanopores suggest that random atomic defects, variations in pore mouth chemistry, and strongly non-monotonic effects with confining diameter can obscure fundamental fluid properties.

Herein, we demonstrate a nanofluidic platform consisting of lithographically segmented, isolated, substrate-bound CNTs to study water under nanometer confinement. We show unequivocally that external water application and internal water filling of CNTs on silicon wafers can be distinguished by Raman spectroscopy: internal water filling causes a blue shift in the Raman radial breathing mode (RBM), while under these conditions external water application does not, as shown by measurements of large numbers of isolated CNTs using air and water-immersion objectives. This creates a contrast between substrate-bound CNTs and other CNT systems – with nanotubes in solution[39,40] and suspended in vapor over a susbtrate[41] – for which the RBM mode may still change with exterior adsorption. We conclude that water filling of isolated CNTs on Si substrates is a rare, often permanent event, occurring no more than 20% of the time, and that the radial breathing mode shift upon fluid filling, $\Delta\omega_{RBM}$, varies non-monotonically with diameter. Specifically, this RBM shift decreases to a minimum of 1.81±0.09 cm^{-1} at a diameter of 0.93±0.08 nm before increasing for larger diameter CNTs. Although complex effects arising from the structure of water inside CNTs can be most accurately described using all-atomistic molecular simulations, here we combine a simple hard-sphere water packing model[33,42] with an elastic shell model of the carbon nanotube[39,40] to describe the variation of $\Delta\omega_{RBM}$ with the CNT diameter. In this way, we capture the quasi-1D molecular packing effects in a simple, analytical model which can also be extended to other fluids.

2.2 Results and Discussion

The platform developed and utilized in this work is shown in **Figure 2-1**. Ultra-long gas-flow aligned carbon nanotubes are grown on SiO_2 using a CVD method developed by Huang *et*

al.[43,44] as described previously by our group.[9,45] Carbon nanotubes are grown using a Nano-C 25 Series APT carbon nanotube suspension as a catalyst solution with methane in hydrogen at 970 °C for 45 minutes, yielding sparse carbon nanotubes with an average pitch around 200 µm and lengths from 5 to 10 mm. A schematic showing ultra-long CNTs on a marked silicon substrate is shown in **Figure 2-1a**. Samples are then etched by photolithography to produce multiple CNT segments of the same diameter and chirality. In this work, we produced and compared long (160 µm) and short (6 µm) segments. After spin-coating with Shipley 1805 photoresist and exposure of 60 mW/mm^2 at 405 nm (Heidelberg MLA150), samples are etched by low-power (6.8 W) oxygen plasma for 3 minutes, a technique that has been used previously for CNT etching.[46–48] An SEM image of several 160 µm CNT segments, and an accompanying schematic, are shown in **Figure 2-1b.** Other samples are instead masked with PDMS then etched identically by low-power oxygen plasma to produce one 2 mm long CNT segment, as identified below.

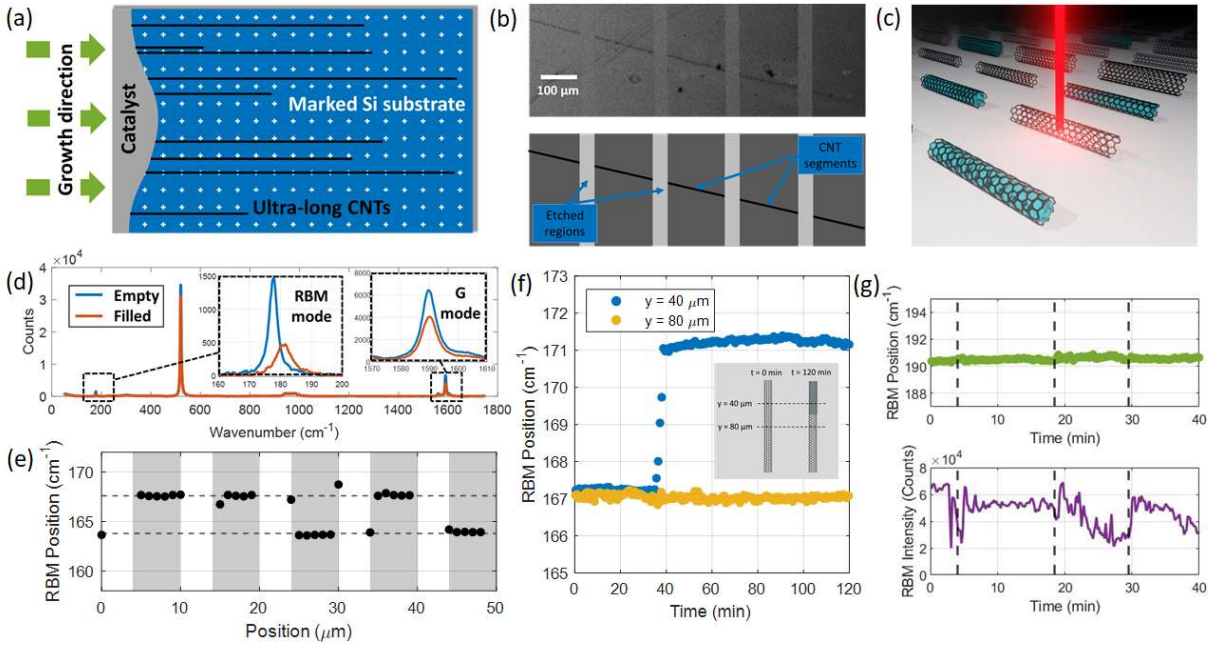

Figure 2-1 | Experimental platform and Raman measurements of CNT fluid filling. (a) Schematic of ultra-long, vertically aligned CNTs grown by chemical vapor deposition on a marked silicon substrate. (b) SEM image showing lithographic segmentation of ultralong CNT into five independent 160 μm long, 1.38 nm diameter CNT segments of identical diameter and chirality, with accompanying schematic. (c) Illustration, not to scale, showing laser spot on empty and filled CNT segments. (d) Raman spectrum of a 1.40 nm diameter CNT in empty (blue) and filled (orange) states with RBM region and G region inset, showing upshift and broadening in RBM mode upon fluid filling. (e) Raman map of five 6 μm long, 1.52 nm diameter CNT segments produced by lithographic segmentation along their length, after immersion in water. Raman spectra taken every 1 μm show two discrete vibrational states, with three filled CNT segments (with high RBM position) and two empty CNT segments (with low RBM position). (f) RBM position *versus* time at two locations (y=40 μm and y=80 μm) on a 160 μm long, 1.49 nm diameter CNT. At t=0, the sample is cooled from ambient temperature to 9 °C, causing water condensation and fluid filling at y=40 μm but not y=80 μm, as shown by the change in Raman radial breathing mode at y=40 μm and illustrated in the accompanying schematic. (g) Exterior water does not affect Raman radial breathing mode position, as shown by plots of RBM position and intensity *versus* time at a single location on a 1.30 nm CNT. Water droplets were added to a substrate at t=4, 18.5 and 29.5 min, causing transient increases in RBM intensity but no change in RBM position.

In general, water filling is indicated by a shift to higher frequency of the Raman radial breathing mode of a carbon nanotube,[9,30,31,49,50] which occurs as the vibrational mode of the nanotube couples to the higher-elastic modulus fluid phase. An illustration showing filled and empty CNT segments is shown in **Figure 2-1c.** A phase transition of the confined water to a phase with still higher elastic modulus – from a liquid-like to a solid-like phase, for instance – leads to further hardening of the RBM mode.[9] **Figure 2-1d** shows Raman spectra of one location on one 1.40 nm diameter CNT before and after water immersion, with RBM and G regions identified.[51] Upon interior fluid filling, the RBM peak upshifts and broadens, while the peak from the silicon substrate at 521 cm^{-1} and the G band remain unchanged. A Raman map of five 6 μm segments of a 1.51 nm CNT is shown in **Figure 2-1e.** We can assign three segments as filled, with a high RBM position around 168 cm^{-1}, and two segments as empty with a low RBM position around 164 cm^{-1}. **Figure 2-1f** and **Figure 2-1g** show the difference in vibrational response of a substrate-bound CNT to interior fluid filling and exterior water adsorption, respectively. **Figure 2-1f** shows interior fluid filling as tracked dynamically at two locations on a 1.49 nm carbon nanotube. In **Figure 2-1f,** the RBM position at two locations (y=40 μm and y=80 μm) on a 160 μm long, 1.49 nm diameter CNT is plotted *versus* time. At t=0, the sample is cooled to 9 °C from ambient temperature. This causes water condensation on the sample and water filling of the CNT. We see that as the fluid enters the nanotube and as it passes 40 μm from the end, a dynamic RBM shift occurs at time t = 36 min. At 80 μm from the end, the filling profile does not reach the laser spot during the 2 hour experiment, so the RBM mode does not shift. The fluid front does not reach this location likely as a result of CNT blocking or clogging. We anticipate that an experimental platform like this one, which allows tracking of fluid filling events with micron- and second-scale resolution inside isolated carbon nanotubes, could be used to analyze the dynamics of fluid filling, either as the progression of a unitary filling front with Lucas-Washburn kinetics[52,53] or the growth of fluid droplets by capillary condensation.[18,54] **Figure 2-1g** shows that exterior water, by contrast, does not cause a shift of the RBM mode. In this experiment, a single location on a 1.30 nm CNT was observed by Raman spectroscopy over time. Water droplets were added to the substrate at three times, as indicated, causing exterior CNT wetting that increases the Raman scattering cross-section and increases the RBM intensity, as shown, but the RBM position does not change. A sample Raman spectrum, showing background subtraction and peak fitting, is shown in supplemental **Figure 2-5.** Taken in combination, these results show the use of lithographically segmented, isolated carbon nanotubes to track interior fluid filling of CNTs spectroscopically in multiple nanofluidic devices of identical diameter.

Lithographic segmentation of ultralong CNTs allows the production of multiple copies – some empty and others filled – of CNTs of the same diameter, chirality, and length. Fluid filling results in segmented, 6 μm-long and 160 μm-long CNTs are shown in **Figure 2-2. Figure 2-2a** shows RBM position *versus* distance along 6 μm segments of a 1.36 nm diameter CNT. Forty segments are shown at 10 μm pitch, for a total distance of 400 μm. A histogram of RBM position is shown at right and an inset, showing 50 μm of distance along the nanotube axis, is shown in **Figure 2-2b.** The RBM position is distributed bimodally, with the low frequency corresponding to an empty state and the high frequency corresponding to a filled state; it is possible to assign individual segments as either filled or empty from their Raman spectra. In **Figure 2-2b**, the first and fourth segments from the left are empty, while the second, third, and fifth segments are filled with water. Grey and white indicate the regions that were masked from etching and exposed,

respectively. The etched regions have low to nonexistent RBM and G modes, confirming successful etching. **Figure 2-2c** shows Raman radial breathing mode frequency for 100 6 μm segments of a 1.52 nm diameter CNT, again showing empty and filled segments, with a histogram and an inset in **Figure 2-2d**. Qualitatively different filling behavior is observed for longer, 160 μm segments in **Figure 2-2e**. RBM position is shown along three 160 μm segments of a 1.48 nm diameter CNT. The RBM states of short CNT segments are terraced as a result of entire segments being empty or filled, but longer CNT segments appear to fill from the ends but clog at some point along their length. This results in RBM modes that change within the segment. In the data shown, four CNT ends appear filled, one CNT end appears empty, and the filling state of one CNT end (the left of the second segment) is uncertain. The RBM position distribution is bimodal, but there are tails and shoulders in the distributions shown in **Figure 2-2a**, **Figure 2-2c**, and **Figure 2-2e**. Specifically, in **Figure 2-2a** and **Figure 2-2c**, there are three features of note in the RBM distribution: variability within 1 cm^{-1} of the empty and filled peaks, weight between the two peaks, and a shoulder at a higher wavenumber than the filled peak. All of this RBM variation falls well within the benchmark of ±2.5 cm^{-1} established previously for isolated, substrate-bound CNTs.[55] Variability within 1 cm^{-1} of the empty and filled peaks is commensurate with the instrument spectral resolution (0.32 cm^{-1}) and can be explained partly by measurement uncertainty. The rest of the spread can be explained by inhomogeneous CNT-substrate interactions, adsorbed contaminants, and other filling states. The Raman radial breathing mode is affected by interactions with an SiO_2 substrate, as shown by Raman comparisons of suspended and substrate-bound CNTs.[56–58] Surface roughness in the SiO_2 substrate, then, could cause spatial heterogeneity in CNT-SiO_2 van der Waals interactions that could result in smearing of the RBM peaks. An inhomogeneous distribution of adsorbed residue from the photolithography process[59,60] could also lead to smearing of the bimodal RBM position distribution. Finally, the spread in RBM could be explained by the existence of partly filled liquid-like states that fall between the empty and filled states, or solid-like states that fall above the filled liquid-like state.[9]

Figure 2-2f shows autocorrelation in RBM position *versus* lag for the three Raman maps from **Figure 2-2a, Figure 2-2c,** and **Figure 2-2e.** For 6 μm segments, there is strong autocorrelation of RBM frequency for lags less than 6 μm and weak autocorrelation for lags beyond 6 μm. This suggests, as can be seen by eye in **Figure 2-2b** and **Figure 2-2d**, that RBM position is strongly correlated within each segment, and largely uncorrelated between segments. The strong correlation within each segment is necessary to assign each segment as empty or filled, while the lack of strong correlation between segments is required to produce largely independent nanofluidic devices. Sections with several consecutive unfilled or filled CNT segments could be a result of incomplete oxygen plasma etching. By contrast, there is strong autocorrelation of the RBM position in 160 μm segments to a lag of 30-40 μm; if a location along a long CNT segment is filled or empty, that filling state may not persist along the entire segment length but it is likely to persist for several dozen micrometers. Generation of CNT segments with lengths between 6 μm and 160 μm, or with lengths exceeding 160 μm, may allow more detailed study of the fraction of pore blocking events as a function of length.

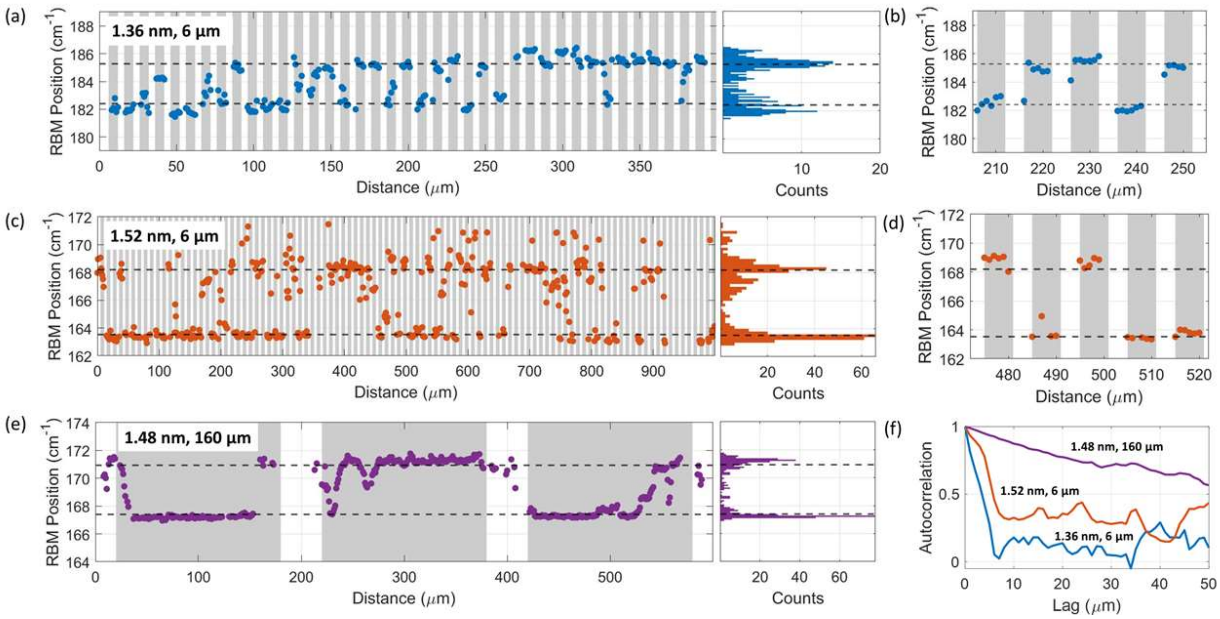

Figure 2-2 | Water filling in 6 µm long and 160 µm long segmented CNTs. (a) RBM position *versus* distance in 1 µm increments along 40 6 µm segments of a 1.36 nm diameter CNT at 10 µm pitch. The RBM position distribution is bimodal, with empty and filled states, as shown by the histogram at right. (b) Inset showing RBM mode over five segments of a 1.36 nm CNT. The first and fourth segments are empty, while the second, third, and fifth segments are water-filled. (c) RBM position *versus* distance along 100 6 µm segments of a 1.52 nm diameter CNT at 10 µm pitch. The RBM position distribution is bimodal, with empty and filled states, as shown by the histogram at right. (d) Inset showing RBM mode over five segments of a 1.52 nm CNT. The second, fourth, and fifth segments are empty, while the first and third segments are water-filled. (e) RBM position *versus* distance along 3 160 µm segments of a 1.48 nm diameter CNT. The first and third segments are largely empty, while the second segment is largely filled. The RBM position distribution is bimodal with empty and filled states, as shown by the histogram at right. (f) Autocorrelation of RBM position with lag in µm. The low autocorrelation in 6 µm segments at lags greater than 6 µm confirms that CNT segments fill independently. RBM position in 160 µm segments, by contrast, shows higher autocorrelation for longer lags.

In order to collect the Raman maps as shown in Figure 2-2, we have devised an automatic setup equipped with a sub-micrometer precision mechanical stage that allows tracking of maximum Raman intensity signals, following a trace of CNTs that extend generally but not perfectly in the direction of gas flow (**Figure 2-6**). Raman xy maps in **Figure 2-6a** show locations of maximum intensity before and after water immersion, and confirm that the location of the carbon nanotube on the substrate is the same before and after treatment. Raman maps of eight other CNT chiralities, each with 49 to 80 segments, generates the statistical data shown in **Figure 2-6b**. The fraction of segments that fill varies widely between samples. This could indicate some systematic blockage to fluid filling along the entire carbon nanotube, for instance an adsorbed layer that was not fully removed during etching or an inner wall that was not resonant with the 532 nm laser and therefore was not observed. In general, these results show that chemical vapor deposition, lithography, etching, and Raman spectroscopy can be used to develop and characterize a nanofluidic platform consisting of multiple copies of the same chirality CNT of predetermined length, with some segments empty and others filled with fluid.

To clarify a point of confusion that has emerged in the literature, successive measurements taken at the same location on the same CNTs show unequivocally that observed RBM shifts are caused by interior fluid filling and not exterior water adsorption or other processes.[38] The assignment of particular spectroscopic shifts and features to CNT filling events remains controversial in some cases because Raman and photoluminescence spectroscopy are indirect probes of nanoconfined water. Chiashi and coworkers suggest, for instance,[38] that the RBM shift in Agrawal *et al.*[9] is due to phase transitions of water outside the CNT rather than confined within. To address this issue, we systematically explored the effects of various conditions and treatments in the carbon nanotube filling process on the RBM mode. **Figure 2-3** shows statistical measurements of carbon nanotube filling, where each dot represents two paired measurements made at the same location on the same diameter carbon nanotube before and after a given treatment. We define $\Delta\omega_{RBM}$ as the shift in RBM frequency in response to a certain treatment as compared to the initial state. **Figure 2-3a** shows repeated Raman measurements made after the sample was removed and reloaded with no intervening treatment; the lack of shifts confirms that the CNTs do not move on the substrate, the RBM mode is stable over time, and the RBM can be measured accurately. **Figure 2-3b** shows the change in radial breathing mode frequency, $\Delta\omega_{RBM}$, before and after 1 hour immersion of non-etched CNTs in water, confirming that adsorption of water to the outside of the CNT does not cause a shift in the RBM mode. This is further verified in **Figure 2-3c**, in which the RBM mode is compared with no treatment to that under a water immersion objective. Since a large majority of samples show no change, we conclude that introduction of water to the outside of a closed CNT does not affect the RBM mode for isolated CNTs on a Si wafer. While other carbon nanotubes, especially those in solution and suspended, exhibit vibrational changes with exterior water adsorption,[30,38,41,61] the lack of RBM change shown here suggests that substrate-bound CNTs may already be water-saturated at ambient temperature (23 °C) and humidity (30-50%).[41,61,62] It could suggest instead that interactions with the substrate or with adsorbed hydrocarbons saturate any effect that exterior water would otherwise have.

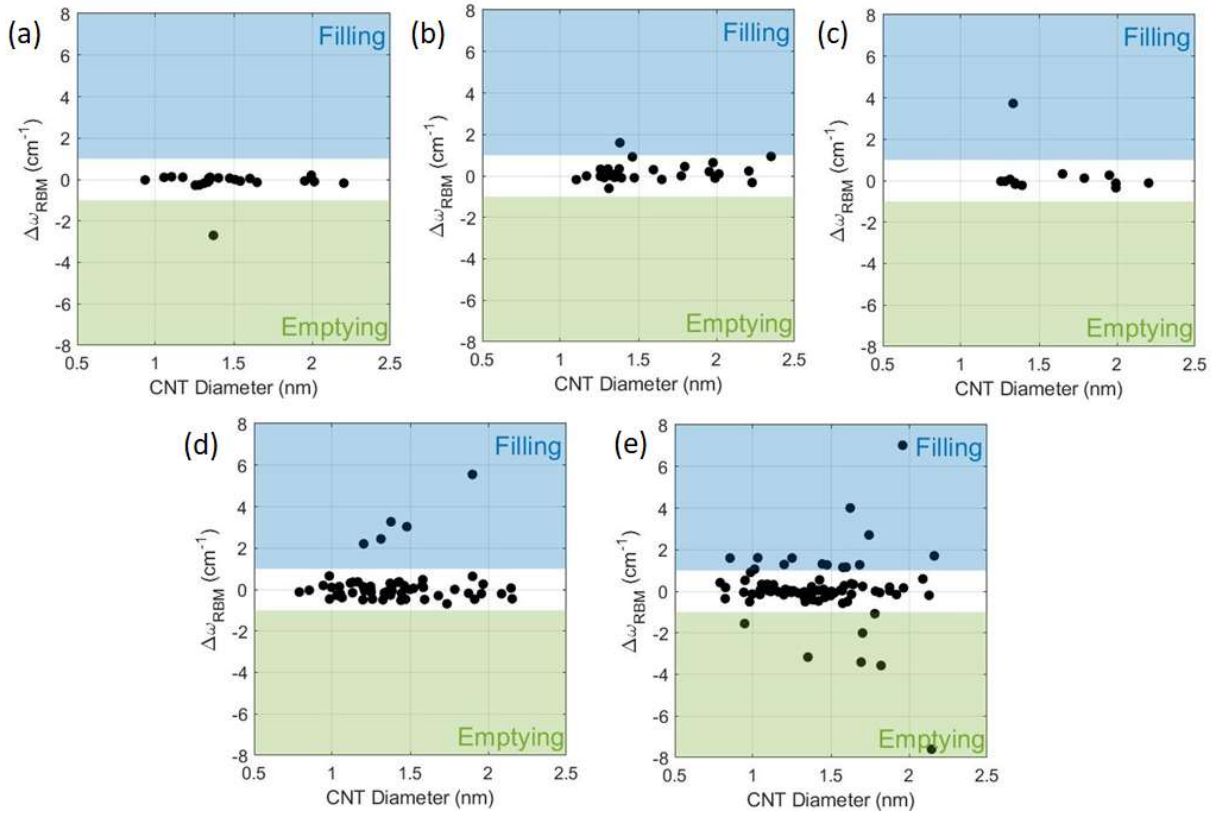

Figure 2-3 | Statistics of water filling of isolated carbon nanotubes. In general, each data point represents paired observations of the same location on the same chirality, 2 mm long substrate-bound CNT. (a) Change in RBM frequency *versus* CNT diameter upon remounting sample and locating CNT with no intervening treatment. (b) Change in RBM frequency *versus* diameter before and after 1 hour H_2O immersion of unetched CNT. (c) Change in RBM frequency *versus* diameter under air objective *versus* water immersion objective. (d) Change in RBM frequency *versus* diameter before and after oxygen plasma etching of CNT ends. (e) Change in RBM frequency *versus* CNT diameter before and after 1 hour H_2O immersion of plasma-etched CNT.

We then measured the overall filling success rate and recorded statistics associated with interior filling after a plasma etch of the CNT ends. **Figure 2-3d** shows $\Delta\omega_{RBM}$ *versus* diameter before and after oxygen plasma etching.[46–48] While a few CNTs show the characteristic RBM upshift that we attribute to fluid filling, the number is low. It is likely that the few "filled" CNTs which filled after etching, even without water immersion, filled either (1) from ambient moisture in the air, despite environmental controls in sample processing, or (2) with acetone or isopropanol from rinsing during photoresist removal. **Figure 2-3e**, by contrast, shows a substantial number of CNTs (16/81, or 19.8%) with high $\Delta\omega_{RBM}$ before and after 1 hour water immersion of pre-etched samples. For all plots, limits of $\Delta\omega_{RBM}$=0.8 cm^{-1} for filling and -0.8 cm^{-1} for emptying are proposed from the distribution of RBM shifts across all samples and by comparison to Raman results for CNT D_2O filling in solution.[30] The few CNTs with a negative RBM shift upon water immersion could have been water-filled with ambient moisture, then emptied at the observed location before the second measurement, though the exact mechanism of emptying remains unclear. Since etched CNT ends and water immersion are both necessary to generate a positive RBM shift in a substantial fraction of CNTs, this shows conclusively that RBM shifts are a result of endohedral water filling, not water adsorption or other events. We observe that water filling tends to be irreversible at relevant time scales; the spectra shown were generally acquired hours after the sample was removed from water, but remain in their filled state indefinitely (*i.e.* months) after water immersion when stored under ambient conditions. Additionally, heating of several samples under two conditions (150 °C, 25 mTorr, 1 hr; 200 °C, 1e-4 Torr, 12 hrs) does not cause emptying, as shown by the RBM position before and after treatment.

Across the diameter range studied, CNT filling is a rare event, with most opened nanotubes not filling upon immersion in water. The fraction of CNTs that fill with water does not vary appreciably with diameter, as shown in **Figure 2-7a.** While the success rate of CNT filling can be increased by a supplemental nitric acid treatment[63,64] which is known to open CNT ends, as shown in **Figure 2-7b**,[65] this comes at the expense of the likely introduction of oxidative sidewall defects and altered water transport.[66] While it is expected that all chiralities can, in principle, fill with water,[30] we attribute the low success rate to pore clogging: with diameters on the nanometer scale, molecular-scale impurities or unfavorable functional groups at the pore mouth can block fluid entrance, and defects and kinks in the pore body can prevent fluid from progressing through the CNT. Other experimental work shows a success rate for substrate-bound CNT opening by oxygen plasma of roughly one in three,[67] while solution-phase experiments eliminate the large fraction of CNTs with closed endcaps only after ultrasonication.[30] Throughout the carbon nanotube literature, use of plasma etching to open CNT ends is ubiquitous.[46,47,69–71] In many studies, without statistical sampling, it is assumed that the application of oxidative treatments results in open nanotubes with 100% certainty, but the results of our current study show otherwise. This illustrates the importance of having independent experimental confirmation that a nanopore is open and fluid-filled for nanofluidic transport applications. The platform introduced in this work, for example, allows both positive and negative controls to be studied, and allows statistical analysis. It also allows the dynamics of filling to be observed, where filled and unfilled regions are identified within the same carbon nanotube.

As an application of the lithographically segmented, isolated CNT platform, we used Raman data of dozens of fluid-filled CNTs to explore the relationship between RBM shift upon fluid filling and CNT diameter. We find that this relationship is non-monotonic and suggests molecular packing effects of water inside the nanotube. The as-collected statistics of CNT water filling allows us to plot the absolute value of RBM shift *versus* CNT diameter (**Figure 2-4a**) for all CNTs before and after water immersion, and before and after etching. These two treatment conditions were combined since they are the two that allow internal water filling, as discussed in **Figure 2-3**, with a large majority of filling events occurring after water immersion of etched samples. Individual paired observations are plotted without confidence intervals, while repeated measurements at dozens to hundreds of empty and filled locations on the same chirality CNT allow calculation of 95% confidence intervals, as shown. A histogram showing the frequency of observed RBM shifts (**Figure 2-4b**) has two peaks and a minimum in between, which justifies a demarcation between empty CNTs ($|\Delta\omega_{RBM}|<0.8$ cm^{-1}) and filled CNTs ($|\Delta\omega_{RBM}|>0.8$ cm^{-1}). CNTs that are presumed to fill are plotted together in **Figure 2-4e** with solution-phase data from Cambré *et al*.[30] and Fagan *et al*.[31] Data from Cambré *et al.*,[30] in combination with data presented here and from Fagan *et al.*,[31] show that the RBM shift upon water filling passes through a minimum within the observed diameter range. Specifically, at a critical diameter of 0.93±0.08 nm, a moving average of $\Delta\omega_{RBM}$ reaches a minimum of 1.81±0.09 cm^{-1} and its standard deviation is also minimized. Above this diameter, $\Delta\omega_{RBM}$ increases with diameter, as noted by Fagan *et al*.[31] This increase is roughly linear, and extends from diameters of 1.0 nm to 2.2 nm for substrate-bound CNTs. While most of the presented data follow the Cambré-Fagan line, certain CNTs with diameters between 1.4 nm and 2.2 nm fall noticeably below this line. This population of CNTs could be partly filled, or could be multi-walled CNTs that fill fully but shift less due to wall-wall interactions; in either case, this population exists in substrate-bound CNT systems but not in solution. In general, it is likely imprudent to make one-to-one correspondences between observations in solution and those on a substrate in **Figure 2-4e**. This is partly due to the difficulty of assigning chiralities in substrate-supported CNTs without the benefit of a fluorescence signature, and partly due to changes in chemical environment in the two experimental systems which may lead to different observed $\Delta\omega_{RBM}$, even as the trends in $\Delta\omega_{RBM}$ with diameter appear broadly similar. Differences between the two systems highlight the need to collect more data for fluid filling of substrate-bound CNTs, particularly below 1 nm in diameter. In order to explain the observed relationship between $\Delta\omega_{RBM}$ and CNT diameter more fully, we developed a model that combines a continuum elastic shell[39,40] with discrete water size effects as inferred from spherical packing of water molecules inside a cylinder.[33,42]

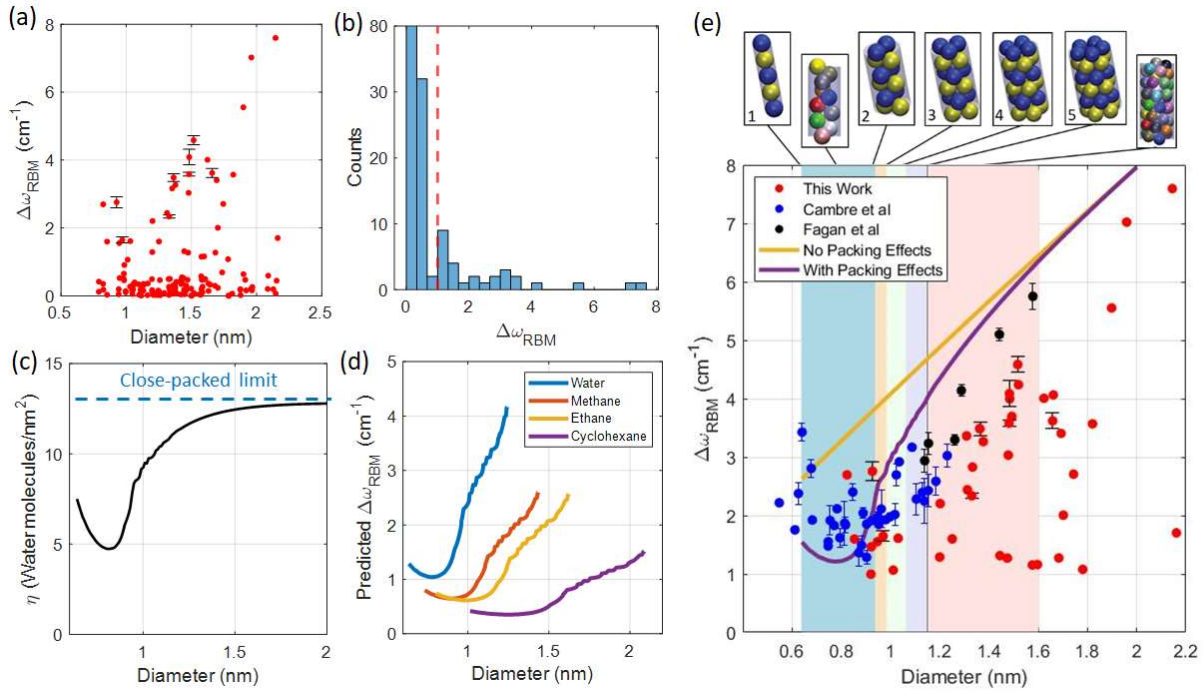

Figure 2-4 | Fluid packing configurations inside CNTs. (a) Each data point represents paired observations of the same location on the same chirality, substrate-bound CNT. The absolute value of RBM shift *versus* diameter for all carbon nanotubes before and after water immersion, and before and after etching, is shown. Individual paired observations do not have confidence intervals, while repeated measurements on the same chirality CNT are shown with 95% confidence intervals. (b) Histogram showing frequency of observation of absolute shifts in RBM; $\Delta\omega_{RBM}$=0.8 cm^{-1} (in red) was set as the threshold for water filling. (c) Areal density of water molecules per CNT surface area as a function of diameter in a hard sphere water packing model. Water molecules are modelled as spheres with radius 0.15 nm in a cylinder with an excluded carbon-water radius of 0.17 nm. (d) Predicted RBM shift *versus* diameter for several fluids with an elastic shell model adapted from Longhurst and Quirke[40] with the addition of hard-sphere molecular packing effects. (e) RBM shift is shown *versus* diameter in CNTs that are presumed to have filled or emptied, with comparison to solution-phase work by Cambré *et al*.[30] and Fagan *et al*.[31] A hard sphere water-packing model (in purple) generally captures the minimum in RBM shift at a diameter of 0.93 nm, while a continuum elastic shell model (in yellow) does not. The critical diameter with minimum $\Delta\omega_{RBM}$ corresponds to a minimally efficient molecular packing: a quasi-1D zigzag chain of water, as shown in schematics at top.[42] Schematics are reprinted in part with permission from Mughal, A.; Chan, H. K.; Weaire, D.; Hutzler, S. Dense Packings of Spheres in Cylinders: Simulations. *Phys. Rev. E* **2012**, *85*, 51305. https://doi.org/10.1103/PhysRevE.85.051305. Copyright 2012 American Physical Society.

As discussed by Longhurst and Quirke,[40] the RBM mode of a carbon nanotube can be modeled as a spatially uniform deformation w(t) of an elastic shell as shown below:[72]

$$\frac{w(t)}{R^2} + \frac{\rho h}{Eh}(1-\upsilon^2)\frac{\partial^2 w(t)}{\partial t^2} = 0 \quad [2.1]$$

where t is time, R is radius, ρ is mass density, h is shell thickness, E is the Young's modulus, and ν is Poisson's ratio. This second-order differential equation has a solution with the following frequency:

$$\omega_0 = \frac{1}{2\pi}\left[\frac{1}{R^2}\left(\frac{Eh}{\rho h(1-\upsilon^2)}\right)\right]^{1/2} \quad [2.2]$$

Using values of $Eh = 360\ J/m^2$, $\rho = 2.27\ g/cm^3$, and $\nu = 0.16$ for the CNT, it is possible to recover a value of $\omega_0 = 232\ [cm^{-1}]/D\ [nm]$ for the unperturbed radial breathing mode in this simple analytical model,[40] which is close to experimental values of $\omega_0 = 248\ [cm^{-1}]/D\ [nm]$.[51] By extension, an elastic shell that is coupled to a second rigid elastic shell experiences spatial deformation w(t) that is subject to:[40]

$$\left(\frac{1}{R^2} + \frac{c}{Eh}(1-\upsilon^2)\right)w(t) + \frac{\rho h}{Eh}(1-\upsilon^2)\frac{\partial^2 w(t)}{\partial t^2} = 0 \quad [2.3]$$

This yields the following frequency:

$$\omega_1 = \frac{1}{2\pi}\left[\frac{1}{R^2}\left(\frac{Eh}{\rho h(1-\upsilon^2)}\right) + \frac{c}{\rho h}\right]^{1/2} \quad [2.4]$$

where c is the area-normalized spring constant exerted by the rigid elastic shell on the elastic shell in question. The RBM shift upon fluid filling, then, is the difference between the two frequencies:

$$\Delta\omega_{RBM} = \omega_1 - \omega_0 \quad [2.5]$$

The interaction between the fluid and the carbon shell is captured entirely by the parameter c, a spring constant per unit area of CNT. We posit that the CNT-fluid interaction can be modeled as a set of independent Hookean springs between fluid molecules and a cylindrical CNT, such that the area-normalized spring constant is the product of a molecule-normalized spring constant k and a fluid areal density η, expressed as:

$$c = k \times \eta \quad [2.6]$$

where the dependencies of k and η with CNT diameter yield the $\Delta\omega_{RBM}$ *versus* D relationship for a fluid-CNT pair. A schematic of this model is shown in supplemental **Figure 2-6.**

In order to determine the packing density of water in a carbon nanotube, we adapt a spherical water packing model that Cambré and Wenseleers developed to interpret density differences in fluid-filled and empty carbon nanotubes upon ultracentrifugation.[33] We estimate

water as a sphere with a van der Waals radius of 0.15 nm and specify an excluded carbon-water radius of 0.17 nm.[33] Simulations of dense packing of equally sized spheres in cylinders[42,73] shows that the densest arrangement of spheres in a cylinder depends on the ratio of the size of the two objects (D/d) and can be uniquely determined for all states in which all spheres make contact with the confining cylinder. Within this range, there are 29 different arrangements, ranging from a single-file line at D/d=1 to zigzag arrangements and more complicated arrangements as D/d approaches 2.72.[42] Beyond this threshold, not all spheres make contact with the confining cylinder; this makes enumeration of sphere configurations and exact determination of geometric properties more difficult.[42] By knowing these packing arrangements, it is possible to determine a volume fraction for spherical water in a cylindrical CNT as a function of CNT diameter[33] as well as the areal molecular density η of interior water molecules that abut the CNT wall. The areal density η, as shown in **Figure 2-3c**, has a minimum at a diameter of 0.81 nm as a result of inefficient packing of spherical water in a quasi-single file zigzag. At very small diameters, single-file chains pack highly efficiently, while at large diameter packing becomes more efficient as the cross section can accommodate more water molecules. The close-packing limit reflects the densest, hexagonal packing of circles in 2D; as the diameter of the CNT gets far larger than the diameter of the water molecules, favorable CNT-water van der Waals interactions should lead to near maximal packing of water at the almost flat CNT interface. At diameters beyond 1.2 nm, the number of possible configurations proliferates and the exact water packing arrangement is unknown, but it is possible to estimate η from an exponential fit of the known η toward the close-packed limit. Since water may not exactly reach this 2D packing density at high diameter, the calculated η is an upper limit and results in a calculated upper limit for $\Delta\omega_{RBM}$ upon fluid filling.

In principle, the molecular spring constant k between each water molecule and the CNT wall may also change with CNT diameter. Here, we assume that the water molecules interact with the carbon atoms of the CNT primarily through Lennard-Jones interactions, which makes it possible to obtain an analytical solution. The classic Lennard-Jones potential describes the interaction between two uncharged molecules as containing a $1/r^6$ long-range attractive term due to van der Waals forces, and a $1/r^{12}$ short-range repulsive term due to orbital overlap:

$$V_{LJ} = 4\varepsilon\left[\left(\frac{\sigma}{r}\right)^{12} - \left(\frac{\sigma}{r}\right)^{6}\right] = -\frac{A}{r^6} + \frac{B}{r^{12}} \qquad [2.7]$$

where ε is the potential well depth, σ is the characteristic Lennard-Jones distance, and A and B are attractive and repulsive constants. This potential can be integrated to produce a potential for the interaction of a molecule with a sheet or cylinder.[74,75] In the case of a molecule at a distance h from a graphene sheet with smeared areal number density η_g instead of discrete carbon atoms, the total potential can be written as:[74]

$$E = \eta \int_S V(r)dS = \eta_g \pi\left(-\frac{A}{2h^4} + \frac{B}{5h^{10}}\right) \qquad [2.8]$$

Similarly, the potential of a particle at a distance h from the central axis of a cylinder with diameter D can be expressed as:[75]

$$E = \frac{3\pi D\eta_g}{16}\left(-AJ_2 + \frac{21B}{32}J_5\right) \quad [2.9]$$

where

$$J_n = \int_{-\pi}^{\pi} \frac{d\theta}{\left(\frac{D^2}{4}+h^2-Dh\,cos\theta\right)^{n+1/2}} \quad [2.10]$$

The effective spring constant for a molecular interaction with a sheet or cylinder is the second derivative of the potential with distance, taken at the point of minimum potential:

$$k(r) = -\frac{\partial F}{\partial r}\Big|_{r=r_{eq}} = -\frac{\partial^2 E}{\partial r^2}\Big|_{r=r_{eq}} \quad [2.11]$$

while this spring constant k may vary with CNT diameter, we assume for this simple, analytical model that the variation is small, effectively using the graphene Lennard-Jones spring constant for carbon nanotubes of varying diameter. This assumption is supported by MD simulations of water inside CNTs, which show sharp density peaks at fixed distance from the CNT wall.[68] The spring constant can be calculated using water-CNT Lennard Jones parameters[40] of $\varepsilon = 0.392\ kJ/mol$ and $\sigma = 0.319\ nm$ using either **Eq 8** or, as indicated by Cox and co-workers,[75] with **Eq 10**. The diameter at which RBM shift maxima or minima occur is sensitive to σ, which is well-established, while the magnitude of the predicted RBM shift is sensitive to ε, estimates for which vary more widely in molecular dynamics simulations.[40,76]

The area-normalized spring constant c can be calculated from the product of η and k, allowing calculation of $\Delta\omega_{RBM}$ *versus* diameter as shown in **Figure 2-4e**. If water packing effects are not taken into account, then $\Delta\omega_{RBM}$ increases linearly with diameter, as suggested in previous analyses.[40] If water packing effects are taken into account, then the analytical model shows a minimum in $\Delta\omega_{RBM}$ at a diameter of 0.78 nm. The experimental data, similarly, shows a minimum in $\Delta\omega_{RBM}$ at a critical diameter of around 0.93±0.08 nm with marked increases in $\Delta\omega_{RBM}$ on both sides of this critical diameter. The moving average and standard deviation of the experimental data is shown in grey in **Figure 2-9**. Within this range, there are five special packings of single-file (0.64 nm), double-file (0.94 nm), triple-file (0.99 nm), quadruple file (1.06), and quintuple-file (1.15 nm) spherical water within the model CNT, as shown by the colored panels in **Figure 2-4e**.[42] These simple regimes are corroborated, to first order, by radial density profiles taken from molecular dynamics simulations,[68] which suggest that a diameter of 0.9 nm is the boundary between a single-file chain of water and an annular shell configuration. The region between the single-file and double-file packings (0.64 nm and 0.94 nm) is a zigzag, quasi-1D water structure with low volumetric fill fraction and low areal density, as shown on top in **Figure 2-4e**. As proposed by Cambré and Wenseleers,[33] the minimum in $\Delta\omega_{RBM}$ at a CNT diameter of 0.93±0.08 nm, then, is likely due to minimally efficient zigzag packing of water into the nanotube at this diameter.

This analytical treatment can be extended to the filling of CNTs with other fluids, as shown for methane, ethane, and cyclohexane in **Figure 2-4d.** This analysis neglects molecular shape, which varies among different solvents. It also assumes that the interactions between fluid

molecules and a carbon nanotube can be adequately expressed as a Lennard-Jones potential, ignoring electrostatic and polarization effects[76] that may alter fluid structure and differ between strongly polar solvents like water and nonpolar solvents like methane, ethane, and cyclohexane. All-atomistic molecular dynamics simulations of CNT fluid filling, which have predominantly focused on water filling[68,76–80] with scant attention to non-aqueous fluids,[81–83] may be able to resolve interaction potentials and confined fluid densities in a way that more accurately predicts the Raman response to fluid filling. In general, this simple analytical model suggests that the Raman radial breathing mode shift upon water filling may exceed that upon filling with methane, ethane, or cyclohexane, with minima in $\Delta\omega_{RBM}$ at different diameters. Experimentally, the relative magnitude of RBM shifts upon aqueous and non-aqueous fluid filling have been reported to date for only a handful of CNT chiralities.[49]

2.3 Conclusions

In this study, we introduced a nanofluidic platform consisting of lithographically segmented, isolated CNTs on a silicon substrate. By photolithographic segmentation, multiple copies of the same diameter and length of carbon nanotube can be subjected to the same fluidic filling conditions and monitored by Raman spectroscopy. In general, water filling events are rare and largely permanent, occurring in less than a quarter of samples. Short, 6 μm CNT segments that are either filled or empty in their entirety, while longer 160 μm segments fill from the ends but in some cases clog along their length. We demonstrate that the Raman radial breathing mode changes only when an opened CNT is immersed in water, thus confirming that for substrate-bound CNTs, the RBM is a sensitive measure of internal fluid filling and not of external water adsorption or other physical processes.

As an application, we used our introduced segmented CNT platform to investigate the diameter dependence of the fluid-induced upshift of the Raman radial breathing mode, $\Delta\omega_{RBM}$. Through development of an analytical shell/spring model, we were able to explain changes in the RBM shift with CNT diameter, and in particular the minimum $\Delta\omega_{RBM}$ at a diameter of 0.93±0.08 nm, as a result of changes in water packing originating from discrete size effects. As water structure changes from an efficient single-file chain to an inefficient zigzag configuration with increasing CNT diameter, $\Delta\omega_{RBM}$ decreases to a minimum of 1.81±0.09 cm^{-1}. Then, as diameter continues to increase, the addition of more water layers and more bulk-like water behavior causes $\Delta\omega_{RBM}$ to increase roughly linearly. These experimental results confirm the usefulness of Raman spectroscopy for tracking water filling processes in carbon nanotubes, and suggest an experimental platform for the study of non-aqueous fluid filling and capillary filling dynamics under conditions of extreme quasi-1D confinement.

2.4 Methods

Growth of Ultra-Long Aligned Carbon Nanotubes: Ultra-long gas-flow aligned carbon nanotubes were grown by chemical vapor deposition[43] on lithographically patterned silicon substrates as described previously, with slight modifications.[9,45] To summarize, one of several catalyst solutions – iron chloride (Sigma Aldrich) or 25 Series APT carbon nanotubes (Nano-C)

– was deposited on one end of a Si wafer. The sample was placed in a quartz tube and CNTs were grown by methane CVD in hydrogen at 970 °C for 45 minutes.

Lithographic Segmentation of Carbon Nanotubes: After initial Raman scans to locate regions of interest, carbon nanotubes were segmented by photolithography. Substrates were spin-coated with Shipley 1805 photoresist (3000 rpm), the sample was exposed (Heidelberg MLA 150 maskless aligner, 405 nm, 60 mW/mm^2), and the photoresist was developed (Microposit CD-26, 60s). The sample was then etched by low-power oxygen plasma (Harrick PDC-32G, 6.8 W) for 3 minutes, rinsed quickly in acetone and isopropanol to remove photoresist, and dried at 200 ℃ for 5 minutes.

Water and Nitric Acid Treatments: For water treatment, samples were immersed in water (Sigma Aldrich, ASTM Type II) for 1 hour, then dried with nitrogen gas. For dynamic filling experiments, ~10 µL water was placed by pipette on the substrate and replenished as needed to replace losses by evaporation. For nitric acid treatment, samples were immersed in 2.6 M HNO_3 (Sigma-Aldrich) for 1 hour before rinsing in water, then dried at 200 ℃ for 5 minutes. Samples were stored in a desiccator chamber between experiments, with Raman spectroscopy and other measurements performed at ambient temperature (23 °C) and humidity (30-50% relative humidity).

Characterization by Raman Spectroscopy: As-synthesized and segmented carbon nanotubes were probed by confocal microRaman spectroscopy (Horiba LabRAM HR Evolution, grating 1800 gr/mm, hole 500 µm, slit 150 µm) with three different objectives (Olympus MPLFLN 50X air-immersion objective, NA=0.8, Olympus MPLFLN 100X air-immersion objective, NA=0.9, and Olympus LUMPLFLN 60X water-immersion objective, NA=1.0) with a 532 nm laser (Invictus, 100 mW) as described previously.[9] The Raman spectrometer was arranged in a backscattering geometry, with polarization of the incident laser parallel to the nanotube axis. Typical settings include a wavenumber range of 50 to 1750 cm^{-1} and 2 accumulations of 5 s, with data collection using Horiba LabSpec 6 software and analyzed in Matlab. The laser spot size was 1 to 2 µm, depending on the objective, making it far larger than the diameter of the CNTs considered in this study, and the spectral resolution was 0.32 cm^{-1}. The sample was mounted on a motorized stage (Märzhäuser Wetzlar SCAN series) with x, y, and z motorized control, and was moved relative to the fixed laser beam.

Data Analysis: A scaled silicon background spectrum was subtracted from the collected spectra to remove silicon Raman features and instrument noise. Peak fitting was done in Matlab using a least-squares method to fit each RBM region and Si region to a single Lorentzian. Typical error associated with determining the peak center was 0.02 cm^{-1}, less than error in instrument calibration. RBM peak position was normalized by Si peak position in calculating $\Delta\omega_{RBM}$ to correct for any instrument miscalibration. Raman spectra that contained an RBM peak within 10 cm^{-1} of one another and were captured within 10 µm of one another's nominal position during successive scans were assigned to the same CNT, with the exception that any pairs with substantially different G lineshapes were rejected. CNT diameter was calculated as:[84]

$$d\,[nm] = \frac{248}{\omega_{RBM}[cm^{-1}]}$$

There are a variety of relationships between ω_{RBM} and diameter for substrate-bound SWCNTs.[85–87] More recent work[88] suggests a slightly different relationship, but with an error in diameter of no more than 0.03 nm across the relevant range. Standard errors of the mean for the critical diameter and critical RBM shift were estimated by a bootstrapping method with 10,000 samples, as shown in **Figure 2-10**.

2.5 Supporting Information

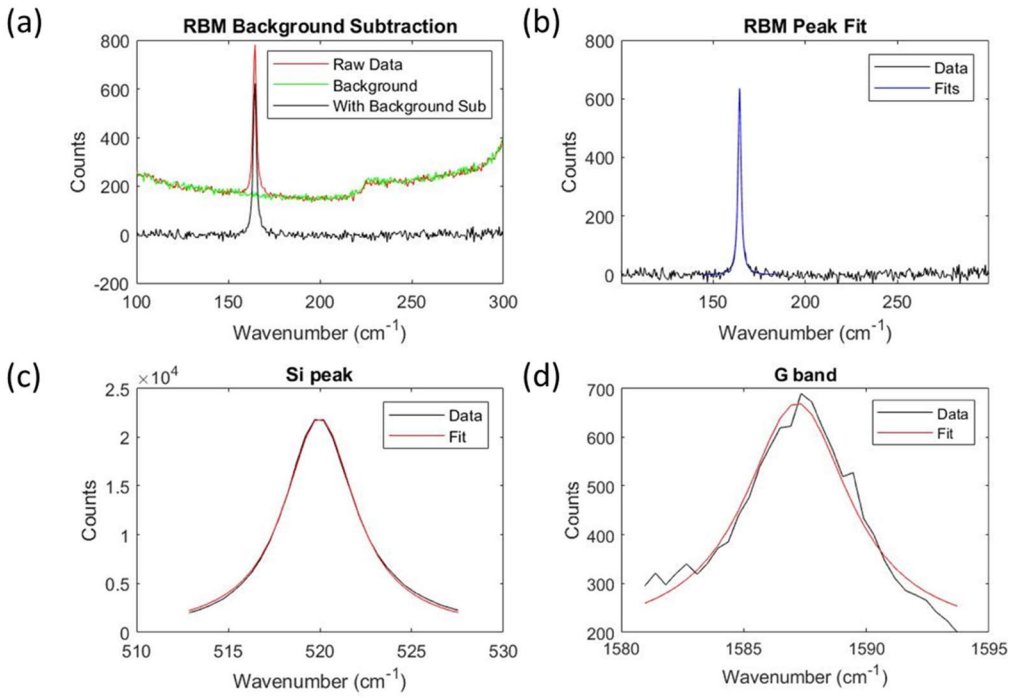

Figure 2-5 | Raman data analysis. A sample Raman spectrum for one 1.51 nm CNT is analyzed. (a) The silicon background multiplied by a constant coefficient and subtracted. (b) After subtraction of a Si background signal, the RBM peak is fit to a single Lorentzian, and the peak position and full-width half maximum are calculated. (c) The Si fit is used to confirm instrument calibration. (d) The G band is used to locate CNTs and confirm that the same CNT is being observed repeatedly.

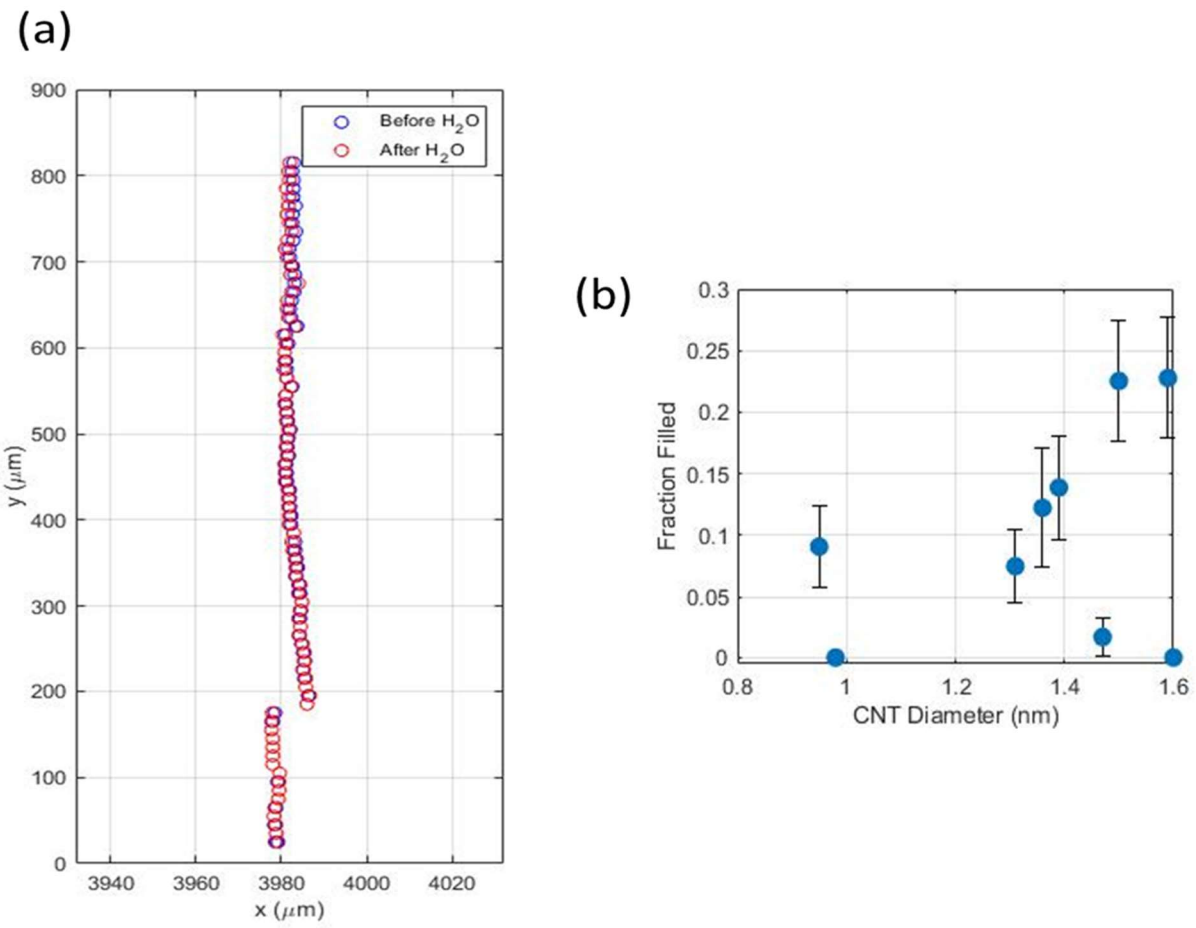

Figure 2-6 | Statistics of filling from lithographically patterned CNTs. (a) Raman xy maps determine the location of etched, segmented CNTs on the silicon substrate before and after water immersion, and confirm that the same substrate-bound CNT is being observed before and after water immersion. (b) Fraction of 6 μm CNT segments filled *versus* diameter for 9 CNT chiralities, ranging from 0.95 to 1.59 nm in diameter. Each point represents observations of between 49 to 80 distinct CNT segments of the same chirality and diameter, with $\Delta\omega_{RBM}$=0.8 cm^{-1} used as the threshold for fluid filling.

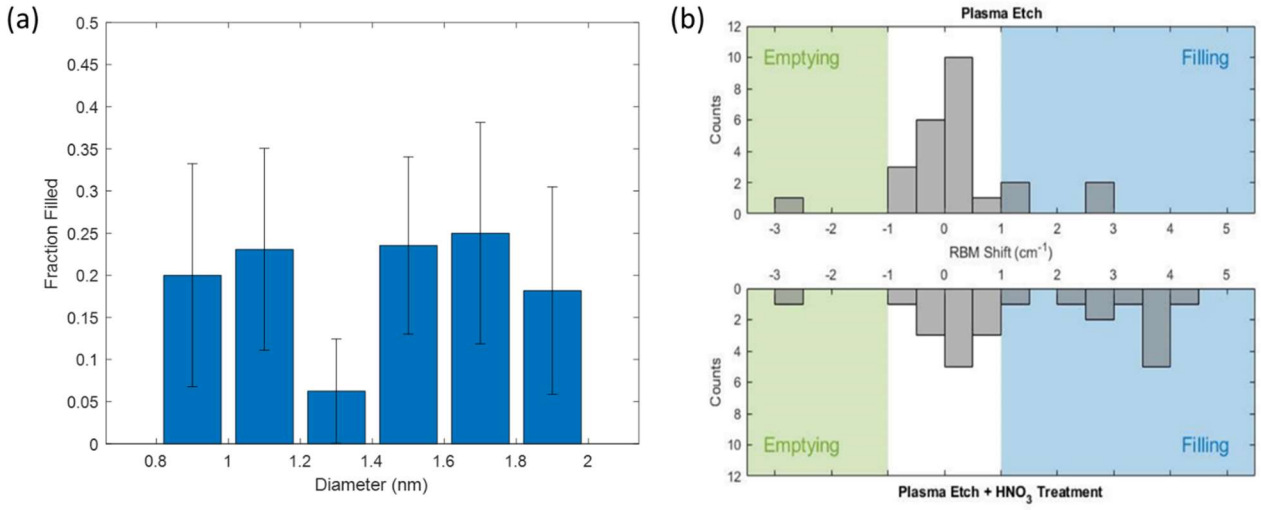

Figure 2-7 | (a) The fraction of CNTs that fill with water, as indicated by an RBM shift above 0.8 cm^{-1}, is shown *versus* diameter from 0.8 nm to 2.0 nm. Variations in fraction filled with diameter are not statistically significant. (b) Effect of nitric acid treatment on water filling of carbon nanotubes. Each data point represents paired observations of the same location on the same chirality, substrate-bound CNT. On top, Raman spectra are taken before and after 1 hr H_2O immersion for CNTs subject to oxygen plasma etching to open CNT ends (6.8 W, 3 min). On bottom, Raman spectra are taken before and after 1 hr H_2O immersion for CNTs subjected to oxygen plasma etching plus supplemental immersion in nitric acid (2.6 M, 1 hr) and subsequent drying. CNTs are more likely to fill with water after immersion in nitric acid than they are without nitric acid treatment, as shown by the difference in $\Delta\omega_{RBM}$ distributions.

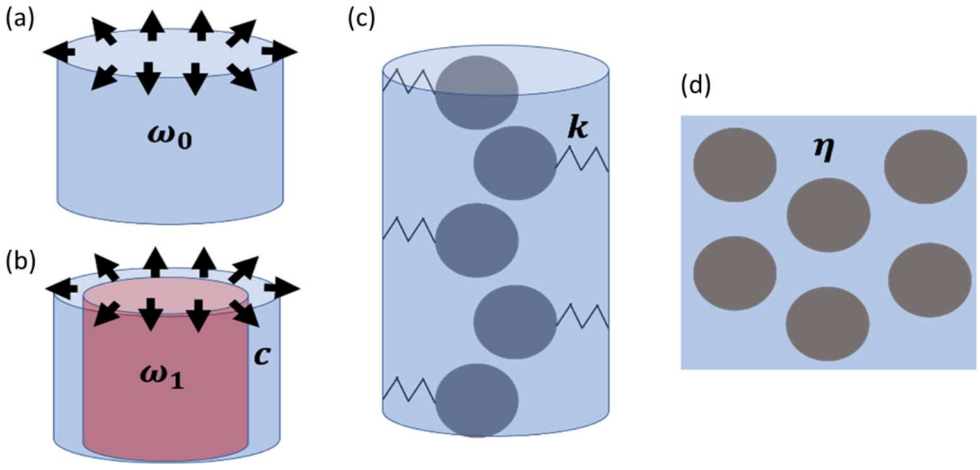

Figure 2-8 | (a-b) In a quasi-continuum model, the change in CNT RBM frequency $\Delta\omega_{RBM} = \omega_1 - \omega_0$ can be related to the area-normalized spring constant c applied by a rigid fluid shell on the elastic shell of the CNT. The spring constant c in this model is the product of (b) the molecular spring constant k, and (c) the fluid areal density η. In this model, η alone is assumed to vary with CNT diameter.

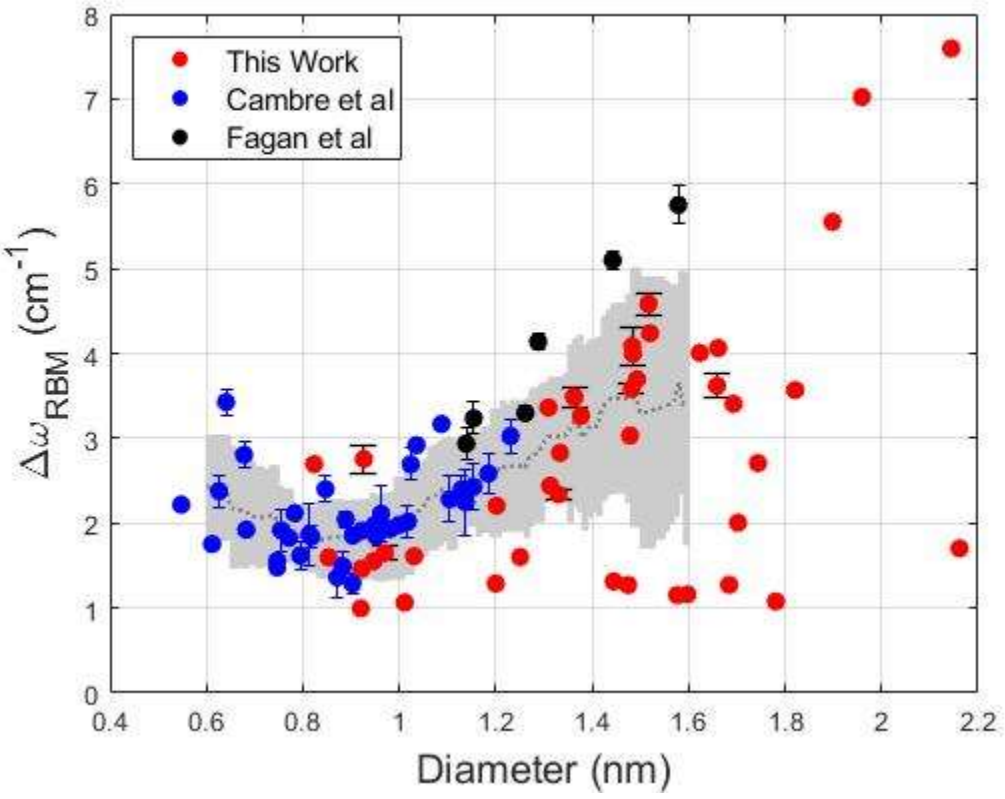

Figure 2-9 | RBM shift is shown *versus* diameter in CNTs that are presumed to have filled or emptied with comparison to solution-phase work by Cambré *et al*.[30] and Fagan *et al*.[31] Individual paired observations do not have confidence intervals, while repeated measurements on the same chirality CNT are shown with 95% confidence intervals. A moving average and standard deviation of $\Delta\omega_{RBM}$ is shown in grey.

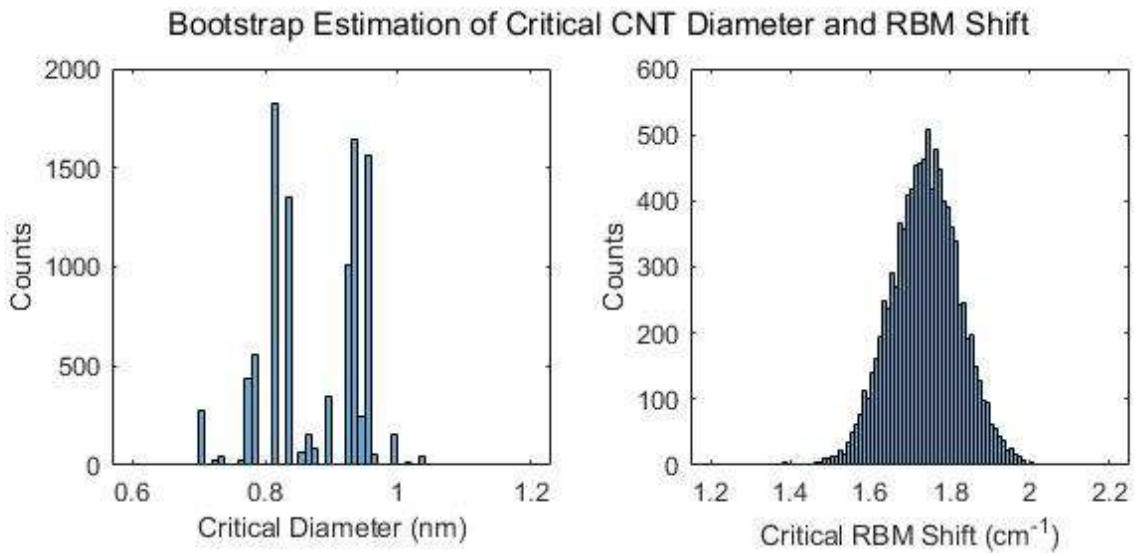

Figure 2-10 | Bootstrap estimation of standard error of the mean in critical CNT diameter (±0.08 nm) and critical RBM shift (±0.09 cm^{-1}). Standard errors of the mean were estimated by analysis of 10,000 bootstrapped samples.

2.6 References

(1) Faucher, S.; Aluru, N.; Bazant, M. Z.; Blankschtein, D.; Brozena, A. H.; Cumings, J.; Pedro De Souza, J.; Elimelech, M.; Epsztein, R.; Fourkas, J. T.; Rajan, A. G.; Kulik, H. J.; Levy, A.; Majumdar, A.; Martin, C.; McEldrew, M.; Misra, R. P.; Noy, A.; Pham, T. A.; Reed, M. *et al*. Critical Knowledge Gaps in Mass Transport through Single-Digit Nanopores: A Review and Perspective. *J. Phys. Chem. C* **2019**, *123* (35). https://doi.org/10.1021/acs.jpcc.9b02178.

(2) Bocquet, L. Nanofluidics Coming of Age. *Nat. Mater.* **2020**, *19* (3), 254–256. https://doi.org/10.1038/s41563-020-0625-8.

(3) Secchi, E.; Marbach, S.; Niguès, A.; Stein, D.; Siria, A.; Bocquet, L. Massive Radius-Dependent Flow Slippage in Carbon Nanotubes. *Nature* **2016**, *537* (7619), 210–213. https://doi.org/10.1038/nature19315.

(4) Qin, X.; Yuan, Q.; Zhao, Y.; Xie, S.; Liu, Z. Measurement of the Rate of Water Translocation through Carbon Nanotubes. *Nano Lett.* **2011**, *11*, 2173–2177. https://doi.org/10.1021/nl200843g.

(5) Tunuguntla, R. H.; Henley, R. Y.; Yao, Y.-C.; Pham, T. A.; Wanunu, M.; Noy, A. Enhanced Water Permeability and Tunable Ion Selectivity in Subnanometer Carbon Nanotube Porins. *Science* **2017**, *357* (6353), 792–796. https://doi.org/10.1126/science.aan2438.

(6) Holt, J.; Park, H. G.; Wang, Y.; Stadermann, M.; Artyukhin, A.; Grigoropoulos, C.; Noy, A.; Bakajin, O. Fast Mass Transport through Sub-2-Nanometer Carbon Nanotubes. *Science* **2006**, 1034–1037. https://doi.org/10.1126/science.1124621.

(7) Sam, A.; Hartkamp, R.; Kumar Kannam, S.; Babu, J. S.; Sathian, S. P.; Daivis, P. J.; Todd, B. D. Fast Transport of Water in Carbon Nanotubes: A Review of Current

Accomplishments and Challenges. *Mol. Simul.* **2020**. https://doi.org/10.1080/08927022.2020.1782401.

(8) Shimizu, S.; Varoon Agrawal, K.; Drahushuk, L. W.; Manohar, N.; Myerson, A. S.; Strano, M. S. Understanding and Analyzing Freezing-Point Transitions of Confined Fluids within Nanopores. *Langmuir* **2015**, *31*, 10113–10118. https://doi.org/10.1021/acs.langmuir.5b02149.

(9) Agrawal, K. V.; Shimizu, S.; Drahushuk, L. W.; Kilcoyne, D.; Strano, M. S.; Varoon Agrawal, K.; Shimizu, S.; Drahushuk, L. W.; Kilcoyne, D.; Strano, M. S.; Agrawal, K. V.; Shimizu, S.; Drahushuk, L. W.; Kilcoyne, D.; Strano, M. S. Observation of Extreme Phase Transition Temperatures of Water Confined inside Isolated Carbon Nanotubes. *Nat. Nanotechnol.* **2017**, *12* (3), 267–273. https://doi.org/10.1038/nnano.2016.254.

(10) Zhang, C.; Gygi, F; Galli, G. Strongly Anisotropic Dielectric Relaxation of Water at the Nanoscale. *J. Phys. Chem. Lett* **2013**, *16*, 29. https://doi.org/10.1021/jz401108n.

(11) Fumagalli, L.; Esfandiar, A.; Fabregas, R.; Hu, S.; Ares, P.; Janardanan, A.; Yang, Q.; Radha, B.; Taniguchi, T.; Watanabe, K.; Gomila, G.; Novoselov, K. S.; Geim, A. K. Anomalously Low Dielectric Constant of Confined Water. *Science* **2018**, *360* (6395), 1339–1342. https://doi.org/10.1126/science.aat4191.

(12) Xie, Q.; Alibakhshi, M. A.; Jiao, S.; Xu, Z.; Hempel, M.; Kong, J.; Park, H. G.; Duan, C. Fast Water Transport in Graphene Nanofluidic Channels. *Nat. Nanotechnol.* **2018**, *13* (3), 238–245. https://doi.org/10.1038/s41565-017-0031-9.

(13) Li, Y.; Chen, H.; Xiao, S.; Alibakhshi, M. A.; Lo, C. W.; Lu, M. C.; Duan, C. Ultrafast Diameter-Dependent Water Evaporation from Nanopores. *ACS Nano* **2019**, *13* (3), 3363–3372. https://doi.org/10.1021/acsnano.8b09258.

(14) Duan, C.; Karnik, R.; Lu, M. C.; Majumdar, A. Evaporation-Induced Cavitation in Nanofluidic Channels. *Proc. Natl. Acad. Sci. U. S. A.* **2012**, *109* (10), 3688–3693. https://doi.org/10.1073/pnas.1014075109.

(15) Rangharajan, K. K.; Mohana Sundaram, P.; Conlisk, A. T.; Prakash, S. Surface Dependent Enhancement in Water Vapor Permeation through Nanochannels. *Analyst* **2018**, *143* (18), 4256–4266. https://doi.org/10.1039/c8an00650d.

(16) Geim, A. K.; Grigorieva, I. V. van der Waals Heterostructures. *Nature* **2013**, *499* (7459), 419–425. https://doi.org/10.1038/nature12385.

(17) Radha, B.; Esfandiar, A.; Wang, F. C.; Rooney, A. P.; Gopinadhan, K.; Keerthi, A.; Mishchenko, A.; Janardanan, A.; Blake, P.; Fumagalli, L.; Lozada-Hidalgo, M.; Garaj, S.; Haigh, S. J.; Grigorieva, I. V.; Wu, H. A.; Geim, A. K. Molecular Transport through Capillaries Made with Atomic-Scale Precision. *Nature* **2016**, *538* (7624), 222–225. https://doi.org/10.1038/nature19363.

(18) Yang, Q.; Sun, P. Z.; Fumagalli, L.; Stebunov, Y. V.; Haigh, S. J.; Zhou, Z. W.; Grigorieva, I. V.; Wang, F. C.; Geim, A. K. Capillary Condensation under Atomic-Scale Confinement. *Nature* **2020**, *588*, 250–256. https://doi.org/10.1038/s41586-020-2978-1.

(19) Majumder, M.; Chopra, N.; Andrews, R.; Hinds, B. Enhanced Flow in Carbon Nanotubes. *Nature* **2005**, *438*, 44.

(20) Majumder, M.; Chopra, N.; Hinds, B. J. Mass Transport through Carbon Nanotube Membranes in Three Different Regimes: Ionic Diffusion and Gas and Liquid Flow. *ACS Nano* **2011**, *5* (5), 3867–3877. https://doi.org/10.1021/nn200222g.

(21) Wu, J.; Gerstandt, K.; Zhang, H.; Liu, J.; Hinds, B. J. Electrophoretically Induced Aqueous Flow through Single-Walled Carbon Nanotube Membranes. *Nat. Nanotechnol.*

2012, *7* (2), 133–139. https://doi.org/10.1038/nnano.2011.240.
(22) Yao, Y. C.; Taqieddin, A.; Alibakhshi, M. A.; Wanunu, M.; Aluru, N. R.; Noy, A. Strong Electroosmotic Coupling Dominates Ion Conductance of 1.5 Nm Diameter Carbon Nanotube Porins. *ACS Nano* **2019**, *13* (11), 12851-12859. https://doi.org/10.1021/acsnano.9b05118.
(23) Kyakuno, H.; Matsuda, K.; Yahiro, H.; Inami, Y.; Fukuoka, T.; Miyata, Y.; Yanagi, K.; Maniwa, Y.; Kataura, H.; Saito, T.; Yumura, M.; Iijima, S. Confined Water inside Single-Walled Carbon Nanotubes: Global Phase Diagram and Effect of Finite Length. *J. Chem. Phys.* **2011**, *134* (24), 244501. https://doi.org/10.1063/1.3593064.
(24) Kyakuno, H.; Fukasawa, M.; Ichimura, R.; Matsuda, K.; Nakai, Y.; Miyata, Y.; Saito, T.; Maniwa, Y. Diameter-Dependent Hydrophobicity in Carbon Nanotubes. *J. Chem. Phys.* **2016**, *145* (6), 64514. https://doi.org/10.1063/1.4960609.
(25) Hassan, J.; Diamantopoulos, G.; Gkoura, L.; Karagianni, M.; Alhassan, S.; Kumar, S. V; Katsiotis, M. S.; Karagiannis, T.; Fardis, M.; Panopoulos, N.; Kim, H. J.; Beazi-Katsioti, M.; Papavassiliou, G. Ultrafast Stratified Diffusion of Water inside Carbon Nanotubes; Direct Experimental Evidence with 2D D−T_2 NMR Spectroscopy. *J. Phys. Chem. C* **2018**, *122*, 18. https://doi.org/10.1021/acs.jpcc.8b01377.
(26) Reiter, G. F.; Kolesnikov, A. I.; Paddison, S. J.; Platzman, P. M.; Moravsky, A. P.; Adams, M. A.; Mayers, J. Evidence for an Anomalous Quantum State of Protons in Nanoconfined Water. *Phys. Rev. B - Condens. Matter Mater. Phys.* **2012**, *85* (4), 45403. https://doi.org/10.1103/PhysRevB.85.045403.
(27) Briganti, G.; Rogati, G.; Parmentier, A.; Maccarini, M.; De Luca, F. Neutron Scattering Observation of Quasi-Free Rotations of Water Confined in Carbon Nanotubes. *Sci. Rep.* **2017**, *7*. https://doi.org/10.1038/srep45021.
(28) Byl, O.; Liu, J.-C.; Wang, Y.; Yim, W.-L.; Johnson, J. K.; Yates, J. T. Unusual Hydrogen Bonding in Water-Filled Carbon Nanotubes. *JACS* **2006**, *128*, 12090–12097. https://doi.org/10.1021/ja057856u.
(29) Dalla Bernardina, S.; Paineau, E.; Brubach, J. B.; Judeinstein, P.; Rouzière, S.; Launois, P.; Roy, P. Water in Carbon Nanotubes: The Peculiar Hydrogen Bond Network Revealed by Infrared Spectroscopy. *J. Am. Chem. Soc.* **2016**, *138* (33), 10437–10443. https://doi.org/10.1021/jacs.6b02635.
(30) Cambré, S.; Schoeters, B.; Luyckx, S.; Goovaerts, E.; Wenseleers, W. Experimental Observation of Single-File Water Filling of Thin Single-Wall Carbon Nanotubes down to Chiral Index (5,3). *Phys. Rev. Lett.* **2010**, *104* (20), 1–4. https://doi.org/10.1103/PhysRevLett.104.207401.
(31) Fagan, J. A.; Huh, J. Y.; Simpson, J. R.; Blackburn, J. L.; Holt, J. M.; Larsen, B. A.; Walker, A. R. H. Separation of Empty and Water-Filled Single-Wall Carbon Nanotubes. *ACS Nano* **2011**, *5* (5), 3943–3953. https://doi.org/10.1021/nn200458t.
(32) Torres-Dias, A. C.; Cambré, S.; Wenseleers, W.; Machon, D.; San-Miguel, A. Chirality-Dependent Mechanical Response of Empty and Water-Filled Single-Wall Carbon Nanotubes at High Pressure. *Carbon N. Y.* **2015**, *95*, 442–451. https://doi.org/10.1016/j.carbon.2015.08.032.
(33) Cambré, S.; Wenseleers, W. Separation and Diameter-Sorting of Empty (End-Capped) and Water-Filled (Open) Carbon Nanotubes by Density Gradient Ultracentrifugation. *Angew. Chemie - Int. Ed.* **2011**, *50* (12), 2764–2768. https://doi.org/10.1002/anie.201007324.

(34) Marcotte, A.; Mouterde, T.; Niguès, A.; Siria, A.; Bocquet, L. Mechanically Activated Ionic Transport across Single-Digit Carbon Nanotubes. *Nat. Mater.* **2020**, *19* (10), 1057–1061. https://doi.org/10.1038/s41563-020-0726-4.
(35) Min, H.; Kim, Y. T.; Moon, S. M.; Han, J. H.; Yum, K.; Lee, C. Y. High-Yield Fabrication, Activation, and Characterization of Carbon Nanotube Ion Channels by Repeated Voltage-Ramping of Membrane-Capillary Assembly. *Adv. Funct. Mater.* **2019**, *29* (27), 1–9. https://doi.org/10.1002/adfm.201900421.
(36) Cambré, S.; Santos, S. M.; Wenseleers, W.; Nugraha, A. R. T.; Saito, R.; Cognet, L.; Lounis, B. Luminescence Properties of Individual Empty and Water-Filled Single-Walled Carbon Nanotubes. *ACS Nano* **2012**, *6* (3), 2649–2655. https://doi.org/10.1021/nn300035y.
(37) Chiashi, S.; Hanashima, T.; Mitobe, R.; Nagatsu, K.; Yamamoto, T.; Homma, Y. Water Encapsulation Control in Individual Single-Walled Carbon Nanotubes by Laser Irradiation. *J. Phys. Chem. Lett.* **2014**, *5* (3), 408–412. https://doi.org/10.1021/jz402540v.
(38) Chiashi, S.; Saito, Y.; Kato, T.; Konabe, S.; Okada, S.; Yamamoto, T.; Homma, Y. Confinement Effect of Sub-Nanometer Difference on Melting Point of Ice-Nanotubes Measured by Photoluminescence Spectroscopy. *ACS Nano* **2019**, *13* (2), 1177–1182. https://doi.org/10.1021/acsnano.8b06041.
(39) Longhurst, M. J.; Quirke, N. The Environmental Effect on the Radial Breathing Mode of Carbon Nanotubes. II. Shell Model Approximation for Internally and Externally Adsorbed Fluids. *J. Chem. Phys.* **2006**, *125* (18), 184705. https://doi.org/10.1063/1.2360943.
(40) Longhurst, M. J.; Quirke, N. The Environmental Effect on the Radial Breathing Mode of Carbon Nanotubes in Water. *J. Chem. Phys.* **2006**, *124* (23), 234708. https://doi.org/10.1063/1.2205852.
(41) Chiashi, S.; Kono, K.; Matsumoto, D.; Shitaba, J.; Homma, N.; Beniya, A.; Yamamoto, T.; Homma, Y. Adsorption Effects on Radial Breathing Mode of Single-Walled Carbon Nanotubes. *Phys. Rev. B - Condens. Matter Mater. Phys.* **2015**, *91* (15), 155415. https://doi.org/10.1103/PhysRevB.91.155415.
(42) Mughal, A.; Chan, H. K.; Weaire, D.; Hutzler, S. Dense Packings of Spheres in Cylinders: Simulations. *Phys. Rev. E* **2012**, *85*, 51305. https://doi.org/10.1103/PhysRevE.85.051305.
(43) Huang, S.; Cai, X.; Liu, J. Growth of Millimeter-Long and Horizontally Aligned Single-Walled Carbon Nanotubes on Flat Substrates. *J. Am. Chem. Soc.* **2003**, *125* (19), 5636–5637. https://doi.org/10.1021/ja034475c.
(44) Huang, S.; Woodson, M.; Smalley, R.; Liu, J. Growth Mechanism of Oriented Long Single Walled Carbon Nanotubes Using "Fast-Heating" Chemical Vapor Deposition Process. *Nano Lett.* **2004**, *4* (6), 1025–1028. https://doi.org/10.1021/nl049691d.
(45) Choi, W.; Ulissi, Z. W.; Shimizu, S. F. E. E.; Bellisario, D. O.; Ellison, M. D.; Strano, M. S. Diameter-Dependent Ion Transport through the Interior of Isolated Single-Walled Carbon Nanotubes. *Nat. Commun.* **2013**, *4* (2397), 1–8. https://doi.org/10.1038/ncomms3397.
(46) Lobo, A. O.; Ramos, S. C.; Antunes, E. F.; Marciano, F. R.; Trava-Airoldi, V. J.; Corat, E. J. Fast Functionalization of Vertically Aligned Multiwalled Carbon Nanotubes Using Oxygen Plasma. *Mater. Lett.* **2012**, *70*, 89–93. https://doi.org/10.1016/j.matlet.2011.11.071.
(47) Huang, S.; Dai, L. Plasma Etching for Purification and Controlled Opening of Aligned Carbon Nanotubes. *J. Phys. Chem. B* **2002**, *106* (14), 3543–3545.

https://doi.org/10.1021/jp014047y.
(48) Lee, C. Y.; Choi, W.; Han, J.-H. H.; Strano, M. S. Coherence Resonance in a Single-Walled Carbon Nanotube Ion Channel. *Science (80-.).* **2010**, *329* (5997), 1320–1324. https://doi.org/10.1126/science.1193383.
(49) Campo, J.; Piao, Y.; Lam, S.; Stafford, C. M.; Streit, J. K.; Simpson, J. R.; Hight Walker, A. R.; Fagan, J. A. Enhancing Single-Wall Carbon Nanotube Properties through Controlled Endohedral Filling. *Nanoscale Horizons* **2016**, *1* (4), 317–324. https://doi.org/10.1039/c6nh00062b.
(50) Wenseleers, W.; Cambré, S.; Čulin, J.; Bouwen, A.; Goovaerts, E. Effect of Water Filling on the Electronic and Vibrational Resonances of Carbon Nanotubes: Characterizing Tube Opening by Raman Spectroscopy. *Adv. Mater.* **2007**, *19* (17), 2274–2278. https://doi.org/10.1002/adma.200700773.
(51) Dresselhaus, M.; Dresselhaus, G.; Saito, R.; Jorio, K. Raman Spectroscopy of Carbon Nanotubes. *Phys. Rep.* **2005**, *49*, 47–99.
(52) Washburn, E. W. The Dynamics of Capillary Flow. *Phys. Rev.* **1921**, *17* (3), 273–283. https://doi.org/10.1103/PhysRev.18.206.
(53) Dimitrov, D. I.; Milchev, A.; Binder, K. Capillary Rise in Nanopores: Molecular Dynamics Evidence for the Lucas-Washburn Equation. *Phys. Rev. Lett.* **2007**, *99* (5), 1–4. https://doi.org/10.1103/PhysRevLett.99.054501.
(54) Zhong, J.; Riordon, J.; Zandavi, S. H.; Xu, Y.; Persad, A. H.; Mostowfi, F.; Sinton, D. Capillary Condensation in 8 nm Deep Channels. *J. Phys. Chem. Lett.* **2018**, *9* (3), 497–503. https://doi.org/10.1021/acs.jpclett.7b03003.
(55) Zhang, D.; Yang, J.; Yang, F.; Li, R.; Li, M.; Ji, D.; Li, Y. (N,m) Assignments and Quantification for Single-Walled Carbon Nanotubes on SiO_2/Si Substrates by Resonant Raman Spectroscopy. *Nanoscale* **2015**, *7*, 10719. https://doi.org/10.1039/c5nr01076d.
(56) Zhang, Y.; Zhang, J.; Son, H.; Kong, J.; Liu, Z. Substrate-Induced Raman Frequency Variation for Single-Walled Carbon Nanotubes. *J. Am. Chem. Soc.* **2005**, *127* (49), 17156–17157. https://doi.org/10.1021/ja056793c.
(57) Zhang, Y.; Son, H.; Zhang, J.; Dresselhaus, M. S.; Kong, J.; Liu, Z. Raman Spectra Variation of Partially Suspended Individual Single-Walled Carbon Nanotubes. *J. Phys. Chem. C* **2007**, *111* (5), 1983–1987. https://doi.org/10.1021/jp065973l.
(58) Steiner, M.; Freitag, M.; Tsang, J. C.; Perebeinos, V.; Bol, A. A.; Failla, A. V.; Avouris, P. How Does the Substrate Affect the Raman and Excited State Spectra of a Carbon Nanotube? *Appl. Phys. A Mater. Sci. Process.* **2009**, *96* (2), 271–282. https://doi.org/10.1007/s00339-009-5211-5.
(59) Gotovac, S.; Honda, H.; Hattori, Y.; Takahashi, K.; Kanoh, H.; Kaneko, K. Effect of Nanoscale Curvature of Single-Walled Carbon Nanotubes on Adsorption of Polycyclic Aromatic Hydrocarbons. *Nano Lett.* **2007**, *7* (3), 583–587. https://doi.org/10.1021/nl0622597.
(60) Cunha, R.; Paupitz, R.; Yoon, K.; Van Duin, A. C. T.; Elías, A. L.; Carozo, V.; Dasgupta, A.; Fujisawa, K.; Lopez, N. P.; Araujo, P. T.; Terrones, M. Raman Spectroscopy Revealing Noble Gas Adsorption on Single-Walled Carbon Nanotube Bundles. *Carbon N. Y.* **2018**, *127*, 312–319. https://doi.org/10.1016/j.carbon.2017.11.017.
(61) Homma, Y.; Chiashi, S.; Yamamoto, T.; Kono, K.; Matsumoto, D.; Shitaba, J.; Sato, S. Photoluminescence Measurements and Molecular Dynamics Simulations of Water Adsorption on the Hydrophobic Surface of a Carbon Nanotube in Water Vapor. *Phys. Rev.*

Lett. **2013**, *110* (15). https://doi.org/10.1103/PhysRevLett.110.157402.
(62) Edwards, P. J.; Wang, B.; Cronin, S. B.; Bushmaker, A. W. Direct Measurement of Water-Assisted Ion Desorption and Solvation on Isolated Carbon Nanotubes. *ACS Nano* **2020,** *14* (12), 16854-16863. https://doi.org/10.1021/acsnano.0c05638.
(63) Zhang, J.; Zou, H.; Qing, Q.; Yang, Y.; Li, Q.; Liu, Z.; Guo, X.; Du, Z. Effect of Chemical Oxidation on the Structure of Single-Walled Carbon Nanotubes. *J. Phys. Chem. B* **2003**, *107* (16), 3712–3718. https://doi.org/10.1021/jp027500u.
(64) Tchoul, M. N.; Ford, W. T.; Lolli, G.; Resasco, D. E.; Arepalli, S. Effect of Mild Nitric Acid Oxidation on Dispensability, Size, and Structure of Single-Walled Carbon Nanotubes. *Chem. Mater.* **2007**, *19* (23), 5765–5772. https://doi.org/10.1021/cm071758l.
(65) Tsang, S. C.; Chen, Y. K.; Harris, P. J. F. F.; Green, M. L. H. H. A Simple Chemical Method of Opening and Filling Carbon Nanotubes. *Nature* **1994**, *372* (6502), 159–162. https://doi.org/10.1038/372159a0.
(66) Majumder, M.; Corry, B. Anomalous Decline of Water Transport in Covalently Modified Carbon Nanotube Membranes. *Chem. Commun* **2011**, *47*, 7683–7685. https://doi.org/10.1039/c1cc11134e.
(67) Rabinowitz, J.; Cohen, C.; Shepard, K. L. An Electrically Actuated, Carbon-Nanotube-Based Biomimetic Ion Pump. **2020**, *20* (2). https://doi.org/10.1021/acs.nanolett.9b04552.
(68) Pascal, T. A.; Goddard, W. A.; Jung, Y. Entropy and the Driving Force for the Filling of Carbon Nanotubes with Water. *PNAS* **2011**, *108* (29), 11794–11798.
(69) Zschoerper, N. P.; Katzenmaier, V.; Vohrer, U.; Haupt, M.; Oehr, C.; Hirth, T. Analytical Investigation of the Composition of Plasma-Induced Functional Groups on Carbon Nanotube Sheets. *Carbon N. Y.* **2009**, *47* (9), 2174–2185. https://doi.org/10.1016/j.carbon.2009.03.059.
(70) Mathur, A.; Roy, S. S.; Hazra, K. S.; Wadhwa, S.; Ray, S. C.; Mitra, S. K.; Misra, D. S.; McLaughlin, J. A. Oxygen Plasma Assisted End-Opening and Field Emission Enhancement in Vertically Aligned Multiwall Carbon Nanotubes. *Mater. Chem. Phys.* **2012**, *134* (1), 425–429. https://doi.org/10.1016/j.matchemphys.2012.03.012.
(71) Pang, P.; He, J.; Park, J. H.; Krstić, P. S.; Lindsay, S. Origin of Giant Ionic Currents in Carbon Nanotube Channels. *ACS Nano* **2011**, *5* (9), 7277–7283. https://doi.org/10.1021/nn202115s.
(72) Wang, C. Y.; Ru, C. Q.; Mioduchowski, A. Free Vibration of Multiwall Carbon Nanotubes. *J. Appl. Phys.* **2005**, *97* (11), 114323. https://doi.org/10.1063/1.1898445.
(73) Pickett, G. T.; Gross, M.; Okuyama, H. Spontaneous Chirality in Simple Systems. *Phys. Rev. Lett.* **2000**, *85* (17), 3652–3655. https://doi.org/10.1103/PhysRevLett.85.3652.
(74) Chan, Y.; Hill, J. M. Modelling Interaction of Atoms and Ions with Graphene. *Micro Nano Lett.* **2010**, *5* (5), 247–250. https://doi.org/10.1049/mnl.2010.0058.
(75) Cox, B. J.; Thamwattana, N.; Hill, J. M. Mechanics of Atoms and Fullerenes in Single-Walled Carbon Nanotubes. II. Oscillatory Behaviour. *Proc. R. Soc. A Math. Phys. Eng. Sci.* **2007**, *463* (2078), 477–494. https://doi.org/10.1098/rspa.2006.1772.
(76) Misra, R. P.; Blankschtein, D. Insights on the Role of Many-Body Polarization Effects in the Wetting of Graphitic Surfaces by Water. *J. Phys. Chem. C* **2017**, *14*, 11. https://doi.org/10.1021/acs.jpcc.7b08891.
(77) Hummer, G.; Rasaiah, J. C.; Noworyta, J. P. Water Conduction through the Hydrophobic Channel of a Carbon Nanotube. *Nature* **2001**, *414* (6860), 188–190. https://doi.org/10.1038/35102535.

(78) Barati Farimani, A.; Aluru, N. R. Existence of Multiple Phases of Water at Nanotube Interfaces. *J. Phys. Chem. C* **2016**, *120* (41), 23763–23771. https://doi.org/10.1021/acs.jpcc.6b06156.
(79) Suk, M. E.; Aluru, N. R. Modeling Water Flow through Carbon Nanotube Membranes with Entrance/Exit Effects. *Nanoscale Microscale Thermophys. Eng.* **2017**, *21* (4), 247–262. https://doi.org/10.1080/15567265.2017.1355949.
(80) Nomura, K.; Kaneko, T.; Bai, J.; Francisco, J. S.; Yasuoka, K.; Zeng, X. C. Evidence of Low-Density and High-Density Liquid Phases and Isochore End Point for Water Confined to Carbon Nanotube. *Proc. Natl. Acad. Sci. U. S. A.* **2017**, *114* (16), 4066–4071. https://doi.org/10.1073/pnas.1701609114.
(81) Supple, S.; Quirke, N. Molecular Dynamics of Transient Oil Flows in Nanopores I: Imbibition Speeds for Single Wall Carbon Nanotubes. *J. Chem. Phys.* **2004**, *121* (17), 8571–8579. https://doi.org/10.1063/1.1796272.
(82) Supple, S.; Quirke, N. Molecular Dynamics of Transient Oil Flows in Nanopores. II. Density Profiles and Molecular Structure for Decane in Carbon Nanotubes. *J. Chem. Phys.* **2005**, *122* (10), 104706. https://doi.org/10.1063/1.1856927.
(83) Kondratyuk, P.; Wang, Y.; Liu, J.; Karl Johnson, J.; Yates, J. T. Inter- and Intratube Self-Diffusion in *n*-Heptane Adsorbed on Carbon Nanotubes. *J. Phys. Chem. C* **2007**, *111* (12), 4578–4584. https://doi.org/10.1021/jp0652704.
(84) Jorio, A.; Saito, R.; Hafner, J. H.; Lieber, C. M.; Hunter, M.; McClure, T.; Dresselhaus, G.; Dresselhaus, M. S. Structural (n, m) Determination of Isolated Single-Wall Carbon Nanotubes by Resonant Raman Scattering. *Phys. Rev. Lett.* **2001**, *86* (6), 1118–1121. https://doi.org/10.1103/PhysRevLett.86.1118.
(85) Yang, F.; Wang, M.; Zhang, D.; Yang, J.; Zheng, M.; Li, Y. Chirality Pure Carbon Nanotubes: Growth, Sorting, and Characterization. *Chemical Reviews* **2020,** *120* (5), 2693-2758. https://doi.org/10.1021/acs.chemrev.9b00835.
(86) Jungen, A.; Popov, V. N.; Stampfer, C.; Durrer, L.; Stoll, S.; Hierold, C. Raman Intensity Mapping of Single-Walled Carbon Nanotubes. *Phys. Rev. B - Condens. Matter Mater. Phys.* **2007**, *75* (4). https://doi.org/10.1103/PhysRevB.75.041405.
(87) Araujo, P. T.; Maciel, I. O.; Pesce, P. B. C.; Pimenta, M. A.; Doorn, S. K.; Qian, H.; Hartschuh, A.; Steiner, M.; Grigorian, L.; Hata, K.; Jorio, A. Nature of the Constant Factor in the Relation between Radial Breathing Mode Frequency and Tube Diameter for Single-Wall Carbon Nanotubes. *Phys. Rev. B - Condens. Matter Mater. Phys.* **2008**, *77* (24), 2–5. https://doi.org/10.1103/PhysRevB.77.241403.
(88) Huang, J.; Wang, Z.; Zhang, J.; Zhang, X.; Ma, J.; Wu, Z. A Novel Composite Conductive Microfiltration Membrane and Its Anti-Fouling Performance with an External Electric Field in Membrane Bioreactors. *Sci Rep* **5,** 9268 (2015). https://doi.org/10.1038/srep09268.

3. Fluid Localization Inside and Outside Double Walled Nanotubes

This chapter has been adapted from "Fluid Localization Inside and Outside Double-Walled Nanotubes by Radial Breathing-Like Vibrational Modes," by Samuel Faucher,[*] Matthias Kuehne,* Haneneh Oliaei, Eveline Mayner, Narayana Aluru, Rahul Prasanna Misra, Daniel Blankschtein, and Michael S. Strano. This manuscript is in preparation, 2022.

Abstract

Carbon nanotubes (CNTs) in the so-called single digit nanopore (SDN) regime are model nanofluidic devices for understanding the thermodynamics and transport of extremely confined fluids. While the radial breathing mode frequency of a single-walled nanotube can be used to measure the density of a CNT-adjacent fluid, this vibrational response alone does not distinguish between a fluid on the outside from one on the inside of the pore. In this work, we show that double-walled CNTs (DWNTs) provide a solution to this ambiguity by allowing one to use the relative magnitude of frequency shifts in its two radial breathing-like modes (RBLMs) to locate the fluid adsorption site. We analyze RBLM frequencies using a linearized elastic shell model coupled through van der Waals interactions described by a Buckingham potential, consistent with experimentally measured DWNT frequencies. We find that fluid adsorption at a DWNT wall necessarily induces a larger blue shift in the RBLM mostly associated with the adjacent wall as opposed to the RBLM mostly associated with the far wall. A dimensionless model extends these results to a large range of DWNT diameters and generalized carbon-carbon and carbon-fluid interactions. The analysis allows for precise determination of the fluid coupling parameter which is a function of the fluid density and strength of the fluid/wall interaction, in agreement with MD simulations. We further predict an adsorption-induced RBLM crossover in large diameter DWNTs. Overall, this analysis increases the utility of CNT fluidic conduits for the study and understanding of confined fluid thermodynamics and transport.

[*] Matthias Kuehne and I contributed equally to this manuscript.

3.1 Introduction

Nanofluidic devices, in which fluids are confined to the nanometer scale, are used to resolve fundamental questions of fluid behavior under extreme confinement[1,2] and in applications including chemical separations, energy harvesting, and biomolecule sequencing.[2–5] Inside so-called single-digit nanopores,[1] where the pore dimension is less than 10 nm and can approach the molecular scale, deviations from bulk thermodynamic and kinetic fluid descriptions are particularly pronounced. In general, nanopore systems require care to distinguish between interior transport through the nanopore and other, parallel channels for mass transport and ion conduction. In nanochannels made from van der Waals assembly of two-dimensional materials,[6,7] helium leak tests confirm molecular transport through the nanopore of interest, while control devices without nanopores are used to localize transport to the interior of the device.[6] Two-dimensional membrane materials, including graphene, exhibit tears that preferentially form along certain orientations[8] and molecular defects that occur with well-defined frequencies.[9] Techniques such as interfacial polymerization are used to repair large tears and cracks which allow non-selective transport,[10] while molecular defects through which transport is desired can either be intrinsic[11,12] or etched.[13,14] In several classes of porous materials, including nanoporous gold[15] and TON-type zeolites,[16] the differentiation of external molecular adsorption from internal adsorption remains difficult.

Carbon nanotubes (CNTs) are promising nanofluidic conduits because of their potential for enhanced slip flow[17] and distorted phase behavior[18] of confined fluids. These properties, which arise due to quantum[19] and classical[20] effects at the graphitic-water interface, make carbon nanotubes useful for applications ranging from membranes[21] to energy storage[22]. However, as in the nanopore systems described above, distinguishing interior and exterior fluid adsorption is key, as either location may play host to different and potentially useful nanofluidic behavior.[23] Interior and exterior CNT sites are often distinguished indirectly in molecular adsorption studies by comparing monolayer adsorption capacity or specific surface area of bulk CNT material before and after a tube opening treatment.[23–25] Similarly, interior filling of CNTs in solution can be inferred by comparing analytical ultracentrifugation or optical spectroscopy of CNT dispersions before and after tube opening, since the CNT exterior remains saturated at all times with dispersing agent and solvent molecules.[26–28] Proton nuclear magnetic resonance studies distinguish interior from exterior fluids such as water either by freezing the exterior and attributing the remaining signal to stem from liquid-like encapsulated water, or by comparing closed and unfilled with opened and filled CNTs.[29–31] The demonstration of nanofluidic transport exclusively in the CNT interior has proven less straightforward, with parallel transport on the CNT exterior or through voids or cracks in an embedding membrane often difficult to rule out.[32] While interior cation transport may give rise to stochastic pore blocking,[33] independent probes able to sense and locate molecular phases associated with CNTs—down to the single tube level—are needed. Transmission electron microscopy, although instrumental in revealing substances at the interior of isolated CNTs,[34–37] remains challenging to integrate with device-level CNT nanofluidic investigations. CNT electromechanical resonators, although supremely mass sensitive even to adsorbate phase change,[38,39] may not readily differentiate between interior and exterior adsorption sites. Photoluminescence (PL) spectroscopy has emerged as a powerful tool to interrogate individual carbon nanotubes, but molecules on their inside and outside affect PL signals in a largely indistinguishable manner through dielectric screening.[40–45] Furthermore, only semiconducting CNTs show PL, with significant quenching observed for tubes with more than one wall.[46]

Vibrational signatures – in particular radial breathing modes and breathing-like modes – can be used as powerful probes of CNT-fluid interactions.[18,47] A CNT has as many radial breathing-like modes as walls:[48] a single-walled carbon nanotube (SWNT) has one radial breathing mode (RBM) and a double-walled carbon nanotube (DWNT) has two radial breathing-like modes (RBLMs), as illustrated in **Figure 1**. The frequencies of these modes can be used to calculate CNT diameter and are sensitive to the van der Waals coupling of nanotube walls with their environment. Specifically, while the RBM frequency of pristine SWNTs has been proposed to follow the relation $\omega_{\mathrm{RBM}}(cm^{-1}) = 227/d\ (\mathrm{nm})$,[48–50] where d is the SWNT diameter in nm, exterior adsorption upshifts this RBM frequency.[48,50,51] However, interior filling has been found to similarly upshift ω_{RBM},[47,52–54] rendering fluid localization based on RBM frequency alone challenging in single-walled systems.

In this work, we demonstrate that interior fluid filling and exterior fluid adsorption in double-walled carbon nanotubes can be unambiguously distinguished by Raman spectroscopy. To do this, we develop continuum elastic shell models of DWNT RBLMs and perform molecular dynamics simulations of DWNTs under conditions of emptiness, internal fluid filling, and external fluid adsorption. While the two RBLMs are coupled oscillations that deviate substantially from their frequencies in comparable SWNT, the low-frequency mode can be largely attributed to the outer wall and the high-frequency mode can be largely attributed to the inner wall;[55] either RBLM blueshifts, in analogy to that of a SWNT, in response to the vdW pressure of an adjacent fluid. Modelling and simulation indicate that a fluid causes a substantial blueshift of the RBLM associated mostly with the wall closest to the fluid, as well as what we term a "sympathetic shift" of the RBLM associated mostly with the wall farther from the fluid. The ability to distinguish interior filling from exterior adsorption opens the door to detailed thermodynamic and kinetic study of CNTs under a wide variety of experimental conditions, progressing toward nanopore devices that take advantage of graphitic slip flow and unusual phase behavior to achieve fluid and ion transport or storage.

3.2 Results and Discussion

Simplified elastic shell models can be used for the analytical description of radial breathing modes.[56] The time-dependent, spatially uniform radial displacement $w(t)$ of a solitary, vibrating elastic shell (**Figure 3-1a**) is as follows:

$$\rho h \frac{\partial^2 w(t)}{\partial t^2} = \frac{-Eh}{(1-\upsilon^2)} \frac{w(t)}{r^2} \qquad [3.1]$$

where ρ is mass density, h is shell thickness, E is Young's modulus, υ is Poisson's ratio, and $r = d/2$ is radius. A solution to Equation 1 of the form $w(t) = We^{i\omega_{\mathrm{RBM}}t}$ gives the RBM frequency as:

$$\omega_{\mathrm{RBM}} = \frac{1}{r}\sqrt{\frac{Eh}{\rho h(1-\upsilon^2)}} \qquad [3.2]$$

This characteristic $\omega_{\mathrm{RBM}} \propto 1/d$ relation (**Figure 3-1b**) allows diameter assignments of SWNTs based on RBM measurements that are commonly done by Raman spectroscopy.[48] For the plot

shown in Figure 1b we have used $Eh = 360\ \mathrm{J/m^2}$, $h = 0.34$ nm, $\rho = 2.27\ \mathrm{g/cm^3}$, and $\nu = 0.16$.[57]

Elastic shell models are readily expanded to describe RBLMs of multi-walled carbon nanotubes.[56,58,59] In a multi-walled system, a given elastic shell with subscript j can couple to adjoining shells, resulting in the following governing equation for the time-dependent radial displacement $w_j(t)$:

$$\rho h \frac{\partial^2 w_j}{\partial t^2} = \frac{-Eh}{1-\nu^2}\frac{w_j}{r_j^2} + \gamma_{j,j+1}\left(w_{j+1} - w_j\right) - \gamma_{j-1,j}\frac{r_{j-1}}{r_j}\left(w_j - w_{j-1}\right) \qquad [3.3]$$

where $j+1$ corresponds to an exterior elastic shell, $j-1$ corresponds to an interior elastic shell, and $\gamma_{j,j+1}$ is the vdW interaction coefficient between shells j and $j+1$. The second and third terms on the right correspond to coupling to an outer and inner elastic shell, respectively. The factor $\frac{r_{j-1}}{r_j}$ can be understood by considering that action equals reaction with opposite direction, and that the inward pressure $p_{j-1,j} = \gamma_{j-1,j}(w_j - w_{j-1})$ exerted by shell j on shell $j-1$ may thus be related to the outward pressure $p_{j,j-1}$ exerted by shell $j-1$ on shell j by $p_{j,j-1} = -r_{j-1}p_{j-1,j}/r_j$.[60,61] Alternative ways of relating $p_{j,j-1}$ and $p_{j-1,j}$ have been proposed.[62] Equation 1 is recovered from Equation 3 by requiring $j = 1$ and by neglecting the 2nd and 3rd terms on the right. Throughout this analysis, $j = 1$ designates the innermost shell of a CNT.

Assuming a solution to Equation 3.3 of the form $w_j(t) = W_j e^{i\omega}$, where W_j is the amplitude and ω is the frequency of the oscillation, yields the following time-independent governing equation:

$$-\rho h\omega^2 W_j = \frac{-Eh}{1-\nu^2}\frac{W_j}{r_j^2} + \gamma_{j,j+1}\left(W_{j+1} - W_j\right) - \gamma_{j-1,j}\frac{r_{j-1}}{r_j}\left(W_j - W_{j-1}\right) \qquad [3.4]$$

For a DWNT where $j = \{1,2\}$, Equation 4 yields the following system of equations:

$$\begin{bmatrix} -\rho h\omega^2 + \frac{Eh}{1-\nu^2}\frac{1}{r_1^2} + \gamma_{\mathrm{CC}} & -\gamma_{\mathrm{CC}} \\ -\gamma_{\mathrm{CC}}\frac{r_1}{r_2} & -\rho h\omega^2 + \frac{Eh}{1-\nu^2}\frac{1}{r_2^2} + \gamma_{\mathrm{CC}}\frac{r_1}{r_2} \end{bmatrix} \begin{bmatrix} W_1 \\ W_2 \end{bmatrix} = \begin{bmatrix} 0 \\ 0 \end{bmatrix} \qquad [3.5]$$

where we have written $\gamma_{\mathrm{CC}} = \gamma_{1,2}$. Equation 5 gives two RBLMs (**Figure 3-1c**): a high-frequency mode ω_{H} characterized by counter-phase oscillation of both walls for which $\operatorname{sgn} W_1 = -\operatorname{sgn} W_2$, and a low frequency mode ω_{L} characterized by in-phase oscillation of both walls for which $\operatorname{sgn} W_1 = \operatorname{sgn} W_2$. In **Figure 3-1d**, we plot the diameter dependence of both modes still assuming $Eh = 360\ \mathrm{J/m^2}$, $h = 0.34$ nm, $\rho = 2.27\ \mathrm{g/cm^3}$, and $\nu = 0.16$,[57] as well as $\gamma_{\mathrm{CC}} = 93.6\ \mathrm{GPa/nm}$ and an inter-tube spacing $\delta r = r_2 - r_1 = 0.35$ nm. The latter two values are determined by considering the tube-tube potential as a function of the interwall spacing, as discussed below. In **Figure 3-1e** we plot $|W_2/W_1|$ for both RBLMs. This serves to illustrate that while ω_{L} and ω_{H} each involve displacement of both CNT walls, ω_{L} is characterized by a displacement mostly of the outer wall while ω_{H} is characterized by a displacement mostly of the inner wall.

While the van der Waals interaction between carbon shells can be described by a Lennard-Jones potential, it is better described by a Buckingham potential. This interaction is often described by a continuum Lennard-Jones potential of the form:[63,64]

$$U(\delta r) = 2\pi\rho_c^2\epsilon\sigma^2\left[0.4\left(\frac{\sigma}{\delta r}\right)^{10} - \left(\frac{\sigma}{\delta r}\right)^{4}\right] \quad [3.6]$$

where δr is the radial intershell separation, $\sigma = 0.34$ nm,[63] $\rho_c = 4/(3\sqrt{3}a_0^2)$ is the areal density of carbon atoms in a graphene sheet with $a_0 = 0.142$ nm the nearest-neighbor carbon-carbon distance in graphene, and ϵ is the well depth of the corresponding pairwise Lennard-Jones potential. A plot of the continuum potential is shown in **Figure 3-1f**. The vdW interaction coefficient between carbon shells j and $j+1$ can be estimated from the potential as:

$$\gamma_{j,j+1} = \frac{d^2U}{d(\delta r)^2}\Big|_{\delta r=\delta r_{j,j+1}} = 8\pi\rho_c^2\epsilon\left(11\frac{\sigma^{12}}{\delta r_{j,j+1}^{12}} - 5\frac{\sigma^6}{\delta r_{j,j+1}^6}\right) \quad [3.7]$$

As can be seen in **Figure 3-1g**, $\gamma_{j,j+1}$ strongly depends on the radial distance δr between neighboring carbon shells. Smaller corrections due to radial effects and chiral angle mismatch between neighboring tubes are not considered in this analysis.[65–67] In our recent work,[68] we were able to assign the radii of three DWNTs by electron diffraction and observe RBLMs in a pristine state. The extracted γ_{CC} values are shown as green dots in Figure 1g, and the best fit by Equation 7 with $\sigma = 0.34$ nm is shown as a black line. While this fit yields $\epsilon = 3.22$ meV, which is comparable to the graphene-graphene value $\epsilon = 2.39$ meV reported in Ref. [63], we obtain only poor agreement with the experimental data. Better agreement with the experiment can only be obtained for both unphysically low values of ϵ and unphysically large values of σ, i.e., the Lennard-Jones potential fails to describe the δr dependence of the intershell vdW coupling. Instead, we turn to a pairwise Buckingham potential of the form $U(r) = A\exp\left(-\frac{r}{s}\right) - \frac{B}{r^6}$, which yields the continuum potential of the form:

$$U(\delta r) = 2\pi\rho_c^2\left[A\exp\left(-\frac{\delta r}{s}\right)s(\delta r + s) - \frac{1}{4}\frac{B}{\delta r^4}\right] \quad [3.8]$$

and a vdW interaction coefficient between carbon shells j and $j+1$ as follows:

$$\gamma_{j,j+1} = 2\pi\rho_c^2\left(\frac{Ae^{-\frac{\delta r}{s}}(\delta r - s)}{s} - \frac{5B}{\delta r^6}\right) \quad [3.9]$$

Requiring a value of s such that a potential well of similar magnitude as for the case of the Lennard-Jones potential in Figure 1f is obtained, we fit our experimental data in Figure 1g with Equation 9 and obtain $A = 2.03 \cdot 10^5$ meV, $B = 2.76 \cdot 10^4$ meV $\cdot$ Å^6, and $s = 0.037$ nm. These values compare with graphene-graphene Buckingham parameters reported by Liu et al.:[69] $A = 3.31 \cdot 10^5$ meV, $B = 9.49 \cdot 10^4$ meV $\cdot$ Å^6, and $s = 0.038$ nm. The discrepancy between experiment and estimates based on the Lennard-Jones potential is corroborated by data from Liu et al.[55] collected on DWNTs in presumably adsorbate-free state, which we have included as grey

data points in Figure 1g. These data agree well with our fit based on the Buckingham potential (green line), which empirically can be stated as

$$\gamma_{j,j+1}(\delta r)\left[\frac{\mathrm{GPa}}{\mathrm{nm}}\right] = 8.011 \cdot 10^6 \cdot \exp\left(-\frac{\delta r}{0.03716}\right) \cdot (\delta r - 0.03716) - \frac{0.202}{\delta r^6} \qquad [3.10]$$

where δr is in nm. We use this expression to estimate γ_{CC} in DWNT as $\gamma_{\mathrm{CC}} = 93.6\ \mathrm{GPa/nm}$ at an example inter-tube spacing of $\delta r = 0.35$ nm.

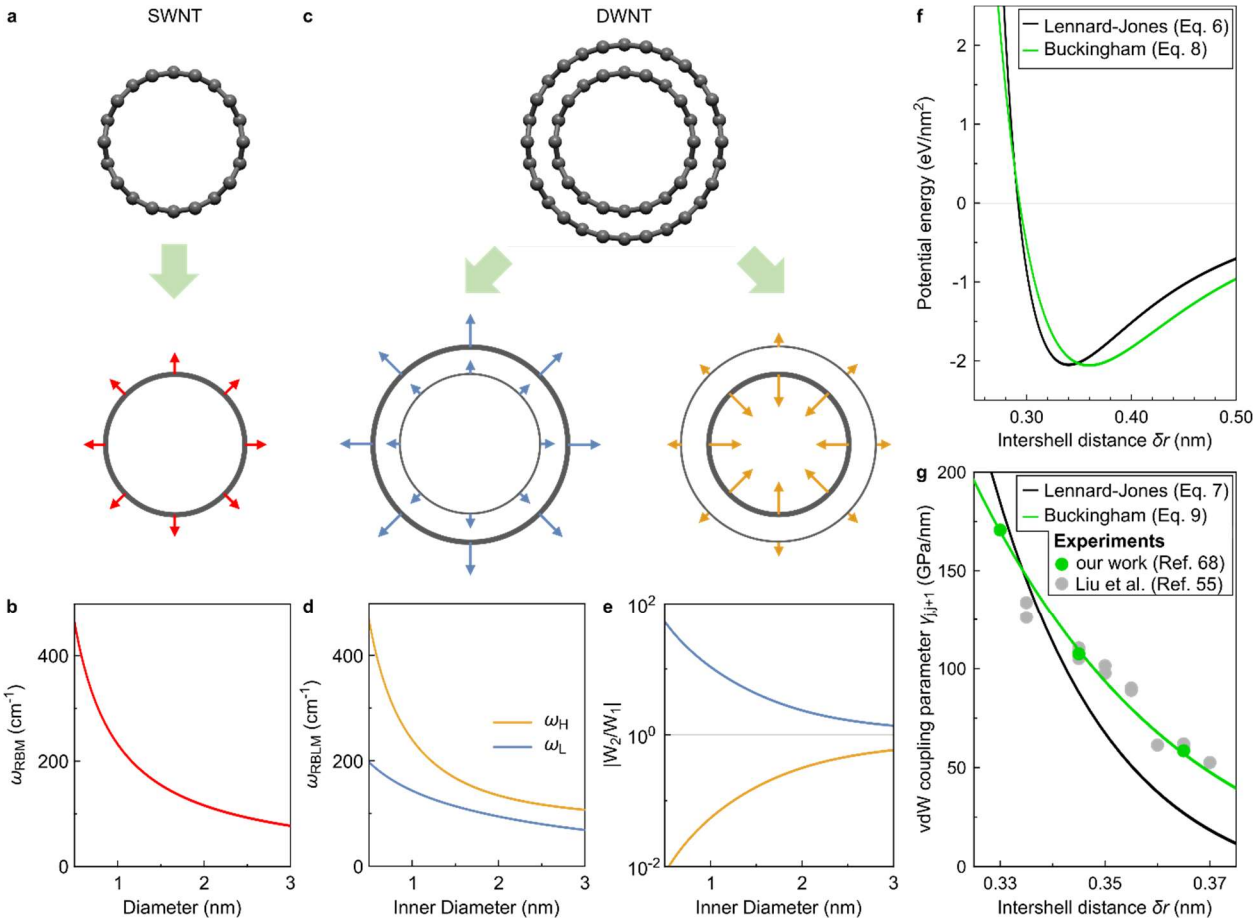

Figure 3-1. Radial breathing(-like) modes of adsorbate-free CNTs. (a) A SWNT has one RBM at frequency ω_{RBM} with phonon displacement pattern (red arrows) strictly in radial direction. (b) Diameter dependence of ω_{RBM} for an adsorbate-free SWNT and the stated parameter values. (c) A DWNT has two RBLMs, a low-frequency one at ω_{L} characterized by in-phase oscillation of both walls and a high-frequency one at ω_{H} characterized by counter-phase oscillation of both walls. The phonon displacement patterns are shown in blue and orange, respectively, and the primary wall associated with each mode is drawn as a thick line. (d) Diameter dependence of ω_{L} and ω_{H} for an adsorbate-free DWNT and the stated parameter values. (e) The absolute value of the ratio of the outer wall displacement W_2 and

the inner wall displacement W_1 quantifies how much a given RBLM is associated with the outer wall. For the illustrated case of an adsorbate-free DWNT, ω_{L} (ω_{H}) is mostly associated with the outer (inner) wall. (f) Continuum van der Waals potentials between carbon walls according to Equations 6 and 8, using parameters obtained for the fits of $\gamma_{j,j+1}(\delta r)$ in g. (g) Van der waals coupling parameter between neighboring carbon shells as a function of intershell distance. Shown are best fits to our experimental data using Equations 7 and 9 as described in the text.

We further extend elastic shell models to account for vdW coupling with molecular adsorbates on the inside and outside of CNTs.[57,61,70,71] This is typically done via a pressure term of the form $p = \gamma_i w(t)$ thought to be exerted by a rigid shell of adsorbed molecules. Here, γ_i is the coupling parameter to the exterior ($i = \mathrm{ext}$) and interior ($i = \mathrm{int}$) adsorbate, given by the second derivative of a fluid-CNT potential of the form of Equation 4 at equilibrium distance σ. For a SWNT, Equation 1 accordingly modifies to yield:[57,70]

$$\rho h \frac{\partial^2 w(t)}{\partial t^2} = -\left(\frac{Eh}{1-v^2} + \gamma_{\mathrm{int}} + \gamma_{\mathrm{ext}}\right)\frac{w(t)}{r^2} \qquad [3.11]$$

For a Lennard-Jones potential, the fluid couplings γ_{int} and γ_{ext} can be decomposed in terms of a potential well depth and equilibrium spacing:[57]

$$\gamma_{\mathrm{i}} = \frac{24K}{s_0^2} \qquad [3.12]$$

where $-0.6K$ is the well depth and s_0 is the fluid-CNT equilibrium spacing. In general, we report results in terms of γ to preserve generality of non-Lennard Jones fluid-CNT potentials. For water, it is possible to estimate values of K and s_0 from experimental results and molecular dynamics simulations. The distance s_0 is fairly well-known across the studied diameter range: it is roughly 0.33 nm inside and outside carbon nanotubes of various sizes from molecular dynamics simulations as discussed below, consistent with reported values of 0.32 nm for MD simulations inside 1.75 nm diameter CNTs[70] and 0.33 nm for MD simulations outside 1.03 nm diameter CNTs.[40] K is more uncertain, ranging from $0.075\ N/m$ to $0.322\ N/m$ in the molecular dynamics simulations discussed below. The K parameter captures the energetics of the water-fluid interaction, and is expected to decrease linearly for sub-monolayer or non-close-packed arrangements of interfacial fluids.

Equation 3.11 suggests that interior and exterior fluids affect the RBM of a SWNT similarly, making their direct distinction challenging based on ω_{RBM} alone, especially if $\gamma_{\mathrm{int}} \approx \gamma_{\mathrm{ext}}$ (Figure 2a-b). The calculated magnitude of RBM shifts on the order of 1-10 cm^{-1} from elastic shell models agrees with experimental studies of CNTs with internal and external fluids.[18,26,47,53,54,72] Molecular dynamics simulations, too, yield comparable blueshifts of ω_{RBM} upon interior and exterior adsorption of water, with exterior adsorption causing slightly larger shifts.[70] Cambre et al.[53] report a similar finding for interior D_2O and exterior deoxycholate. Hence, in order to distinguish interior and exterior adsorption in the case of SWNTs, other factors such as the sample history, opening procedures, and control experiments on unfilled specimen have to be considered.[47,52] We note that under almost any experimental condition,

SWNTs show finite van der Waals coupling with their exterior environment, making the introduction of a finite γ_{ext} relevant for accurate diameter assignments.[50,73]

DWNT allow the differentiation of interior filling from exterior adsorption. To account for coupling to interior/exterior fluids, Equation 3-5 is modified to yield:[61,71]

$$\begin{bmatrix} -\rho h\omega^2 + \frac{Eh}{1-\nu^2}\frac{1}{r_1^2} + \gamma_{\text{CC}} + \gamma_{\text{int}} & -\gamma_{\text{CC}} \\ -\gamma_{\text{CC}}\frac{r_1}{r_2} & -\rho h\omega^2 + \frac{Eh}{1-\nu^2}\frac{1}{r_1^2} + \gamma_{\text{CC}}\frac{r_1}{r_2} + \gamma_{\text{ext}} \end{bmatrix} \begin{bmatrix} W_1 \\ W_2 \end{bmatrix} = \begin{bmatrix} 0 \\ 0 \end{bmatrix} \qquad [3.13]$$

As a result, exterior (interior) adsorption causes a substantial blueshift in the low-frequency (high-frequency) mode ω_{L} (ω_{H}). Both modes are shifted when there is fluid on both sides of the DWNT. In this way, different fluid filling/adsorption configurations can be distinguished by Raman spectroscopy. In **Figure 3-2c-d** we show results for DWNT using $\gamma_{\text{CW}} = 32.6\ \text{GPa/nm}$, a value taken from Raman RBM shifts in 43 substrate-supported SWNT and DWNT upon water immersion.[47] This corresponds to a value of $K = 0.148\ N/m$ at $s_0 = 0.33\ nm$, as in Eq. 12 above. In DWNT (**Figure 3-2d**), the relative magnitude of RBLM shifts allows the differentiation of internal fluid filling from external fluid adsorption. Upon internal filling, $\Delta\omega_{\text{H}}$ is greater than $\Delta\omega_{\text{L}}$ across the diameter range studied, while the reverse is true for external adsorption. We explain this as a "primary shift" and a "sympathetic shift" of the RBLMs of DWNT. The primary shift is the blueshift of the RBLM associated mostly with the wall nearest the fluid, and is large in magnitude, while the sympathetic shift is the blueshift of the RBLM associated mostly with the wall further from the fluid, and is smaller in magnitude. In the case where both interior and exterior are in contact with fluid, this picture breaks down as both $\Delta\omega_{\text{H}}$ and $\Delta\omega_{\text{L}}$ have substantial shifts. We confirm that ω_{H} primarily corresponds to the inner wall and ω_{L} primarily corresponds to the outer wall over the diameter range in question in **Figure 3-2e**, with absolute amplitude ratios far from one, especially on the smaller size of the studied size range. The ratio of shifts for internal filling and external adsorption is shown in **Figure 3-2f.** At diameters below 3 nm, internal filling and external adsorption can be easily distinguished by Raman spectroscopy, with RBLM shift ratios far from one.

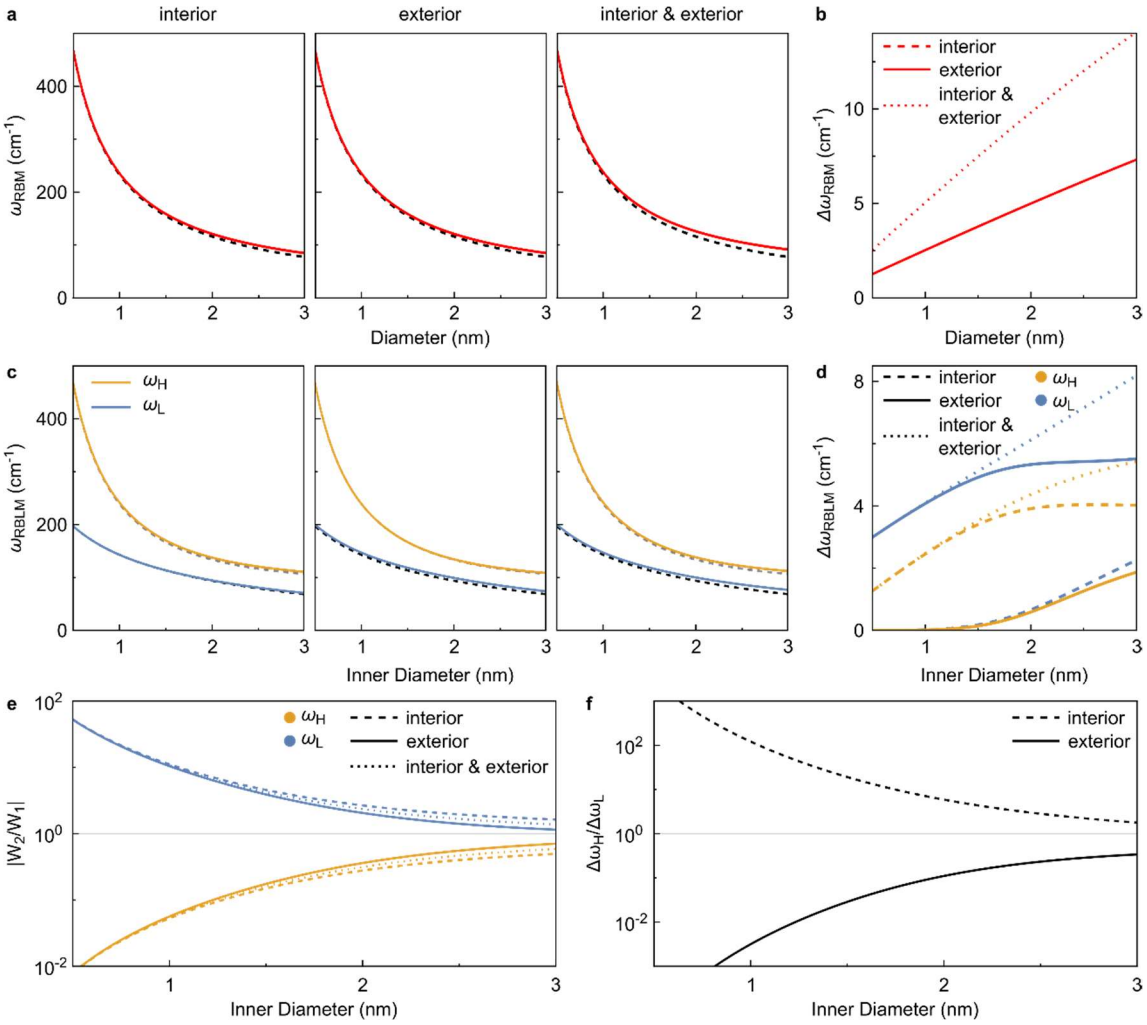

Figure 3-2. Radial breathing(-like) modes of CNTs in the presence of interior and/or exterior adsorbates. (a-d) Radial breathing(-like) modes of (a,b) SWNT and (c,d) DWNT for the three adsorbate configurations. (b) Shift in RBM frequency $\Delta\omega_{\mathrm{RBM}}$ with respect to the adsorbate-free state of a SWNT. Interior filling and exterior adsorption (solid line) cannot be distinguished. Fluid on both sides of the SWNT causes an additive effect in the RBM shift (dotted line). (d) Shift in RBLM frequencies with respect to the adsorbate-free state of a DWNT. Upon interior filling (solid lines), there is a larger shift in the inner wall (red) and a smaller, sympathetic shift in the outer wall (blue). Upon exterior fluid adsorption (dashed lines), there is a larger shift in the outer wall (blue) and a smaller, sympathetic shift in the inner wall (red). Upon exterior and interior fluid adsorption (dotted lines), both the inner and outer walls undergo substantial shifts. (e) Amplitude ratio in DWNT as a function of diameter. In all cases, the high-frequency mode ω_{H} is an out-of-phase vibration that predominates in the inner shell, while the low-frequency mode ω_{L} is an in-phase vibration that predominates in the outer shell. Mode mixing between shells increases with diameter. (f) Ratio of RBLM shift in high frequency mode, $\Delta\omega_{\mathrm{H}}$, to that in the low frequency mode, $\Delta\omega_{\mathrm{L}}$, as a function of diameter under conditions of interior fluid filling and exterior fluid adsorption.

This analysis assumes a particular form of the elastic shell model, in which water affects carbon shell vibrations through a fixed vdW pressure with the near carbon shell. Two alternative models can be proposed, but neither fundamentally changes the main conclusions. First, we consider the case in which water behaves not as a fixed vdW pressure but as a separate elastic shell. In this case, Equation 3 simplifies to an eigenvalue problem containing two carbon shells and, at most, two water shells. While the elastic properties of a molecular water shell at ambient temperature and pressure are somewhat ill-defined,[18] and alternative descriptions are possible,[74] this model also suggests that water induces a primary shift of the RBLM associated mostly with the nearest carbon wall, and induces a sympathetic shift of the RBLM associated mostly with the farther carbon wall (see **Supporting Information**). Second, we consider a case in which water exerts a fixed vdW pressure not only on the near shell but also on the far shell. While this necessarily reduces the distinction between internal filling and external adsorption in DWNT, they can still be distinguished (see **Supporting Information**).

The results in **Figure 3-2** demonstrate the use of DWNT vibrational modes to distinguish between interior and exterior fluids, assuming parameter values from the literature, but this analysis can be generalized to any double-walled nanotube system, including a DWNT-water system with different interaction parameters as well as a system with a non-carbon double-walled nanotube, non-aqueous fluid, or both. To extend this analysis, we non-dimensionalize the elastic shell model to calculate normalized changes in high and low-frequency modes as a function of key parameters. Eq. 3.5 can be non-dimensionalized to:

$$\begin{bmatrix} -\frac{\xi}{\xi_{00}} + \frac{\xi_{01}}{\xi_{00}} + \frac{\hat{\gamma}}{\xi_{00}} + \frac{\hat{\gamma}_{\text{int}}}{\xi_{00}} & -\frac{\hat{\gamma}}{\xi_{00}} \\ -\frac{\hat{\gamma}}{\xi_{00}}\left(\frac{\xi_{02}}{\xi_{01}}\right)^{\frac{1}{2}} & -\frac{\xi}{\xi_{00}} + \frac{\xi_{02}}{\xi_{00}} + \frac{\hat{\gamma}}{\xi_{00}}\left(\frac{\xi_{02}}{\xi_{01}}\right)^{\frac{1}{2}} + \frac{\hat{\gamma}_{\text{ext}}}{\xi_{00}} \end{bmatrix} \begin{bmatrix} W_1 \\ W_2 \end{bmatrix} = \begin{bmatrix} 0 \\ 0 \end{bmatrix} \qquad [3.14]$$

where ξ_{ij} is the squared vibrational frequency, ω_{ij}^2, under condition i for wall j, where $i = 0$ refers to a SWNT mode (without shell-shell or shell-fluid coupling), $i = 1$ refers to a DWNT mode (without shell-fluid coupling), $i = 2$ refers to a DWNT mode with fluid, $j = 1$ refers to the inner shell, and $j = 2$ refers to the outer shell. The modified shell-shell interaction parameter $\hat{\gamma}$ and shell-fluid parameters $\hat{\gamma}_{\text{int}}$ and $\hat{\gamma}_{\text{ext}}$ are defined as follows:

$$\hat{\gamma} = \frac{\gamma}{\rho h} \qquad \hat{\gamma}_{\text{int}} = \frac{\gamma_{\text{int}}}{\rho h} \qquad \hat{\gamma}_{\text{ext}} = \frac{\gamma_{\text{ext}}}{\rho h} \qquad [3.15]$$

The ratio in normalized shifts in squared frequency can be expressed as follows:

$$\Omega_{\text{L}}/\Omega_{\text{H}} = \frac{\frac{\xi_{21}-\xi_{11}}{\xi_{11}}}{\frac{\xi_{22}-\xi_{12}}{\xi_{12}}} \qquad [3.16]$$

This ratio is dependent on four dimensionless groups, as per Eq. 3.13. These are ξ_{02}/ξ_{01}, a proxy for nanotube size; $\hat{\gamma}/\xi_{01}$, a non-dimensionalized shell-shell interaction; $\hat{\gamma}_{int}/\xi_{01}$, a non-dimensionalized interior fluid interaction; and $\hat{\gamma}_{\text{ext}}/\xi_{01}$, a non-dimensionalized exterior fluid interaction. **Figure 3-3** shows the normalized shift in squared frequency upon internal fluid

filling and external fluid adsorption inside double-walled nanotube systems as a function of these parameters.

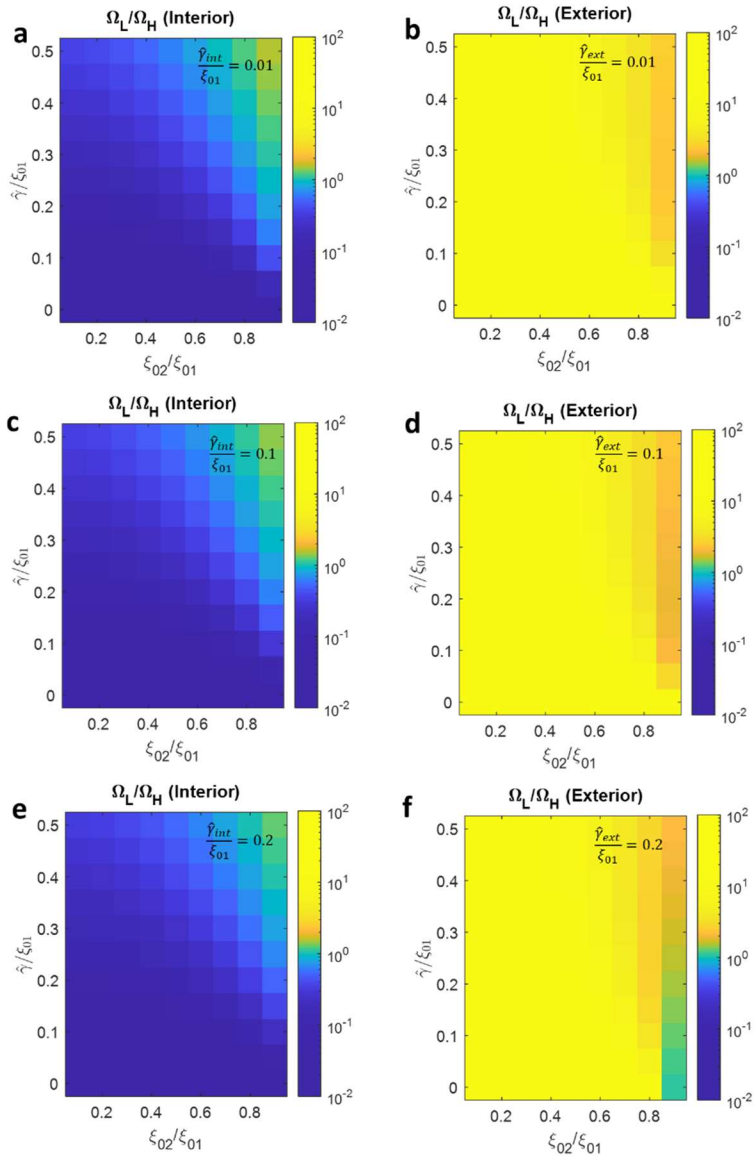

Figure 3-3. Generalized vibrational shifts in DWNTs upon interior fluid filling and exterior fluid adsorption. (a-f) The ratio in normalized squared frequency shifts, $\Omega_{\mathrm{L}}/\Omega_{\mathrm{H}}$, as a function of the normalized DWNT size, ξ_{02}/ξ_{01}, and normalized inter-shell coupling $\hat{\gamma}/\xi_{01}$ for interior fluid filling (a,c,e) and exterior fluid adsorption (b,d,f). Values below one indicate large changes in the high-frequency vibrational mode, which are associated with interior fluid filling. Values above one indicate large changes in the low-frequency mode, which are associated with exterior fluid adsorption. The ratio of the non-dimensionalized shift in low and high-frequency modes is largely independent of the magnitude of the interior and exterior fluid coupling, which is $\hat{\gamma}_{\mathrm{int}}/\xi_{01} = \hat{\gamma}_{\mathrm{ext}}/\xi_{01} = 0.01$ in (a-b), $\hat{\gamma}_{\mathrm{int}}/\xi_{01} = \hat{\gamma}_{\mathrm{ext}}/\xi_{01} = 0.1$ in (c-d), and $\hat{\gamma}_{\mathrm{int}}/\xi_{01} = \hat{\gamma}_{\mathrm{ext}}/\xi_{01} = 0.2$ in (e-f).

The ratio in normalized squared frequency, $\Omega_{\mathrm{L}}/\Omega_{\mathrm{H}}$, is shown versus normalized DWNT size, ξ_{02}/ξ_{01}, and normalized inter-shell coupling, $\hat{\gamma}/\xi_{01}$ for the case of interior fluid filling (**Figure 3-3a,c,e**) and exterior fluid adsorption (**Figure 3-3b,d,f**). In general, the fact that the shift in the low-frequency mode predominates upon exterior adsorption and the shift in the high-

frequency mode predominates upon interior filling, as shown in **Figure 3-3a-f**, extends the concepts of a primary RBLM shift and an induced, sympathetic RBLM shift to a broad array of double-walled nanotube systems, including CNT molecular models with varying parameters, nanotubes made of boron nitride and transition metal dichalcogenides, and nanotube systems with non-aqueous fluids. The parameter range shown includes physical CNTs and BNNTs in the single-digit nanopore range, as shown in the Supplementary Information. The parameters corresponding to the fluid interactions ($\hat{\gamma}_{\text{int}}/\xi_{01}$ and $\hat{\gamma}_{\text{ext}}/\xi_{01}$), in particular, indicate the percent change in RBLM frequency upon fluid adsorption. Given that CNTs with RBLMs between 100 cm^{-1} and 400 cm^{-1} shift around 1-15 cm^{-1} upon fluid adsorption, $\hat{\gamma}_{\text{int}}/\xi_{01}$ and $\hat{\gamma}_{\text{ext}}/\xi_{01}$ on the order of 0.01 and 0.1 are appropriate.

To complement the use of continuum elastic shell models, we performed molecular dynamics (MD) simulations of DWNT in three fluidic configurations: 1) pristine, i.e., without fluid, 2) with interior water, and 3) with exterior water. The dynamics of each nanotube and the covalent interactions have been modeled with the adaptive intermolecular reactive bond order (AIREBO) potential.[75] This potential introduces attractive and repulsive interaction modifications as well as nonbonded interactions and torsional potentials to the reactive empirical bond order potential (REBO).[76] The AIREBO potential can be expressed in the following form

$$E = \frac{1}{2}\sum_i \sum_{j\neq i}\left[E_{ij}^{\text{REBO}} + \sum_{k\neq i}\sum_{l\neq i,j,k} E_{kijl}^{\text{TORSION}} + E_{ij}^{LJ}\right] \quad [3.17]$$

We employ either the Lennard-Jones potential (Eq. 3.6) or the Buckingham potential (Eq. 3.8) to describe the non-covalent C-C pair interactions between adjacent nanotubes. The energy and distance parameters are chosen in accordance with the values for graphene-graphene interaction obtained by Girifalco *et al.*[63] Furthermore, to study water, the TIP4P/2005[77] model is used in which $-1.1128e$ and $0.5564e$ partial charges are placed on the oxygen and hydrogen atoms, respectively. The oxygen-hydrogen bond distance was kept fixed at 0.9572 Å and their bond angle at $104.52°$. The Lennard-Jones interaction parameters between oxygen atoms are defined with $\varepsilon_{OO} = 0.1852$ kcal mol^{-1} as the binding energy and $\sigma_{OO} = 3.1589$ Å as the equilibrium distance. Moreover, the interaction of water and carbon atoms is modeled with a Lennard-Jones potential with $\varepsilon_{OC} = 0.1138$ kcal mol^{-1} and $\sigma_{OC} = 3.3487$ Å. The size of the tube in z direction is 10 nm approximately. Periodic boundary conditions are applied to the tube in the axial direction to obtain an infinite tube and high aspect ratio. The LAMMPS package[78] is used to perform MD simulations by using the Verlet algorithm[79] for time integration with a time step of 0.5 fs. A cutoff of 12 Å is used to compute the short-range interactions. Moreover, a particle-particle particle-mesh algorithm is used for long-range electrostatic interactions. The equilibration and production simulations are performed by following the procedure of Wu *et al.*.[80] The velocity information is dumped every 10 timesteps to obtain sufficient statistics for accurate calculation of the RBM frequency. The average radial velocity of the CNT, v_r, is found using the data dumped every 5 fs. Then, Fourier transformation is applied to the radial velocity autocorrelation to obtain the power spectral density:

$$PSD(\omega) = \int_0^\infty \frac{\langle v_r(t)\, v_r(0)\rangle}{\langle v_r(0)\, v_r(0)\rangle} \cos\omega t \; dt \quad [3.18]$$

Finally, a Lorentzian curve is fit to the power spectral density that helps to locate the peak and RBM frequency.

The elastic shell model developed here makes predictions about RBLM frequencies in the presence of interior and exterior fluids and aligns well with molecular dynamics simulations, as shown in **Figure 3-4.** As an example, the low and high frequency modes of a (19,3)@(22,11) DWNT are plotted in **Figure 3-4a** as predicted by elastic shell models and all-atom molecular dynamics simulations in a variety of states: empty, with interior fluid, and with exterior fluid. Interior fluid filling (solid line) and exterior adsorption (dotted line) can be easily distinguished from one another by frequency shifts in ω_{H} and ω_{L}, respectively. This observation holds irrespective of the model used. Overall, elastic shell model results appear to yield a slightly better quantitative match with MD simulations that used the Lennard-Jones C-C potential (Eq. 3.6) rather than the Buckingham C-C potential (Eq. 3.8). While this may be a coincidence, a more detailed analysis of the intertube coupling and experimental verification will inform the identification of the most accurate description in the future. Snapshots from MD simulations are shown in **Figure 3-4b**.

The DWNT elastic shell model can inform on the possible presence of adsorbates in experimental data sets. Chirality-assigned DWNT from TEM from Liu *et al.*[55] and Rochal *et al.*[71] are shown in **Figure 3-4c**. Assuming the carbon shell parameters listed above, including the dependence of γ_{CC} on the interlayer spacing as shown in **Figure 3-1g**, allows the calculation of frequency trajectories for different values of γ_{int} and γ_{ext}, as shown by the solid and dashed lines. The RBLM frequencies reported by Liu *et al.*[55] are consistent with DWNT measured under adsorbate-free conditions, such as can be obtained through sufficient heating with the Raman excitation laser. However, the authors did not provide details about their experimental conditions that could inform how the adsorbate-free state was reached. Instead, the measured RBLM frequencies from Rochal *et al.*[71] fall along the dashed lines and are therefore most consistent with DWNT with exterior adsorbates. While Rochal *et al.*[71] note that adsorbates explain differences between their data and that of Liu *et al,*[55] the analysis presented here extends to consider interior fluid filling and its distinguishability from empty and externally adsorbed cases.

While it is generally the case that the high-frequency mode ω_{H} primarily represents the inner shell of a DWNT, and the low-frequency mode ω_{L} primarily represents the outer shell, this is not true in all circumstances. Specifically, with strong coupling to an external fluid, the outer shell-dominant mode can become higher frequency than the inner shell-dominant mode. This behavior is shown in **Figure 3-4d** for a DWNT with an inner diameter of 1.5 nm. As the external coupling constant γ_{ext} increases, the low frequency mode ω_{L} increases in frequency until an avoided crossing at which point ω_{H} predominates in the outer shell, as shown by the intersection in the RBLM amplitude in **Figure 3-4e**. Within the description of Equation 12, we predict this cross-over to occur at

$$\gamma_{\mathrm{ext}}^{\mathrm{crossover}} = \gamma_{\mathrm{int}} + \frac{Eh}{1-\nu^2}\left(\frac{1}{r_1^2} - \frac{1}{r_2^2}\right) + 2\gamma_{\mathrm{CC}}\left(1 - \frac{\mathrm{r_1}}{\mathrm{r_2}}\right) \qquad [3.19]$$

While this is theoretically possible at any DWNT diameter, it is only relevant at experimentally accessible fluid-CNT couplings for large DWNT, as shown in **Figure 3-4f**. The experimentally observed CNT-water coupling from previous study, $\gamma_{\mathrm{CW}} = 32.6\ \mathrm{GPa/nm}$,[47] is indicated by a

dotted red line and corresponds to values of $K = 0.148\ N/m$ at $s_0 = 0.33\ nm$ as in Eq. 3.12. With this magnitude of fluid-CNT coupling, and at diameters larger than 5 nm, caution in interpreting RBLMs is advised, as ω_{H} could represent either primarily the inner shell or outer shell depending on experimental conditions. Experimentally, however, it may be challenging to synthesize such large diameter DWNTs. Also, their characterization by Raman spectroscopy requires careful separation of Raman and Rayleigh scattered light, as RBLMs have lower frequencies as the DWNT diameter increases.

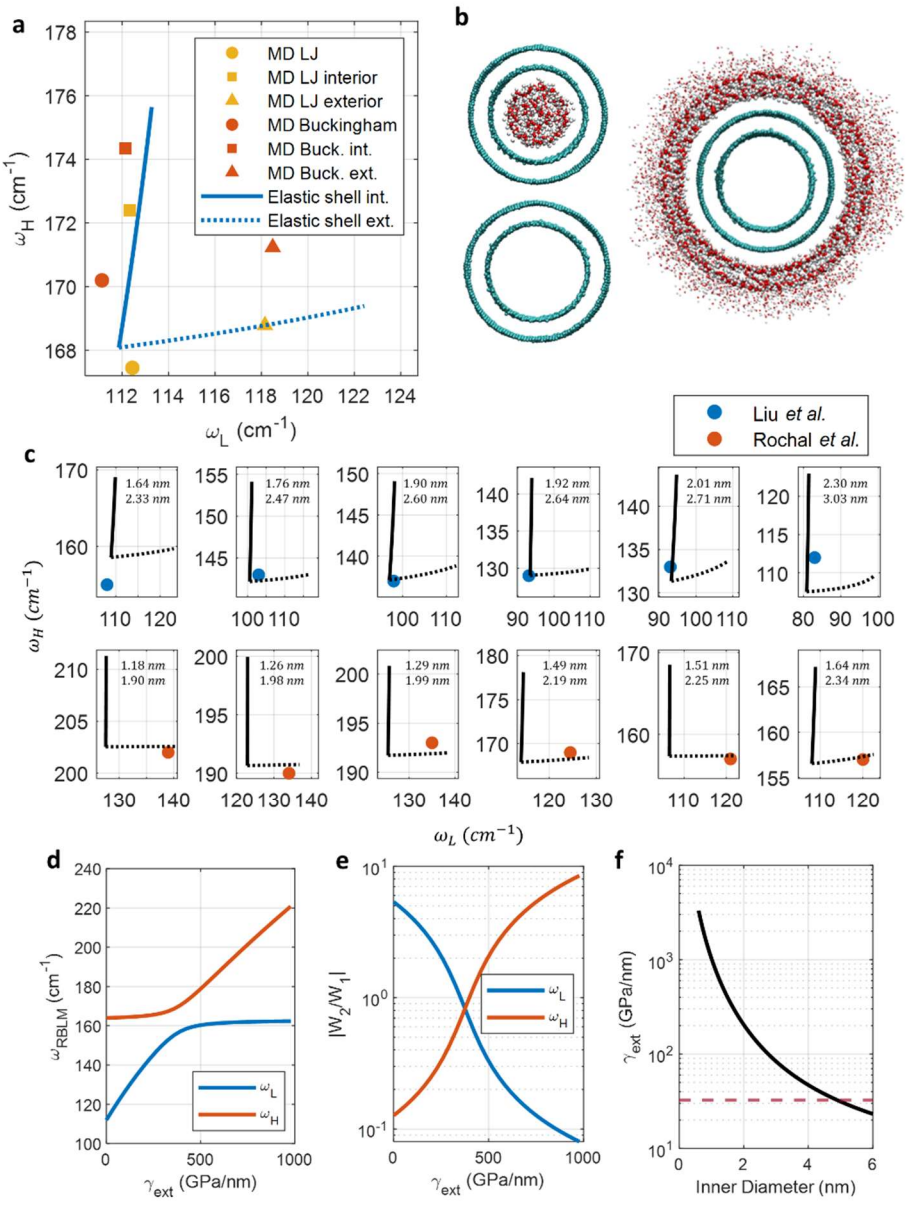

Figure 3-4. Predictions and validation of elastic shell DWNT model. (a) Comparison among molecular dynamics simulation using Lennard Jones (MD LJ) and Buckingham (MD Buckingham) potentials and elastic shell model of (19,3)@(22,11) DWNT under conditions of emptiness, interior fluid filling (+int), and exterior fluid adsorption (+ext). Reasonable agreement between atomistic simulation and continuum models confirms the utility of elastic shell models in analyzing and predicting DWNT behavior in the presence of fluids. (b) Molecular dynamics simulation snapshots showing DWNT interior fluid filling and exterior adsorption, with depletion distance $s_0 = 0.33\ nm$ in both cases. (c) Application of elastic shell models showing frequency changes upon internal fluid filling and external fluid adsorption in chirality-assigned DWNT observed from Liu *et al.*[55] and Rochal *et al.*[71] The RBLMs observed by Liu *et al.*[55] are consistent with DWNT measured under adsorbate-free

conditions, while those observed by Rochal *et al.*[71] are consistent with DWNT with external adsorption (dotted lines) but not internal fluid filling (solid lines). (d-e) RBLM frequencies and amplitudes over a broad range of exterior interaction parameter γ_{ext} in a 1.5 nm inner diameter DWNT, showing an avoided mode crossing beyond which the high-frequency mode is dominated by displacement of the outer tube. (f) The value of γ_{ext} required to observe mode crossover as a function of diameter. While mode crossing is theoretically possible at any diameter, it is only practicable given fluid-water interaction parameters (red dashed line) in large DWNT, with inner diameters over 5 nm.

3.3 Conclusions

In this paper, we demonstrate that double-walled carbon nanotubes, unlike single-walled carbon nanotubes, can distinguish between interior fluid filling and exterior fluid adsorption. We do this by developing elastic shell models of DWNT when exposed to internal and external fluids, which reveal blueshifts in the coupled radial breathing-like modes of the two carbon shells. There is a primary shift in the mode that predominantly corresponds to the shell closest to the fluid, with a sympathetic shift in the mode that predominantly corresponds to the shell farther from the fluid. This observation holds for one assumed set of CNT parameters, but it also holds for a more general set of double-walled tube-fluid systems, which could include non-CNT tubes and non-aqueous fluids. Experimentally, carbon nanotubes are comparatively easy to study by resonant Raman spectroscopy, with electronic resonances in the visible,[81] while boron nitride nanotubes require UV excitation and are substantially less well-studied.[82,83] Other nanotubes with diameters in the single-digit regime, including MoS_2 and WS_2, have been grown and characterized by Raman, but without the ability to observe RBLMs.[84,85] Finally, composite multi-walled nanotubes of different materials – so called 1D vdW heterostructures[86] – may exhibit exotic electronic, optical, and fluidic properties, but have only recently been synthesized. Fluid-filling with non-aqueous fluids, similarly, is underexplored.

For water filling of carbon nanotubes, we expect that thermodynamic and kinetic parameters – for instance, the enthalpy of adsorption of water to the CNT, and the water diffusion coefficient – will vary substantially between water that is confined inside the CNT and water that is adsorbed to the outside. Water at the interior CNT interface and water at the exterior CNT interface has different properties as a result of varying dipole orientation, hydrogen bond structure, dissociation constant, and solvation properties. While these molecular effects cannot be taken into account by continuum elastic shell models, the predictive capacity of elastic shell models is clear in distinguishing between interior and exterior water in DWNT, and thereby advancing nanofluidic experimental work in general. We expect that DWNT will be highly useful as platforms for thermodynamic and kinetic studies of water under nanoconfinement in the coming years, with vibrational characterization of fluid filling states used as an important tool in characterizing nanofluidic interfacial behavior.

3.4 Supplementary Information

1. Inclusion of direct van der Waals interactions between non-adjacent shells

The figures shown in the main text use the parameters γ_{int} for an effective coupling between the inner wall of a DWNT and an interior fluid, and the parameter γ_{ext} for an effective coupling between the outer wall of a DWNT and an exterior fluid. We consider the effect of the van der Waals coupling between the fluid and the non-adjacent DWNT shell here. The interaction between a fluid and a carbon shell can be modelled as a Lennard-Jones potential with a similar form to that of the carbon-carbon Lennard-Jones potential described in the main text:[1,2]

$$U(w) = K\left[0.4\left(\frac{s_0}{s_0+w}\right)^{10} - \left(\frac{s_0}{s_0+w}\right)^{4}\right] \quad [3.20]$$

Where the well depth is $-0.6K$, the equilibrium water-carbon distance is s_0, and the deviation from this distance is w. The second derivative of this potential is:

$$\frac{d^2U}{dw^2} = K\left[\frac{44\ {s_0}^{10}}{(s_0+w)^{12}} - \frac{20\ {s_0}^{4}}{(s_0+w)^{6}}\right] \quad [3.21]$$

The ratio in effective coupling between the nearest water layer, which is at the equilibrium distance ($w = 0$), and the far water layer, for which $w \approx s_0$, is as follows:

$$\frac{\gamma_{near\ shell}}{\gamma_{far\ shell}} = \frac{\left.\frac{d^2U}{dw^2}\right|_{w=0}}{\left.\frac{d^2U}{dw^2}\right|_{w=s_0}} = \frac{24K/\ {s_0}^2}{-0.3018\ K/\ {s_0}^2} = -79.53 \quad [3.22]$$

Since $abs(\frac{\gamma_{near\ shell}}{\gamma_{far\ shell}}) \gg 1$, we neglect the direct van der Waals interaction between an interior fluid and an outer DWNT shell, or between an exterior fluid and an interior DWNT shell.

2. Elastic shell model with water as an elastic shell

In contrast to the expression used in the main text, where water layers were modelled as fixed pressures, water layers can also be modelled as independent elastic shells. In this case, Eq. 4 from the main text expands from a two by two matrix to an n by n matrix, where n includes water and carbon shells. The vibrational frequencies represent modes of the carbon shells and the water shell(s), though the water shell frequencies are essentially non-physical. While the material properties of an elastic water shell are less well-defined than that of a carbon shell, we assume the following values for the elastic water shell: $E_H h_H = 0.68\ J/m^2$, $h_H = 0.34\ nm$, $\rho_H = 0.997\ g/cm^3$, and $\nu_H = 0.45$.[3] The quantitative values of $\Delta\omega_{RBM}$ (**Figure 3-5a** and **Figure 3-5b**) do not show quantitative agreement with those in the main text, but the observation of the primary and sympathetic shift upon interior fluid filling and exterior fluid adsorption (**Figure 3-5d**) remains the same.

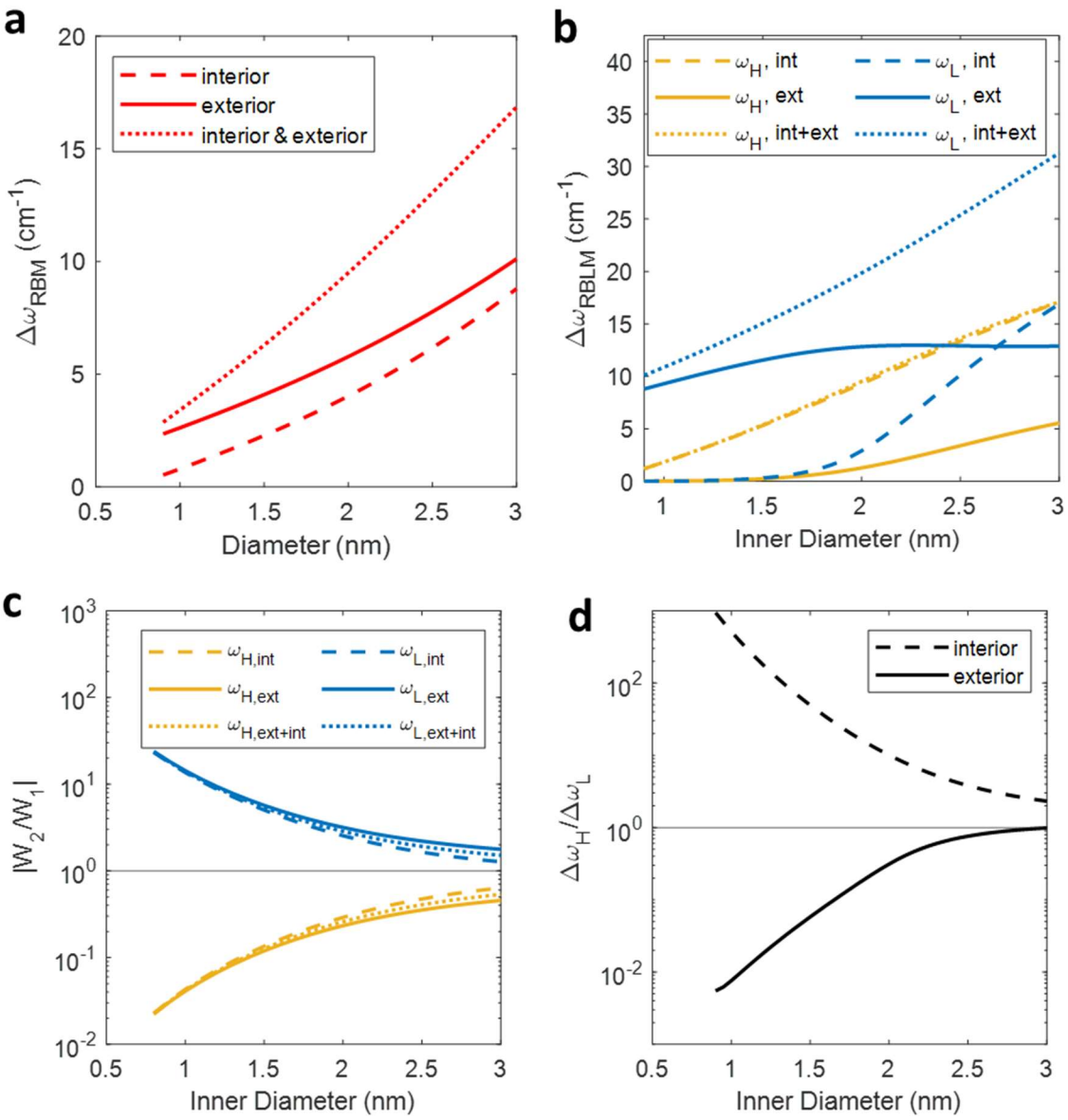

Figure 3-5. RBM shifts in SWNT and DWNT systems with fluid modelled as an elastic shell. (a) RBM shifts upon interior, exterior, and interior/exterior water coupling in SWNT as a function of diameter. (b) RBLM shifts in high and low frequency modes upon interior water filling, exterior water adsorption, and both as a function of inner diameter. (c) Intensity ratios for high and low frequency modes as a function of inner diameter. (d) Ratio of RBLM shift in high frequency mode to low frequency mode upon interior water filling and exterior water adsorption as a function of inner diameter.

3. Parameter Estimation in Non-Dimensional Model

The parameter space covered in the non-dimensional model includes double-walled nanotubes of interest in the single-digit nanopore regime. The range of ξ_{02}/ξ_{01} considered, from 0.1 to 0.9, covers a broad range of double-walled carbon nanotube and boron nitride nanotube diameters, as

shown in **Figure 3-6a**. The range of $\hat{\gamma}/\xi_{01}$considered, also from 0.1 to 0.9, extends past the range of inter-tube coupling observed in experimental DWNT systems (**Figure 3-6b**), as determined by Raman spectra of chirality-assigned DWNTs, for which the diameters and the coupled DWNT RBLM modes in a nominally pristine state are both known.[4] Whether the experimentally observed RBLM modes[4] in **Figure 3-6b** are actually in a pristine state can be disputed, and would affect the quantitative results but not the qualitative conclusion that the studied parameter range is adequate for physical DWNT systems.

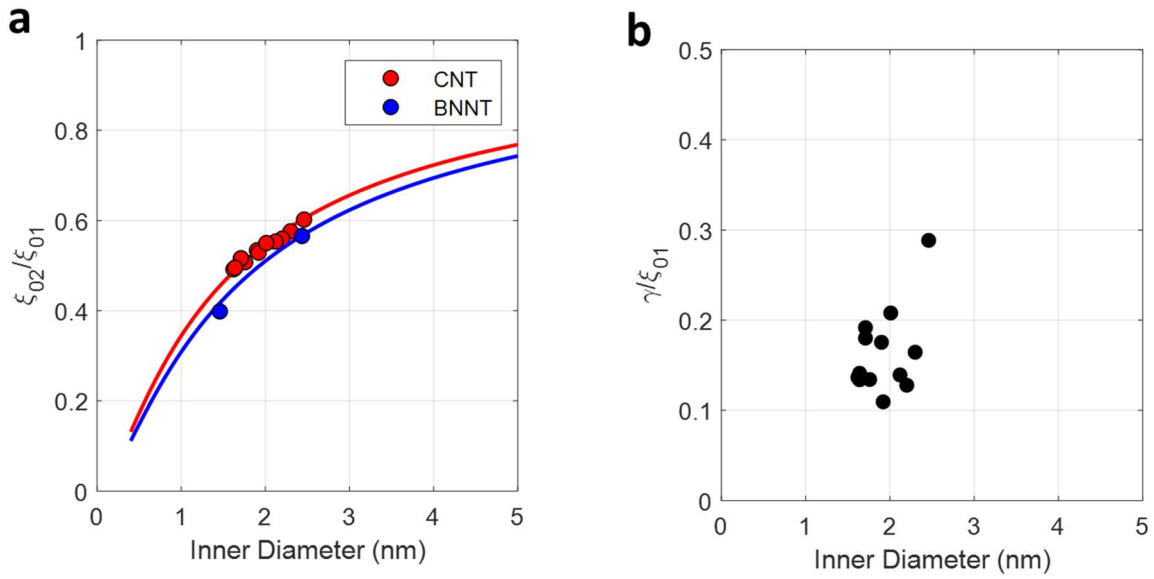

Figure 3-6. (a) Variation of the parameter $\xi_{02}/\xi_{01}$with nanotube size in carbon nanotubes (red) and boron nitride nanotubes (blue). Variation in intertube spacing, as taken from experimental studies[4,5] with electron diffraction (points), results in slight discrepancies from mean values (lines). (b) Estimate of normalized inter-shell coupling $\hat{\gamma}/\xi_{01}$ as a function of inner diameter, taken from 13 chirality-assigned double-walled carbon nanotubes.[4]

(1) Longhurst, M. J.; Quirke, N. The Environmental Effect on the Radial Breathing Mode of Carbon Nanotubes in Water. *J. Chem. Phys.* **2006**, *124* (23), 234708. https://doi.org/10.1063/1.2205852.

(2) Girifalco, L. A.; Hodak, M.; Lee, R. S. Carbon Nanotubes, Buckyballs, Ropes, and a Universal Graphitic Potential. *Phys. Rev. B - Condens. Matter Mater. Phys.* **2000**, *62* (19), 13104–13110. https://doi.org/10.1103/PhysRevB.62.13104.

(3) Agrawal, K. V.; Shimizu, S.; Drahushuk, L. W.; Kilcoyne, D.; Strano, M. S. Observation of Extreme Phase Transition Temperatures of Water Confined inside Isolated Carbon Nanotubes. *Nat. Nanotechnol.* **2017**, *12* (3), 267–273. https://doi.org/10.1038/nnano.2016.254.

(4) Liu, K.; Hong, X.; Wu, M.; Xiao, F.; Wang, W.; Bai, X.; Ager, J. W.; Aloni, S.; Zettl, A.; Wang, E.; Wang, F. Quantum-Coupled Radial-Breathing Oscillations in Double-Walled Carbon Nanotubes. *Nat. Commun.* **2013**, *4*, 1–6. https://doi.org/10.1038/ncomms2367.

(5) Arenal, R.; Kociak, M.; Loiseau, A.; Miller, D. J. Determination of Chiral Indices of Individual Single- And Double-Walled Boron Nitride Nanotubes by Electron Diffraction. *Appl. Phys. Lett.* **2006**, *89* (7). https://doi.org/10.1063/1.2335379.

3.5 References

(1) Faucher, S.; Aluru, N.; Bazant, M. Z.; Blankschtein, D.; Brozena, A. H.; Cumings, J.; Pedro De Souza, J.; Elimelech, M.; Epsztein, R.; Fourkas, J. T.; Rajan, A. G.; Kulik, H. J.; Levy, A.; Majumdar, A.; Martin, C.; McEldrew, M.; Misra, R. P.; Noy, A.; Pham, T. A.; Reed, M.; Schwegler, E.; Siwy, Z.; Wang, Y.; Strano, M. Critical Knowledge Gaps in Mass Transport through Single-Digit Nanopores: A Review and Perspective. *J. Phys. Chem. C* **2019**, *123* (35), 21309–21326. https://doi.org/10.1021/acs.jpcc.9b02178.

(2) Bocquet, L. Nanofluidics Coming of Age. *Nat. Mater.* **2020**, *19* (3), 254–256. https://doi.org/10.1038/s41563-020-0625-8.

(3) Park, H. G.; Jung, Y. Carbon Nanofluidics of Rapid Water Transport for Energy Applications. *Chem. Soc. Rev.* **2014**, *43* (2), 565–576. https://doi.org/10.1039/C3CS60253B.

(4) Deamer, D.; Akeson, M.; Branton, D. Three Decades of Nanopore Sequencing. *Nat. Biotechnol.* **2016**, *34* (5). https://doi.org/10.1038/nbt.3423.

(5) Werber, J. R.; Osuji, C. O.; Elimelech, M. Materials for Next-Generation Desalination and Water Purification Membranes. *Nat. Rev. Mater.* **2016**, *1*. https://doi.org/10.1038/natrevmats.2016.18.

(6) Radha, B.; Esfandiar, A.; Wang, F. C.; Rooney, A. P.; Gopinadhan, K.; Keerthi, A.; Mishchenko, A.; Janardanan, A.; Blake, P.; Fumagalli, L.; Lozada-Hidalgo, M.; Garaj, S.; Haigh, S. J.; Grigorieva, I. V.; Wu, H. A.; Geim, A. K. Molecular Transport through Capillaries Made with Atomic-Scale Precision. *Nature* **2016**, *538* (7624), 222–225. https://doi.org/10.1038/nature19363.

(7) Fumagalli, L.; Esfandiar, A.; Fabregas, R.; Hu, S.; Ares, P.; Janardanan, A.; Yang, Q.; Radha, B.; Taniguchi, T.; Watanabe, K.; Gomila, G.; Novoselov, K. S.; Geim, A. K. Anomalously Low Dielectric Constant of Confined Water. *Science (80-.).* **2018**, *360* (6395), 1339–1342. https://doi.org/10.1126/science.aat4191.

(8) Kim, K.; Artyukhov, V. I.; Regan, W.; Liu, Y.; Crommie, M. F.; Yakobson, B. I.; Zettl, A. Ripping Graphene: Preferred Directions. *Nano Lett.* **2012**, *12* (1), 293–297. https://doi.org/10.1021/nl203547z.

(9) Govind Rajan, A.; Silmore, K. S.; Swett, J.; Robertson, A. W.; Warner, J. H.; Blankschtein, D.; Strano, M. S. Addressing the Isomer Cataloguing Problem for Nanopores in Two-Dimensional Materials. *Nat. Mater.* **2019**, *18* (2), 129–135. https://doi.org/10.1038/s41563-018-0258-3.

(10) Kafiah, F. M.; Khan, Z.; Ibrahim, A.; Karnik, R.; Atieh, M.; Laoui, T. Monolayer Graphene Transfer onto Polypropylene and Polyvinylidenedifluoride Microfiltration Membranes for Water Desalination. *Desalination* **2016**, *388*, 29–37. https://doi.org/10.1016/j.desal.2016.02.027.

(11) O'Hern, S. C.; Stewart, C. A.; Boutilier, M. S. H.; Idrobo, J. C.; Bhaviripudi, S.; Das, S. K.; Kong, J.; Laoui, T.; Atieh, M.; Karnik, R. Selective Molecular Transport through Intrinsic Defects in a Single Layer of CVD Graphene. *ACS Nano* **2012**, *6* (11), 10130–10138. https://doi.org/10.1021/nn303869m.

(12) Yuan, Z.; He, G.; Faucher, S.; Kuehne, M.; Li, S. X.; Blankschtein, D.; Strano, M. S. Direct Chemical Vapor Deposition Synthesis of Porous Single-Layer Graphene Membranes with

High Gas Permeances and Selectivities. *Adv. Mater.* **2021**, *33* (44), 1–9. https://doi.org/10.1002/adma.202104308.

(13) O'Hern, S. C.; Boutilier, M. S. H.; Idrobo, J. C.; Song, Y.; Kong, J.; Laoui, T.; Atieh, M.; Karnik, R. Selective Ionic Transport through Tunable Subnanometer Pores in Single-Layer Graphene Membranes. *Nano Lett.* **2014**, *14* (3), 1234–1241. https://doi.org/10.1021/nl404118f.

(14) Koenig, S. P.; Wang, L.; Pellegrino, J.; Bunch, J. S. Selective Molecular Sieving through Porous Graphene. *Nat. Nanotechnol.* **2012**, *7* (11), 728–732. https://doi.org/10.1038/nnano.2012.162.

(15) Tan, Y. H.; Davis, J. A.; Fujikawa, K.; Ganesh, N. V.; Demchenko, A. V.; Stine, K. J. Surface Area and Pore Size Characteristics of Nanoporous Gold Subjected to Thermal, Mechanical, or Surface Modification Studied Using Gas Adsorption Isotherms, Cyclic Voltammetry, Thermogravimetric Analysis, and Scanning Electron Microscopy. *J. Mater. Chem.* **2012**, *22* (14), 6733–6745. https://doi.org/10.1039/c2jm16633j.

(16) Maesen, T. L. M.; Krishna, R.; van Baten, J. M.; Smit, B.; Calero, S.; Castillo Sanchez, J. M. Shape-Selective n-Alkane Hydroconversion at Exterior Zeolite Surfaces. *J. Catal.* **2008**, *256* (1), 95–107. https://doi.org/10.1016/j.jcat.2008.03.004.

(17) Secchi, E.; Marbach, S.; Niguès, A.; Stein, D.; Siria, A.; Bocquet, L. Massive Radius-Dependent Flow Slippage in Carbon Nanotubes. *Nature* **2016**, *537* (7619), 210–213. https://doi.org/10.1038/nature19315.

(18) Agrawal, K. V.; Shimizu, S.; Drahushuk, L. W.; Kilcoyne, D.; Strano, M. S. Observation of Extreme Phase Transition Temperatures of Water Confined inside Isolated Carbon Nanotubes. *Nat. Nanotechnol.* **2017**, *12* (3), 267–273. https://doi.org/10.1038/nnano.2016.254.

(19) Kavokine, N.; Bocquet, M. L.; Bocquet, L. Fluctuation-Induced Quantum Friction in Nanoscale Water Flows. *Nature* **2022**, *602* (7895), 84–90. https://doi.org/10.1038/s41586-021-04284-7.

(20) Misra, R. P.; Blankschtein, D. Insights on the Role of Many-Body Polarization Effects in the Wetting of Graphitic Surfaces by Water. *J. Phys. Chem. C* **2017**, *121* (50), 28166–28179. https://doi.org/10.1021/acs.jpcc.7b08891.

(21) Sianipar, M.; Kim, S. H.; Khoiruddin; Iskandar, F.; Wenten, I. G. Functionalized Carbon Nanotube (CNT) Membrane: Progress and Challenges. *RSC Adv.* **2017**, *7* (81), 51175–51198. https://doi.org/10.1039/c7ra08570b.

(22) Pomerantseva, E.; Bonaccorso, F.; Feng, X.; Cui, Y.; Gogotsi, Y. Energy Storage: The Future Enabled by Nanomaterials. *Science (80-.).* **2019**, *366* (6468). https://doi.org/10.1126/science.aan8285.

(23) Kondratyuk, P.; Yates, J. T. Molecular Views of Physical Adsorption inside and Outside of Single-Wall Carbon Nanotubes. *Acc. Chem. Res.* **2007**, *40* (10), 995–1004. https://doi.org/10.1021/ar700013c.

(24) Dillon, A. C.; Jones, K. M.; Bekkedahl, T. A.; Kiang, C. H.; Bethune, D. S.; Heben, M. J. Storage of Hydrogen in Single-Walled Carbon Nanotubes. *Nature* **1997**, *386* (6623), 377–379. https://doi.org/10.1038/386377a0.

(25) Kuznetsova, A.; Yates, J. T.; Liu, J.; Smalley, R. E. Physical Adsorption of Xenon in Open Single Walled Carbon Nanotubes: Observation of a Quasi-One-Dimensional Confined Xe Phase. *J. Chem. Phys.* **2000**, *112* (21), 9590–9598. https://doi.org/10.1063/1.481575.

(26) Wenseleers, W.; Cambré, S.; Čulin, J.; Bouwen, A.; Goovaerts, E. Effect of Water Filling

on the Electronic and Vibrational Resonances of Carbon Nanotubes: Characterizing Tube Opening by Raman Spectroscopy. *Adv. Mater.* **2007**, *19* (17), 2274–2278. https://doi.org/10.1002/adma.200700773.

(27) Cambré, S.; Wenseleers, W. Separation and Diameter-Sorting of Empty (End-Capped) and Water-Filled (Open) Carbon Nanotubes by Density Gradient Ultracentrifugation. *Angew. Chemie - Int. Ed.* **2011**, *50* (12), 2764–2768. https://doi.org/10.1002/anie.201007324.

(28) Campo, J.; Cambré, S.; Botka, B.; Obrzut, J.; Wenseleers, W.; Fagan, J. A. Optical Property Tuning of Single-Wall Carbon Nanotubes by Endohedral Encapsulation of a Wide Variety of Dielectric Molecules. *ACS Nano* **2021**, *15* (2), 2301–2317. https://doi.org/10.1021/acsnano.0c08352.

(29) Chen, Q.; Herberg, J. L.; Mogilevsky, G.; Wang, H. J.; Stadermann, M.; Holt, J. K.; Wu, Y. Identification of Endohedral Water in Single-Walled Carbon Nanotubes by 1H NMR. *Nano Lett.* **2008**, *8* (7), 1902–1905. https://doi.org/10.1021/nl080569e.

(30) Liu, X.; Pan, X.; Zhang, S.; Han, X.; Bao, X. Diffusion of Water inside Carbon Nanotubes Studied by Pulsed Field Gradient NMR Spectroscopy. *Langmuir* **2014**, *30* (27), 8036–8045. https://doi.org/10.1021/la500913r.

(31) Das, A.; Jayanthi, S.; Deepak, H. S. M. V.; Ramanathan, K. V.; Kumar, A.; Dasgupta, C.; Sood, A. K. Single-File Diffusion of Confined Water inside SWNTs: An NMR Study. *ACS Nano* **2010**, *4* (3), 1687–1695. https://doi.org/10.1021/nn901554h.

(32) Kim, Y. T.; Joo, S. H.; Min, H.; Lee, J.; Moon, S. M.; Byeon, M.; Hong, T. E.; Strano, M. S.; Han, J. H.; Kwak, S. K.; Lee, C. Y. The Exterior of Single-Walled Carbon Nanotubes as a Millimeter-Long Cation-Preferring Nanochannel. *Chem. Mater.* **2018**, *30* (15), 5184–5193. https://doi.org/10.1021/acs.chemmater.8b01802.

(33) Lee, C. Y.; Choi, W.; Han, J.-H. H.; Strano, M. S. Coherence Resonance in a Single-Walled Carbon Nanotube Ion Channel. *Science (80-.).* **2010**, *329* (5997), 1320–1324. https://doi.org/10.1126/science.1193383.

(34) Stepanek, I.; Maurin, G.; Bernier, P.; Gavillet, J.; Loiseau, A. Cutting Single Wall Carbon Nanotubes. *Mater. Res. Soc. Symp. - Proc.* **2000**, *593*, 119–122. https://doi.org/10.1557/proc-593-119.

(35) Ajayan, P. M.; Lijima, S.; Iijima, S. Capillarity-Induced Filling of Carbon Nanotubes. *Nature* **1993**, *361* (6410), 333–334. https://doi.org/10.1038/361333a0.

(36) Gadd, G. E.; Blackford, M.; Moricca, S.; Webb, N.; Evans, P. J.; Smith, A. M.; Jacobsen, G.; Leung, S.; Day, A.; Hua, Q. The World's Smallest Gas Cylinders? *Science (80-.).* **1997**, *277* (5328), 933–936. https://doi.org/10.1126/science.277.5328.933.

(37) Mattia, D.; Gogotsi, Y. Review: Static and Dynamic Behavior of Liquids inside Carbon Nanotubes. *Microfluid. Nanofluidics* **2008**, *5* (3), 289–305. https://doi.org/10.1007/s10404-008-0293-5.

(38) Wang, Z.; Wei, J.; Morse, P.; Gregory Dash, J.; Vilches, O. E.; Cobden, D. H. Phase Transitions of Adsorbed Atoms on the Surface of a Carbon Nanotube. *Science (80-.).* **2010**, *327* (5965), 552–555. https://doi.org/10.1126/science.1182507.

(39) Noury, A.; Vergara-Cruz, J.; Morfin, P.; Plaçais, B.; Gordillo, M. C.; Boronat, J.; Balibar, S.; Bachtold, A. Layering Transition in Superfluid Helium Adsorbed on a Carbon Nanotube Mechanical Resonator. *Phys. Rev. Lett.* **2019**, *122* (16), 1–6. https://doi.org/10.1103/PhysRevLett.122.165301.

(40) Homma, Y.; Chiashi, S.; Yamamoto, T.; Kono, K.; Matsumoto, D.; Shitaba, J.; Sato, S. Photoluminescence Measurements and Molecular Dynamics Simulations of Water

Adsorption on the Hydrophobic Surface of a Carbon Nanotube in Water Vapor. *Phys. Rev. Lett.* **2013**, *110* (15). https://doi.org/10.1103/PhysRevLett.110.157402.

(41) Ma, X.; Cambré, S.; Wenseleers, W.; Doorn, S. K.; Htoon, H. Quasiphase Transition in a Single File of Water Molecules Encapsulated in (6,5) Carbon Nanotubes Observed by Temperature-Dependent Photoluminescence Spectroscopy. *Phys. Rev. Lett.* **2017**, *118* (2). https://doi.org/10.1103/PhysRevLett.118.027402.

(42) Chiashi, S.; Saito, Y.; Kato, T.; Konabe, S.; Okada, S.; Yamamoto, T.; Homma, Y. Confinement Effect of Sub-Nanometer Difference on Melting Point of Ice-Nanotubes Measured by Photoluminescence Spectroscopy. *ACS Nano* **2019**, *13* (2), 1177–1182. https://doi.org/10.1021/acsnano.8b06041.

(43) Saito, Y.; Tanaka, Y.; Yamaguchi, G.; Kato, T.; Konabe, S.; Chiashi, S.; Homma, Y. Temperature Dependence of Photoluminescence Spectra from a Suspended Single-Walled Carbon Nanotube with Water Adsorption Layer. *J. Appl. Phys.* **2021**, *129* (1), 6–11. https://doi.org/10.1063/5.0031611.

(44) Chiashi, S.; Hanashima, T.; Mitobe, R.; Nagatsu, K.; Yamamoto, T.; Homma, Y. Water Encapsulation Control in Individual Single-Walled Carbon Nanotubes by Laser Irradiation. *J. Phys. Chem. Lett.* **2014**, *5* (3), 408–412. https://doi.org/10.1021/jz402540v.

(45) Cambré, S.; Santos, S. M.; Wenseleers, W.; Nugraha, A. R. T.; Saito, R.; Cognet, L.; Lounis, B. Luminescence Properties of Individual Empty and Water-Filled Single-Walled Carbon Nanotubes. *ACS Nano* **2012**, *6* (3), 2649–2655. https://doi.org/10.1021/nn300035y.

(46) Yang, S.; Parks, A. N.; Saba, S. A.; Ferguson, P. L.; Liu, J. Photoluminescence from Inner Walls in Double-Walled Carbon Nanotubes: Some Do, Some Do Not. *Nano Lett.* **2011**, *11* (10), 4405–4410. https://doi.org/10.1021/nl2025745.

(47) Faucher, S.; Kuehne, M.; Koman, V. B.; Northrup, N.; Kozawa, D.; Yuan, Z.; Li, S. X.; Zeng, Y.; Ichihara, T.; Misra, R. P.; Aluru, N.; Blankschtein, D.; Strano, M. S. Diameter Dependence of Water Filling in Lithographically Segmented Isolated Carbon Nanotubes. *ACS Nano* **2021**, *15* (2), 2778–2790. https://doi.org/10.1021/acsnano.0c08634.

(48) Jorio, A.; Saito, R.; Dresselhaus, G.; Dresselhaus, M. S. *Raman Spectroscopy in Graphene Related Systems*; John Wiley & Sons, 2011. https://doi.org/10.1002/9783527632695.

(49) Mahan, G. D. Oscillations of a Thin Hollow Cylinder: Carbon Nanotubes. *Phys. Rev. B - Condens. Matter Mater. Phys.* **2002**, *65* (23), 1–7. https://doi.org/10.1103/PhysRevB.65.235402.

(50) Araujo, P. T.; Maciel, I. O.; Pesce, P. B. C.; Pimenta, M. A.; Doorn, S. K.; Qian, H.; Hartschuh, A.; Steiner, M.; Grigorian, L.; Hata, K.; Jorio, A. Nature of the Constant Factor in the Relation between Radial Breathing Mode Frequency and Tube Diameter for Single-Wall Carbon Nanotubes. *Phys. Rev. B - Condens. Matter Mater. Phys.* **2008**, *77* (24), 2–5. https://doi.org/10.1103/PhysRevB.77.241403.

(51) Liu, K.; Wang, W.; Wu, M.; Xiao, F.; Hong, X.; Aloni, S.; Bai, X.; Wang, E.; Wang, F. Intrinsic Radial Breathing Oscillation in Suspended Single-Walled Carbon Nanotubes. *Phys. Rev. B - Condens. Matter Mater. Phys.* **2011**, *83* (11), 1–4. https://doi.org/10.1103/PhysRevB.83.113404.

(52) Wenseleers, W.; Cambré, S.; Čulin, J.; Bouwen, A.; Goovaerts, E. Effect of Water Filling on the Electronic and Vibrational Resonances of Carbon Nanotubes: Characterizing Tube Opening by Raman Spectroscopy. *Adv. Mater.* **2007**, *19* (17), 2274–2278. https://doi.org/10.1002/adma.200700773.

(53) Cambré, S.; Schoeters, B.; Luyckx, S.; Goovaerts, E.; Wenseleers, W.; Cambr??, S.;

Schoeters, B.; Luyckx, S.; Goovaerts, E.; Wenseleers, W. Experimental Observation of Single-File Water Filling of Thin Single-Wall Carbon Nanotubes down to Chiral Index (5,3). *Phys. Rev. Lett.* **2010**, *104* (20), 1–4. https://doi.org/10.1103/PhysRevLett.104.207401.

(54) Fagan, J. A.; Huh, J. Y.; Simpson, J. R.; Blackburn, J. L.; Holt, J. M.; Larsen, B. A.; Walker, A. R. H. Separation of Empty and Water-Filled Single-Wall Carbon Nanotubes. *ACS Nano* **2011**, *5* (5), 3943–3953. https://doi.org/10.1021/nn200458t.

(55) Liu, K.; Hong, X.; Wu, M.; Xiao, F.; Wang, W.; Bai, X.; Ager, J. W.; Aloni, S.; Zettl, A.; Wang, E.; Wang, F. Quantum-Coupled Radial-Breathing Oscillations in Double-Walled Carbon Nanotubes. *Nat. Commun.* **2013**, *4*, 1–6. https://doi.org/10.1038/ncomms2367.

(56) Wang, C. Y.; Ru, C. Q.; Mioduchowski, A. Applicability and Limitations of Simplified Elastic Shell Equations for Carbon Nanotubes. *J. Appl. Mech. Trans. ASME* **2004**, *71* (5), 622–631. https://doi.org/10.1115/1.1778415.

(57) Longhurst, M. J.; Quirke, N. The Environmental Effect on the Radial Breathing Mode of Carbon Nanotubes in Water. *J. Chem. Phys.* **2006**, *124* (23), 234708. https://doi.org/10.1063/1.2205852.

(58) Popov, V. N.; Henrard, L. Breathinglike Phonon Modes of Multiwalled Carbon Nanotubes. *Phys. Rev. B - Condens. Matter Mater. Phys.* **2002**, *65* (23), 2354151–2354156. https://doi.org/10.1103/PhysRevB.65.235415.

(59) Wang, C. Y.; Ru, C. Q.; Mioduchowski, A. Free Vibration of Multiwall Carbon Nanotubes. *J. Appl. Phys.* **2005**, *97* (11), 114323. https://doi.org/10.1063/1.1898445.

(60) Wang, C. Y.; Ru, C. Q.; Mioduchowski, A. Pressure Effect on Radial Breathing Modes of Multiwall Carbon Nanotubes. *J. Appl. Phys.* **2005**, *97* (2). https://doi.org/10.1063/1.1836007.

(61) Hue, J. W.; Hirschmann, T. C.; Kim, Y. A.; Muramatsu, H.; Barbosa Neto, N. M.; Araujo, P. T. Environmental Effects, Intertube Interactions and σ-π Bond Re-Hybridization in Bundles of Double- and Triple-Walled Carbon Nanotubes. *Carbon N. Y.* **2020**, *158*, 651–661. https://doi.org/10.1016/j.carbon.2019.11.037.

(62) Lu, W. B.; Liu, B.; Wu, J.; Xiao, J.; Hwang, K. C.; Fu, S. Y.; Huang, Y. Continuum Modeling of van Der Waals Interactions between Carbon Nanotube Walls. *Appl. Phys. Lett.* **2009**, *94* (10). https://doi.org/10.1063/1.3099023.

(63) Girifalco, L. A.; Hodak, M.; Lee, R. S. Carbon Nanotubes, Buckyballs, Ropes, and a Universal Graphitic Potential. *Phys. Rev. B - Condens. Matter Mater. Phys.* **2000**, *62* (19), 13104–13110. https://doi.org/10.1103/PhysRevB.62.13104.

(64) Lu, W. B.; Wu, J.; Jiang, L. Y.; Huang, Y.; Hwang, K. C.; Liu, B. A Cohesive Law for Multi-Wall Carbon Nanotubes. *Philos. Mag.* **2007**, *87* (14–15), 2221–2232. https://doi.org/10.1080/14786430701344558.

(65) Bellarosa, L.; Bakalis, E.; Melle-Franco, M.; Zerbetto, F. Interactions in Concentric Carbon Nanotubes: The Radius vs the Chirality Angle Contributions. *Nano Lett.* **2006**, *6* (9), 1950–1954. https://doi.org/10.1021/nl061066g.

(66) Hirschmann, T. C.; Araujo, P. T.; Muramatsu, H.; Rodriguez-Nieva, J. F.; Seifert, M.; Nielsch, K.; Kim, Y. A.; Dresselhaus, M. S. Role of Intertube Interactions in Double-and Triple-Walled Carbon Nanotubes. *ACS Nano* **2014**, *8* (2), 1330–1341. https://doi.org/10.1021/nn500420s.

(67) Gordeev, G.; Wasserroth, S.; Li, H.; Flavel, B.; Reich, S. Moiré-Induced Vibrational Coupling in Double-Walled Carbon Nanotubes. *Nano Lett.* **2021**, *21* (16), 6732–6739.

https://doi.org/10.1021/acs.nanolett.1c00295.
(68) Kuehne, M.; Faucher, S.; Misra, R. P.; Oliaei, H.; Li, H.; Yang, J. F.; Penn, A.; Yuan, Z.; Li, S. X.; He, G.; Zhang, G.; Koman, V. B.; Majumdar, A.; Aluru, N.; Blankschtein, D.; Strano, M. S. Unpublished Work. **2022**.
(69) Liu, Z.; Gao, J.; Zhang, G.; Cheng, Y.; Zhang, Y. W. From Two-Dimensional Nano-Sheets to Roll-up Structures: Expanding the Family of Nanoscroll. *Nanotechnology* **2017**, *28* (38). https://doi.org/10.1088/1361-6528/aa7bf8.
(70) Longhurst, M. J.; Quirke, N. The Environmental Effect on the Radial Breathing Mode of Carbon Nanotubes. II. Shell Model Approximation for Internally and Externally Adsorbed Fluids. *J. Chem. Phys.* **2006**, *125* (18), 184705. https://doi.org/10.1063/1.2360943.
(71) Rochal, S.; Levshov, D.; Avramenko, M.; Arenal, R.; Cao, T. T.; Nguyen, V. C.; Sauvajol, J. L.; Paillet, M. Chirality Manifestation in Elastic Coupling between the Layers of Double-Walled Carbon Nanotubes. *Nanoscale* **2019**, *11* (34), 16092–16102. https://doi.org/10.1039/c9nr03853a.
(72) Kuehne, M.; Faucher, S.; Liew, M.; Yuan, Z.; Li, S. X.; Ichihara, T.; Zeng, Y.; Gordiichuk, P.; Koman, V. B.; Kozawa, D.; Majumdar, A.; Strano, M. S. Impedance of Thermal Conduction from Nanoconfined Water in Carbon Nanotube Single-Digit Nanopores. *J. Phys. Chem. C* **2021**, *125* (46), 25717–25728. https://doi.org/10.1021/acs.jpcc.1c08146.
(73) Jorio, A.; Dresselhaus, Gene Dresselhaus, M. S. *Carbon Nanotubes: Advanced Topics in the Synthesis, Structure, Properties and Applications*; Springer, 2008; Vol. 11. https://doi.org/10.1016/s1369-7021(08)70021-x.
(74) Longhurst, M. J.; Quirke, N. Pressure Dependence of the Radial Breathing Mode of Carbon Nanotubes: The Effect of Fluid Adsorption. *Phys. Rev. Lett.* **2007**, *98* (14), 6–9. https://doi.org/10.1103/PhysRevLett.98.145503.
(75) Stuart, S. J.; Tutein, A. B.; Harrison, J. A. A Reactive Potential for Hydrocarbons with Intermolecular Interactions. *J. Chem. Phys.* **2000**, *112* (14), 6472–6486. https://doi.org/10.1063/1.481208.
(76) Brenner, D. W. Empirical Potential for Hydrocarbons for Use in Simulating the Chemical Vapor Deposition of Diamond Films. *Phys. Rev. B* **1990**, *42* (15), 9458–9471. https://doi.org/10.1103/PhysRevB.42.9458.
(77) Abascal, J. L. F.; Vega, C. A General Purpose Model for the Condensed Phases of Water: TIP4P/2005. *J. Chem. Phys.* **2005**, *123* (23). https://doi.org/10.1063/1.2121687.
(78) Plimpton, S. Fast Parallel Algorithms for Short-Range Molecular Dynamics. *J. Comput. Phys.* **1995**, *117* (1), 1–19.
(79) Verlet, L. Computer "Experiments" on Classical Fluids. I. Thermodynamical Properties of Lennard-Jones Molecules. *Phys. Rev.* **1967**, *159* (1), 98. https://doi.org/10.1103/PhysRev.159.98.
(80) Wu, Y.; Aluru, N. R. Graphitic Carbon–Water Nonbonded Interaction Parameters. *J. Phys. Chem. B* **2013**, *117* (29), 8802–8813. https://doi.org/10.1021/JP402051T.
(81) Dresselhaus, M.; Dresselhaus, G.; Saito, R.; Jorio, K. Raman Spectroscopy of Carbon Nanotubes. *Phys. Rep.* **2005**, *49*, 47–99.
(82) Arenal, R.; Kociak, M.; Loiseau, A.; Miller, D. J. Determination of Chiral Indices of Individual Single- And Double-Walled Boron Nitride Nanotubes by Electron Diffraction. *Appl. Phys. Lett.* **2006**, *89* (7). https://doi.org/10.1063/1.2335379.
(83) Arenal, R.; Ferrari, A. C.; Reich, S.; Wirtz, L.; Mevellec, J. Y.; Lefrant, S.; Rubio, A.; Loiseau, A. Raman Spectroscopy of Single-Wall Boron Nitride Nanotubes. *Nano Lett.*

2006, *6* (8), 1812–1816. https://doi.org/10.1021/nl0602544.
(84) Viršek, M.; Jesih, A.; Milošević, I.; Damnjanović, M.; Remškar, M. Raman Scattering of the MoS2 and WS2 Single Nanotubes. *Surf. Sci.* **2007**, *601* (13), 2868–2872. https://doi.org/10.1016/j.susc.2006.12.050.
(85) Damnjanović, M.; Vuković, T.; Milošević, I. Symmetry-Based Study of MoS2 and WS2 Nanotubes. *Isr. J. Chem.* **2017**, *57* (6), 450–460. https://doi.org/10.1002/ijch.201600043.
(86) Xiang, R.; Inoue, T.; Zheng, Y.; Kumamoto, A.; Qian, Y.; Sato, Y.; Liu, M.; Tang, D.; Gokhale, D.; Guo, J.; Hisama, K.; Yotsumoto, S.; Ogamoto, T.; Arai, H.; Kobayashi, Y.; Zhang, H.; Hou, B.; Anisimov, A.; Maruyama, M.; Miyata, Y.; Okada, S.; Chiashi, S.; Li, Y.; Kong, J.; Kauppinen, E. I.; Ikuhara, Y.; Suenaga, K.; Maruyama, S. One-Dimensional van Der Waals Heterostructures. *Science (80-.).* **2020**, *367* (6477), 537–542. https://doi.org/10.1126/science.aaz2570.

4. Observation and Thermodynamic Analysis of Water Filling: the Sealed Ampoule

This chapter has been adapted from "Observation and Thermodynamic Analysis of Partially Water-Filled 1.35 nm and 1.48 nm Diameter Carbon Nanotubes: The Sealed Ampoule," by Samuel Faucher, Matthias Kuehne, Hananeh Oliaei, Rahul Prasanna Misra, Sylvia Xin Li, Ge Zhang, Narayana R. Aluru, and Michael S. Strano. This manuscript was submitted for publication in 2022.

Abstract

Recent measurements of fluids under extreme confinement, including water within narrow carbon nanotubes, exhibit marked deviations from continuum theoretical descriptions. In this work, we generate precise carbon nanotube replicates which are filled with water, sealed from external mass transfer, and studied over a wide temperature range by Raman spectroscopy. We study segments which are empty, partially filled, and completely filled with condensed water from -80 °C to 120 °C. Partially filled, nanodroplet states contain sub-micron vapor-like and liquid-like domains and are analyzed using a Clausius-Clapeyron-type model, yielding water enthalpies of vaporization of 25.0 kJ/mol and 22.1 kJ/mol inside closed 1.35 nm and 1.48 nm diameter carbon nanotubes, lower than the bulk value. Favored partial filling fractions vary between different-sized carbon nanotubes, highlighting the effect of sub-nanometer changes in confining diameter on fluid properties and suggesting the promise of molecular engineering of nanoconfined liquid/vapor interfaces for water treatment or membrane distillation.

4.1 Introduction

The behavior of fluids inside nanoscale pores has important implications for chemical separations,[1,2] water desalination,[3,4] energy storage and conversion devices,[5,6] transport in biological cells,[7] and flow in geologic media.[8] Under extreme levels of confinement inside single digit nanopores, where the characteristic length approaches molecular dimensions, the gap between experimental observation and predictive theory of fluid properties is exceptionally wide.[9] Also, in nanofluidics more broadly, confined multiphase flows – and in particular nanoconfined liquid/vapor interfaces – have outsized importance. For instance, membrane distillation relies on differential transport of vapor and liquid through a nanoporous membrane,[10] nanoscale capillary condensation models are essential for gas recovery from shale and other low-permeability geologic media,[8] cavitation contributes to adsorption/desorption hysteresis inside nanometer-scale pores,[11] and nanoscale vapor gaps may allow ion rejection from water while maintaining high permeability.[12] With few exceptions,[12,13] however, experimental platforms capable of measuring partial filling behavior under nanoconfinement have not been realized. Specifically, inside isolated single-digit nanopores,[9] with confining diameters less than 10 nm, partially filled pores have not been studied as functions of temperature and confining diameter. Such measurements are critical to generating the experimental data to validate much needed theoretical descriptions of fluid thermodynamics under conditions of extreme confinement.

Carbon nanotubes are model nanofluidic systems for studies of extreme confinement, with diameters of atomic precision that can accommodate even single file fluid phases.[14–17] As SDNs, carbon nanotubes exhibit diameter-dependent transport[18] and unique phase behavior[19,20] at the carbon-water interface, with geometric precision that results directly from the graphene lattice. These characteristics make carbon nanotube nanofluidic systems particularly promising for applications involving the water-energy nexus.[21] With respect to transport, individual carbon nanotubes play host to exceptionally fast slip flow, as measured electronically[22] and by optical microscopy of tracer particles[18] under applied hydrostatic pressure. Enhanced flow can be predicted by corrections to Hagen-Poiseuille theory,[23] linking transport results inside isolated carbon nanotubes with less precise but more readily available measurements of membranes and multi-pore systems.[24,25] Thermodynamically, phase boundaries of water inside isolated single-digit carbon nanotubes vary non-monotonically with confining diameter in ways that cannot be explained by existing theories.[19] Finally, recent advances in fabrication of isolated carbon nanotube systems by segmentation of ultra-long carbon nanotubes into shorter segments[26,27] allow comparison between filled and empty segments of the same diameter and chirality carbon nanotube.

Herein, we observe sealed, isolated carbon nanotubes that are empty, completely filled with liquid water, and partially water-filled. Detailed data on partially filled carbon nanotubes supports the observation of temperature-stable sub-micron domains in the axial direction. Raman spectroscopy of carbon nanotube segments over a wide range of temperatures yields the liquid phase filling fraction that can be calculated as a function of temperature, showing thermal hysteresis below room temperature and allowing estimation of thermodynamic properties of water at the nanoscale, including the enthalpy of phase transition between vapor-like and liquid-like states. Favored filling fractions vary among different sized carbon nanotubes, highlighting that sub-nanometer changes in confining diameter can have dramatic effects on fluid structure

and behavior under extreme confinement. The existence of temperature-stable partial filling states has implications for fluid and ion transport through carbon nanotubes and other nanoporous materials, potentially providing avenues to reduce ion permeation while maintaining high permeability toward water and other neutral solutes.

4.2 Results and Discussion

Our study utilizes a previously introduced platform to study isolated, segmented carbon nanotubes (CNTs). [19,26–28] Ultra-long carbon nanotubes were grown on marked silicon substrates by chemical vapor deposition of methane in hydrogen, using a carbon nanotube solution as a catalyst, as reported previously.[19,26,28] CNTs were cut by a focused gallium ion beam to produce segments with lengths from 10 μm to 160 μm. CNTs were then characterized by Raman spectroscopy using a 532 nm laser to estimate diameter and determine fluid filling state (**Figure 4-1**). We observe water-filled, partly filled, and empty CNT segments (**Figure 4-1a**). The Raman radial breathing mode (RBM), an axisymmetric CNT vibrational mode,[29] is known to harden upon fluid filling as the nanotube couples to a higher elastic-modulus fluid phase.[16,30,31] For the substrate-supported CNTs used in this study, we observe an RBM blueshift upon water immersion only for a subset of FIB-cut CNT segments, consistent with stochastic interior filling.[26] We do not observe a blueshift upon water-immersion of as-grown CNTs that are not segmented, suggesting that any fluids that adsorb to the exterior surface of the CNT do so persistently and saturate any RBM shift originating from the exterior CNT wall.[26]

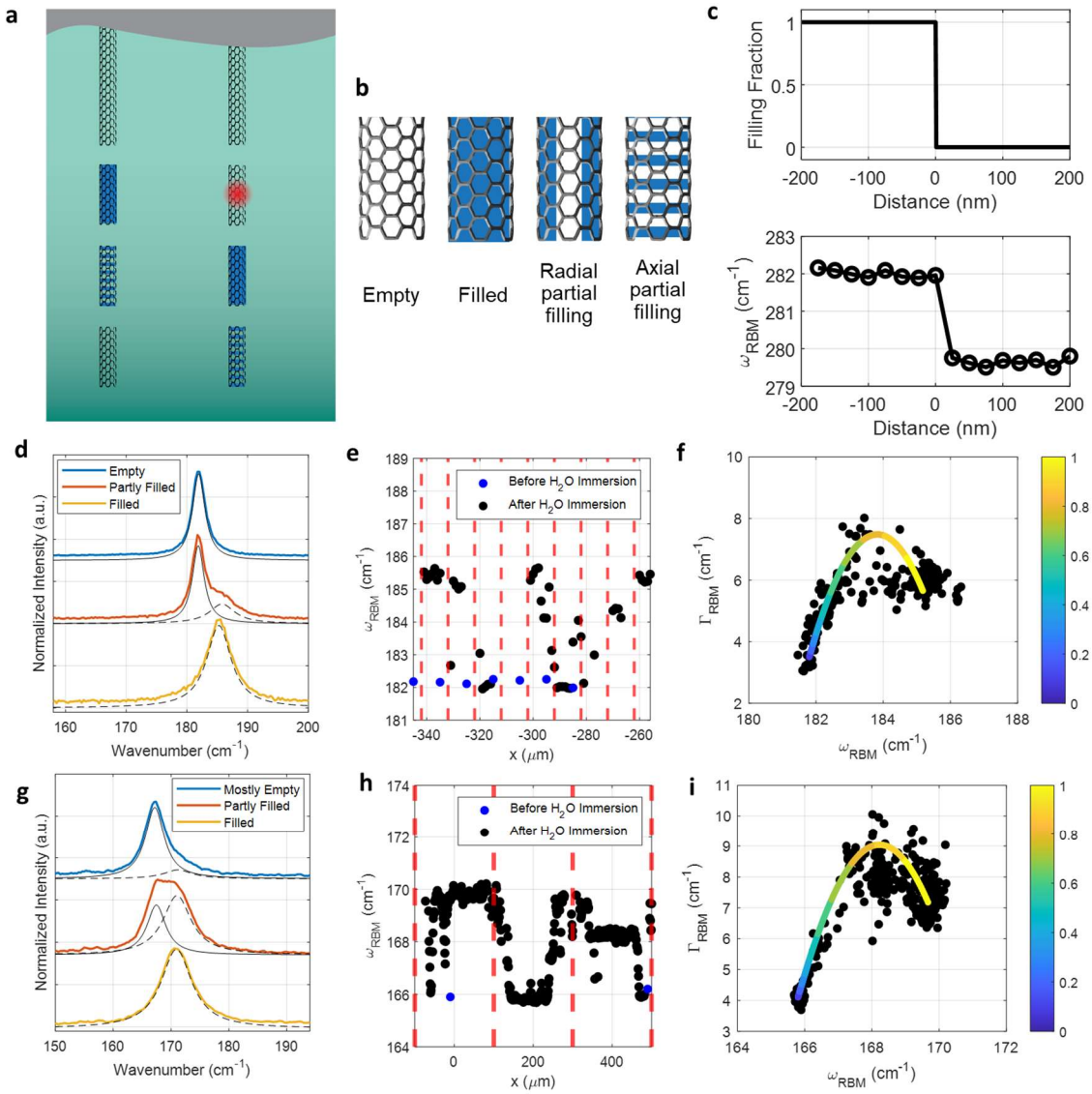

Figure 4-1 | Water-filled, partly filled, and empty carbon nanotube segments. (a) Illustration, not to scale, showing two ultra-long carbon nanotubes. Each carbon nanotube has been cut into several segments, which can be water-filled, partly water-filled, or empty. An illustrated laser spot is focused on one of the segments. (b) Partial filling can be axial or radial in nature; Raman spectroscopy results are indicative of axial partial filling. (c) Molecular dynamics simulations of Raman radial breathing mode (RBM) of a (6,6) CNT with a 200 nm empty domain and a 200 nm filled domain. RBM shifts due to changes in the filling state can be observed at the nanometer scale. (d-f) Raman RBM spectra of empty, partly filled, and filled locations in a 1.35 nm CNT, showing (d) raw spectra, (e) RBM frequency as a function of position along the tube axis for nine 10 µm-long FIB-cut CNT segments, and (f) the frequency versus FWHM of the RBM, confirming that most of the dispersion can be explained by a superposition of different weights of empty and filled peaks. (g-i) Raman RBM spectra of empty, partly filled, and filled locations in a 1.48 nm CNT,

showing (g) raw spectra, (h) RBM frequency as a function of position along the tube axis for three 160 μm-long FIB-cut CNT segments, and (i) frequency versus FWHM of the RBM.

Molecular dynamics simulations predict differences in Raman spectra under different partial filling conditions (**Figure 4-1b**), with the magnitude of the RBM shift upon fluid filling consistent with previous experimental and theoretical work.[16,26,31,32] Using a 280 nm segment of a (6,6) CNT, with a diameter of 0.83 nm, we compute the RBM at 20 nm increments from the autocorrelation of the radial velocity (**Figure 4-1c**).[33,34] The transition from a high-frequency RBM state to a low-frequency RBM state is sharp to below the ~20 nm scale, far less than the ~1 μm spot size of far-field Raman spectroscopy. This shows that the RBM frequency changes locally on the nanometer scale. Homogeneity of fluid filling state within the laser spot, therefore, guarantees a homogeneous, single-peak RBM; conversely, heterogeneity of the RBM demonstrates sub-micron variations in fluid filling. We observe heterogenous partial filling with sub-micron domains in multiple segments of CNTs of two different diameters: 1.48 nm (**Figure 4-1d-f**) and 1.35 nm (**Figure 4-1g-i**). Some locations along the length of the CNT show raw Raman spectra that can be fit by a single, narrow Lorentzian (**Figure 4-1d** and **Figure 4-1g**, blue) and represent empty CNT locations, while others can be fit by a single, broader Lorentzian at higher wavenumber and are assigned as filled (yellow), as in previous work.[19,26] A third class of points, though, consists of superpositions of these two extremes, with visible fits to two Lorentzians (orange). This indicates axial partial filling (**Figure 4-1b**). By contrast, we assign a single-peak, intermediate RBM between the empty and filled states to indicate radial partial filling, in line with analytical models of RBM shifts in the presence of concentric fluid shells.[35] While we may observe radial partial filling in previous experimental work, in the form of RBM shifts upon filling which fall far below spherical packing models for confined fluid density,[26] we do not report radial partial filling here.

Raman lineshapes can be fit with a single Lorentzian or two-peak Lorentzian (Supplementary Information). Fitting Raman spectra with one Lorentzian as a function of position along the length of multiple segments, we observe CNT locations at low wavenumber (empty) and high wavenumber (filled) with largely independent filling of discrete CNT segments, in line with previous experimental results,[26] as well as weight at intermediate wavenumber consistent with partial filling (**Figure 4-1e** and **Figure 4-1h**). In order to assess RBM behavior relative to filled and empty states, we fit all spectra to a single Lorentzian and plot the peak position, ω_{RBM}, and full-width half maximum, Γ_{RBM}, as shown (**Figure 4-1f** and **Figure 4-1i**). The apparent location of a single Lorentzian fit to the sum of different weights of fixed empty and filled Lorentzians is shown. Since the data cluster near the colored curve, we conclude that a large majority of variation in observed RBM behavior can be explained as varying weights – or filling fractions – of one empty and one filled state.

A linear elastic shell model for CNTs provides a description of the RBM frequency in terms of physical parameters.[32,35,36] The terahertz time-dependent displacement of the CNT wall, w(t), follows:

$$\frac{\partial^2 w}{\partial t^2} = -\left(\frac{Eh}{\rho h(1-\nu^2)R^2} + \frac{24K}{s_0^2 \rho h} + \frac{c_{sub}}{\rho h}\right) w \qquad [4.1]$$

where w is displacement, t is time, E is Young's modulus, h is wall thickness, ρ is mass density, ν is Poisson's ratio, K is the Lennard-Jones interaction parameter between a fluid and a CNT shell, s_0 is the fluid-CNT interaction distance, and c_{sub} is the coupling to an exterior substrate. From this, one can calculate the RBM frequency:

$$\omega_{RBM} = \sqrt{\frac{Eh}{\rho h(1-\nu^2)R^2} + \frac{24K}{s_0^2 \rho h} + \frac{c_{sub}}{\rho h}} \quad [4.2]$$

The substrate interaction c_{sub} is calculated as 91.8 N m^{-1} nm^{-2},[37] allowing a determination of the CNT diameter from the empty RBM frequency, using values of $E = 360\ J/m^2$, $h = 0.34\ nm$, $\rho = 2270\ kg/m^3$, and $\nu = 0.16$.[35] The diameters as determined by this model are similar to fits to empirical models (Supplementary Information).[38]

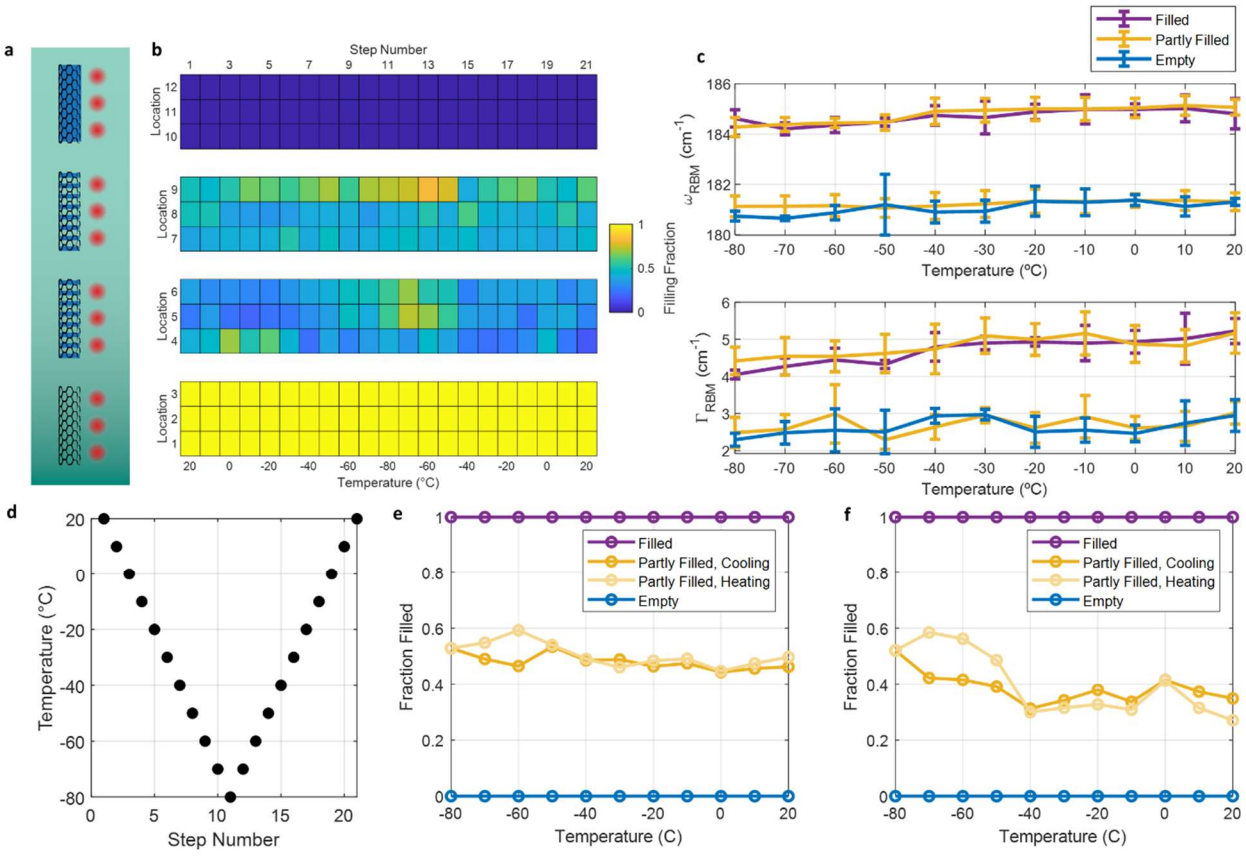

Figure 4-2 | Temperature stability of partial water filling and thermal filling hysteresis inside a 1.35 nm diameter CNT. (a) Schematic showing observation of 12 locations, at 2 μm pitch, on four non-adjacent 10 μm CNT segments. (b) Filling fraction as a function of temperature and location, showing one filled segment, two partly filled segments, and one empty segment. (c) Mean and standard deviations of RBM frequency and full-width half maximum for the three filled locations, three empty, locations, and six partly filled locations. Partial filling is a superposition of empty and filled vibrational states at all temperatures. (d) Temperature treatment of the sample. (e-f) Fractional filling of the two partly filled CNT

segments as a function of temperature, both shown with empty and filled segments for comparison. The filling fraction changes slightly with temperature, with thermal hysteresis at lower temperatures.

We report variations of filled, partly filled, and empty CNT segments with changes in temperature (**Figure 4-2** and **Figure 4-3**), including broad temperature stability of partly filled segments with differences in filling fraction upon cooling and heating. We determine the filling fraction, f, by the relative intensities of the two peaks in a two-peak Lorentzian fit:

$$f = \frac{I_2}{I_1 + I_2} \quad [4.3]$$

In actuality, fluid filling induces changes in CNT electronic transitions which affect the Raman resonance condition,[39,40] potentially affecting the linearity between RBM peak intensity and fractional filling. While there are differences in mean intensity between entirely filled and entirely empty CNT segments (**Figure 4-5**), this effect is neglected here. First we observe 12 locations in four 10 μm segments of a 1.35 nm CNT (shown schematically in **Figure 4-2a**) with a likely chirality[41] of (12,8) at temperatures from 20 °C to -80 °C and back (**Figure 4-2d**), with intra-segment spacing of 2 μm. One segment appears entirely empty at all temperatures (**Figure 4-2b**, Locations 10-12). One segment remains entirely filled with water at all temperatures (Locations 1-3). However, two segments show what we assign as partial filling after FIB and water immersion treatment at all temperatures (Locations 4-6 and 7-9). At each temperature, the partly filled spectra are superpositions of filled and empty spectra (**Figure 4-2c**). The filled and empty RBM positions are largely invariant with temperature within experimental error, but there is slight RBM broadening with increasing temperature in both filled and empty modes. Temperature-dependent RBM linewidth broadening is a result of anharmonic processes and phonon scattering, though the magnitude of this effect is constrained by the high Debye temperature of CNTs.[44] We then analyze the mean filling fraction for each of the four segments as a function of temperature (**Figure 4-2e-f**). While there are changes in filling fraction with temperature, the system returns to the same filling fraction after temperature cycling in dry air; we conclude from this that the CNT segments are likely closed systems which behave like "sealed ampoules". It remains unclear whether carbonaceous debris or dangling bonds at the segment ends are responsible for the reseal after opening. We have observed instances of tubes that remain persistently open after FIB processing, and the study of these open systems will be the subject of a future study.

We observe thermal hysteresis at low temperature in the partly filled segments; the filling fraction at low temperature upon cooling is lower than the filling fraction upon heating, showing non-equilibrium path dependence in the distribution of liquid and vapor in the CNT (**Figure 4-2e-f**). Water sorption hysteresis inside nanopores is commonly associated with capillary condensation,[45–49] and has been observed inside nanoporous materials for reasons attributable to both fluid adsorption thermodynamics and pore mouth/pore network effects.[49] In 2D and 3D systems, the surface tension cost of a phase boundary scales with the size of the domain; this is not true in quasi-1D systems like carbon nanotubes.[50] This means that there is no driving force toward complete phase separation, explaining the persistence of nanodroplet states over a broad range of temperatures. Experiments and simulations of liquid-vapor phase transitions and liquid-liquid phase transitions in nanopores show alternating domains with a characteristic size that

decreases with temperature.[50,51] Even at low temperature, however, liquid and vapor domain sizes must remain smaller than the ~1 μm laser spot, since Raman observations show partial filling states across all studied temperatures.

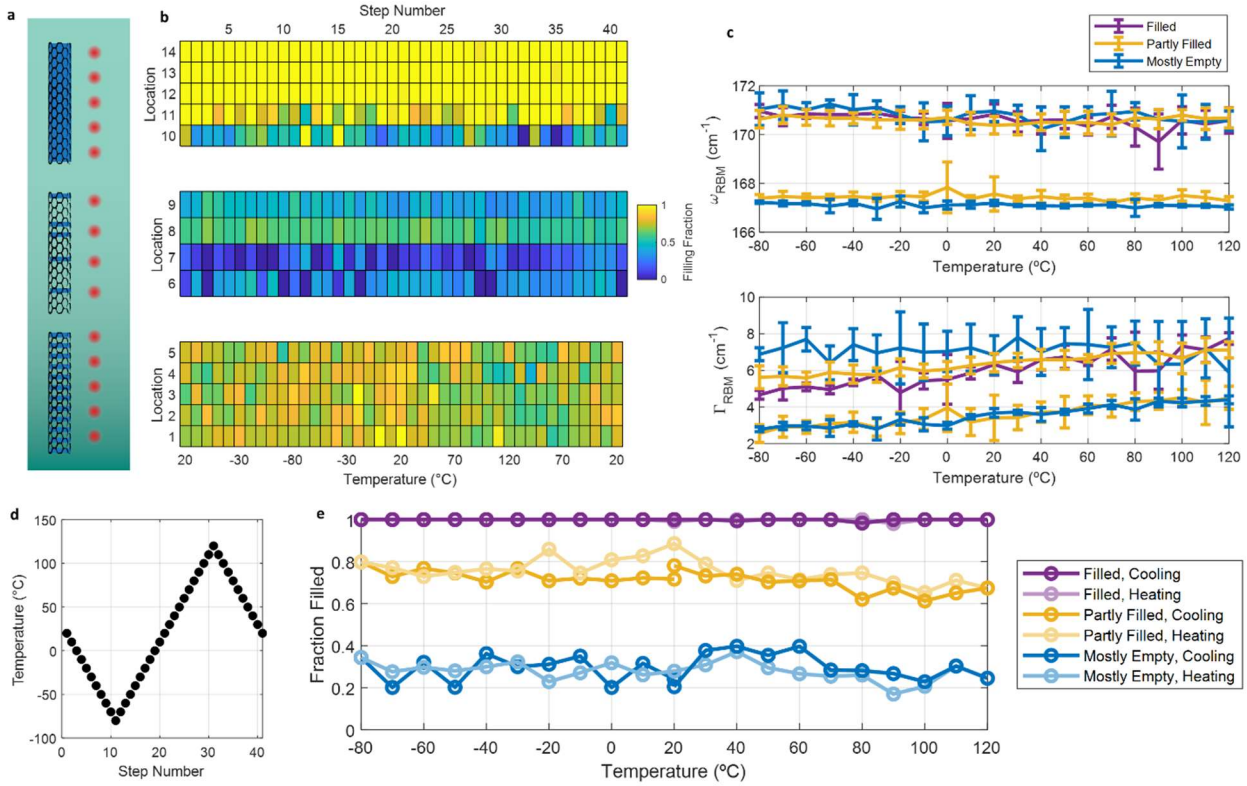

Figure 4-3 | Temperature stability of partial water filling and thermal filling hysteresis inside a 1.48 nm CNT. (a) Schematic showing observation of 11 locations, at 30 μm pitch, on three adjacent 160 μm CNT segments. (b) Filling fraction as a function of temperature and location, showing one filled segment, one partly filled segment, and one largely empty segment. (c) Mean and standard deviations of RBM frequency and full-width half maximum for three mostly empty locations (locations 6,7 and 9), five partly filled locations (locations 1-5), and three filled locations (locations 12-14). Partial filling is a superposition of empty and filled vibrational states at all temperatures. (d) Temperature treatment of the sample. (e) Fractional filling of the partly filled CNT segment as a function of temperature, with filled segment and mostly empty segment for comparison. The filling fraction changes slightly with temperature, with thermal hysteresis at intermediate temperatures.

Temperature-dependent behavior of multiple segments of a different carbon nanotube with a diameter of 1.48 nm and likely chirality[41] of (12,10) shows qualitatively similar partial filling behavior to that in a 1.35 nm CNT (**Figure 4-3**). Fourteen locations on three 160 μm carbon nanotube segments (**Figure 4-3a**) were studied at temperatures below and above ambient temperature (**Figure 4-3d**), with 30 μm spacing within segments. One largely filled segment, one largely empty segment, and one partly filled segment were observed. Negative correlations in filling fraction between neighboring locations in the same segment (for instance, Location 6 and 7 from Step Number 10 to 20) are indicative of diffusion between higher and lower

concentration regions between successive temperature measurements (**Figure 4-3b**). As in the case of the 1.35 nm diameter CNT (**Figure 4-2**), partial filling is a superposition of filled and empty states, RBM position does not vary substantially with temperature but linewidth does broaden at higher temperature (**Figure 4-3c**), and a phase transition is observed between vapor-like and liquid-like states in an apparently closed system (**Figure 4-3e**). We detect hysteresis in filling fraction inside partly filled CNTs, though at intermediate temperatures and not at low temperatures as observed in the 1.35 nm diameter CNT. The stability of the two-phase region over the temperature range -80 °C to 120 °C indicates non-bulklike liquid and vapor behavior and diverges from previously published work.[19] Previous work from our group investigating water inside carbon nanotubes, including a 1.44 nm diameter CNT, shows transitions from a completely empty state, to a liquid-like state, to a further blueshifted, solid-like state, within the temperature range studied here.[19] We attribute the lack of complete emptying or filling – even at -80 °C and 120 °C – to the closed nature of the system, as best observed at multiple locations along the length of the CNT.

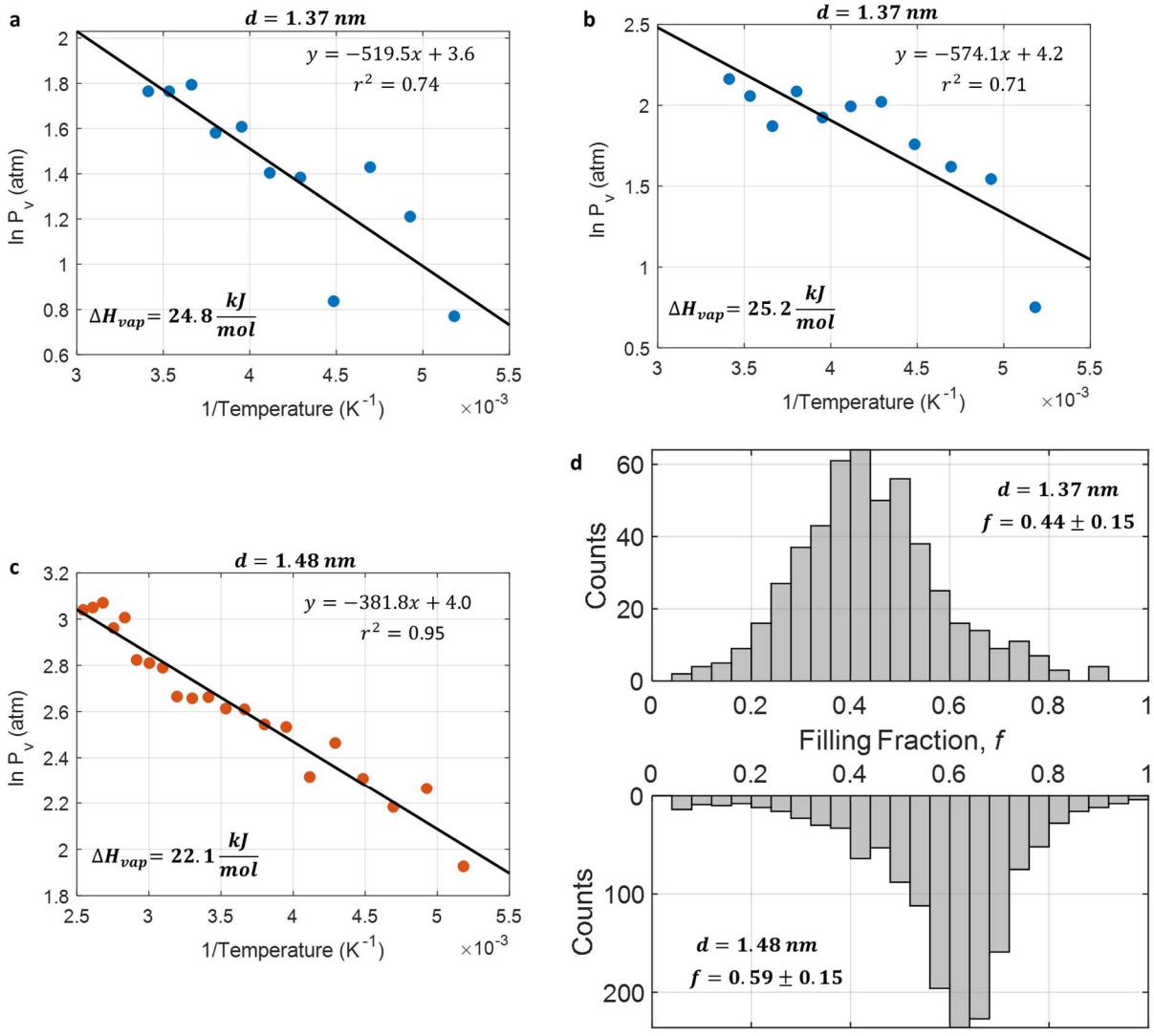

Figure 4-4 | (a-b) The enthalpy of vaporization of water confined within two partly filled segments of a 1.35 nm diameter CNT can be calculated by fitting to a Clausius-Clapeyron type equation, with plots of natural log of the vapor pressure versus inverse temperature shown. The estimated enthalpies of vaporization, 24.8 kJ/mol and 25.2 kJ/mol, are lower than the enthalpy of vaporization of bulk water. (c) Natural log of pressure versus inverse temperature inside a 1.48 nm diameter CNT. The enthalpy of vaporization in this system is 22.1 kJ/mol. (d) Observed partial filling states for 1.35 and 1.48 nm diameter CNTs across all temperatures. The favored filling fraction is substantially different between the two, showing the effect of confining diameter on partial fluid filling.

Experimental observations by Raman spectroscopy are consistent with the coexistence of a liquid-like state and a vapor-like state inside a closed system. Next, we develop a simple thermodynamic model based on the Clausius-Clapeyron equation to calculate the enthalpy of phase change between vapor-like and liquid-like states, with values lower than the bulk enthalpy of vaporization of water (**Figure 4-4**). Simulations show that there are multiple potential intra-pore phase transitions among adsorbed, vapor, and bulk-like phases as a function of pore hydrophobicity and pore size.[45,47] Nonetheless, we consider a simple liquid-vapor phase transition model to extract thermodynamic parameters. Assuming that the CNT contains only water, which can be in a bulk-like liquid state or ideal gas state, then:

$$n_{tot} = \rho_L V_L + \frac{P_V V_V}{RT} \quad [4.4]$$

where n_{tot} is total number of moles of water in the closed system. The filling fraction can be expressed as $f = V_L/V$, and defining a total molar filling fraction $\eta = n_{tot}/(\rho_L V)$ allows the expression of the vapor pressure as:

$$P_V(T) = \frac{RT\rho_L}{1-f}(\eta - f) \quad [4.5]$$

The vapor pressure can be related to the enthalpy of phase change by the confined fluid Clausius-Clapeyron Equation, which considers the effect of curvature on vapor pressure according to the expression:[52,53]

$$\ln P_V(T) = -\left[\frac{\Delta H_{vap}}{R} - \frac{2vT}{r}\frac{d\gamma}{dT}\right]\frac{1}{T} + C \quad [4.6]$$

where ΔH_{vap} is the enthalpy of vaporization, v is the liquid molar volume, and γ is the liquid-vapor surface tension. We estimate $d\gamma/dT$ across a broad temperature range as -0.16 mN/(m K),[54] a bulk liquid water density of $\rho_L = 997\ kg/m^3$, and assume a value of η for each of the three data sets from the maximum observed filling fraction from the heating cycle. Plotting as $\ln P_V$ versus $1/T$ (**Figure 4-4a-c**), we calculate enthalpies of vaporization of 24.8 kJ/mol and 25.2 kJ/mol for the two partly filled segments of the 1.35 nm diameter CNT, and 22.1 kJ/mol for the 1.48 nm diameter CNT. These are lower than the enthalpy of vaporization of bulk water (40.65 kJ/mol) but higher than its enthalpy of fusion (6.00 kJ/mol).[55] Note that the confined fluid Clausius-Clapeyron Equation decouples the role of the curvature and the enthalpy of vaporization on the vapor pressure (see Eq. 6). Therefore, the reduction in enthalpy of

vaporization is reflective of confinement-induced changes in the thermodynamic properties of water molecules. This low enthalpy of phase change could indicate weak hydrogen bonding under extreme confinement, particularly for water at the water-carbon interface.[45,56] Finally, we record histograms for the observed filling fraction inside 1.35 and 1.48 nm CNTs (**Figure 4-4d**). The difference in most commonly observed filling fraction between the two diameters highlights the possibility of controlling interfacial transport or tuning nanodroplet domain size with only angstrom changes in confining diameter.

In this paper, we demonstrate the existence of partly filled, closed carbon nanotubes as observed by Raman spectroscopy. Through growth and FIB segmentation of ultra-long CNTs, we observe empty, filled, and partially filled segments of CNTs with diameters of 1.35 and 1.48 nm. Partly filled, nanodroplet states have liquid-like and vapor-like domains with scales far below the Raman laser spot size (~1 μm) which are stable over a broad range of temperatures (-80 °C to 120 °C). While the empty and fluid-filled vibrational states do not change appreciably with temperature, their relative weight does, in agreement with a liquid-vapor phase transition inside a closed system. Thermal hysteresis suggests non-equilibrium, metastable trapping of nanoscale vapor-like and liquid-like domains, in agreement with theory and previous experimental results inside quasi-1D systems. Applying a confined fluid Clausius-Clapeyron-type model which accounts for curvature-dependent effects, we extract enthalpies of phase change of 25.0 kJ/mol inside a 1.35 nm diameter CNT and 22.1 kJ/mol inside a 1.48 nm diameter CNT that are below the bulk enthalpy of vaporization, likely because of changes in the hydrogen bond structure under confinement.

Finally, transport across a nanoscale liquid/vapor interface offers engineering possibilities that transport within a single phase material does not.[12] Engineering partly filled nanopore systems with particular nanodroplet domain sizes and filling fractions may be possible by tuning pore diameter and by chemical functionalization to change the strength of the pore-fluid interaction. Future work will include measuring flux of pure liquids and ions through fully filled and partly filled carbon nanotube segments, and the exploration of patterns and mechanisms for the variation of favored partial filling states with pore diameter.

4.3 Supplementary Information

4.3.1 Methods

Sample Fabrication: Ultra-long, isolated carbon nanotubes were grown by chemical vapor deposition on marked silicon substrates as reported previously with slight changes.[1–4] Custom silicon substrates with dimensions 9 mm by 14 mm were prepared with identifiable lithographic marks on a 200 μm grid. A small volume, typically 0.7 μL, of APT 25 series carbon nanotube solution (Nano-C) was deposited as a catalyst solution on each marked silicon wafer. CNTs were grown by methane chemical vapor deposition in hydrogen at 970 °C for 45 minutes, producing ultra-long carbon nanotubes with diameters from 0.6 nm to 3 nm and lengths up to 1 cm. A dual-beam FIB/SEM instrument (FEL Helios 600i) was used to segment CNTs of interest into segments of lengths ranging from 10 μm to 160 μm. Segmentation was performed with a focused gallium ion beam (30 kV, 9 pA, 5 μs dwell time, 100 passes). Care was taken to avoid exposure of the rest of the CNT to the Ga^+ beam, and of the entire CNT to the electron beam. Ultra-pure (ASTM Type II) water was used for water immersion.

Raman spectroscopy: Samples were then observed by confocal micro-Raman spectroscopy (Horiba LabRAM HR Evolution with Invictus 100 mW 532 nm laser, grating 1800 gr/mm, hole 500 μm, slit 150 μm, Olympus MPLFLN 50X air objective) in air after water immersion, as shown in the illustration. The Raman instrument is set up in a backscattering geometry, with linear polarization of the incident laser along the nanotube axis. Temperature measurements were done under dry air flow using a sealed temperature stage with a liquid nitrogen pump (Linkam Scientific THMS350EV with LNP95). CNTs were identified based on their characteristic Raman scattering response. We selected for CNTs with a single RBM resonant at 532 nm excitation.

There are various relationships between RBM frequency and diameter. We can compare the elastic shell model discussed in the main text to the empirical model by Zhang et al[5] for single-walled carbon nanotubes supported in silicon substrates:

$$\omega_{RBM}(cm^{-1}) = \frac{235.9}{d\ (nm)} + 5.5 \qquad [4.7]$$

The difference in estimated diameter (1.35 nm versus 1.34 nm from Zhang et al[5], and 1.48 nm versus 1.46 nm) is no more than 2%. We generated best estimates of the (n,m) chiralities of the 1.35 nm CNT and 1.48 nm CNT – (12,8) and (12,10), respectively – using the Kataura plot from Saito et al.[6] by minimizing both the error in the resonance condition between the 532 nm excitation and an electronic transition in candidate chiralities and the error in calculated diameter. Using these chirality assignments, it is possible to back-calculate the substrate interactions c_{sub} on a sample by sample basis, which are calculated as $c_{sub} = 114.8\ N\ m^{-1}nm^{-2}$ for the 1.35 nm CNT and $c_{sub} = 104.4\ N\ m^{-1}nm^{-2}$ for the 1.48 nm CNT. These are similar to the value of $c_{sub} = 91.8\ N\ m^{-1}nm^{-2}$ from Jorio et al[7] as provided in the main text, confirming that the diameter and chirality assignments are self-consistent and likely accurate. The fluid-CNT interaction parameter[8] is on the order of $K \approx 0.5\ kJ/mol$ and the fluid-CNT distance is $s_0 \approx 0.35\ nm$, resulting in comparable shifts from the substrate effect and from the interior fluid.

Lorentzian fitting: Raman lineshapes can be fit to a single Lorentzian:[9]

$$y = \frac{2\Gamma I/\pi}{(x-\omega)^2+4\Gamma^2} + C \quad [4.8]$$

with intensity I (counts), peak center ω (cm^{-1}), and full-width half maximum (FWHM) Γ (cm^{-1}), and a flat background C. Raman lineshapes under conditions of partial filling can be fit to a two-peak Lorentzian:

$$y = \frac{2\Gamma_1 I_1/\pi}{(x-\omega_1)^2+4{\Gamma_1}^2} + \frac{2\Gamma_2 I_2/\pi}{(x-\omega_2)^2+4{\Gamma_2}^2} + C \quad [4.9]$$

with two peak intensities I_1 and I_2, peak locations ω_1 and ω_2, and FWHMs Γ_1 and Γ_2 for peak 1 (empty) and blueshifted peak 2 (filled).

Molecular dynamics: Molecular dynamics simulations were performed to calculate RBM frequencies along the length of a CNT that was partly filled and partly empty. Covalent carbon-carbon interactions in the CNT were modeled with the adaptive intermolecular reactive bond order (AIREBO) potential.[10,11] The TIP4P/2005 model was used for water.[12] The LAMMPS package[13] was used with a Verlet algorithm,[14] with a time step of 0.5 fs and a cutoff of 12 Å for short-range interactions. The average radial velocity of the CNT was calculated, and the Fourier transform of the radial velocity autocorrelation yields the power spectra density, which determines the frequency of the RBM.

4.3.2 Change of Raman RBM Intensity

Fluid filling may change CNT electronic structure, affecting the Raman resonance condition and increasing or decreasing the intensity of the RBM mode upon fluid filling. **Figure 4-5** shows the distribution and mean intensity of the RBM mode in the two CNTs studied. In the 1.35 nm CNT, fluid filling decreases RBM intensity, while in the 1.48 nm CNT, fluid filling increases RBM intensity. While the filling fraction f could be calculated by scaling to these mean intensities, we choose not to do this but instead to calculate filling fraction from the direct ratio of weighted intensities in a two-Lorentzian fit. This approach neglects changes in CNT resonance upon fluid filling/emptying, but does not bias the results by taking into account differences in intensity that are unrelated to scattering cross-section but rather to sample focus and laser placement.

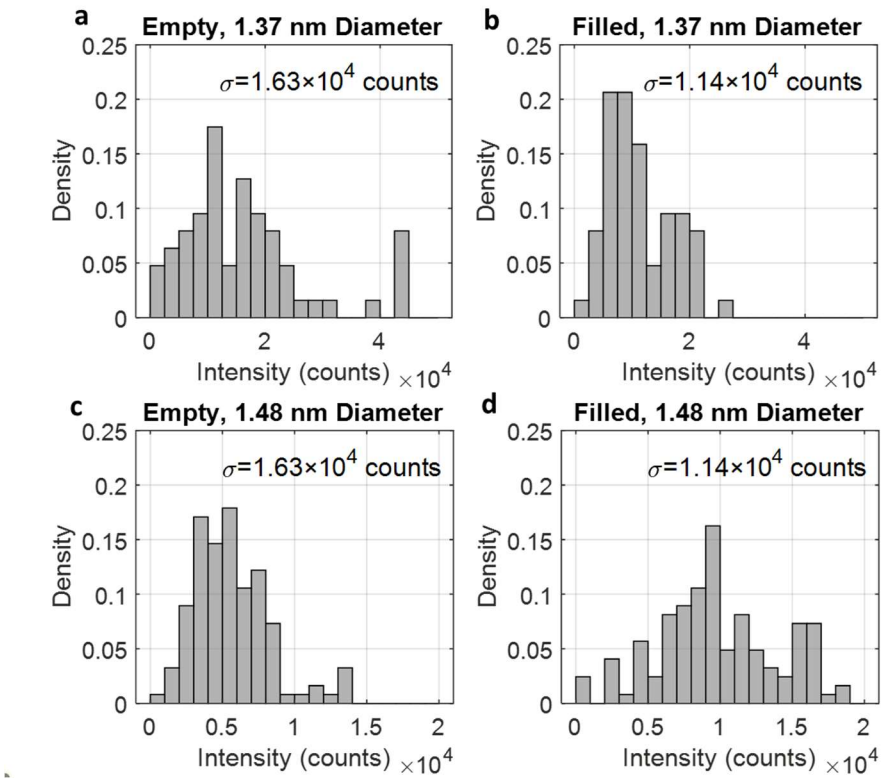

Figure 4-5 | RBM intensity in entirely empty and entirely filled spectra of 1.35 and 1.48 nm diameter carbon nanotubes.

4.3.3 Effect of laser heating

The effect of laser heating on the temperature can be estimated by the Raman G band, which is known to vary with temperature. The G band is shown versus temperature at fixed laser power:

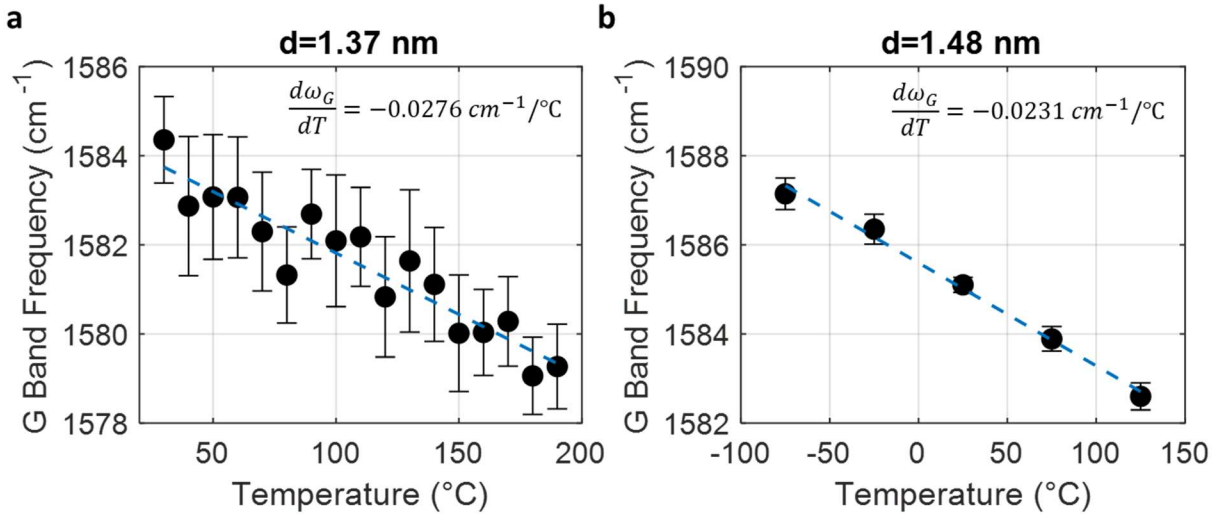

Figure 4-6 | G band frequency versus temperature at fixed laser power. The G band under low and high laser power provides an estimate of the degree of laser heating. Under these conditions, laser heating can be disregarded.

Heterogeneity of G band with position along the CNT explains the large error bars in the 1.35 nm CNT, while the G band is more homogenous on the case of the 1.48 nm CNT. At the laser power used for observation of partly filled segments of the 1.35 nm CNT (2.93 mW) and 1.48 mW CNT (24.91 mW), the difference in G band position under this laser power and very low laser power (276 μW) can be calculated (1.35 nm: $\Delta\omega_G = -0.06 \pm 0.08\ cm^{-1},\ n = 4$, and 1.48 nm: $\Delta\omega_G = -0.29 \pm 0.10\ cm^{-1},\ n = 3$) and the magnitude of laser-heating at ambient conditions can be estimated (1.35 nm: 2.3 ± 3.0 ℃, 1.48 nm: 12.4 ± 4.1 ℃) given the G band temperature sensitivity from **Figure 4-5**. Given the low magnitude of laser-induced heating and its uncertainty, laser heating is neglected in the analysis of phase behavior inside partly filled carbon nanotubes, as discussed in the main text.

In principle, the RBM has also been observed to redshift with increasing temperature[15,16] as a result of C-C bond softening and, to a lesser degree, CNT radial thermal expansion,[15] with a temperature dependence on the order of -0.005 cm^{-1}/K to -0.01 cm^{-1}/K.[15,16] The magnitude of this effect, however, is dependent on bundling and substrate effects, and is not observed here.

4.4 References

1. Gin, D. & Noble, R. Designing the Next Generation of Chemical Separation Membranes. *Science (80-.).* **332**, 674–676 (2011).
2. Qu, H. *et al.* Selective filling of n-hexane in a tight nanopore. *Nat. Commun.* **12**, 1–8 (2021).
3. Werber, J. R., Osuji, C. O. & Elimelech, M. Materials for next-generation desalination and water purification membranes. *Nat. Rev. Mater.* **1**, (2016).
4. Joshi, R. K. *et al.* Precise and ultrafast molecular sieving through graphene oxide membranes. *Science (80-.).* **343**, 752–754 (2014).
5. Siria, A. *et al.* Giant osmotic energy conversion measured in a single transmembrane boron nitride nanotube. *Nature* **494**, 455–458 (2013).
6. Gao, J., Feng, Y., Guo, W. & Jiang, L. Nanofluidics in two-dimensional layered materials: Inspirations from nature. *Chem. Soc. Rev.* **46**, 5400–5424 (2017).
7. Borgnia, M., Nielsen, S., Engel, A. & Agre, P. Cellular and Molecular Biology of the Aquaporin Water Channels. *Annu. Rev. Biochem.* **68**, 425–458 (1999).
8. Barsotti, E., Tan, S. P., Saraji, S., Piri, M. & Chen, J. H. A review on capillary condensation in nanoporous media: Implications for hydrocarbon recovery from tight reservoirs. *Fuel* **184**, 344–361 (2016).
9. Faucher, S. *et al.* Critical Knowledge Gaps in Mass Transport through Single-Digit Nanopores: A Review and Perspective. *J. Phys. Chem. C* **123**, 21309–21326 (2019).
10. Lawson, K. W. & Lloyd, D. R. Membrane distillation. *J. Memb. Sci.* **124**, 1–25 (1997).
11. Rasmussen, C. J. *et al.* Cavitation in metastable liquid nitrogen confined to nanoscale pores. *Langmuir* **26**, 10147–10157 (2010).
12. Lee, J., Laoui, T. & Karnik, R. Nanofluidic transport governed by the liquid/vapour interface. *Nat. Nanotechnol.* **9**, 317–323 (2014).
13. Duan, C., Karnik, R., Lu, M. C. & Majumdar, A. Evaporation-induced cavitation in nanofluidic channels. *Proc. Natl. Acad. Sci. U. S. A.* **109**, 3688–3693 (2012).
14. Berezhkovskii, A. & Hummer, G. Single-file transport of water molecules through a carbon nanotube. *Phys. Rev. Lett.* **89**, 064503/1-064503/4 (2002).
15. Zuo, G., Shen, R., Ma, S. & Guo, W. Transport properties of single-file water molecules inside a carbon nanotube biomimicking water channel. *ACS Nano* **4**, 205–210 (2010).
16. Cambré, S. *et al.* Experimental observation of single-file water filling of thin single-wall carbon nanotubes down to chiral index (5,3). *Phys. Rev. Lett.* **104**, 1–4 (2010).
17. Ma, X., Cambré, S., Wenseleers, W., Doorn, S. K. & Htoon, H. Quasiphase Transition in a Single File of Water Molecules Encapsulated in (6,5) Carbon Nanotubes Observed by Temperature-Dependent Photoluminescence Spectroscopy. *Phys. Rev. Lett.* **118**, (2017).
18. Secchi, E. *et al.* Massive radius-dependent flow slippage in carbon nanotubes. *Nature* **537**, 210–213 (2016).
19. Agrawal, K. V. *et al.* Observation of extreme phase transition temperatures of water confined inside isolated carbon nanotubes. *Nat. Nanotechnol.* **12**, 267–273 (2017).
20. Shimizu, S. *et al.* Understanding and Analyzing Freezing-Point Transitions of Confined Fluids within Nanopores. *Langmuir* **31**, 10113–10118 (2015).
21. Bocquet, L. Nanofluidics coming of age. *Nat. Mater.* **19**, 254–256 (2020).
22. Qin, X., Yuan, Q., Zhao, Y., Xie, S. & Liu, Z. Measurement of the Rate of Water

Translocation through Carbon Nanotubes. *Nano Lett.* **11**, 2173–2177 (2011).
23. Heiranian, M. & Aluru, N. R. Nanofluidic Transport Theory with Enhancement Factors Approaching One. *ACS Nano* **14**, 272–281 (2020).
24. Holt, J. K. *et al.* Fast mass transport through sub-2-nanometer carbon nanotubes. *Science* **312**, 1034–7 (2006).
25. Majumder, M., Chopra, N. & Hinds, B. J. Mass Transport through Carbon Nanotube Membranes in Three Different Regimes: Ionic Diffusion and Gas and Liquid Flow. *ACS Nano* **5**, 3867–3877 (2011).
26. Faucher, S. *et al.* Diameter Dependence of Water Filling in Lithographically Segmented Isolated Carbon Nanotubes. *ACS Nano* **15**, 2778–2790 (2021).
27. Kuehne, M. *et al.* Impedance of Thermal Conduction from Nanoconfined Water in Carbon Nanotube Single-Digit Nanopores. *J. Phys. Chem. C* **125**, 25717–25728 (2021).
28. Choi, W. *et al.* Diameter-dependent ion transport through the interior of isolated single-walled carbon nanotubes. *Nat. Commun.* **4**, 1–8 (2013).
29. Dresselhaus, M., Dresselhaus, G., Saito, R. & Jorio, K. Raman spectroscopy of carbon nanotubes. *Phys. Rep.* **49**, 47–99 (2005).
30. Wenseleers, W., Cambré, S., Čulin, J., Bouwen, A. & Goovaerts, E. Effect of water filling on the electronic and vibrational resonances of carbon nanotubes: Characterizing tube opening by Raman spectroscopy. *Adv. Mater.* **19**, 2274–2278 (2007).
31. Fagan, J. A. *et al.* Separation of empty and water-filled single-wall carbon nanotubes. *ACS Nano* **5**, 3943–3953 (2011).
32. Longhurst, M. J. & Quirke, N. The environmental effect on the radial breathing mode of carbon nanotubes in water. *J. Chem. Phys.* **124**, 234708 (2006).
33. Plimpton, S. Fast Parallel Algorithms for Short-Range Molecular Dynamics. *J. Comput. Phys.* **117**, 1–19 (1995).
34. Wu, Y. & Aluru, N. R. Graphitic Carbon–Water Nonbonded Interaction Parameters. *J. Phys. Chem. B* **117**, 8802–8813 (2013).
35. Longhurst, M. J. & Quirke, N. The environmental effect on the radial breathing mode of carbon nanotubes. II. Shell model approximation for internally and externally adsorbed fluids. *J. Chem. Phys.* **125**, 184705 (2006).
36. Wang, C. Y., Ru, C. Q. & Mioduchowskl, A. Applicability and limitations of simplified elastic shell equations for carbon nanotubes. *J. Appl. Mech. Trans. ASME* **71**, 622–631 (2004).
37. Jorio, A., Saito, R., Dresselhaus, G. & Dresselhaus, M. S. *Raman Spectroscopy in Graphene Related Systems*. *Raman Spectroscopy in Graphene Related Systems* (John Wiley & Sons, 2011). doi:10.1002/9783527632695.
38. Zhang, D. *et al.* (n,m) Assignments and quantification for single-walled carbon nanotubes on SiO2/Si substrates by resonant Raman spectroscopy. *Nanoscale* **7**, 10719–10727 (2015).
39. Campo, J. *et al.* Enhancing single-wall carbon nanotube properties through controlled endohedral filling. *Nanoscale Horizons* **1**, 317–324 (2016).
40. Campo, J. *et al.* Optical Property Tuning of Single-Wall Carbon Nanotubes by Endohedral Encapsulation of a Wide Variety of Dielectric Molecules. *ACS Nano* **15**, 2301–2317 (2021).
41. Saito, R., Hofmann, M., Dresselhaus, G., Jorio, A. & Dresselhaus, M. S. Raman spectroscopy of graphene and carbon nanotubes. *Adv. Phys.* **60**, 413–550 (2011).

42. Raravikar, N. R. *et al.* Temperature dependence of radial breathing mode Raman frequency of single-walled carbon nanotubes. *Phys. Rev. B - Condens. Matter Mater. Phys.* **66**, 1–9 (2002).
43. Zhou, Z. *et al.* Temperature dependence of the Raman spectra of individual carbon nanotubes. *J. Phys. Chem. B* **110**, 1206–1209 (2006).
44. Jorio, A. *et al.* Linewidth of the Raman features of individual single-wall carbon nanotubes. *Phys. Rev. B - Condens. Matter Mater. Phys.* **66**, 1154111–1154118 (2002).
45. Brovchenko, I., Geiger, A. & Oleinikova, A. Water in nanopores. I. Coexistence curves from Gibbs ensemble Monte Carlo simulations. *J. Chem. Phys.* **120**, 1958–1972 (2004).
46. Brovchenko, I. & Oleinikova, A. Effect of Pore Size on the Condensation/Evaporation Transition of Confined Water in Equilibrium with Saturated Bulk Water. *J. Phys. Chem. B* **115**, 9990–10000 (2011).
47. De La Llave, E., Molinero, V. & Scherlis, D. A. Water filling of hydrophilic nanopores. *J. Chem. Phys.* **133**, (2010).
48. De La Llave, E., Molinero, V. & Scherlis, D. A. Role of confinement and surface affinity on filling mechanisms and sorption hysteresis of water in nanopores. *J. Phys. Chem. C* **116**, 1833–1840 (2012).
49. Findenegg, G. H., Jähnert, S., Akcakayiran, D. & Schreiber, A. Freezing and melting of water confined in silica nanopores. *ChemPhysChem* **9**, 2651–2659 (2008).
50. Gelb, L. D. & Gubbins, K. E. Liquid-liquid phase separation in cylindrical pores: Quench molecular dynamics and Monte Carlo simulations. *Phys. Rev. E - Stat. Physics, Plasmas, Fluids, Relat. Interdiscip. Top.* **56**, 3185–3196 (1997).
51. Gelb, L. D. & Müller, E. A. Location of phase equilibria by temperature-quench molecular dynamics simulations. *Fluid Phase Equilib.* **203**, 1–14 (2002).
52. Koutsoyiannis, D. Clausius-Clapeyron equation and saturation vapour pressure: Simple theory reconciled with practice. *Eur. J. Phys.* **33**, 295–305 (2012).
53. Tan, S. P. & Piri, M. Heat of capillary condensation in nanopores: New insights from the equation of state. *Phys. Chem. Chem. Phys.* **19**, 5540–5549 (2017).
54. Floriano, M. A. & Angell, C. A. Surface tension and molar surface free energy and entropy of water to -27.2 °C. *J. Phys. Chem.* **94**, 4199–4202 (1990).
55. Lide, D. R. *et al.* CRC Handbook of Chemistry and Physics. 2660 (2004).
56. Liu, A. J., Durian, D. J., Herbolzheimer, E. & Safran, S. A. Wetting transitions in a cylindrical pore. *Phys. Rev. Lett.* **65**, 1897–1900 (1990).

5. Thermally Driven Fluid Phase Transitions at Carbon Nanotube Interfaces

This chapter has been adapted from "Thermally Driven Reversible Fluid Phase Transitions at Carbon Nanotube Interfaces," by Matthias Kuehne,* Samuel Faucher,* Rahul Prasanna Misra, Hananeh Oliaei, Haokun Li, Jingfan Yang, Aubrey Penn, Zhe Yuan, Sylvia Xin Li, Guangwei He, Ge Zhang, Volodymyr B. Koman, Arun Majumdar, Narayana Aluru, Daniel Blankschtein, and Michael S. Strano. This manuscript is in preparation, 2022.

Abstract

Fluid adsorption in porous materials is key for applications in catalysis, filtration, and energy storage. The relevant thermodynamics of confined and interfacial fluids differ significantly from the one of their bulk form, in particular when reduced to the single digit nanometer scale. Nanoconfinement may aid to stabilize unusual fluid phases and dictate extremely sensitive dependencies of thermodynamic parameters on the system size. Their resolution has been hampered by the finite pore size distribution in common materials. Here, we investigate fluids associated with individual carbon nanotubes (CNTs) by Raman spectroscopy and study their phase behavior as a function of temperature and environmental condition. We uncover fully reversible transitions between vapor and liquid-like states of various interior and exterior fluids including water, based on their effect on the CNT's Raman-active radial breathing(-like) mode(s). Grand canonical molecular dynamics simulations support the applicability of a Temkin adsorption model, which we use to extract the heat of adsorption ΔH_{ads}. The analysis reveals a non-monotonic dependence of ΔH_{ads} on pore size for interior water.

* Matthias Kuehne and I contributed equally to this manuscript.

5.1 Introduction

At the single digit nanometer scale, confined and interfacial fluids display distinct thermodynamic properties dictated by the geometry of and coupling with the wall material. Knowledge gaps persist regarding fluid transport and thermodynamics at this scale,[1,2] including for substances as mundane as water.[3] Carbon nanotubes (CNTs) have emerged as a prime model system in this space that allow for the investigation of fluid phases at their interior and exterior.[4,5] Molecules inside CNTs may assume structural configurations that are distinct from their bulk form, in particular when the CNT diameter is comparable to the size of the confined molecules. For example, unusual ice phases are expected to manifest when water is confined in CNT single digit nanopores.[6] Non-monotonic dependencies of confined water phase transition temperatures on CNT diameter have been predicted[7] and recently observed in optical studies of individual, isolated CNTs.[8,9] In CNTs with diameters in the sub-nm range, single file water is achieved with each water molecule forming at most two hydrogen bonds.[10] In this regime, water was found to display additional quasi-phase transitions upon cooling.[11] Beyond water,[12] CNTs may be filled with a large variety of fluids,[13] rendering CNTs a truly versatile testbed for thermodynamics under confinement. In addition, fluids may adsorb on the CNT exterior,[4,5,14] and without special precautions the CNT exterior tends to be covered with molecular adsorbates.[15-24] Exterior adsorbates determine CNT device performance,[25] and their reversible desorption has been proposed for the realization of all-optical memories.[26] Annealing procedures under ultrahigh vacuum conditions were devised to initialize clean CNT surfaces for the study of phase transitions of exterior noble gas adsorbates.[27,28]

Raman spectroscopy of CNT radial breathing(-like) modes (RBMs) and G modes allows to separately probe fluids associated with a CNT as well as its local temperature.[8,29] RBMs are zone-center optical phonons with displacement pattern in strictly radial direction, and each CNT has as many RBMs as constituent walls.[30] Fluid molecules mostly affect the RBM associated with the wall they directly interface with through van der Waals coupling, inducing a characteristic upshift in RBM frequency.[18,20,30-33] RBMs of CNTs consisting of more than one concentric wall further lend themselves for fluid localization (interior vs. exterior).[34] G modes in turn are tangential optical modes characteristic of sp2 carbon and known to downshift in frequency with increasing temperature, and hence are commonly used as built-in thermometers.[8,29,35-37] Raman spectroscopy has been used to interrogate water both at the inside of CNTs[8,11,38-41] and at their outside.[18,20]

Herein, we study reversible phase transitions of fluids at the interior and exterior of individual CNTs with diameters in the single digit nanopore regime using micro-Raman spectroscopy. We drive phase transitions thermally by varying the Raman excitation laser power, and determine the local CNT temperature from its G mode frequency. While the latter downshifts linearly with increasing temperature, we find RBMs of water-filled CNTs to display reversible, sigmoidal-type RBM softening that we rationalize as a liquid-vapor phase transition of the confined fluid. We conduct grand canonical molecular dynamics simulations of liquid-vapor phase change of water in CNTs, and find a Temkin adsorption model to well capture the observed physics. We further observe a distinct but similarly reversible RBM softening on as-grown, free-standing CNTs, which in the light of our analysis we attribute to reversible adsorption of an exterior fluid molecular phase, likely of hydrocarbons. We analyze our

measurements of a total of 17 different CNTs using the Temkin adsorption model (as well as alternatives) to extract CNT diameter, adsorption site, and fluid-resolved parameters governing the observed phase change behavior and mechanical coupling to the CNTs.

5.2 Results

We studied CNTs on silicon substrates by micro-Raman spectroscopy as illustrated in Figure 5-1a. These CNTs were synthesized by gas-flow aligned chemical vapor deposition, which results in a sparse array of parallel, millimeter-long CNTs.[42] CNTs were located based on their characteristic Raman scattering response. Our CNTs vary in wall number and bundledness (see Supporting Information for statistics), and we selected for CNTs with one or two resonant RBMs. We typically find observed RBMs of as-grown CNTs to be unresponsive to liquid water immersion.[8,41] This attests to (1) saturated van der Waals coupling with the exterior environment even before immersion, and (2) as-grown tubes being closed for fluid filling. However, fluid exposure after tube cutting by oxygen plasma etching[8,41,43] or focused ion beam milling[29] can lead to CNT filling which causes a characteristic RBM blueshift.[8,29,38,41] Using either approach, we divided millimeter-long CNTs into 10-100 μm long segments. Some of these segments filled upon liquid water immersion while others remained unfilled as shown in **Figure 5-1b**.

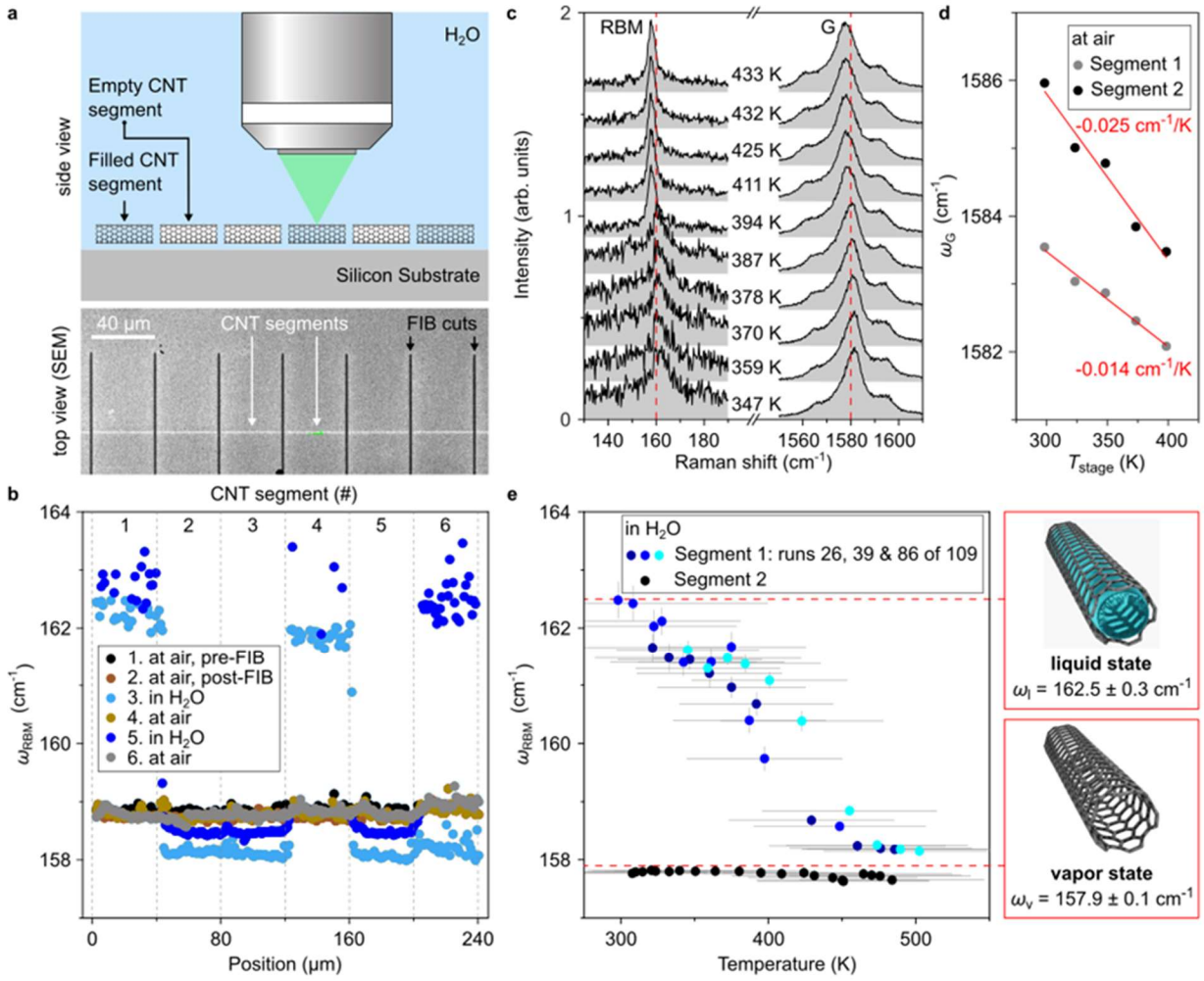

Figure 5-1 | Micro-Raman spectroscopy of substrate-supported CNTs. a, Schematic side view of the experiment (top panel): multiple segments of the same CNT were studied under water immersion. Bottom panel: scanning electron micrograph of a CNT after segmentation by focused ion beam milling. **b**, Frequency of an observed radial breathing mode repeatedly measured along the same six 40 μm-long segments of a CNT. Upon water immersion, the RBM frequency of segments 1, 4, and 6 upshifts, while segments 2, 3, and 5 remain empty. All segments are empty at air. **c**, Raman spectra of CNT segment 1 acquired at different levels of laser power under water immersion. Laser heating induces softening of both G mode and RBM (red lines are guides for the eye). RBM and G band spectral regions have been normalized (separately) and offset for clarity. **d**, Linear dependence of the G mode on temperature, separately calibrated for each segment using a temperature stage. Temperature values shown in **c** are determined using the linear fits shown in **d**. **e**, RBM frequency as function of local CNT temperature for segments 1 and 2 measured under water immersion. Only the filled segment (#1) shows a reversible transition between an upshifted RBM frequency, ω_l, and an RBM frequency similar to the one of the empty segment, ω_v. We assign these two states as a liquid-like state and a vapor-like state of water in the CNT, respectively.

We used the Raman excitation laser to locally heat a CNT. Raman spectra acquired on filled segment 1 under water immersion and at different laser power are shown in **Figure 5-1c**. The G band displayed a linear downshift with increasing temperature,[8,29,35-37] which was separately calibrated for each segment to serve as built-in thermometer, see **Figure 5-1d**. Temperature values in Figure 1c are determined using the calibrated slope $d\omega_{\mathrm{G}}/dT$, with the highest G band frequency measured during the experiment set to 295 K. We extract ω_{RBM} values from single-Lorentzian fits of the data and plot them as function of temperature in Figure 1e. In contrast to the G band, the local RBM frequency ω_{RBM} of segment 1 reversibly transitions between a high-frequency state ω_l at low temperature and a low-frequency state ω_v at high temperature, approximately following a sigmoid centered at $T^* \approx 400$ K. We interpret this behavior as a phase transition of water inside the CNT segment between a liquid state at low temperature and a vapor state at high temperature.[8] The vapor state frequency ω_v approaches the RBM frequency of the unfilled segment, which in turn does not display a pronounced temperature dependence within the explored temperature interval. In particular, the sigmoid-like transition observed in the water-filled segment is entirely absent in the unfilled segment.

We convert measured RBM frequencies into fractional coverage $q = \text{occupied area}/\text{total area}$ of the first shell of molecules at the fluid-CNT interface based on an elastic shell model.[31,32] For a single-walled CNT, the vapor state RBM frequency ω_v is

$$\omega_v^2 = \frac{1}{R^2} \cdot \frac{Eh}{\rho h(1-\nu^2)} \qquad [5.1]$$

where R is the SWCNT radius, E is the Young modulus, h is the SWCNT wall thickness, ρ is the mass density, and ν is the Poisson ratio. The liquid state RBM frequency ω_l is defined as

$$\omega_l^2 = \omega_v^2 + \frac{\gamma}{\rho h} \qquad [5.2]$$

where γ is an area-normalized spring constant characterizing the van der Waals coupling between the carbon shell and the first shell of adsorbed molecules, see Figure 2a for an illustration. γ is related to the second derivative of the potential between the two shells. If we define the area-normalized spring constant at fractional coverage q as $q\gamma$, we can write

$$\omega^2 = \omega_v^2 + \frac{q\gamma}{\rho h} \qquad [5.3]$$

where ω is the RBM frequency at fractional coverage q. It follows that

$$q = \frac{\omega^2 - \omega_v^2}{\omega_l^2 - \omega_v^2} \qquad [5.4]$$

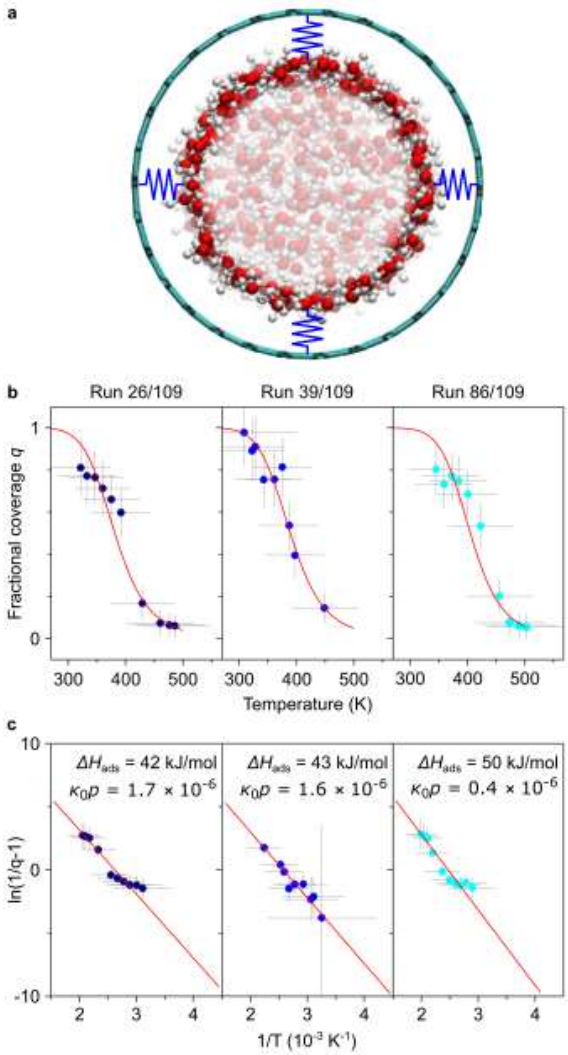

Figure 5-2 | Fluid sensing via the radial breathing mode. a, Molecular dynamics cross-section of a water-filled, single-walled CNT. Highlighted is the first layer of water molecules which yields the dominant contribution to shifting the RBM frequency of the carbon shell

through van der Waals coupling. **b**, Fractional coverage q of molecules in the first shell of fluid molecules extracted from the filled segment data in Figure 5-1d using Equation 4. Red curves are Langmuir adsorption isobars with parameters shown in **c**. **c**, Same data as in **b** plotted in linearized form according to Equation 6. Red lines are linear fits of the data that yield the stated best fit parameters.

To convert an observed RBM frequency ω into q using Equation 4, we define ω_v (at which $q = 0$) as the lowest observed frequency and ω_l (at which $q = 1$) as the highest observed frequency for a given RBM that indicates a reversible phase transition similar to the filled segment data in **Figure 5-1e**. Though in this manner ω_v is determined at much higher temperature than ω_l, we systematically found RBM frequencies to display only very minor if at all measurable intrinsic temperature dependence, see the empty segment data in **Figure 5-1e**. We independently confirm the smallness of temperature-induced intrinsic RBM frequency shifts using molecular dynamics simulations in the Supporting Information. We believe the intrinsic temperature dependence of RBM frequencies has been concealed in previous experimental studies,[36,37,44-47] possibly due to bundling that gives rise to intertube coupling effects[37] or reversible fluid adsorption we report on further below. Though Equation 4 has been derived for a single-walled CNT, it also is a very good approximation for converting ω to q in the case of CNTs consisting of more than one concentric wall, see Supporting Information. We thus use Equation 4 for any observed RBM.

In Figure 2b, we plot the fractional coverage q determined from the filled segment 1 data in Figure 1d using $\omega_v = 157.9 \pm 0.1\ \mathrm{cm}^{-1}$ and $\omega_L = 162.5 \pm 0.3\ \mathrm{cm}^{-1}$, the respective minimum and maximum RBM frequencies measured during 109 temperature cycles (the complete dataset is available in the Supporting Information). We find the observed temperature dependence of q to be reasonably well described in terms of a Langmuir adsorption model of the form

$$q = \frac{\kappa p}{1+\kappa p} = \frac{\kappa_0 p \exp\left(\frac{\Delta H_{\mathrm{ads}}}{RT}\right)}{1+\kappa_0 p \exp\left(\frac{\Delta H_{\mathrm{ads}}}{RT}\right)} \qquad [5.5]$$

Here, $\kappa = \kappa_0 \exp\left(\frac{\Delta H_{\mathrm{ads}}}{RT}\right)$ is the Langmuir constant, p is pressure, ΔH_{ads} is the enthalpy of adsorption, and R is the molar gas constant. Equation 5 can be rendered in linearized form as follows:

$$\ln\left(\frac{1}{q} - 1\right) = -\frac{\Delta H_{\mathrm{ads}}}{R}\frac{1}{T} - \ln \kappa_0 p \qquad [5.6]$$

As we show in **Figure 5-2c**, we obtain reasonable linear fits of the data in $\ln\left(\frac{1}{q} - 1\right)$ vs. $\frac{1}{T}$ space. This indeed suggests Langmuir adsorption as a promising mechanism to describe the observed fluid phase transition.

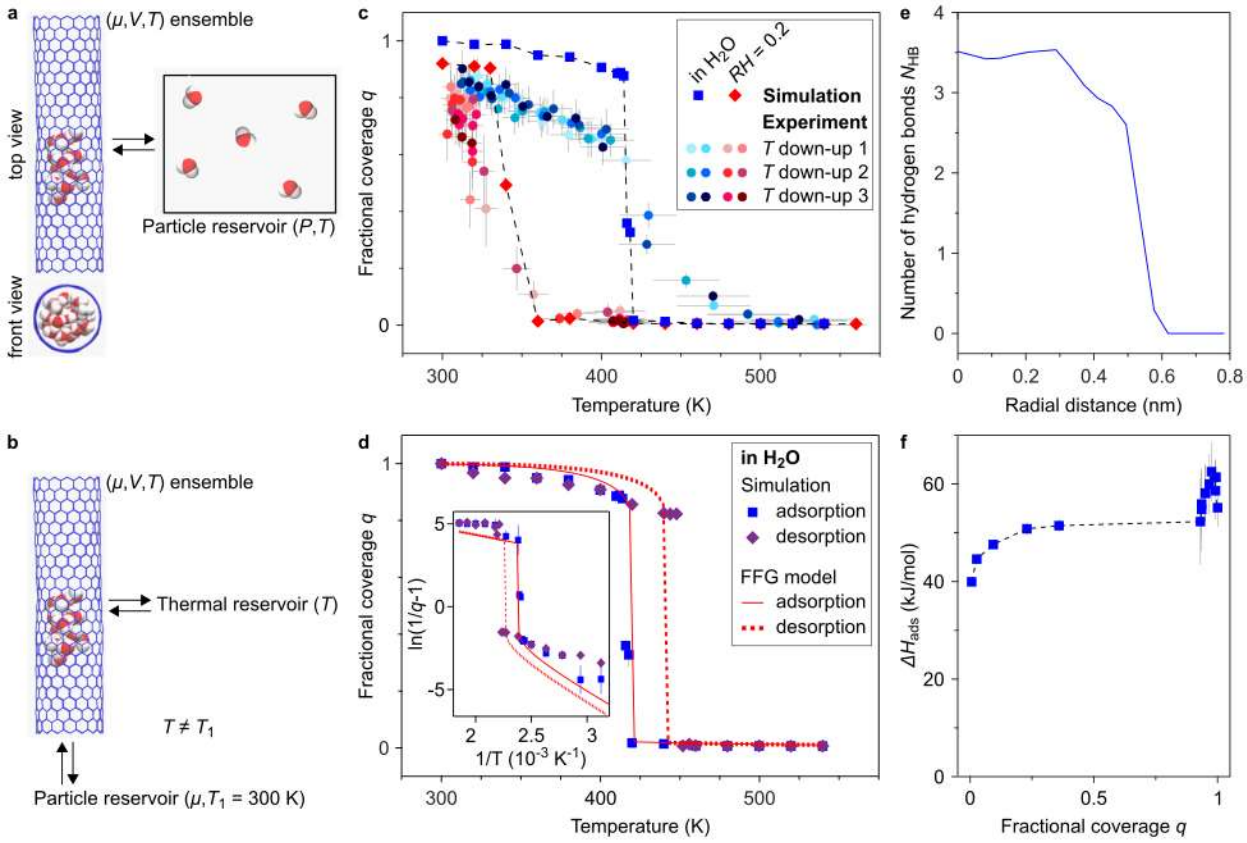

Figure 5-3 | Reversible liquid-vapor phase change of water inside CNTs. a, Grand-canonical Monte Carlo simulations of water adsorption inside single-walled CNTs. The snapshot illustrates that for low filling fractions (e.g., $q \sim 0.1$), the CNT is only partially filled with water. **b**, Scheme for the computation of the adsorption isobar at different temperatures using an iterative approach, where a hybrid statistical mechanical ensemble is simulated using a combination of grand canonical Monte Carlo and canonical MD simulations with the water inside the CNT exchanging water molecules and energy with two fictitious reservoirs: a particle reservoir maintained at a constant chemical potential of μ and a separate thermal reservoir maintained at a temperature T. The isobar is simulated by fixing μ and varying T. **c**, Comparison of measured and computed water adsorption isobars at different levels of relative humidity (see text for the definition of the fractional coverage, q). Simulations were carried out for a (20,0) SWCNT of 1.57 nm diameter. **d**, Simulated adsorption and desorption isobars in a (20,0) SWCNT. Also shown are best fits using the Temkin theory, Equation 7. **e**, Profile of the number of hydrogen bonds per water molecule as a function of the radial distance from the CNT center at $T = 300$ K. **f**, Variation of the isosteric heat of adsorption as a function of the fractional coverage q, estimated directly from statistical mechanics according to Equation 8.

In **Figure 5-3** we present grand canonical molecular dynamics (GCMD) simulations of water adsorption in a representative (20,0) single-walled CNT, further detailed in the Supporting Information. **Figure 5-3a** is a schematic of the simulation performed to determine the amount of water molecules N inside this SWCNT as a function of pressure P and temperature T.

Equilibrium is attained when the chemical potential μ of water molecules inside the SWCNT is equal to the one of water molecules in a fictitious reservoir held at P and T. Figure 3b illustrates the scheme of refined hybrid statistical mechanics simulations that better match our experimental conditions: the system is equilibrated iteratively with two fictitious reservoirs. The first is a (particle) reservoir of water molecules held at μ and $T_1 = 300\ K$, and the second is a thermal reservoir at $T \neq T_1$. We allowed for sufficient time steps for the system to converge and repeated the simulation at different T for a given P to obtain the "adsorption isobars' shown in Figure 3c. The fractional coverage was obtained as $q = \langle N(T) \rangle / \langle N_w(300\ \mathrm{K}) \rangle$ where $N_w(300\ \mathrm{K})$ is the number of water molecules in the SWCNT when immersed in water at 300 K. At high temperature, the SWCNT is found to be mostly empty with $q \sim 0$. At low temperature instead, the SWCNT is filled with water under both conditions with q approaching 1. According to our simulations, the filling fraction increases significantly within a narrow temperature interval approximately centered around 420 K for the case of water immersion and 340 K for $RH = 20\ \%$. We understand this behavior as capillary condensation of water inside the SWCNT. At low filling fractions, we generally find water molecules to cluster inside the SWCNT as shown by the snapshots in Figure 3a–b. Hence, q can be directly compared to values determined from our experiment using Eq. 5-4. Such a comparison is shown in Figure 3c for a CNT measured (1) under water immersion and (2) at air with $RH \approx 20\ \%$. The observed RBM of this CNT, $\omega_v = 154.9\ \mathrm{cm}^{-1}$, corresponds to a wall with diameter comparable to the one of the (20,0) SWCNT in our simulation. Our simulation and experimental results agree well, in particular regarding the big difference in temperature at which capillary condensation occurs under water immersion vs. at ambient air. At temperatures below and above the capillary condensation, q extracted from our experimental data seems to display a stronger dependence on temperature than suggested by our simulations. While this could be a characteristic of nanoconfined water, it might also stem from a fluid-unrelated temperature dependence of the RBM frequency itself which we did not correct for prior to applying Eq. 5-4.

In **Figure 5-3c**, we show results from GCMD simulations of both the adsorption and desorption cycles of water inside a (20,0) SWCNT. While both curves overlap at the low and high ends of the studied temperature range, we find that capillary evaporation happens at ~25 K higher temperature than capillary condensation. Such hysteresis is characteristic of nanoconfined water and indicates first-order character of the phase transition.[3] The confined fluid is metastable within this hysteresis region. Furthermore, our simulation results are nonlinear in $\ln\left(\frac{1}{q} - 1\right)$ vs. $\frac{1}{T}$ space, see inset to Figure 3c. This can be explained by the importance of molecular interactions not captured by the simple Langmuir model in Eq. 5-5. Instead, we turn to a Temkin adsorption model of the form

$$q = \frac{\kappa_0 p \exp\left(\frac{\Delta H_{\mathrm{ads}}(1-\alpha q)}{RT}\right)}{1+\kappa_0 p \exp\left(\frac{\Delta H_{\mathrm{ads}}(1-\alpha q)}{RT}\right)} \qquad [5.7]$$

Here, α is the so-called Temkin parameter. Eq. 5-7 is similar to the Frumkin-Fowler-Guggenheim adsorption model, in which -α is written as the product of n neighbors per adsorption site to bind with and the additional binding energy E_p per pair of molecules that interact. Nonlinear model fits of the GCMD data in Figure 3c with Eq. 5-7 yield $\Delta H_{\mathrm{ads}} =$

9.6 kJ/mol (9.5 kJ/mol) and $\alpha = -2.43$ (-2.6) for the adsorption (desorption) isobar assuming a constant $\kappa_0 p = 1.2 \times 10^{-3}$. These fits are plotted as a continuous (dashed) curve, respectively.

We have further evaluated the binding energy for the water-water and the water-CNT interactions. This binding energy includes contributions from many-body polarization effects and has been computed using the analytical formula and methodology reported previously.[48] Per water molecule, we obtain a water-CNT binding energy of -8.2 kJ/mol and a water-water binding energy of -41 kJ/mol. In Figure 3e we show the number of hydrogen bonds per water molecule N_{HB} plotted as a function of radial distance from the central tube axis for the fully water filled (20,0) SWCNT at 300 K. While N_{HB} approaches the maximum value of 4 at the tube center, it drops to zero near the SWCNT wall. The importance of the water-CNT interaction further affects the isosteric heat of adsorption, which we determine directly using

$$\Delta H_{\mathrm{ads}} = RT - \frac{\partial\langle E\rangle}{\partial\langle N\rangle} = RT - \frac{\langle EN\rangle - \langle E\rangle\langle N\rangle}{\langle N^2\rangle - \langle N\rangle^2} \qquad [5.8]$$

Here, E is the total energy of the water molecules.

We now turn to free-standing CNTs that were grown over arrays of slits in silicon substrates, some of which were TEM-compatible as shown in Figure 5-4a. CVD synthesis resulted in CNTs that span multiple if not all of these slits.[29] Electron microscopy reveals a high degree of bundling of neighboring free-standing CNTs, in particular when the average separation between CNTs is smaller than the slit width, see Supporting Information. We selected for CNTs with 1-2 resonant RBMs, and studied as-grown CNTs first to minimize the likelihood of accidental fluid filling. Figure 5-4 shows an isolated double-wall CNT that we co-localized by Raman spectroscopy and TEM. Due to the large slit width, electron beam-induced vibrations of the free-standing CNT impeded atomic resolution imaging. Nonetheless, the TEM image in **Figure 5-4b** shows that the CNT is isolated as opposed to bundled. The electron diffraction pattern (EDP) in **Figure 5-4c** unambiguously identifies it as double-walled.[22] A CNT chirality assignment of (19,3)@(22,11) (inner@outer wall) best agrees with the measured EDP as we also illustrate by comparison to the simulated EDP shown on the right hand side of **Figure 5-4c**. Both RBMs of the as-grown (19,3)@(22,11) double-wall CNT were observed at 633 nm excitation, and both displayed reversible RBM softening and narrowing upon laser heating as shown in **Figure 5-4d**. From single-Lorentzian fits of the data, we extract highest RBM frequencies near room temperature: $\omega_l = 167.5\ \mathrm{cm}^{-1}$ for the high-frequency mode and $\omega_l = (122.7 \pm 1.3)\ \mathrm{cm}^{-1}$ for the low-frequency mode. We state standard errors from the nonlinear model fit if greater than 0.1 cm^{-1}. Also, full-widths at half maxima (FWHMs) are largest near room temperature: $2.4\ \mathrm{cm}^{-1}$ for the high-frequency mode and $(12.0 \pm 7.0)\ \mathrm{cm}^{-1}$ for the low-frequency mode. RBM frequencies significantly decreased upon heating to above 380 K, where the lowest observed RBM frequencies are $\omega_v = 166.1\ \mathrm{cm}^{-1}$ for the high-frequency mode and $\omega_v = 110.3\ \mathrm{cm}^{-1}$ for the low-frequency mode, and the smallest observed FWHMs are $1.4\ \mathrm{cm}^{-1}$ for the high-frequency mode and $0.9\ \mathrm{cm}^{-1}$ for the low-frequency mode. Thus, the decrease in frequency and linewidth of the low-frequency mode upon heating are both about ten times larger than the ones of the high-frequency mode. Furthermore, both modes shift in sync as demonstrated by the cross-correlation coefficient approaching 1 at zero time lag (see Supporting Information). The behavior is fully reversible as can be seen from three consecutive heating cycles shown in **Figure 5-4e**. Reversibility also reflects in the cross-correlation coefficient

approaching 1 at a time lag equal to the repeat time of the experiment. All 11 free-standing segments of this DWCNT show the same behavior, and the upshifted state ω_l is observed evenly along their length, see Figure 4c. The transition appeared largely unchanged and similarly reversible when measured at 7.4 × 10^{-4} mbar and at 2.5 mbar.

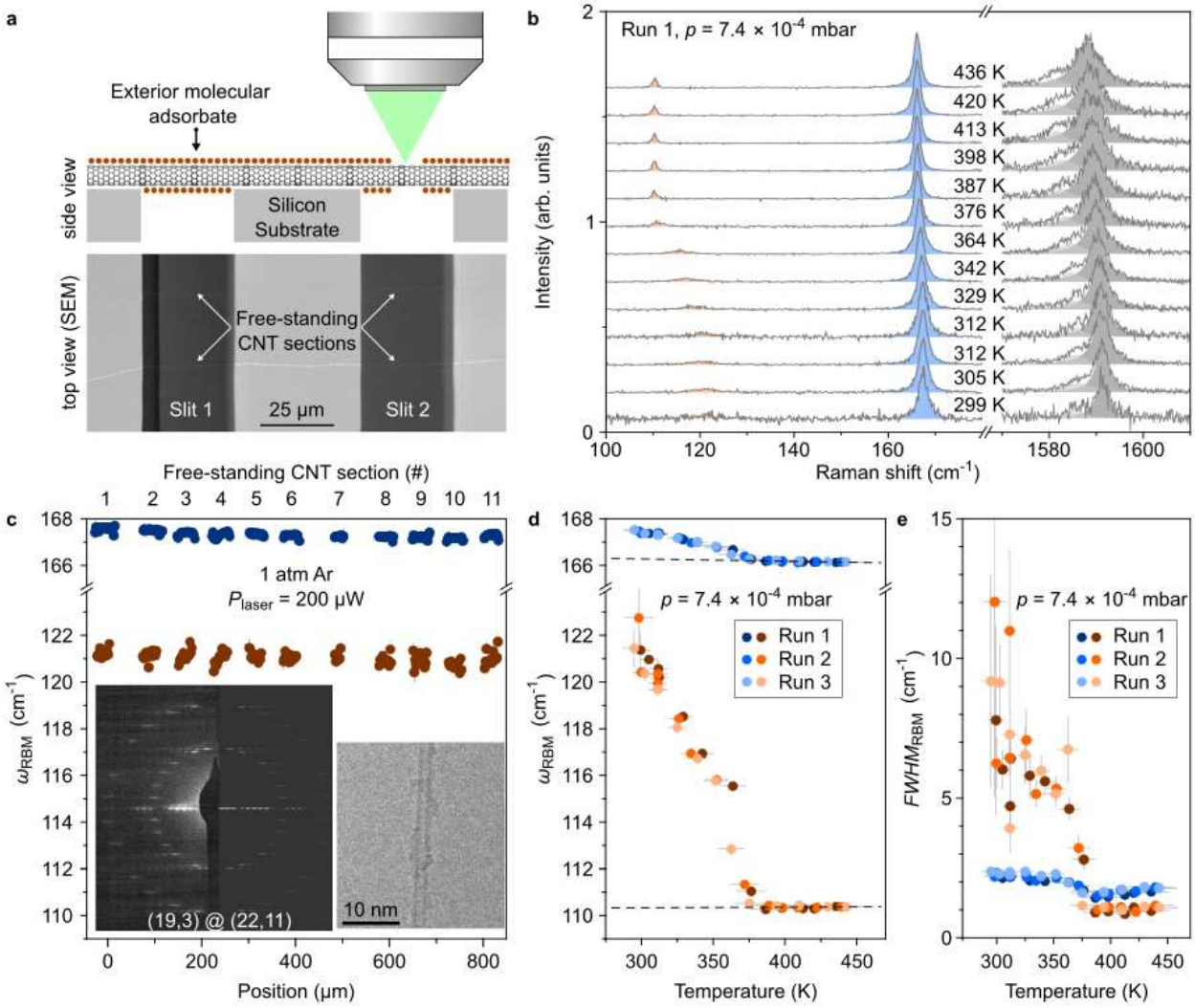

Figure 5-4 | Micro-Raman spectroscopy of as-grown, free-standing CNTs. a, Schematic side view of the experiment (top panel): multiple free-standing sections of the same as-grown CNT were studied in different gas atmospheres and at varying pressure. Bottom panel: scanning electron micrograph of free-standing CNTs. **b**, Raman spectra of an isolated, free-standing (19,3)@(22,11) double-wall CNT acquired at different levels of laser power. RBM and G band spectral regions have been normalized (separately) and offset for clarity. **c**, RBM frequencies as a function of position extracted from single-Lorentzian fits of the data measured along all 11 free-standing sections of the same (19,3)@(22,11) CNT. The left inset shows the measured (left half) and simulated (right half) electron diffraction pattern used for chirality assignment. The right inset is a TEM image of the same CNT. **d**, The temperature dependence shows a correlated frequency shift of both RBMs. **e**, Full-width at half maximum of both RBMs as a function of temperature.

We interpret this reversible RBM softening observed on as-grown, free-standing CNTs as a transition between a state where the exterior CNT surface is covered with fluid molecules near room temperature and a desorbed state at high temperature, akin to previous reports.[15,16,26] This transition is distinct from the interior fluid phase transition above and is best observed when the RBM associated with the outermost wall of a CNT can be measured in experiment, as is the case for the DWCNT shown in **Figure 5-4**. Because the outer wall couples directly to exterior molecules, the low-frequency RBM that is mostly associated with this wall experiences the largest shifts in frequency and linewidth upon their desorption. This is exactly opposite to the case of interior fluid filling of DWCNTs reported previously,[8] which primarily affects the high-frequency mode. Because RBMs of DWCNTs are in-phase and counter-phase oscillations of the two constituent walls, coupling to a fluid will affect both modes, albeit the one associated mostly with the wall further away from the fluid to lesser extent.[34] The in-sync shift of the high-frequency mode in **Figure 5-4d** can be explained as such a 'sympathetic' shift. This characteristic is equally observed in Molecular Dynamics simulations and predicated by analytical elastic shell models.[34]

The following characteristics further distinguish the reversible adsorption of molecules on the CNT exterior from the interior fluid phase transition above. (1) We find molecular adsorption to be homogeneous along the entire length of a CNT. This is illustrated in Figure 5-3f, which shows the near room temperature RBMs of the (19,3)@(22,11) DWNCT measured along all 11 free-standing segments in 2 μm steps. The Raman scattering response of this CNT was not measurable in the substrate-supported regions between the slits using any of our three laser lines. We do not observe any desorbed regions as we have observed empty regions within otherwise filled CNT segments.[41] (2) We have not observed irreversible desorption of a CNT as we have observed emptying of some fluid-filled CNTs. That is, the room temperature state always remained an adsorbate-covered state within both the time resolution of our experiment (several 10 s to minutes) and the pressure range accessible to us: 10^{-5} to 10^{3} mbar. (3) While variations in water vapor pressure drastically changed the adsorption isobar of interior water (**Figure 5-3c**), changes in water vapor pressure did not appreciably affect isobars measured for exterior adsorption. (4) For CNTs that were allowed to sit at room temperature for days or weeks (under vacuum, inert gas or ambient conditions), we have noticed a significant difference between the first laser heating-induced desorption and immediately subsequent desorption cycles, see the Supporting Information. That is, higher temperatures were required to achieve the desorbed state in the first heating ramp, while reversible adsorption/desorption happened at lower temperatures thereafter. Such behavior has previously been reported for exterior adsorption on CNTs.[15] So far, we have not observed it for interior fluids. (5) We consistently find RBMs of a desorbed CNT to be characterized by narrow linewidths approaching 1 cm^{-1} or lower. Such low linewidths were previously reported for the high-frequency RBM of as-grown DWCNTs, and rationalized by the outer wall shielding the inner wall from influences of the outer environment.[49] This is similar to what we report here, where the room-temperature FWHM of the high-frequency RBM is consistently smaller than the one of the low-frequency RBM. Upon desorption, the low-frequency RBM's FWHM decreases substantially and becomes comparable to the one of the high-frequency RBM. This is consistent with a fully desorbed state. In contrast, heating fluid-filled substrate-bound CNTs above the interior fluid phase transition tends not to yield as narrow FWHMs, attesting to residual vdW coupling with the exterior environment.

We have physically separated all free-standing segments of the (19,3)@(22,11) DWCNT by FIB cutting and immersed the sample in a bath of liquid water. While water immersion resulted in the loss of Raman signal for most of the free-standing sections, suggesting these did not survive the procedure, an upshift of the high-frequency mode indicative of fluid filling was measured on the surviving section 4 (see Supporting Information). However, efficient cooling by the surrounding liquid did not allow us to induce a fluid phase transition within the available laser power range (up to 6.07 mW; see Supporting Information). Instead, we turn to a different isolated (28,5)@(28,18) DWCNT shown in **Figure 5-5**. Both RBMs of this DWCNT were observed at 785 nm excitation and were measured along all 13 free-standing sections under different sample and environmental conditions as shown in **Figure 5-5a**. Similar to the (19,3)@(22,11) DWCNT, an exterior fluid phase transition is observed on the as-grown (28,5)@(28,18) DWCNT, see Figure 5b. This exterior fluid phase transition is unresponsive to an eight orders of magnitude change in pressure, compare panels 1 and 2 of **Figure 5-5b**. The low-frequency RBM mostly associated with the outer wall is upshifted due to the exterior fluid along all 13 free-standing sections. Upon FIB cutting and in high relative humidity, an additional 5 cm^{-1} upshift of the high-frequency RBM that we attribute to water filling is observed on 10 out of 13 sections, while it remains unshifted for 1 out of 13 sections (section 6). Poor signal-to-noise ratio did not allow reliable analysis of sections 4 and 13. Similar to the substrate-bound tube data in **Figure 5-1b**, the additional shift of the high-frequency RBM was reversed upon decreasing the relative humidity, consistent with tube emptying. The data in the rightmost panel of **Figure 5-5b** reveals RBM shifts due to reversible fluid phase transitions both at the interior and exterior of this DWCNT. Interior and exterior fluid phase transitions need not be correlated, and this is revealed for example by an upshift of the high-frequency mode indicating filling while the low-frequency mode remains near $\omega_v = 78.7\ cm^{-1}$ down to lower temperature during the second cool-down cycle shown in the rightmost panel.

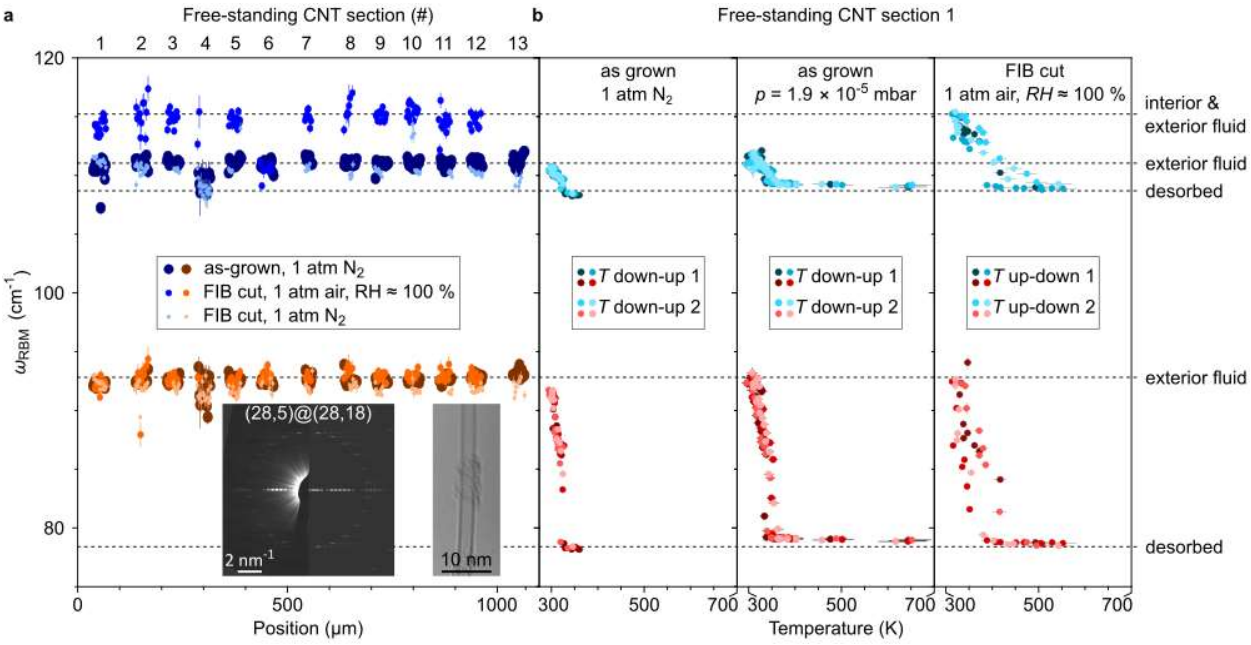

Figure 5-5 | Interior and exterior fluid phase transitions in an isolated, free-standing (28,5)@(28,18) DWCNT. a, RBM frequencies as a function of position measured along all

13 free-standing sections before (i.e., as grown) and after their physical separation by FIB cutting and in different environments. The left inset shows the measured (left half) and simulated (right half) electron diffraction pattern used for chirality assignment. The right inset is a TEM image of the DWCNT. **b**, Fluid phase transitions measured on free-standing CNT section 1 under different sample and environmental conditions.

In order to identify the nature of the exterior fluid, we have explored a range of environmental conditions in addition the ones shown in **Figure 5-5b**, see Supporting Information. However, the room temperature state of the (28,5)@(28,18) DWCNT's low-frequency RBM remained unchanged, even after heating the sample to 100 C in vacuum for over 24 hours or after baking the vacuum chamber with loaded sample at 90 C for over 24 hours. Water is a potential candidate, as this molecular species is known to typically dominate the residual gas composition in high vacuum chambers, but the adsorption mechanism discussed at length in the context of **Figure 5-3** as well as previous experiments[18,20] suggest a layer of water not to be stable on the CNT exterior at water vapor pressures < 1 mbar. Exterior water would need to be somehow stabilized at lower pressures, and conceivably this could be achieved if it was trapped below or within amorphous carbon material, a common synthesis residue on the exterior of CNTs including ours, see insets to **Figure 5-4c** and **Figure 5-5a**. However, this amorphous carbon typically does not form a complete exterior shell that would likely be required to stabilize a full layer of water. Nonspecific adsorption of hydrocarbons is a possible alternative explanation for the observed exterior fluid phase transition. Those are ubiquitous in laboratory environments worldwide, are commonly found on 2D materials surfaces even after annealing in high vacuum,[50] and are known to play a key role in determining the wettability of graphene and graphite.[51] Their low concentration in the air could explain why varying the pressure in our experiment does not have an immediate effect on the exterior fluid phase transition.

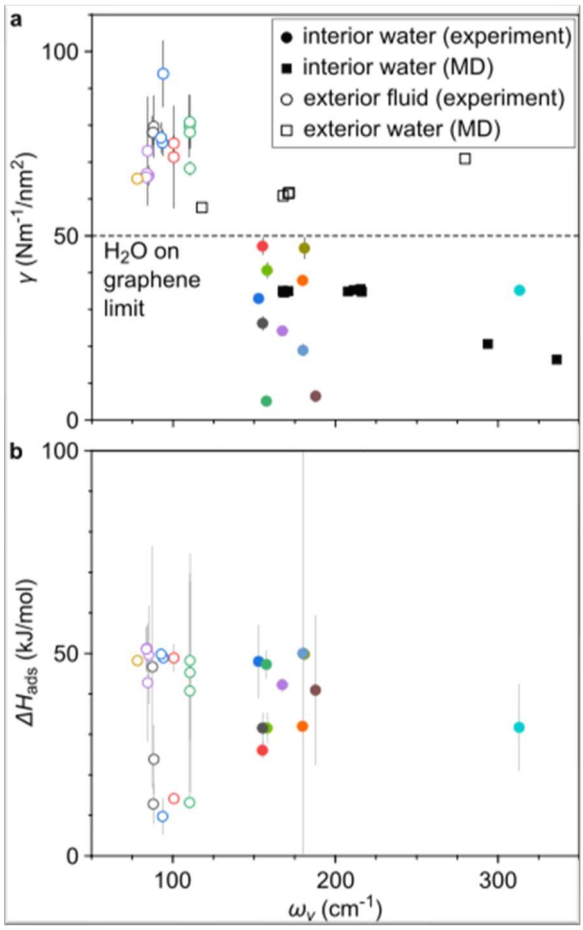

Figure 5-6 | Mechanical and thermodynamic parameters extracted from the analysis of reversible fluid phase transitions observed in 17 different CNTs. Data points of identical style represent measurements on different sections of the same CNT. **a**, Carbon-fluid coupling parameter γ determined using Eq. 5-2. Also shown are results from molecular dynamics (MD) simulations of interior and exterior water on single-walled CNTs. The dashed line represents the limit of infinite radius, i.e., $\omega_v \to 0$, towards which γ values for interior and exterior water converge in our simulation. **b**, ΔH_{ads} values extracted from fits of the data with the Temkin model, Eq. 5-7.

In the following we limit our analysis to interior phase transitions of fluids in substrate-bound CNT segments and the exterior fluid phase transition in free-standing CNT sections. For each CNT studied, we converted ω_{RBM} to q values according to Eq. 5-4 for the mode associated with the wall nearest the fluid, and converted ω_{G} to T values using a unique $\omega_{\mathrm{G}}(T_{\mathrm{stage}})$ calibration for each segment or section. We fit the resulting $q(T)$ data to the Temkin model (Eq. 5-7) using a direct nonlinear model fit procedure in q vs. T space. The Temkin parameter α was allowed to vary for each individual temperature ramp, reflecting the fact that the fluid phase transition could pass through different metastable configurations for different temperature ramps. At the same time, we fit for a unique value of ΔH_{ads}, which we expect to be characteristic rather of the nature of the CNT-fluid couple and not of particular metastable phases of a given interfacial or confined fluid. We prevent Eq. 5-7 from becoming multi-valued for large α by doing a Maxwell construction. A

detailed account of the analysis is included in the Supporting Information, and the main results are shown in **Figure 5-6**.

Figure 5-6a shows the CNT-fluid coupling parameter γ extracted from our experimental data using Eq. 5-2. We have applied Eq. 5-2 to the RBM associated mostly with the wall nearest the fluid, i.e., the innermost wall in the case of interior water and the outermost wall in the case of exterior fluids. Overall, γ tends be larger for exterior fluids than for interior fluids, similar to what has been estimated in Refs. [32,39]. We find a similar trend in results from molecular dynamics simulations we have performed for the case of water adsorption on single-walled CNTs. Simulation results are included in **Figure 5-6a** and suggest $\gamma < 50\ \mathrm{Nm^{-1}/nm^2}$ for water at the interior of the SWCNTs studied, while $\gamma > 50\ \mathrm{Nm^{-1}/nm^2}$ for water at the exterior. We have verified that values for interior and exterior water converge towards a flat sheet (graphene) limit of $50\ \mathrm{Nm^{-1}/nm^2}$ in our simulation.

Figure 5-6b shows the enthalpy of adsorption values as a function of tube size. Overall we find ΔH_{ads} on the order of several 10 kJ/mol, comparable to the estimates based on our simulations of interior water above. The apparent variations in ΔH_{ads} among different segments of the same CNT are largely compensated by respective variations in $|\alpha|$: best fits were obtained either with large ΔH_{ads} and small $|\alpha|$, or with small ΔH_{ads} and large $|\alpha|$, see Supporting Information. For the case of interior water, ΔH_{ads} shows a non-monotonic dependence on tube size.

5.3 Methods

Sample fabrication. Carbon nanotubes were grown on lithographically patterned silicon substrates by gas-flow aligned chemical vapor deposition (CVD).[42] We used a low gas-flow variant[8,29,41,52] with methane as feed stock and iron particles contained in 25 Series APT carbon nanotubes (Nano-C; we drop cast a solution of them on one end of the the substrate) as the catalyst. CVD growth was done at 970 C and 4 sccm:2 sccm H_2:CH_4, resulting in a sparse array of parallel, millimeter-long CNTs oriented in gas flow direction. CNTs were cut into segments by either one of two methods reported previously: (1) oxygen plasma etching using a photoresist mask[41] or (2) focused ion beam (FIB) milling using the 30 kV Ga^+ beam of a dual-beam FIB/SEM instrument[29].

Raman spectroscopy. We locate CNTs based on their characteristic Raman scattering response,[30] using a confocal micro-Raman spectrometer in backscattering geometry equipped with 532 nm, 633 nm, and 785 nm laser lines. We calibrated the temperature dependence of the G band for each CNT segment by measuring Raman spectra as a function of substrate temperature T_{stage} which was controlled using a commercial variable temperature stage (Linkam THS350V). Additional laser-induced heating was minimized by placing the sample in an ambient pressure gas environment (air, N_2, or Ar) and by using very low laser power to record these calibration Raman spectra (on the order of 10 μW). The frequency of the most intense G band component ω_{G} was determined via a Lorentzian curve fit of each spectrum, and the resulting $\omega_{\mathrm{G}}(T_{\mathrm{stage}})$ calibration data was fit to a line.[41] In agreement with the literature and previous reports, we typically find its slope $d\omega_G/dT \approx -0.02\ \mathrm{cm^{-1}/K}$.[29,35-37,46,53-55] We study reversible fluid phase transitions with the samples immersed in different environments including liquid immersions, air at ambient pressure and variable relative humidity (using a home-built humidity control system), inert gas atmosphere

at ambient pressure, and vacuum. In all cases, we vary the local temperature of the CNT under study by attenuating the incident excitation laser beam using a set of discrete and continuous optical density filters. We determine the local temperature of a CNT segment under study based on the measured G band frequency ω_{G} and its calibrated $d\omega_G/dT$ dependence.

Transmission electron microscopy (TEM). Transmission electron microscopy and diffraction of suspended tubes were performed on a Thermo Fisher Themis Z G3 60-300 kV (scanning) transmission electron microscope. The microscope was operated at 60 kV, below the knock-on damage threshold for carbon nanotubes. A 100 μm objective aperture was used to improve image contrast and reduce delocalization. Electron diffraction patterns were collected with a 20 nm diameter parallel beam on a Ceta CMOS camera.

5.4 References

1 Faucher, S. *et al.* Critical Knowledge Gaps in Mass Transport through Single-Digit Nanopores: A Review and Perspective. *J Phys Chem C* **123**, 21309-21326, doi:10.1021/acs.jpcc.9b02178 (2019).

2 Kavokine, N., Netz, R. R. & Bocquet, L. Fluids at the Nanoscale: From Continuum to Subcontinuum Transport. *Annual Review of Fluid Mechanics* **53**, 377-410, doi:10.1146/annurev-fluid-071320-095958 (2021).

3 Brovchenko, I. & Oleinikova, A. *Interfacial and Confined Water*. (Elsevier, Amsterdam, The Netherlands, 2008).

4 Kondratyuk, P. & Yates, J. T. Molecular Views of Physical Adsorption Inside and Outside of Single-Wall Carbon Nanotubes. *Acc. Chem. Res.* **40**, 995-1004, doi:10.1021/ar700013c (2007).

5 *Adsorption and Phase behavior in Nanochannels and Nanotubes*. (Springer Netherlands, 2010).

6 Koga, K., Gao, G. T., Tanaka, H. & Zeng, X. C. Formation of ordered ice nanotubes inside carbon nanotubes. *Nature* **412**, 802-805, doi:10.1038/35090532 (2001).

7 Takaiwa, D., Hatano, I., Koga, K. & Tanaka, H. Phase diagram of water in carbon nanotubes. *Proceedings of the National Academy of Sciences of the United States of America* **105**, 39, doi:10.1073/pnas.0707917105 (2008).

8 Agrawal, K. V., Shimizu, S., Drahushuk, L. W., Kilcoyne, D. & Strano, M. S. Observation of extreme phase transition temperatures of water confined inside isolated carbon nanotubes. *Nature Nanotechnology* **12**, 267-273, doi:10.1038/nnano.2016.254 (2017).

9 Chiashi, S. *et al.* Confinement Effect of Sub-nanometer Difference on Melting Point of Ice-Nanotubes Measured by Photoluminescence Spectroscopy. *ACS Nano* **13**, 1177-1182, doi:10.1021/acsnano.8b06041 (2019).

10 Hummer, G., Rasaiah, J. C. & Noworyta, J. P. Water conduction through the hydrophobic channel of a carbon nanotube. *Nature* **414**, 188-190, doi:10.1038/35102535 (2001).

11 Ma, X., Cambré, S., Wenseleers, W., Doorn, S. K. & Htoon, H. Quasiphase Transition in a Single File of Water Molecules Encapsulated in (6,5) Carbon Nanotubes Observed by Temperature-Dependent Photoluminescence Spectroscopy. *Physical Review Letters* **118**, 027402, doi:10.1103/PhysRevLett.118.027402 (2017).

12 Pascal, T. A., Goddard, W. A. & Jung, Y. Entropy and the driving force for the filling of carbon nanotubes with water. *Proceedings of the National Academy of Sciences of the*

United States of America **108**, 11794-11798, doi:10.1073/pnas.1108073108 (2011).
13 Campo, J. *et al.* Optical Property Tuning of Single-Wall Carbon Nanotubes by Endohedral Encapsulation of a Wide Variety of Dielectric Molecules. *ACS Nano* **15**, 2301-2317, doi:10.1021/acsnano.0c08352 (2021).
14 Ulbricht, H., Zacharia, R., Cindir, N. & Hertel, T. Thermal desorption of gases and solvents from graphite and carbon nanotube surfaces. *Carbon* **44**, 2931-2942, doi:10.1016/j.carbon.2006.05.040 (2006).
15 Finnie, P., Homma, Y. & Lefebvre, J. Band-Gap Shift Transition in the Photoluminescence of Single-Walled Carbon Nanotubes. *Phys. Rev. Lett.* **94**, doi:10.1103/PhysRevLett.94.247401 (2005).
16 Milkie, D. E. *et al.* Controlled Switching of Optical Emission Energies in Semiconducting Single-Walled Carbon Nanotubes. *Nano Lett.* **5**, 1135-1138, doi:10.1021/nl050688j (2005).
17 Meyer, J. C. *et al.* Raman Modes of Index-Identified Freestanding Single-Walled Carbon Nanotubes. *Phys. Rev. Lett.* **95**, 217401, doi:10.1103/PhysRevLett.95.217401 (2005).
18 Homma, Y. *et al.* Photoluminescence Measurements and Molecular Dynamics Simulations of Water Adsorption on the Hydrophobic Surface of a Carbon Nanotube in Water Vapor. *Phys. Rev. Lett.* **110**, 157402, doi:10.1103/PhysRevLett.110.157402 (2013).
19 Edwards, P. J., Wang, B., Cronin, S. B. & Bushmaker, A. W. Direct Measurement of Water-Assisted Ion Desorption and Solvation on Isolated Carbon Nanotubes. *ACS Nano* **14**, 16854-16863, doi:10.1021/acsnano.0c05638 (2020).
20 Chiashi, S. *et al.* Adsorption effects on radial breathing mode of single-walled carbon nanotubes. *Phys. Rev. B* **91**, 155415, doi:10.1103/PhysRevB.91.155415 (2015).
21 Dean, K. A., von Allmen, P. & Chalamala, B. R. Three behavioral states observed in field emission from single-walled carbon nanotubes. *J. Vac. Sci. Technol. B* **17**, 1959-1969, doi:10.1116/1.590856 (1999).
22 Levshov, D. I. *et al.* Accurate determination of the chiral indices of individual carbon nanotubes by combining electron diffraction and Resonant Raman spectroscopy. *Carbon* **114**, 141-159, doi:10.1016/j.carbon.2016.11.076 (2017).
23 Rochal, S. *et al.* Chirality manifestation in elastic coupling between the layers of double-walled carbon nanotubes. *Nanoscale* **11**, 16092-16102, doi:10.1039/C9NR03853A (2019).
24 Hue, J.-W. *et al.* Environmental effects, intertube interactions and σ-π bond re-hybridization in bundles of double- and triple-walled carbon nanotubes. *Carbon* **158**, 651-661 (2020).
25 Chen, Y.-F. & Fuhrer, M. S. Tuning from Thermionic Emission to Ohmic Tunnel Contacts via Doping in Schottky-Barrier Nanotube Transistors. *Nano Lett.* **6**, 2158-2162 (2006).
26 Uda, T., Ishii, A. & Kato, Y. K. Single Carbon Nanotubes as Ultrasmall All-Optical Memories. *ACS Photonics* **5**, 559-565, doi:10.1021/acsphotonics.7b01104 (2018).
27 Wang, Z. *et al.* Phase transitions of adsorbed atoms on the surface of a carbon nanotube. *Science* **327**, 552-555 (2010).
28 Noury, A. *et al.* Layering Transition in Superfluid Helium Adsorbed on a Carbon Nanotube Mechanical Resonator. *Phys. Rev. Lett.* **122**, 165301, doi:10.1103/PhysRevLett.122.165301 (2019).
29 Kuehne, M. *et al.* Impedance of Thermal Conduction from Nanoconfined Water in Carbon Nanotube Single-Digit Nanopores. *J. Phys. Chem. C* **125**, 25717-25728, doi:10.1021/acs.jpcc.1c08146 (2021).

30 Jorio, A., Saito, R., Dresselhaus, G. & Dresselhaus, M. S. *Raman Spectroscopy in Graphene Related Systems*. (Wiley-VCH, Weinheim, Germany, 2011).
31 Longhurst, M. J. & Quirke, N. The environmental effect on the radial breathing mode of carbon nanotubes in water. *J. Chem. Phys.* **124**, 234708, doi:10.1063/1.2205852 (2006).
32 Longhurst, M. J. & Quirke, N. The environmental effect on the radial breathing mode of carbon nanotubes. II. Shell model approximation for internally and externally adsorbed fluids. *J. Chem. Phys.* **125**, 184705, doi:10.1063/1.2360943 (2006).
33 Araujo, P. T. *et al.* Nature of the constant factor in the relation between radial breathing mode frequency and tube diameter for single-wall carbon nanotubes. *Phys. Rev. B* **77**, 241403, doi:10.1103/PhysRevB.77.241403 (2008).
34 Faucher, S. *et al.* Vibrational Signatures of Internal and External Fluid Filling in Double-Walled Carbon Nanotubes. *in preparation* (2022).
35 Huang, F. *et al.* Temperature dependence of the Raman spectra of carbon nanotubes. *J. Appl. Phys.* **84**, 4022-4024, doi:10.1063/1.368585 (1998).
36 Li, H. D. *et al.* Temperature dependence of the Raman spectra of single-wall carbon nanotubes. *Appl. Phys. Lett.* **76**, 2053-2055, doi:10.1063/1.126252 (2000).
37 Raravikar, N. R. *et al.* Temperature dependence of radial breathing mode Raman frequency of single-walled carbon nanotubes. *Phys. Rev. B* **66**, 235424, doi:10.1103/PhysRevB.66.235424 (2002).
38 Wenseleers, W., Cambré, S., Čulin, J., Bouwen, A. & Goovaerts, E. Effect of Water Filling on the Electronic and Vibrational Resonances of Carbon Nanotubes: Characterizing Tube Opening by Raman Spectroscopy. *Adv. Mater.* **19**, 2274-2278 (2007).
39 Cambré, S., Schoeters, B., Luyckx, S., Goovaerts, E. & Wenseleers, W. Experimental Observation of Single-File Water Filling of Thin Single-Wall Carbon Nanotubes Down to Chiral Index (5,3). *Phys. Rev. Lett.* **104**, 207401, doi:10.1103/PhysRevLett.104.207401 (2010).
40 Fagan, J. A. *et al.* Separation of Empty and Water-Filled Single-Wall Carbon Nanotubes. *ACS Nano* **5**, 3943-3953, doi:10.1021/nn200458t (2011).
41 Faucher, S. *et al.* Diameter Dependence of Water Filling in Lithographically Segmented Isolated Carbon Nanotubes. *ACS Nano* **15**, 2778-2790, doi:10.1021/acsnano.0c08634 (2021).
42 Huang, S., Cai, X. & Liu, J. Growth of Millimeter-Long and Horizontally Aligned Single-Walled Carbon Nanotubes on Flat Substrates. *J. Am. Chem. Soc.* **125**, 5636-5637, doi:10.1021/ja034475c (2003).
43 Lee, C. Y., Wonjoon, C., Jae-Hee, H. & Strano, M. S. Coherence Resonance in a Single-Walled Carbon Nanotube Ion Channel. *Science* **329**, 1320-1324, doi:10.1126/science.1193383 (2010).
44 Ci, L. *et al.* Temperature dependence of resonant Raman scattering in double-wall carbon nanotubes. *Appl. Phys. Lett.* **82**, 3098-3100, doi:10.1063/1.1572959 (2003).
45 Zhou, Z. *et al.* The intrinsic temperature effect of Raman spectra of double-walled carbon nanotubes. *Chem. Phys. Lett.* **396**, 372-376, doi:10.1016/j.cplett.2004.08.004 (2004).
46 Zhang, Y., Xie, L., Zhang, J., Wu, Z. & Liu, Z. Temperature Coefficients of Raman Frequency of Individual Single-Walled Carbon Nanotubes. *J. Phys. Chem. C* **111**, 14031-14034, doi:10.1021/jp075058f (2007).
47 Song, L. *et al.* Temperature dependence of Raman spectra in single-walled carbon nanotube rings. *Appl. Phys. Lett.* **92**, 121905, doi:10.1063/1.2891870 (2008).

48 Misra, R. P. & Blankschtein, D. Insights on the Role of Many-Body Polarization Effects in the Wetting of Graphitic Surfaces by Water. *J. Phys. Chem. C* **121**, 28166-28179, doi:10.1021/acs.jpcc.7b08891 (2017).
49 Pfeiffer, R. *et al.* Unusual High Degree of Unperturbed Environment in the Interior of Single-Wall Carbon Nanotubes. *Phys. Rev. Lett* **90**, 225501, doi:10.1103/PhysRevLett.90.225501 (2003).
50 Haigh, S. J. *et al.* Cross-sectional imaging of individual layers and buried interfaces of graphene-based heterostructures and superlattices. *Nat. Mater.* **11**, 764-767, doi:10.1038/nmat3386 (2012).
51 Li, Z. *et al.* Effect of airborne contaminants on the wettability of supported graphene and graphite. *Nat Mater* **12**, 925-931, doi:10.1038/nmat3709 (2013).
52 Jin, Z. *et al.* Ultralow Feeding Gas Flow Guiding Growth of Large-Scale Horizontally Aligned Single-Walled Carbon Nanotube Arrays. *Nano Lett.* **7**, 2073-2079, doi:10.1021/nl070980m (2007).
53 Bassil, A., Puech, P., Tubery, L., Bacsa, W. & Flahaut, E. Controlled laser heating of carbon nanotubes. *Appl. Phys. Lett.* **88**, 173113, doi:10.1063/1.2199467 (2006).
54 Hsu, I. K. *et al.* Optical measurement of thermal transport in suspended carbon nanotubes. *Appl. Phys. Lett.* **92**, 1-4, doi:10.1063/1.2829864 (2008).
55 Deshpande, V. V., Hsieh, S., Bushmaker, A. W., Bockrath, M. & Cronin, S. B. Spatially Resolved Temperature Measurements of Electrically Heated Carbon Nanotubes. *Phys. Rev. Lett.* **102**, 105501, doi:10.1103/PhysRevLett.102.105501 (2009).

6. Dynamics of Fluid Filling

This chapter has been adapted from "Water Filling in Isolated Sub-2 nm Carbon Nanotubes Occurs by Nucleation and Growth" by Samuel Faucher, Matthias Kuehne, and Michael S. Strano. This manuscript is in preparation, 2022.

Abstract

Confinement of a fluid to a nanometer-sized pore affects the motion of that fluid, including its diffusion and hydrodynamic flow. Water-filled carbon nanotubes are model nanofluidic systems, with predictions of ultrafast slip flow at small diameters. However, the mechanism of fluid filling and emptying inside the narrowest carbon nanotubes is unknown, and probing the fluidic state of an individual carbon nanotube dynamically remains difficult. Here we show that capillary filling inside sub-2 nm diameter carbon nanotubes occurs by nucleation and growth of condensed-phase domains in the pore middle, not by unidirectional filling from the pore mouth. We achieve micrometer and second-scale fluid filling resolution by Raman spectroscopy inside carbon nanotubes with diameters from 0.90 to 1.66 nm, estimating liquid diffusion coefficients of 10^{-11} m^2/s, slower than in the bulk. Our results demonstrate the breakdown of continuum mechanisms, including the Washburn equation, for capillary filling under conditions of 1D nanoconfinement.

6.1 Introduction

Inside so-called single-digit nanopores, or those with a characteristic dimension less than 10 nm, the governing equations of fluid transport remain largely unknown.[1] This knowledge gap persists despite the presence and motion of nanoconfined fluids in membranes,[2–4] batteries,[5] geologic media, and biological cells.[6] The dynamics of capillary filling were described first by Washburn,[7] giving an eponymous equation where fluid penetration distance in a capillary scales with the square root of time. The Washburn-type, continuum picture of nanopore filling is accurate at length scales ranging from the millimeter scale down to capillaries with diameters in the tens of nanometers.[8] Over the last decade, improvements in nanofabrication and synthesis of low-dimensional materials have enabled material platforms to study fluid dynamics inside single-digit nanometer and even Angstrom-scale capillaries with increasing precision, including inside isolated carbon nanotubes[9] and two-dimensional van der Waals assemblies.[10,11]

Carbon nanotubes are model nanofluidic systems. Inside carbon nanotubes, fluids exhibit a variety of unusual behavior, including phase boundaries that deviate from bulk phase behavior of water[12] and so-called slip flow[9,13], in which flow rates under an applied hydrodynamic pressure exceed predictions from the Hagen-Poiseuille equation by up to several orders of magnitude. Secchi et al.[9] report large diameter-dependent slip lengths inside isolated carbon nanotubes with diameters ranging from 15 nm to 50 nm by use of hydrodynamic tracer particles in a fluidic cell, with flow enhancements on the order of 25 inside the narrowest studied CNTs and no observed flow enhancement inside boron nitride nanotubes.[9] Other groups report ultrafast diffusion inside ensembles carbon nanotubes with diameters from 2.3 nm to 8 nm by NMR,[14,15] and non-monotonic changes in flow rates through graphene-based two-dimensional nanochannels with heights on the atomic scale,[11] but observations inside single, isolated carbon nanotubes with diameters less than 10 nm are scarce.

In this paper, we report that filling inside isolated, sub-2 nm carbon nanotubes occurs by nucleation and growth of condensed-phase domains in the middle of the nanotube, rather than a Washburn-type mechanism starting at an open nanotube end. We demonstrate filling and emptying transitions inside numerous carbon nanotubes ranging from 0.90 to 1.66 nm in diameter, with filling studied nearly simultaneously at multiple locations along the CNT axis by Raman spectroscopy inside 1.46 and 1.66 nm diameter carbon nanotubes. Across this diameter regime, diffusion of condensed-phase water is slower than in the bulk, with diffusion coefficients on the order of 10^{-11} m^2/s. Kinetic Monte Carlo (KMC) simulations of water nucleation and growth allow qualitative fits and estimation of relevant rates in the capillary filling process inside 1.46 nm and 1.66 nm diameter carbon nanotubes, including the rates of nucleation and diffusion of liquid-like and vapor-like domains.

6.2 Results

A schematic of the experimental platform is shown in **Figure 6-1a.** As in previous work,[16,17] we grow ultra-long carbon nanotubes by chemical vapor deposition on marked silicon substrates. Carbon nanotubes are grown by methane CVD in hydrogen at 970 °C for 45 minutes.

CNTs are then cut by a gallium focused ion beam to produce segments of identical diameter and lengths between 40 μm and 160 μm. These carbon nanotube segments can be independently identified as filled, empty, or partly water-filled. We introduce water to the system in one of three ways, as indicated in the schematic in **Figure 6-1a**. First, droplets of water can be placed near the ends of the segment. Second, the sample can be cooled to near the dew point at ambient humidity to induce capillary filling. Third, the sample can be immersed in water. Monitoring of the fluidic filling state inside the carbon nanotubes is done by Raman spectroscopy, as described previously.[12,16] The Raman radial breathing mode (RBM), an axisymmetric vibrational mode, can be used to determine carbon nanotube diameter and to determine the fluid filling state of the system. Carbon nanotube diameter can be determined by RBM position in an empty state. While there are numerous relationships between ω_{RBM} and d, which depend slightly on sample preparation and environment,[18] we use the relationship for carbon nanotubes on Si/SiO_2 substrates from Zhang et al.:[19]

$$\omega_{RBM}(cm^{-1}) = \frac{235.9}{d\ (nm)} + 5.5 \qquad [6.1]$$

Occasionally, after introduction of fluid, the RBM mode blueshifts and broadens on the minute timescale, as shown for a 0.90 nm diameter CNT in **Figure 6-1b** and a 1.30 nm diameter CNT in **Figure 6-1c**. The shift in Raman RBM peak position and full-width half maximum (FWHM) during fluid filling or emptying can be described as varying weights of two Lorentizans: a narrow, low-frequency peak corresponding to an empty state with integrated intensity I_e and a broad, high frequency state with integrated intensity I_f. We define a filling fraction, q, according to the following expression:

$$q = \frac{I_f}{I_e + I_f} \qquad [6.2]$$

This formulation neglects changes in Raman scattering cross-section or electronic resonances upon fluid filling.

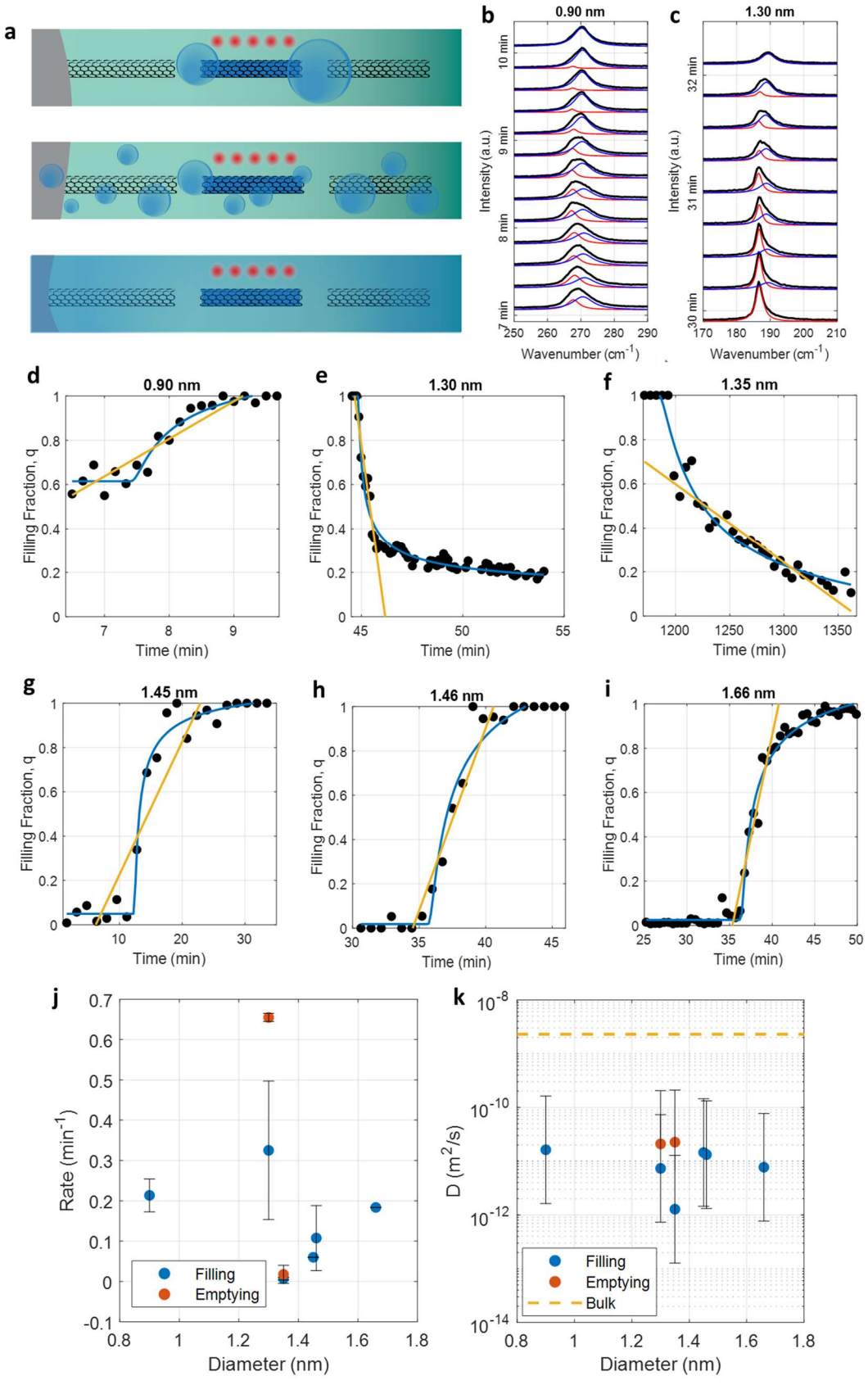
a
b
0.90 nm
10 min
9 min
8 min
7 min
Intensity (a.u.)
250 260 270 280 290
Wavenumber (cm-1)
c
1.30 nm
32 min
31 min
30 min
Intensity (a.u.)
170 180 190 200 210
Wavenumber (cm-1)
d
0.90 nm
Filling Fraction, q
Time (min)
e
1.30 nm
Filling Fraction, q
Time (min)
f
1.35 nm
Filling Fraction, q
Time (min)
g
1.45 nm
Filling Fraction, q
Time (min)
h
1.46 nm
Filling Fraction, q
Time (min)
i
1.66 nm
Filling Fraction, q
Time (min)
j
Rate (min-1)
Filling
Emptying
Diameter (nm)
k
D (m2/s)
Filling
Emptying
Bulk
Diameter (nm)

Figure 6-1 | Observation of dynamic changes in fluid filling state inside isolated, susbtrate-bound carbon nanotubes by Raman spectroscopy. (a) Schematic showing platform consisting of isolated, segmented, substrate-bound carbon nanotubes. Water is introduced by adding droplets, cooling to the dew point, or immersing the sample. (b) Stacked spectra showing a filling transition inside a 0.90 nm diameter CNT by observation of the Raman radial breathing mode. (c) Stacked spectra showing a filling transition inside a 1.30 nm diameter CNT by observation of the RBM. (d-i) Fluid filling transitions inside isolated carbon nanotubes, showing filling fraction, q, versus time for filling (d,g,h,i) and emptying (e,f) transitions inside carbon nanotubes with diameters of 0.90 nm, 1.30 nm, 1.35 nm, 1.45 nm, 1.46 nm, and 1.66 nm. Yellow lines indicate linear fits used to determine filling rate, while blue lines indicate error function fits to a diffusion model. (g) Filling and emptying rate versus carbon nanotube diameter, as taken from linear fits from panels d-i and others. (h) Liquid-like self-diffusion coefficient, D, versus carbon nanotube diameter, as taken from error function nfits from panels d-i and others. Across the studied diameter regime, diffusion inside carbon nanotubes is slower than in the bulk.

We observe 19 fluid filling and emptying transitions inside carbon nanotubes of six diameters (0.90 nm, 1.30 nm, 1.35 nm, 1.45 nm, 1.46 nm, and 1.66 nm). An exemplary data set for each of the six diameters, showing four filling transitions and two emptying transitions as observed at a single location along the length of the CNT, are shown in **Figure 6-1d-i.** Observed transitions include transitions from fully empty to fully filled states, as well as transitions to and from partial filling states for which $0 < q < 1$. The experimental data showing filling fraction versus time can be fit to several different models: a linear fit to determine filling rate, a diffusion model to calculate the self-diffusion coefficient of nanoconfined liquid-like water, or an Avrami model based on the kinetics of crystallization. First, we consider a simple linear fit to determine the filling rate. Linear fits are shown in yellow in **Figure 6-1d-i**, and these data sets and others were used to generate the estimates of filling rate (in min-1) versus diameter for filling and emptying transitions as shown in **Figure 6-1j**. Error bars indicate standard deviations, as applicable.

If the density of the liquid-like phase far exceeds the density of the vapor-like phase, then the capillary condensation process is necessarily a mass transport process, and the experimental data can be fit to diffusion models. Diffusion in highly confined geometries can either be Fickian in nature, in which case the mean-squared displacement is proportional to time, or it can be anomalous.[20] Fick's second law of diffusion in 1D is as follows:

$$\frac{\partial C}{\partial t} = D\frac{\partial^2 C}{\partial x^2} \qquad [6.3]$$

with initial condition $q(x,0) = 0$ and boundary conditions $q(0,t) = 1$ and $\lim_{x\to\infty} q(x,t) = 0$, we recover the common expression for diffusion into a semi-infinite slab:

$$q(x,t) = 1 - \mathrm{erf}\left(\frac{x}{2\sqrt{Dt}}\right) \qquad [6.4]$$

Since the time onset of diffusion is unknown, and may depend on a rare tube opening or nucleation event that cannot be directly experimentally observed, we fit the filling profiles to a piecewise function:

$$q(x,t) = \begin{cases} C & t \le t_0 \\ B\left[1 - erf\left(\frac{A}{\sqrt{t-t_0}}\right)\right] + C & t > t_0 \end{cases} \quad [6.5]$$

where the diffusion coefficient can be found from $D = X^2/(4A^2)$, and X is the distance from the filled location to the location of observation. The distance between the nearest CNT end and the location of observation is known in all 19 data sets, but the characteristic length over which diffusion occurs is nonetheless difficult to determine. We do not know in all cases if both CNT ends are open, or just one, and diffusion could take place from a fully filled region within the CNT rather than the bulk water bath at the pore mouth. As such, the diffusive length scale is uncertain and estimates of the diffusion coefficient are accurate only to the order of magnitude scale, as shown in **Figure 6-1k**. In the case where the density of the liquid-like phase is comparable to the density of the vapor-like phase, then the diffusion model described above is not appropriate. In this case, the observed behavior can be best described as a crystallization kinetics process and should instead be fit using the Avrami equation in analogy with previous work studying polymer phase transitions in nanoconfined geometries.[21,22]

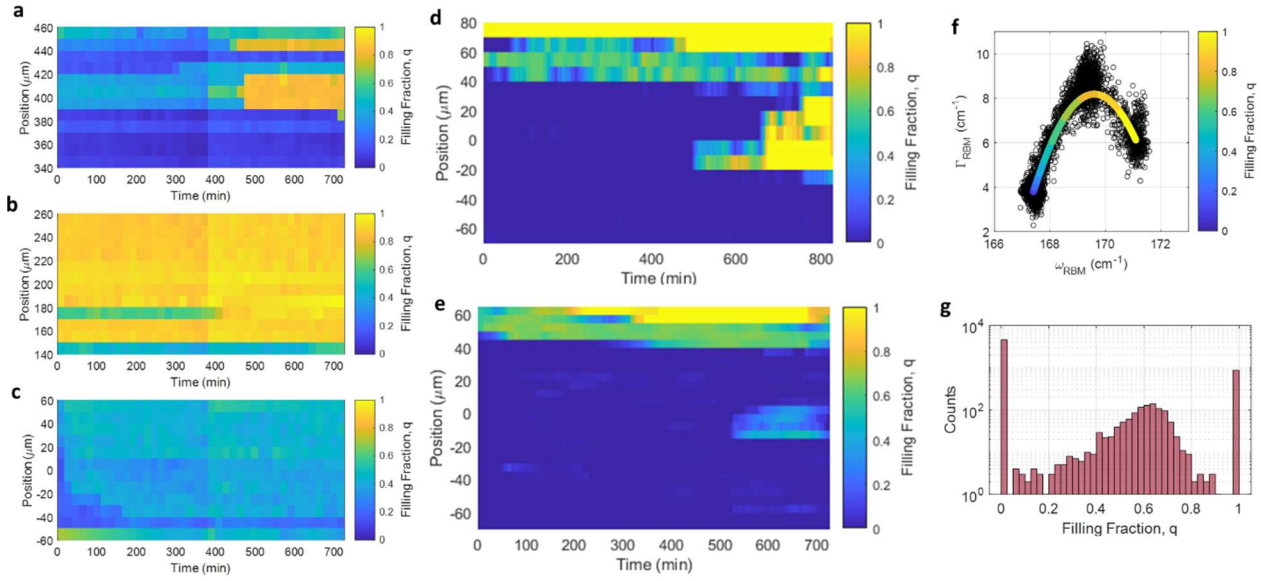

Figure 6-2 | Dynamics of water filling inside 1.46 nm diameter carbon nanotubes, showing fluid filling by nucleation and growth. (a-c) Filling inside three 160 μm segments of 1.46 nm carbon nanotubes, as observed simultaneously by Raman spectroscopy upon water immersion. The top segment fills by nucleation and growth, with two nucleation events between 400 min and 500 min. The middle segment remains filled over the course of the experiment, while the bottom segment remains largely empty. (d) Filling by nucleation and growth inside another 160 μm

segment, as observed by reducing the temperature to the dew point. (e) Slight partial filling by nucleation and growth inside another 160 μm segment, as observed by reducing the temperature to the dew point. (f) Plot showing RBM position (ω_{RBM}) versus full-width half maximum (Γ_{RBM}) for the filling experiment in panel d. Weighted Lorentzian sums to the two endpoints are fit to a single Lorentzian, as shown by the colored curve. (g) Histogram showing frequency of observation of empty, partially filled, and filled carbon nanotubes.

To make more conclusive determinations about the dynamics of fluid filling, we develop methods to observe fluid filling nearly simultaneously at multiple locations along the axis of several 1.46 nm diameter carbon nanotubes (**Figure 6-2**). These carbon nanotube devices were produced by lithographic segmentation of one ultra-long 1.46 diameter carbon nanotube, producing separate nanotubes that can fill or empty independently as described previously.[16] We observe 3 160 μm segments simultaneously at 10 μm pitch. One segment (**Figure 6-2a**) transitions from empty to fluid-filled over the course of the experiment, while another segment (**Figure 6-2b**) remains filled over the course of the experiment and a third (**Figure 6-2c**) remains largely empty over the course of the experiment. Nanotube capillary filling does not follow a Washburn-type profile, in which a liquid-like state penetrates inward from an open end of the nanotube. Instead, fluid filling occurs by nucleation at two locations at distinct times (440 μm at 450 min, and 400 μm at 470 min), followed by growth of liquid-like nuclei. Carbon nanotube capillary filling by liquid-like nucleation and growth is confirmed by two additional, non-simultaneous measurements on two different CNT segments on the same sample (**Figure 6-2d** and **Figure 6-2e**). In **Figure 6-2f,** we plot the RBM frequency (ω_{RBM}) versus full-width half maximum (Γ_{RBM}) for the data from the filling experiment in **Figure 6-2d.** The data lie closely along a curve separating two states – an empty state and a filled state – and consisting of fits of linear sums of the two endpoint Lorentzians to a single Lorentzian. This confirms that the observed variation in RBM position and FWHM correspond to linear combinations of an empty and a filled state, justifying q as an appropriate descriptor of the fluidic state of the nanotube at an arbitrary position and time. In this same experiment, fully empty and fully filled CNT locations are most frequently observed (**Figure 6-2g**), but partial filling states are also observed with a maximum at $q = 0.6$.

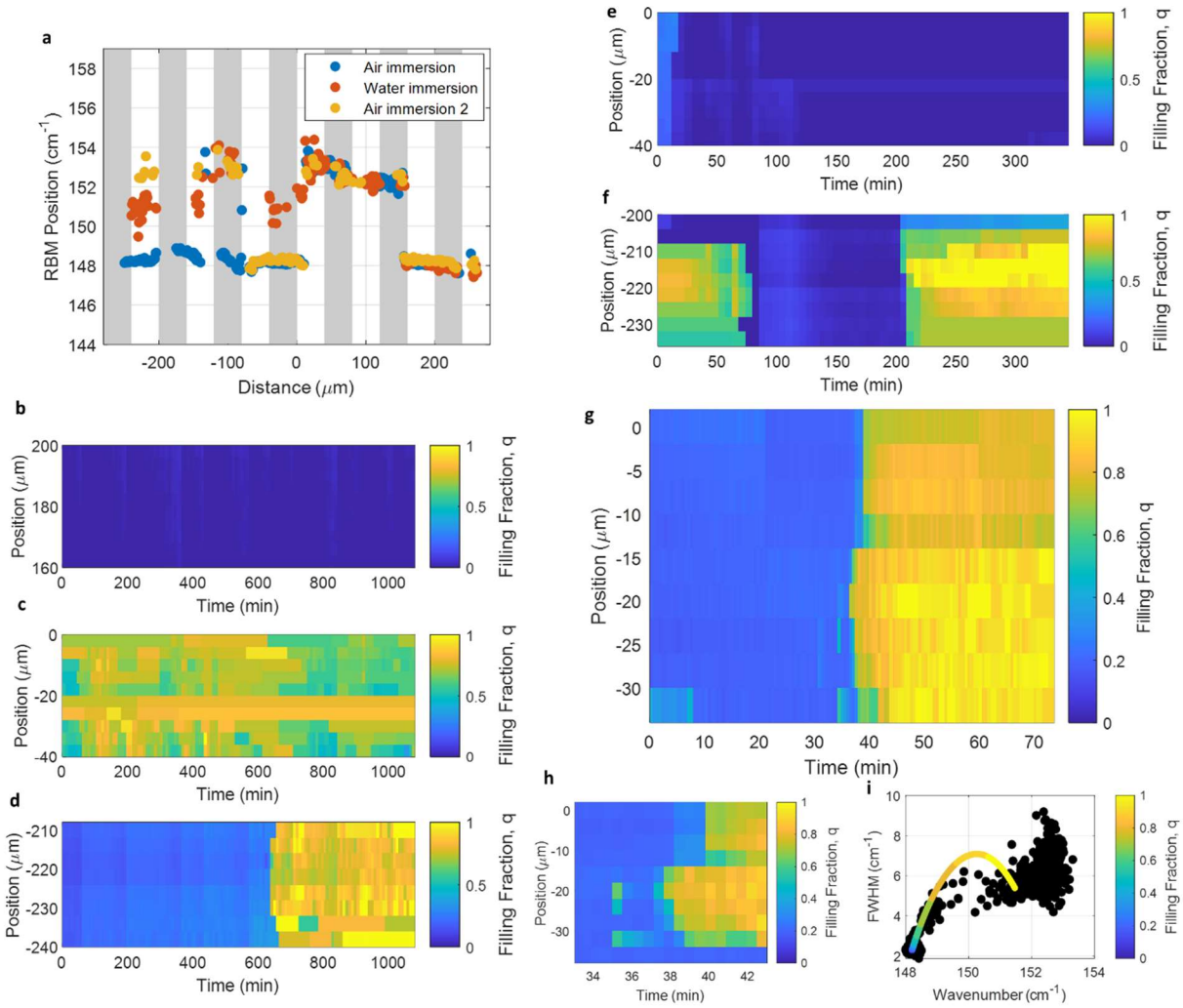

Figure 6-3 | Dynamics of water filling inside 1.66 nm diameter carbon nanotubes, showing fluid filling by nucleation and growth under conditions of water and air immersion. (a) RBM position versus distance along the nanotube axis. CNT segments are shown by alternating grey and white shading. (b-d) Fluid filling behavior of three 40 μm segments upon immersion in water at time zero. One segment remains empty, one segment fills immediately, and one segment fills by nucleation and growth after 640 minutes. (e-f) Fluid emptying behavior of two 40 μm segments upon removal from water at time zero. One segment empties immediately, while the other empties and subsequently fills under ambient humidity. (g-h) Filling of a single 40 μm segment in ambient humidity air by nucleation and growth, with inset in panel h. (i) Plot showing RBM position versus full-width half maximum, taken from the data in panel g. Weighted Lorentzian sums to the two endpoints are fit to a single Lorentzian, as shown by the colored curve.

Next, we observe dynamics of water filling inside 1.66 nm diameter carbon nanotubes (**Figure 6-3**), with 40 μm long segments that are observed by Raman spectroscopy at 4 μm pitch. Under air immersion (**Figure 6-3a**, blue markers), most segments are empty, but a few segments

have already filled under ambient conditions, where segmentation is shown by grey and white stripes. Upon water immersion (**Figure 6-3b-d**, t=0), one segment remains empty (**Figure 6-3b**), one segment fills immediately and remains filled (**Figure 6-3c**), and one segment remains empty until a nucleation event occurs around 640 minutes, leading to complete nanotube filling (**Figure 6-3d**). After the dynamic experiment, and still under water immersion, most segments are in a high RBM, filled state (**Figure 6-3a,** orange markers), but some segments do not fill under any conditions as a likely result of CNT end obstruction.[16] Upon removal from water into ambient air (**Figure 6-3e-f,** t=0), one formerly filled segment empties immediately (**Figure 6-3e**), while another empties non-monotonically before refilling due likely to nucleation of ambient water vapor (**Figure 6-3f**). A subsequent scan along the axis of the CNT in air (**Figure 6-3a,** yellow markers) shows a mix of filled and empty CNT segments. Finally, observation of a single segment with high temporal resolution under air immersion (**Figure 6-3g**, with inset **Figure 6-3h**) shows clear filling by nucleation and growth, with time resolution of 10 s and spatial resolution of 4 μm. While much of the data is described by a single filling parameter q between one empty and one filled state (**Figure 6-3i**), there is a large degree of spread at high filling fractions. This may indicate the presence of multiple different fluid phases or configurations[12,23] inside 1.66 nm diameter CNTs that do not exist inside smaller, 1.45 nm diameter CNTs.

Finally, we perform kinetic Monte Carlo (KMC) simulations to compare parameters of fluid filling to experimental results. In the KMC simulation (**Figure 6-4**), we consider a 1D carbon nanotube domain containing vacuum, vapor, and liquid, with a diffusing vapor phase and a stationary liquid phase. The dynamics of the system depend principally on the diffusion rate of vapor and the nucleation rate of vapor to liquid. System dynamics also depend upon two probabilities: the entrance probability at the pore mouth,[24] and the condensation probability for a vapor molecule that is incident on the vapor-liquid interface,[25] both of which are assumed to be order 1.[25] Sample simulation runs and averages over 1000 runs are shown for sample parameter values: $D{\sim}10^{-1}\ m^2/s$ and $k_{nuc}{\sim}10^{-4}\ s^{-1}\mu m^{-1}$ (**Figure 6-4a-c**), and $D{\sim}10^{-12}m^2/s$ and $k_{nu}\ {\sim}10^{-5}\ s^{-1}\mu m^{-1}$ (**Figure 6-4d-f**). Squared error fit between filling data (**Figure 6-2b,d,e**) and mean KMC filling trajectory is optimized at $D{\sim}10^{-12}m^2/s$ and $k_{nuc}{\sim}10^{-5}\ s^{-1}\mu m^{-1}$. At faster nucleation rates, nucleation occurs before vapor can diffuse throughout the CNT, leading to preferential filling near the pore edge without filling in the middle. This is not observed in experiment. As in the experimental data sets where fluid filling was observed at a single location (**Figure 6-1**), water diffusion under nanoconfinement appears slower than in the bulk.

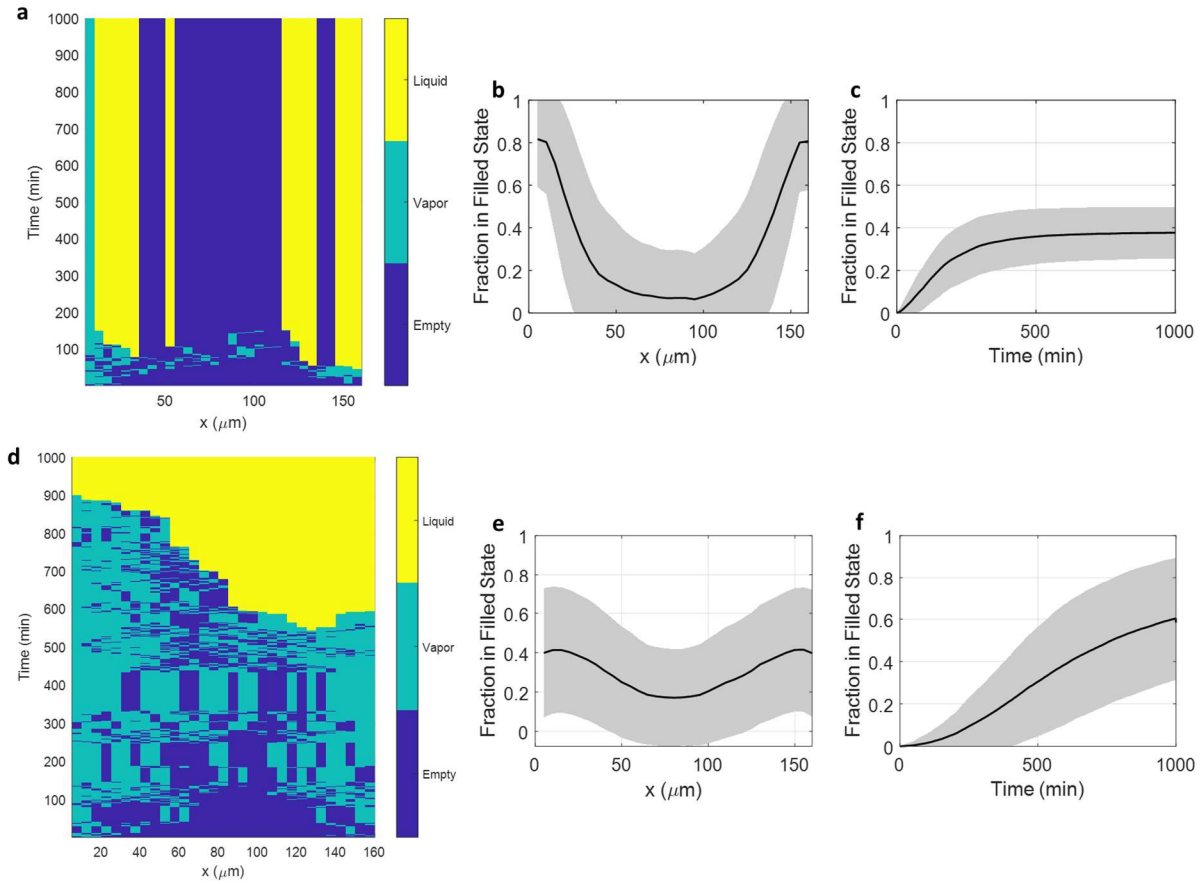

Figure 6-4 | Kinetic Monte Carlo (KMC) simulations showing dynamics of nucleation and growth inside isolated carbon nanotubes. (a) Sample trajectory of a 160 μm carbon nanotube segment showing empty, vapor, and liquid domains with parameters $D = 10^{-12} m^2/s$ and $k_{nuc} = 10^{-4}\, s^{-1}\mu m^{-1}$. (b-c) The mean and standard deviation over 1000 simulations, showing mean filling fraction q as a function of position and time, for parameters $D = 10^{-12} m^2/s$ and $k_{nuc} = 10^{-4}\, s^{-1}\mu m^{-1}$. (d) Sample trajectory of a 160 μm carbon nanotube segment showing empty, vapor, and liquid domains with parameters $D = 10^{-1}\ m^2/s$ and $k_{nuc} = 10^{-5}\, s^{-1}\mu m^{-1}$. (e-f) The mean and standard deviation over 1000 simulations, showing mean filling fraction q as a function of position and time, for parameters $D = 10^{-1}\ m^2/s$ and $k_{nuc} = 10^{-5}\, s^{-1}\mu m^{-1}$.

6.3 Discussion

Previous studies of nanofluidic transport inside isolated single-digit nanopores, and particularly inside carbon nanotubes[9] and van der Waals assemblies with 2D material spacers,[11] studied flow dynamics under conditions of complete nanopore filling. This study, by contrast, addresses the dynamics of nanopore filling and emptying transitions, partly because these transitions have been neglected in precision nanopore systems, with few exceptions,[10] and partly because the spectroscopic techniques that we have developed distinguish between empty and

filled carbon nanotubes but do not directly detect fluid or ion flow. While there are substantial uncertainties in transport parameters as extracted from these measurements inside isolated, substrate-bound CNTs, we show that the diffusion coefficient of water inside carbon nanotubes of various diameters from 0.90 nm to 1.66 nm is roughly 10^{-11} to $10^{-12} m^2/s$, far less than the bulk self-diffusion coefficient of liquid water, $2.3 \times 10^{-9}\, m^2/s$ at 25 ℃.

We conclude that capillary filling under these conditions of extreme nanoconfinement does not follow a Washburn-type mechanism, but rather proceeds by nucleation and growth with slow diffusion. The lack of unidirectional, Washburn-type filling precludes the calculation of a slip flow from capillary filling measurements inside sub-2 nm carbon nanotubes, preventing the extension of the CNT slip length results from Secchi et al.[9] to still lower diameters. Yet this lack of monotonicity, and the unexpected mechanism by which CNTs near the atomic scale fill with liquid-like water, even under water immersion, opens substantial new opportunities as well. Fluid filling by condensation and growth in CNT and related nanopore systems may be useful applications in which phase interfaces and multiphase flows are desired, including membrane distillation.

6.4 Methods

Carbon nanotube growth and segmentation. Ultra-long carbon nanotubes were grown on marked silicon substrates by chemical vapor deposition as described previously.[12,16,17,26] A CNT-containing catalyst solution (Nano-C APT 25, 0.7 µL) was deposited on a custom-made 9 mm by 14 mm Si wafer with lithographic marks for localization. CNTs were grown at 970 °C for 45 minutes in a mixed methane/hydrogen gas feed, then cut into 40 µm segments or 160 µm segments by a gallium focused ion beam (FEI Helios 600i). Typical conditions for FIB cutting were 30 kV, 9 pA, 5 µs dwell time, and 100 passes. Ultra-pure water (ASTM Type II, Sigma Aldrich) was used for water droplet and water immersion experiments.

Raman spectroscopy. A confocal micro-Raman spectrometer (Horiba LabRAM HR Evolution with Invictus 100 mW 532 nm laser) was used for Raman spectroscopy. Observation of a single carbon nanotube requires resonance between an electronic transition in the carbon nanotube and the laser excitation;[27,28] the large majority of as-grown CNTs that were not strongly resonant were not studied in this analysis. Typical spectrometer settings include a diffraction grating with 1800 gr/mm, hole 500 µm, and slit 150 µm. The Raman instrument is configured in a backscattering geometry, with linear polarization of light along the axis of the nanotube. The acquisition time was varied from sample to sample to balance temporal and spatial resolution with signal-to-noise ratio. A typical spectrum required acquisition for 2 to 10 s. Dew point condensation measurements required the use of a liquid nitrogen cooled microscope temperature stage (Linkam Scientific THMS350EV with LNP95).

Data analysis. Raman lineshapes were fit to a single Lorentzian curve:

$$y = \frac{2\Gamma I/\pi}{(x-\omega)^2+4\Gamma^2} + C \qquad [6.6]$$

with intensity I (counts), peak position ω (cm^{-1}), and full-width half maximum (FWHM) Γ (cm^{-1}), and background C. Raman lineshapes were also fit to two-peak Lorentzians:

$$y = \frac{2\Gamma_1 I_1/\pi}{(x-\omega_1)^2+4{\Gamma_1}^2} + \frac{2\Gamma_2 I_2/\pi}{(x-\omega_2)^2+4{\Gamma_2}^2} + C \quad [6.7]$$

with two peak intensities I_1 and I_2, peak centers ω_1 and ω_2, and FWHMs Γ_1 and Γ_2 in the empty state (1) and filled state (2). The filling fraction, q, was calculated from the magnitude of I_1 and I_2 as described in the main text. Data analysis, KMC simulations, and optimization were performed in Matlab, with optimization to non-linear error function fits using fmincon.

6.5 References

1. Faucher, S. *et al.* Critical Knowledge Gaps in Mass Transport through Single-Digit Nanopores: A Review and Perspective. *J. Phys. Chem. C* **123**, 21309–21326 (2019).
2. Cohen-Tanugi, D. & Grossman, J. C. Water desalination across nanoporous graphene. *Nano Lett.* **12**, 3602–3608 (2012).
3. Werber, J. R., Osuji, C. O. & Elimelech, M. Materials for next-generation desalination and water purification membranes. *Nat. Rev. Mater.* **1**, (2016).
4. Falk, K., Sedlmeier, F., Joly, L., Netz, R. R. & Bocquet, L. Molecular Origin of Fast Water Transport in Carbon Nanotube Membranes: Superlubricity versus Curvature Dependent Friction. *Nano Lett.* **10**, 4067–4073 (2010).
5. Pomerantseva, E., Bonaccorso, F., Feng, X., Cui, Y. & Gogotsi, Y. Energy storage: The future enabled by nanomaterials. *Science (80-.).* **366**, (2019).
6. Borgnia, M., Nielsen, S., Engel, A. & Agre, P. Cellular and Molecular Biology of the Aquaporin Water Channels. *Annu. Rev. Biochem.* **68**, 425–458 (1999).
7. Washburn, E. W. The dynamics of capillary flow. *Phys. Rev.* **17**, 273–283 (1921).
8. Dimitrov, D. I., Milchev, A. & Binder, K. Capillary rise in Nanopores: Molecular dynamics evidence for the Lucas-Washburn equation. *Phys. Rev. Lett.* **99**, 1–4 (2007).
9. Secchi, E. *et al.* Massive radius-dependent flow slippage in carbon nanotubes. *Nature* **537**, 210–213 (2016).
10. Yang, Q. *et al.* Capillary condensation under atomic-scale confinement. *Nature* **588**, 250–256 (2020).
11. Radha, B. *et al.* Molecular transport through capillaries made with atomic-scale precision. *Nature* **538**, 222–225 (2016).
12. Agrawal, K. V., Shimizu, S., Drahushuk, L. W., Kilcoyne, D. & Strano, M. S. Observation of extreme phase transition temperatures of water confined inside isolated carbon nanotubes. *Nat. Nanotechnol.* **12**, 267–273 (2017).
13. Heiranian, M. & Aluru, N. R. Nanofluidic Transport Theory with Enhancement Factors Approaching One. *ACS Nano* **14**, 272–281 (2020).
14. Hassan, J. *et al.* Ultrafast Stratified Diffusion of Water Inside Carbon Nanotubes; Direct Experimental Evidence with 2D D−T 2 NMR Spectroscopy. *J. Phys. Chem. C* **122**, 18 (2018).
15. Liu, X., Pan, X., Zhang, S., Han, X. & Bao, X. Diffusion of water inside carbon nanotubes studied by pulsed field gradient NMR spectroscopy. *Langmuir* **30**, 8036–8045 (2014).
16. Faucher, S. *et al.* Diameter Dependence of Water Filling in Lithographically Segmented Isolated Carbon Nanotubes. *ACS Nano* **15**, 2778–2790 (2021).

17. Kuehne, M. *et al.* Impedance of Thermal Conduction from Nanoconfined Water in Carbon Nanotube Single-Digit Nanopores. *J. Phys. Chem. C* **125**, 25717–25728 (2021).
18. Yang, F. *et al.* Chirality Pure Carbon Nanotubes: Growth, Sorting, and Characterization. *Chemical Reviews* vol. 120 2693–2758 (2020).
19. Zhang, D. *et al.* (n,m) Assignments and quantification for single-walled carbon nanotubes on SiO2/Si substrates by resonant Raman spectroscopy. *Nanoscale* **7**, 10719–10727 (2015).
20. Striolo, A. The mechanism of water diffusion in narrow carbon nanotubes. *Nano Lett.* **6**, 633–639 (2006).
21. Avrami, M. Kinetics of phase change. I: General theory. *J. Chem. Phys.* **7**, 1103–1112 (1939).
22. Woo, E., Huh, J., Jeong, Y. G. & Shin, K. From homogeneous to heterogeneous nucleation of chain molecules under nanoscopic cylindrical confinement. *Phys. Rev. Lett.* **98**, (2007).
23. Nomura, K. *et al.* Evidence of low-density and high-density liquid phases and isochore end point for water confined to carbon nanotube. *Proc. Natl. Acad. Sci. U. S. A.* **114**, 4066–4071 (2017).
24. Noy, A. Kinetic model of gas transport in carbon nanotube channels. *J. Phys. Chem. C* **117**, 7656–7660 (2013).
25. Lee, J., Laoui, T. & Karnik, R. Nanofluidic transport governed by the liquid/vapour interface. *Nat. Nanotechnol.* **9**, 317–323 (2014).
26. Choi, W. *et al.* Diameter-dependent ion transport through the interior of isolated single-walled carbon nanotubes. *Nat. Commun.* **4**, 1–8 (2013).
27. Jorio, A. *et al.* Characterizing carbon nanotube samples with resonance Raman scattering. *New J. Phys.* **5**, (2003).
28. Jorio, A., Saito, R., Dresselhaus, G. & Dresselhaus, M. S. *Raman Spectroscopy in Graphene Related Systems*. *Raman Spectroscopy in Graphene Related Systems* (John Wiley & Sons, 2011). doi:10.1002/9783527632695.

7. A Virucidal Face Mask Based on the Reverse-flow Reactor Concept

This chapter has been adapted from "A Virucidal Face Mask Based on the Reverse-flow Reactor Concept for Thermal Inactivation of SARS-CoV-2," by Samuel Faucher, Daniel James Lundberg, Xinyao Anna Liang, Xiaojia Jin, Rosalie Phillips, Dorsa Parviz, Jacopo Buongiorno, and Michael S. Strano, *AIChE J.* **2021**, *67* (6), 1–15. https://doi.org/10.1002/aic.17250.

Abstract

While facial coverings reduce the spread of SARS-CoV-2 by viral filtration, masks capable of viral inactivation by heating can provide a complementary method to limit transmission. Inspired by reverse-flow chemical reactors, we introduce a new virucidal face mask concept driven by the oscillatory flow of human breath. The governing heat and mass transport equations are solved to evaluate virus and CO_2 transport. Given limits imposed by the kinetics of SARS-CoV-2 thermal inactivation, human breath, safety, and comfort, heated masks may inactivate SARS-CoV-2 to medical-grade sterility. We detail one design, with a volume of 300 mL at 90 °C, that achieves a 3-log reduction in viral load with minimal impedance within the mask mesh, with partition coefficient around 2. This is the first quantitative analysis of virucidal thermal inactivation within a protective face mask, and addresses a pressing need for new approaches for personal protective equipment during a global pandemic.

7.1 Introduction

Face masks reduce the rate of person-to-person transmission of coronaviruses, influenza, and other respiratory viruses from breath and coughing.[1–3] During the COVID-19 pandemic, widespread adoption of effective masks has led to improved health outcomes around the world.[1,4] Face masks, however, are not uniformly effective in preventing person-to-person viral spread, and availability during the COVID-19 pandemic has often been limited.[3] An overwhelming majority of masks that have been employed during the pandemic, including N95 respirators, reduce viral transport by mechanical filtration at ambient temperature.[5] In contrast, there has been a dearth of versions designed around thermal viral inactivation and sterilization of air flow.

As an engineering problem, the cyclic reversal of air flow associated with human inhalation and exhalation enables a particular chemical reactor design: the reverse-flow reactor. A reverse-flow reactor[6–9] periodically reverses the direction of the convective feed through a one-dimensional reactor, typically a packed bed, to propagate a reactive zone over lengths that exceed the physical dimensions of the reactor. After the first patent filing by Frederick Cottrell in 1935,[10] reverse-flow reactors have been used industrially for nearly a half century and are well-studied.[6,8,11,12] This type of reactor offers several advantages when compared to unidirectional packed bed reactors. Depending on the frequency of flow direction switching, the reaction zone for an exothermic reaction can extend beyond the physical limits of the reactor in both directions, increasing conversion, reducing the need for heat exchange, limiting reactor fouling,[6] and improving stability to fluctuating inputs.[11] Coupling between heat and momentum transfer results in several periodic steady states.[12] While canonical reverse-flow reactors involve exothermic reactions, reverse-flow reactor designs can be applied to endothermic and mixed endothermic-exothermic systems as well.[12] In the case of a heated mask, the reaction (i.e. thermal inactivation of SARS-CoV-2) is not appreciably endothermic or exothermic, decoupling the temperature profile from the extent of reaction. In a strict sense, this eliminates some of the advantages of a reverse-flow reactor design. The reverse-flow concept in a virucidal mask, however, is imposed by the oscillations of human breath, not consciously selected by the engineer. Concepts taken from reverse-flow reactors, particularly the idea of distinct operating regimes delineated by bifurcation variables,[7] can be applied to a heated mask and yield insight to its design.

A heated mask to inactivate SARS-CoV-2 represents a new concept for personal protective equipment to address a critical and timely challenge. Thermal inactivation in a non-mask context has been widely discussed as a way to sterilize surfaces and objects to prevent transmission of the coronavirus.[13–15] Air circulation and heating of rooms and buildings has been proposed to reduce spread of SARS-CoV-2 in air as well.[16] With respect to masks, mechanical filtration is the main mechanism of pathogen impedance to date. N95 respirators and other mechanical filtration masks operate by interception, inertial impaction, and diffusion of particles, resulting in rejection of a majority of particles with sizes from the sub-micron scale to micron scale.[5] While N95 respirators are recommended for use in health care environments,[17] they are designed for single use and widespread adoption by non-healthcare workers can lead to shorages.[18] Reusable masks, such as cloth masks, offer substantial social benefit but may not offer adequate levels of protection from coronavirus in all circumstances,[19] while efforts to reuse masks (like N95 respirators) that are designed for single use may also reduce filtration efficiency.[20–22] Mask shortages, the generation of waste from single-use facemasks, and the

spread of the COVID-19 pandemic to regions of the world with weaker healthcare infrastructure present an urgent need to reconsider designs and concepts for protective face masks.[3,23] In response, we propose a mask that blocks SARS-CoV-2 by thermal inactivation rather than mechanical filtration. Such masks have not been analyzed before in detail, making this the first quantitative analysis of the temperatures, volumes, and materials that could be used for thermal inactivation of a pathogen in a protective face mask.

In this work, we present a concept for a reusable facemask which contains a heated, porous mesh to thermally inactivate SARS-CoV-2. We formulate coupled mass and energy balances across a mask to create a design space that maps the operating temperature, mask volume, and air flow to viral load reduction and CO_2 accumulation. We analyze the wearable heated mask as a thermochemical reverse-flow reactor, and explore its design given three key model inputs: (1) oscillatory breath flow, (2) first-order thermal inactivation of SARS-CoV-2, and (3) a maximum allowable pressure drop. We propose a 300 mL mask that operates at a temperature of 90 °C, containing a copper mesh with an approximate mesh diameter of 0.1 mm. We show that this mask design can achieve a 3-log reduction in virus concentration with moderate viral impedance, in which virus particles travel one-third as fast as air inside the mask, or a 6-log reduction in virus concentration with higher viral impedance. By considering adsorption and desorption mechanisms and setting an overall pressure drop constraint, we determine that these partition coefficients can likely be achieved. These results show that a heated face mask is a promising, new design to reduce person-to-person spread of SARS-CoV-2, and will inform future prototyping and more detailed 3D modelling of pathogen thermal inactivation in heated face masks.

7.2 Problem Statement

A heated mask for thermal inactivation of SARS-CoV-2 contains a well-specified interior volume with a porous mesh, insulating outer layer, inlets to the bulk, and outlets to the nose and mouth, as shown in **Figure 7-1a-b**. This can be conceptualized as a 1D domain of length L, as shown in **Figure 7-1c-d**. The mask design is bounded by several constraints, including the volume and period of human breath, coronavirus inactivation kinetics, and a maximum pressure drop for safety and comfort. Within this design space, the optimal face mask is compact, achieves high viral inactivation, allows CO_2 exhalation, operates within a safe temperature range, and can be battery-powered for an extended time. These performance metrics, particularly the log reduction in viral concentration, depend on the mask volume, temperature, and a partition coefficient K_p. Five aspects of problem formulation – human breath, SARS-CoV-2 thermal inactivation, mass transfer, heat transfer, and viral impedance – are discussed below.

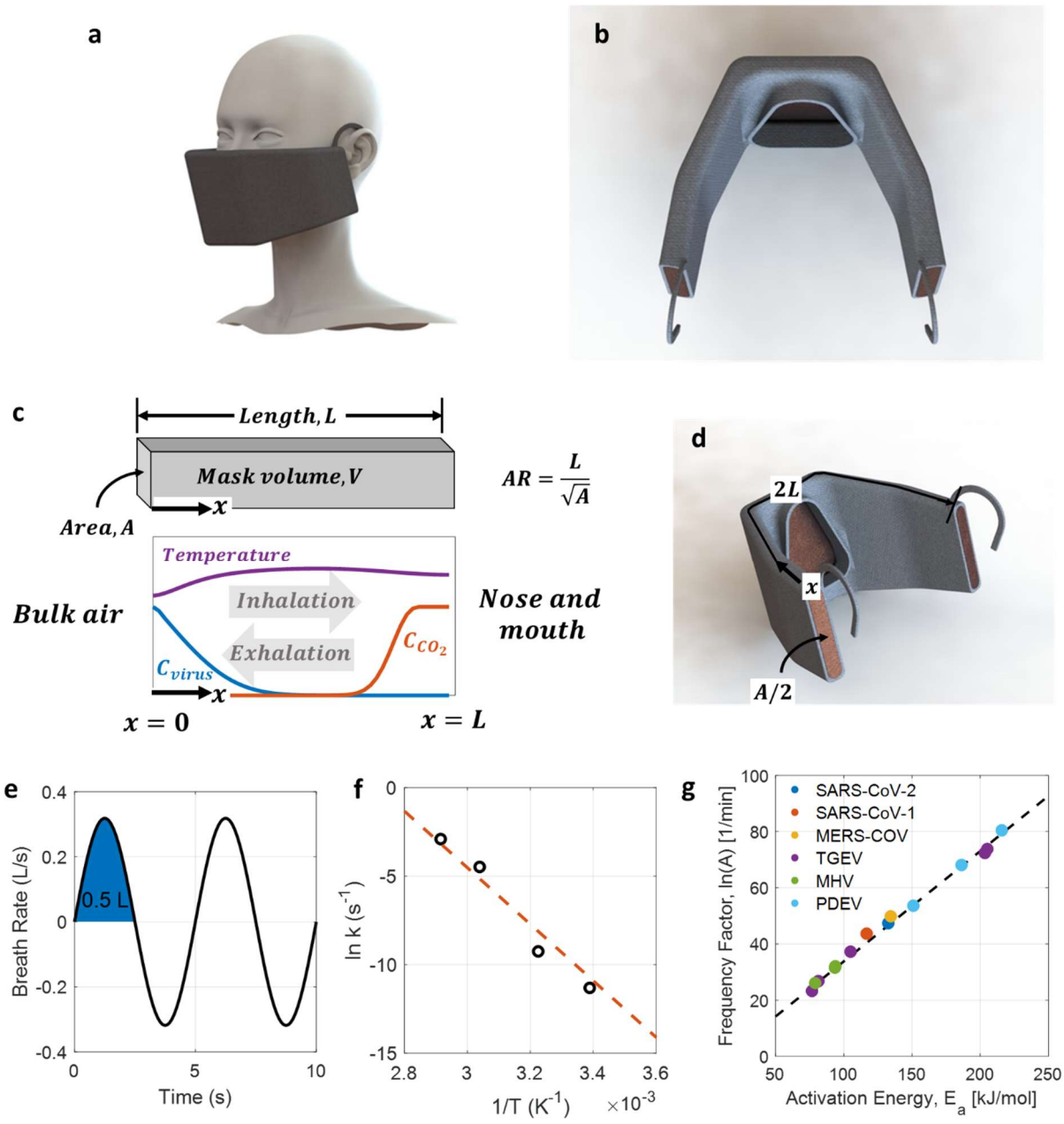

Figure 7-1 | Heated mask design and problem formulation. (a) CAD drawing of a 0.3 L mask. The final proposed design is a mask with a volume of 0.3 L at an operating temperature of 90 °C, which can cause thermal inactivation of SARS-CoV-2 and operate comfortably with insulation and cooling. (b) A second CAD drawing of a 0.3 L mask, showing a porous 0.6 mm diameter copper mesh interior, 0.3 cm thick neoprene insulation, two inlets for air on the sides of the mask, and one outlet to the nose and mouth. (c) The interior of the mask can be modelled as a 1D domain extending from bulk air at $x = 0$ to the nose and mouth at $x = x_{max}$. The mask length, cross-sectional area, and aspect ratio are defined. Temperature, virus concentration, and CO_2 concentration vary with position and time within the domain. Neumann and Danckwerts boundary conditions are enforced at $x = 0$ and $x = L$, and switch

with inhalation and exhalation. (d) CAD drawing showing the 1D coordinate system and dimensions superimposed on the 3D mask.
(e) Sinusoidal approximation of human breath waveform, with a period of 5 seconds and a tidal volume of 0.5 L. (f) Thermal inactivation of SARS-CoV-2 follows first order kinetics, with a linear relationship between the natural log of the rate constant, ln k, and inverse temperature, 1/T. Data reproduced from Chin et al.[27] (g) Thermal inactivation of SARS-CoV-2 is well-characterized, with first-order rate parameters following a Meyer-Neldel rule in agreement with other coronaviruses like the first Severe Acute Respiratory Syndrome coronavirus (SARS-CoV-1), Middle East Respiratory Syndrome (MERS-CoV), Transmissible Gastroenteritis Virus (TGEV), Mouse Hepatitis Virus (MHV), and Porcine Epidemic Diarrhea Virus (PEDV). Data reproduced from Yap et al.[28]

Human Breath: The oscillations of human breath impose a periodically reversing flow through the mask, in analogy with a reverse-flow reactor. The tidal volume, which is the volume of air displaced between inhalation and exhalation, is assumed to be 0.5 L,[24] while the period is assumed to be 5 seconds.[24] To ensure comfort, the pressure drop is held below 60 Pa L^{-1} s^{-1} at maximum flow, which represents the threshold for detection of inspiratory resistance.[25] The velocity within the mask, $U(t)$, is assumed to be sinusoidal:[26]

$$U(t) = U_{max} \cdot \sin\left(\frac{2\pi t}{\tau}\right) \quad [7.1]$$

Where U_{max} is the maximum velocity and τ is the period. The assumed breath waveform is shown in **Figure 7-1e.** Positive velocities represent inhalation, and negative velocities represent exhalation.

Thermal Inactivation of SARS-CoV-2: The thermal inactivation of a virus, including SARS-CoV-2, follows well-characterized kinetics. It can be conceptualized as a first-order chemical reaction with a rate that varies with temperature as shown below:

$r = -k(T)C$ [7.2]

where r is the reaction rate, k is the first-order rate constant for thermal inactivation, and C is viral concentration. The rate of thermal inactivation of SARS-CoV-2 was fit following an Arrhenius relationship of the following form:

$$\ln(k) = -\frac{E_a}{RT} + \ln(A) \quad [7.3]$$

where k is the first-order rate constant for thermal inactivation, E_a is the activation energy for inactivation, R the gas constant, T the temperature, and A the frequency factor. We fit experimental data obtained from Chin et al.[27] for SARS-CoV-2, as shown in **Figure 7-1f**, to find an activation energy of 132.6 kJ mol^{-1} and a natural log of the frequency factor, $\ln(A)$, of 47.4. The correlation between the two fit parameters, E_a and $\ln(A)$, follows a Meyer-Neldel rule that is suggestive of protein denaturation at high temperatures,[28] and is in agreement with the kinetics of thermal inactivation of a broad range of other coronaviruses, including the first Severe Acute Respiratory Syndrome coronavirus (SARS-CoV-1), Middle East Respiratory Syndrome (MERS-CoV), Transmissible Gastroenteritis Virus (TGEV), Mouse Hepatitis Virus (MHV), and Porcine

Epidemic Diarrhea Virus (PEDV), as reported by Yap et al[28] and plotted in **Figure 7-1g**. While experimental data for thermal inactivation of SARS-CoV-2 extends only from room temperature to 70 °C, data and model predictions for several coronaviruses collected by Jiang et al.[29] extend to temperatures of 120 °C and justify the kinetics assumed in this analysis, as shown in **Figure 7-S1.**

Mass Transfer: A 1D reaction-convection-diffusion model was used to analyze the concentration of virus and carbon dioxide inside a domain which extends through a mask from the mouth to bulk air. The governing equation for this system is as follows:[30]

$$\frac{\partial C(x,t)}{\partial t} = -U(t)\frac{\partial C(x,t)}{\partial x} + D_e\frac{\partial^2 C(x,t)}{\partial x^2} + r(C,x,t) \quad [7.4]$$

where x is position, t is time, and D_e is the dispersion coefficient.

The dispersion coefficient for the virus traveling within the mask is estimated as 5×10^5 m^2/s, taken from experimental evaluations of dispersion resulting from fluid flow through a mesh-screen packed column.[31] Virus concentration in exhaled breath is assumed to be zero, while virus concentration in the bulk is set to an arbitrary value C_0. During inhalation, Neumann boundary conditions are applied at the mouth and Danckwerts boundary conditions at the mask edge; these conditions are switched for exhalation.[32,33] Partial differential equations within the 1D mask domain were solved in MATLAB using function *pdepe* to obtain profiles of virus concentration, CO_2 concentration, and temperature during inhalation and exhalation.

Heat Transfer: The temperature distribution is governed by a similar equation to that of the concentration profiles. The temperature and concentration PDEs are not coupled: the temperature profile determines the concentration profiles, but the concentration profiles do not affect the temperature profile due to the negligible heat of reaction. The mask is assumed to contain a porous copper mesh which is heated by Joule heating, causing thermal inactivation of virus as well as slowing viral transport. Rapid thermal equilibrium between the mesh packing and air is assumed, while radiative heat transfer, work done by pressure changes, and viscous dissipation are ignored.[34] Validation of thermal equilibrium approximation is included in the supplementary section. Under these simplifications, the governing equation for the thermal distribution within a mask containing solid and fluid phases is as follows:

$$(\rho c)_m\frac{\partial T}{\partial t} + (\rho c_p)_f\varphi U_0\frac{\partial T}{\partial x} = k_m\frac{\partial^2 T}{\partial x^2} + q - \frac{h_{eff}P_m(T-T_{amb})}{A_c} \quad [7.5]$$

$$(\rho c)_m = (1-\varphi)(\rho c)_s + \varphi(\rho c_v)_f \quad [7.6]$$

$$k_m = (1-\varphi)k_s + \varphi k_f \quad [7.7]$$

$$q = \frac{W}{A_c * L} \quad [7.8]$$

$$\frac{1}{h_{eff}} = \frac{1}{h_f} + \frac{L_{ins}}{k_{ins}} \quad [7.9]$$

The subscripts s and f refer to a solid phase (i.e. copper mesh) and a fluid phase (i.e. virus-laden air), respectively. c is the specific heat of copper and is taken as 400 W mK^{-1}, c_p is the specific heat at constant pressure of the fluid and is taken as 1020 J kg^{-1} K^{-1}, U_0 is the superficial velocity of the fluid, k_m is the effective thermal conductivity, q is the heat production per unit volume, W is the imposed electric power, A_c is the mask flow area, L is the length of the mask, P_m is the perimeter, T_{amb} is the ambient temperature taken as 20 °C, h_{eff} is the effective heat transfer coefficient, h_f is the free convection heat transfer coefficient for air on the outside surface of the mask and is taken as 2 W m^{-2} K^{-1}, and L_{ins} and k_{ins} are the thickness and thermal conductivity of insulator material, which we assume for sake of comparison is neoprene and 0.3 cm thick. The porosity of the mesh, φ, is taken as a constant 0.9. During inhalation, the outflow Neumann boundary condition is applied at the mouth and the Danckwerts boundary condition at the mask edge.[32,33] During exhalation, the boundary conditions are flipped:

$$k_m \frac{dT(x=0,t_{inh})}{dx} A_f = \dot{m} C_p (T|_{x=0} - T_{amb}), \dot{m} > 0 \quad [7.10]$$

$$-k_m \frac{dT(x=a,t_{in})}{dx} = 0 \quad [7.11]$$

$$k_m \frac{dT(x=a,t_{exh})}{dx} A_f = \dot{m} C_p \left(T|_{x=a} - T_{body}\right), \dot{m} < 0 \quad [7.12]$$

$$-k_m \frac{dT(x=0,t_{ex})}{dx} = 0 \quad [7.13]$$

Physically speaking, heat transferred at the outer surface of the mask preheats the cold air that enters the mask when inhaling (**Equation 10**) when exhaling, air that is breathed out also heats up due to the heat transfer at the mask-mouth interface (**Equation 12**). The temperature of the air entering the mask is taken to be 20 °C, and the temperature of the exhaled air is taken to be 37 °C.

Viral Impedance: Virus in the mask is subject to thermal inactivation, but it is also impeded by the porous mesh as in other masks that operate purely by filtration. Numerous mathematical models have been developed to predict the particle transport and retention in porous media, using either macroscopic or microscopic approaches.[35,36] Macroscopic methods use the particle transport equation in a continuous media:

$$\varphi \frac{\partial C}{\partial t} + \frac{\partial (UC)}{\partial x} = -\Lambda UC \quad [7.14]$$

in which Λ is the filtration coefficient, which is related to many parameters including pore structure, particle size distribution, and the particle-surface interactions that govern the particle adsorption and release on/from the surface. Theoretical calculation of Λ is very difficult, so its value is usually determined experimentally.[37–39]

On the other hand, microscopic approaches investigate the particle retention at pore scale, using direct models such as CFD-DEM6 or, more recently, pore network modeling.[40–43] Pore network modelling starts with force balances on a single particle, accounting for hydrodynamic

drag, body force, electrostatic, van der Waals, and inertial force and relating the particle velocity to fluid velocity:

$$U_p = U - \frac{1}{6\pi\mu R}(F_B + F_E + F_V) \quad [7.15]$$

in which U_p is the particle velocity, F_B is body force, F_E is the electrostatic force and F_V is the van der Waals force. Estimates for each force term can be determined from particle and surface potentials. In addition to advection, the Brownian diffusion of virus must also be included in its microscopic transport formulation. Additionally, particle retention in the porous mesh occurs via particle adsorption and binding to the mesh. Each of these steps may be explained by a combination of phenomena including gravitation sedimentation, Brownian motion, and surface forces. Eventually, these single-particle equations must be applied to an interconnected network of pores and throats.[44] In the absence of an experimentally measured filtration coefficient and other parameters for SARS-CoV-2 and to avoid the complicated pore network modeling, a simple model relating the virus velocity to bulk air velocity must be used. We introduce a simple model of viral impedance within the mask, where the virus is subject to slowing according to a partition coefficient K_p as shown below:

$$U_{vir} = \frac{U}{1+K_p} \quad [7.16]$$

In this case, U_{vir} is the effective virus velocity and U is the bulk air velocity. Viral impedance occurs because virus particles adsorb to the copper mesh and desorb from the copper mesh in two first-order processes. The partition coefficient K_p can be defined as the ratio of these two rates:

$$K_p = \frac{k_{ads}}{k_{des}} \quad [7.17]$$

where k_{ads} is the virus adsorption rate constant, while k_{des} is the virus desorption rate constant. Mask performance metrics, including viral inactivation and CO_2 concentration, can be calculated as a function of mask volume, mean temperature, and partition coefficient K_p.

7.3 Results and Discussion

7.3.1 Mask Design

Equation 4 and **Equation 5**, which govern temperature, virus concentration, and CO_2 concentration within the mask as function of position and time, were solved in Matlab using function *pdepe*. Time-variant virus, CO_2, and temperature profiles for a 300 mL mask operating at a mean temperature of 90 °C are shown in **Figure 7-2**, with inhalation in **Figure 7-2a-c** and exhalation in **Figure 7-2d-f**. Boundary conditions, as described above, fix the virus and CO_2 concentrations at the mask-bulk air interface ($x = 0$) and mask-mouth interface ($x = L$) during inhalation and exhalation, in accordance with the coordinate system presented in **Figure 7-1c**. The CO_2 concentration of exhalation was fixed at the mask-mouth interface at 3.8%, while the

CO_2 concentration in bulk air is essentially zero. During inhalation, in **Figure 7-2a,** virus is inhaled but does not reach the mask-mouth interface due to viral impedance and thermal inactivation. A large majority of non-inactivated virus is exhaled, as shown in **Figure 7-2d.** CO_2, by contrast, is transported faster and is not subject to thermal inactivation. Air with near-zero CO_2 concentration is inhaled in **Figure 7-2b**, while air with high CO_2 concentration is exhaled in **Figure 7-2e** and transported across the mask to the bulk. For this design, a mean temperature of 80 °C, as shown in **Figure 7-2c** and **Figure 7-2f**, is achieved with a power input of 18.89 W. Concentration and temperature profiles for candidate designs with different volumes and temperatures are similar to the profiles shown.

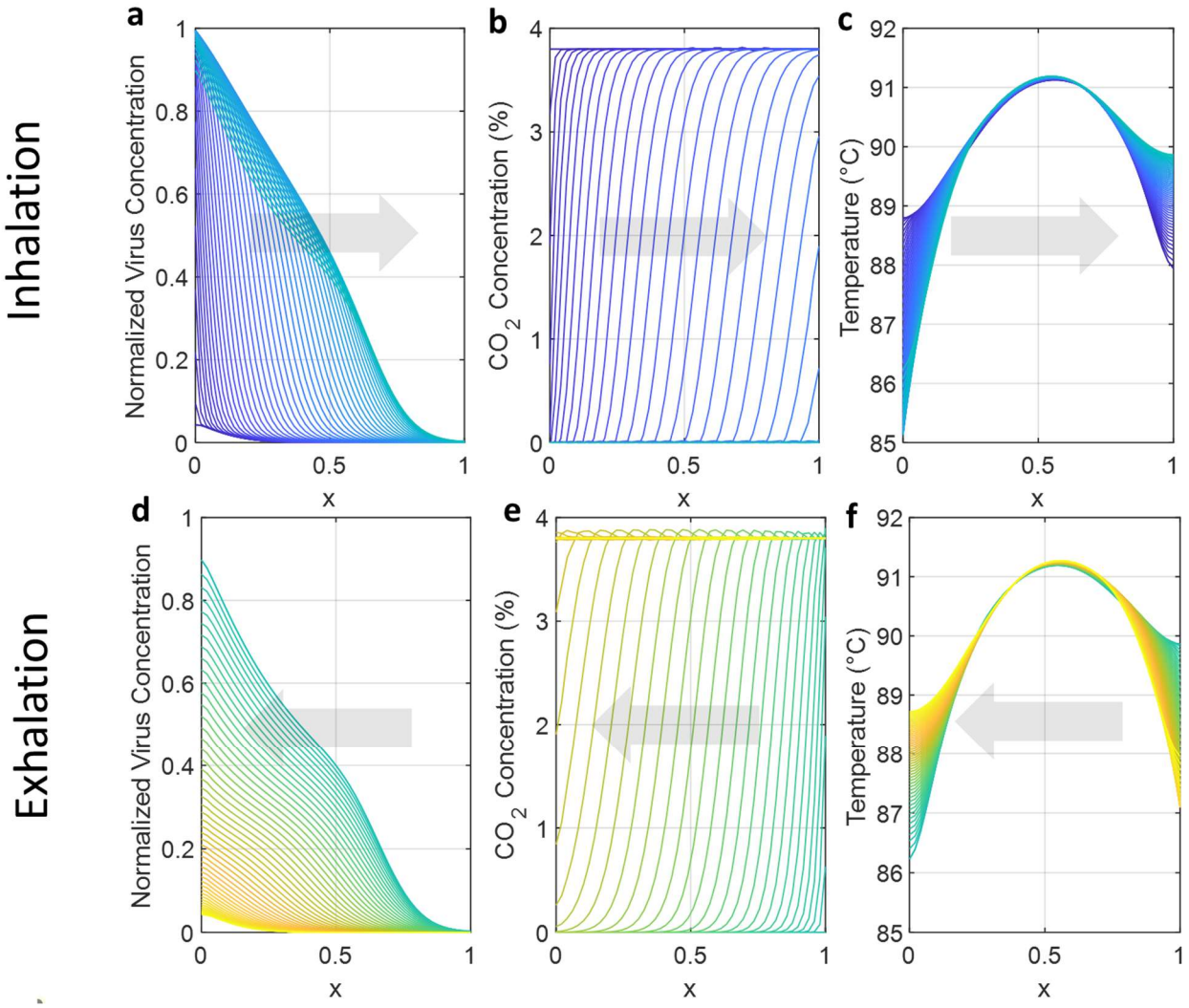

Figure 7-2 | Viral concentration, CO_2 concentration, and temperature vary with position and time during a single 5 s cycle of inhalation (a,b,c) and exhalation (d,e,f) in the 1D mask model. The mask extends from bulk air ($x = 0$) to the mouth ($x = 1$). In this case, the mask volume is 0.3 L, the aspect ratio is 3, the partition coefficient (K_p) is 2, and the power is 18.89 W, generating a mean temperature of 90 °C. (a) During inhalation, virus is impeded and inactivated, and is generally not transported from the bulk to the mouth. (b) During

inhalation, low-CO_2 concentration air is inhaled. (c) The mean temperature during inhalation is 90 °C, with slight variations. (d) During exhalation, active virus in the mask is generally transported back to the bulk. (e) During exhalation, CO_2 is transported from the mouth through the mask. (f) The mean temperature during exhalation is 90 °C, with slight variations.

Power requirements, average inhaled CO_2 concentration, and log viral inactivation are shown in **Figure 7-3** for masks ranging from 0.1 L to 1 L in volume, operating temperatures ranging from 40 °C to 140 °C, and K_p ranging from 0 to 10**.** Power requirements range from 3.79 W for a 0.1 L mask at 40 °C to 52.96 W for a 1 L mask at 140 °C. CO_2 concentration, as expected, does not vary with temperature, but varies strongly with mask volume. Given the poor mixing in the mask, the mask volume must be less than the human tidal volume (500 mL) in order to achieve a non-hazardous CO_2 concentration.[45] By comparing $\log_{10}$ viral reduction at low temperature to that at high temperature in **Figure 7-3**, the effect of thermal inactivation can be distinguished from the effect of filtration. This is shown explicitly in supplemental **Figure 7-S2**, which calculates the ratio of $\log_{10}$ viral reduction versus that at low temperature, as a function of mask temperature and volume. Thermal inactivation has an appreciable effect on SARS-CoV-2 transport at temperatures above 80 °C.

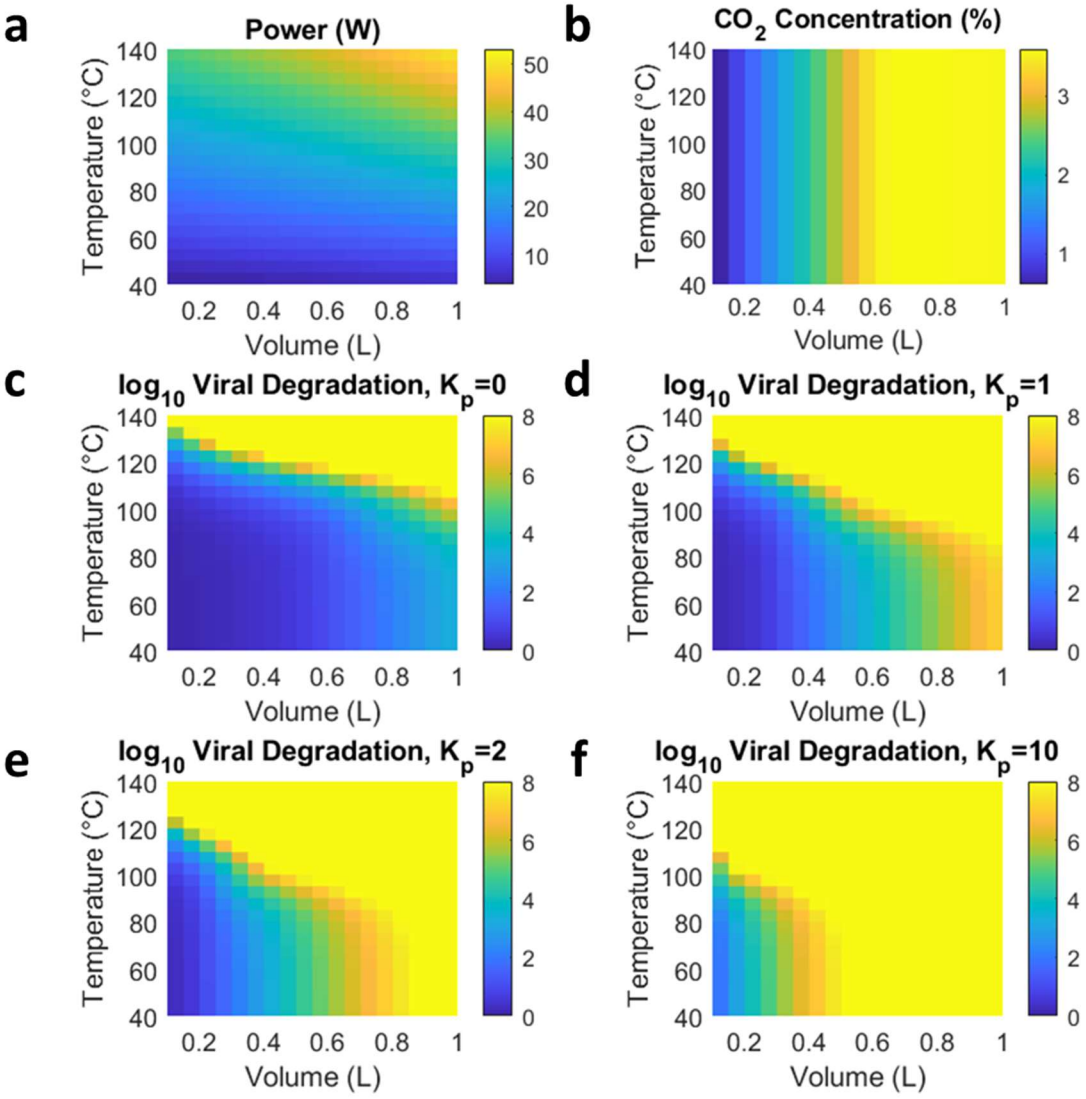

Figure 7-3. (a) Required power at steady state as a function of mask volume and operating temperature. Power requirements range from 3.79 W for a 0.1 L mask at 40 °C to 52.96 W for a 1 L mask at 140 °C. (b) Inhaled CO_2 concentration, averaged over a breath cycle. CO_2 concentration increases with increasing mask volume but is invariant with operating temperature. (c-f) $\log_{10}$ viral inactivation as a function of mask volume and mean operating temperature. Results are plotted for several values of the partition coefficient, K_p, which captures impedance of virus in the porous mask mesh, with $K_p=0$ indicating that virus is transported with the same velocity as air in the mask, while $K_p \gg 1$ indicates substantial slowing of viral particles relative to air.

Performance of heated masks in achieving specified log reductions in SARS-CoV-2 is presented in **Figure 7-4**. The required operating temperature to induce a specified viral load inactivation is plotted as a function of mask volume for a range of values of the partition

coefficient K_p. Two thresholds for viral inactivation are shown: a 3-log, or thousand-fold, reduction in inhaled viral concentration, and a 6-log, or million-fold, reduction in inhaled viral concentration. In general, 6-log reduction is the standard for sterilization.[46] In all cases, the mask aspect ratio – defined as the ratio of mask length to the geometric mean of cross-sectional dimensions – was set to 3.

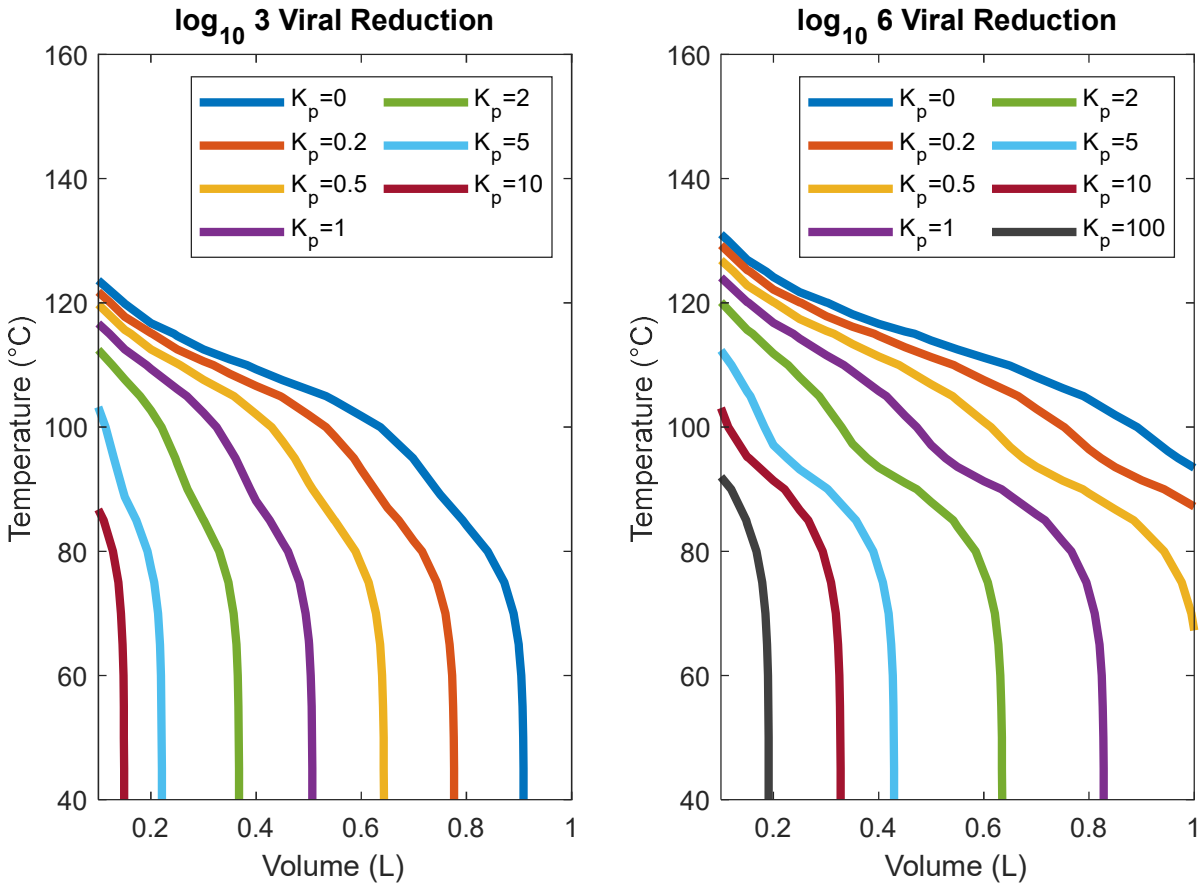

Figure 7-4. (a) Mask volume and operating temperature that are required to achieve 3-log reduction in SARS-CoV-2 concentration through a heated mask. Results are plotted as a function of a partition coefficient, K_p, which captures impedance of virus in the porous mask mesh, with $K_p = 0$ indicating that virus is transported with the same velocity as air in the mask, while $K_p \gg 1$ indicates substantial slowing of viral particles relative to air. A 3-log reduction in inhaled virus can be achieved in masks with volumes less than 0.4 L at temperatures below 100 °C if there is slight viral impedance in the mask ($K_p > 1$). (b) Mask volume and operating temperature that are required to achieve 6-log reduction, or sterilization, of SARS-CoV-2 concentration through a heated mask. A 6-log reduction in inhaled virus can be achieved in masks with volumes less than 0.4 L at temperatures below 100 °C with moderate viral impedance in the mask ($K_p > 2$).

A 3-log viral reduction can be achieved in a compact mask (<0.5 L) at a reasonable operating temperature (<100 °C) if viral transport is impeded moderately in the mask ($K_p > 1$),

as shown in **Figure 7-4a**. A 6-log viral reduction can be achieved within the same volume and temperature constraints with slightly higher virus impedance in the mask ($K_p > 2$), as shown in **Figure 7-4b**. Without viral impedance, where $K_p = 0$, temperatures exceeding 100 °C or volumes approaching 1 L are required to achieve 3-log viral reduction, while temperatures exceeding 100 °C and volumes exceeding 1 L are required to achieve 6-log viral reduction. The case of no viral impedance represents a worst-case scenario for mask function, as any reasonable mesh design would combine thermal inactivation with filtration and particle impedance to some degree.

Two regimes are apparent in **Figure 7-4**: At low temperatures, below 90 °C, viral reduction is due largely to viral impedance. Vertical lines in this range show that there is little temperature dependence, with large differences in required volume for different levels of K_p. By contrast, at high temperatures above 90 °C, viral reduction is due largely or entirely to thermal inactivation. The inflection and flattening of curves in this range show that the degree of viral reduction is substantially temperature dependent above 90 °C but decreasingly dependent on viral impedance, with only minor differences in required volume for different levels of K_p. At high temperatures, the virus is thermally inactivated so rapidly that viral reduction obtained for lower and higher values of K_p become nearly identical. While this is extremely promising for viral inactivation, operating at temperatures above 100 °C presents issues for power requirements and human safety. In general, the presence of these two regions and the transition between them suggests a tradeoff between heated mask volume and heated mask temperature. A small, hot mask can achieve a similar level of viral inactivation as a larger, cooler mask. The secondary tradeoff, however, is in CO_2 levels and user comfort; a small mask allows for lower CO_2 levels during inhalation, while a large mask can be operated at a milder temperature.

The optimal mask design is located at the knee of the curves in **Figure 7-4a-b**. This volume and temperature will make maximum use of both thermal inactivation and traditional filtration to reduce viral transport and ensure safety for the mask wearer and those around them. The mask volume also determines the CO_2 concentration: a mask volume below the tidal volume of 500 mL is necessary to allow sufficient CO_2 transport for comfortable breathing. Based on these criteria, we choose a mask volume of 300 mL and an operating temperature of 90 °C. Renderings of a 300 mL mask, showing a porous copper mesh interior, 0.3 cm thick neoprene insulation, two air inlets on the sides of the mask, and an outlet to the nose and mouth, are shown in **Figure 7-1a** and **Figure 7-1b**. The neoprene insulation constitutes most of the mask mass of 350 g without batteries, for a total mass of 600 g with batteries. Full details of the proposed design are compiled in **Table 7-1**.

7.3.2 Mask Performance Regimes

In analogy with reverse-flow chemical reactors,[9] the mask design space can be split into distinct regimes with qualitative differences in performance, as shown in **Figure 7-5**.

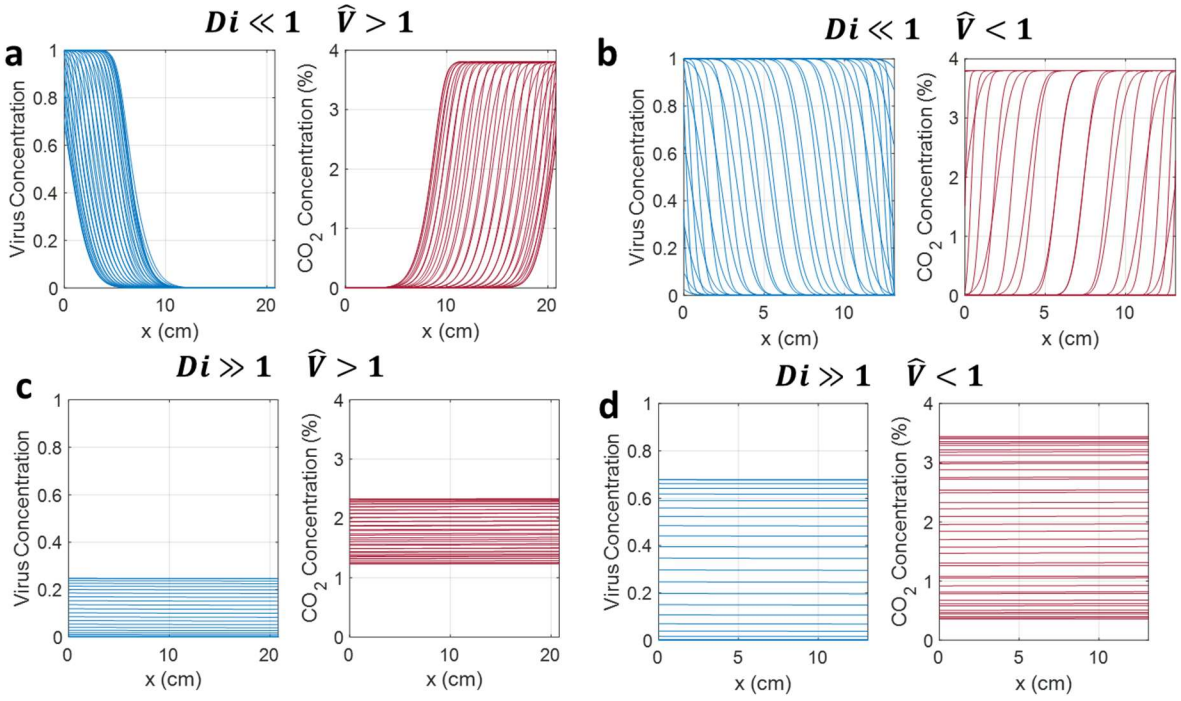

Figure 7-5. In analogy with reverse-flow chemical reactors, behavior of a heated mask can be split into different regimes depending on dispersion number Di and reduced volume $\hat{V}$. (a) The low Di, high $\hat{V}$ limit ("plastic bag limit") does not allow virus to reach the mouth but does not provide adequate ventilation. (b) The low Di, low $\hat{V}$ limit ("straw limit") provides ventilation but may allow viral inhalation depending on the viral inactivation rate. This is the most promising regime. (c) The large, well-mixed limit. Virus and CO_2 are well-mixed within the mask volume regardless of volume. (d) The small, well-mixed limit. At high Di, there is no bifurcation at $\hat{V} = 1$, so the small, well-mixed limit displays qualitatively similar behavior to the large, well-mixed limit, with temporal fluctuations in virus and CO_2 concentration during the breath cycle but near-zero spatial concentration gradients.

The four regimes are characterized by two dimensionless groups: the dispersion number (Di) and the reduced volume ($\hat{V}$). The reduced volume $\hat{V}$ is the ratio of mask volume to breath tidal volume; in the case of a reverse-flow reactor, this is the ratio of the residence time to the switching time:

$$\hat{V} = \frac{V_{mask}}{V_T} \qquad [7.18]$$

The dispersion number captures dispersion of reactants in a reactor. A reactor with $Di \gg 1$ will behave as a stirred-tank reactor, while a reactor with $Di \ll 1$ will behave as a plug-flow reactor:

$$Di = \frac{D_e}{UL} \qquad [7.19]$$

In this case, the $\boldsymbol{Di \ll 1}$ $\boldsymbol{\hat{V} > 1}$ limit, as shown in **Figure 7-5a**, has a large mask volume and is poorly mixed. While this means that the virus is not transported from the bulk to the

mouth, it also does not allow transport of CO_2 out. We can call this the *plastic bag limit*, and it is not suitable for a protective facemask. There is a sharp bifurcation at $\widehat{\boldsymbol{V}} = \mathbf{1}$, beyond which is the $\boldsymbol{Di} \ll \mathbf{1}$ $\widehat{\boldsymbol{V}} < \mathbf{1}$ regime, as shown in **Figure 7-5b**. In this regime, the mask volume is small but poorly mixed, leading to near-complete transport of CO_2 out of the mask at the end of exhalation. This *straw limit* is promising for a heated mask, provided that thermal inactivation of virus is suitably fast. In the *well-mixed limit*, with $\boldsymbol{Di} \gg \mathbf{1}$, there is no strong qualitative difference at $\widehat{\boldsymbol{V}} = \mathbf{1}$. These cases are shown in **Figure 7-5c** and **Figure 7-5d**. In both a small mask (**Figure 7-5c)** and large mask (**Figure 7-5d)**, the high level of mixing means that there are virtually no spatial gradients in virus and CO_2 concentration, but there are strong temporal gradients during the breath cycle. In these cases, virus concentration is maximized after inhalation, while CO_2 concentration is maximized after exhalation.

Given the flow rate of human breath and dispersion coefficients of air in porous media, the dispersion number in the proposed mask designs is likely to be small regardless of the exact mask volume and operating temperature, so the well-mixed cases with $\boldsymbol{Di} \gg \mathbf{1}$ are not immediately physically relevant. Nonetheless, it is important to compare the problem of heated mask design problem to these regimes of reverse-flow reactor transport. In a general sense, we can see that the ideal heated mask would impede virus transport but not CO_2 transport, combining filtration and thermal inactivation to act in the "*plastic bag"* limit toward virus particles but the "*straw"* limit toward exhaled CO_2.

7.3.3 Pressure Drop and Viral Impedance

The success of the proposed mask in inactivating SARS-CoV-2 relies on achieving viral impedance, as captured by K_p, without exceeding a maximum pressure drop. The structure and solidity of the mask mesh are critically important for both criteria. Specifically, the pressure drop constraint specifies a minimum mesh size for a given mask volume, while the mesh size dictates the expected viral impedance value, K_p. As shown in **Figure 7-6a-b,** our analysis suggests that in a 300 mL mask with a solidity of 0.1 and a copper mesh with diameter 0.1 mm will likely be able to achieve a viral impedance value of $K_p = 2$. This supports the conclusion that our proposed mask, with a size of 300 mL at an operating temperature of 90 °C, will be able to cause a 3-log reduction in viral concentration.

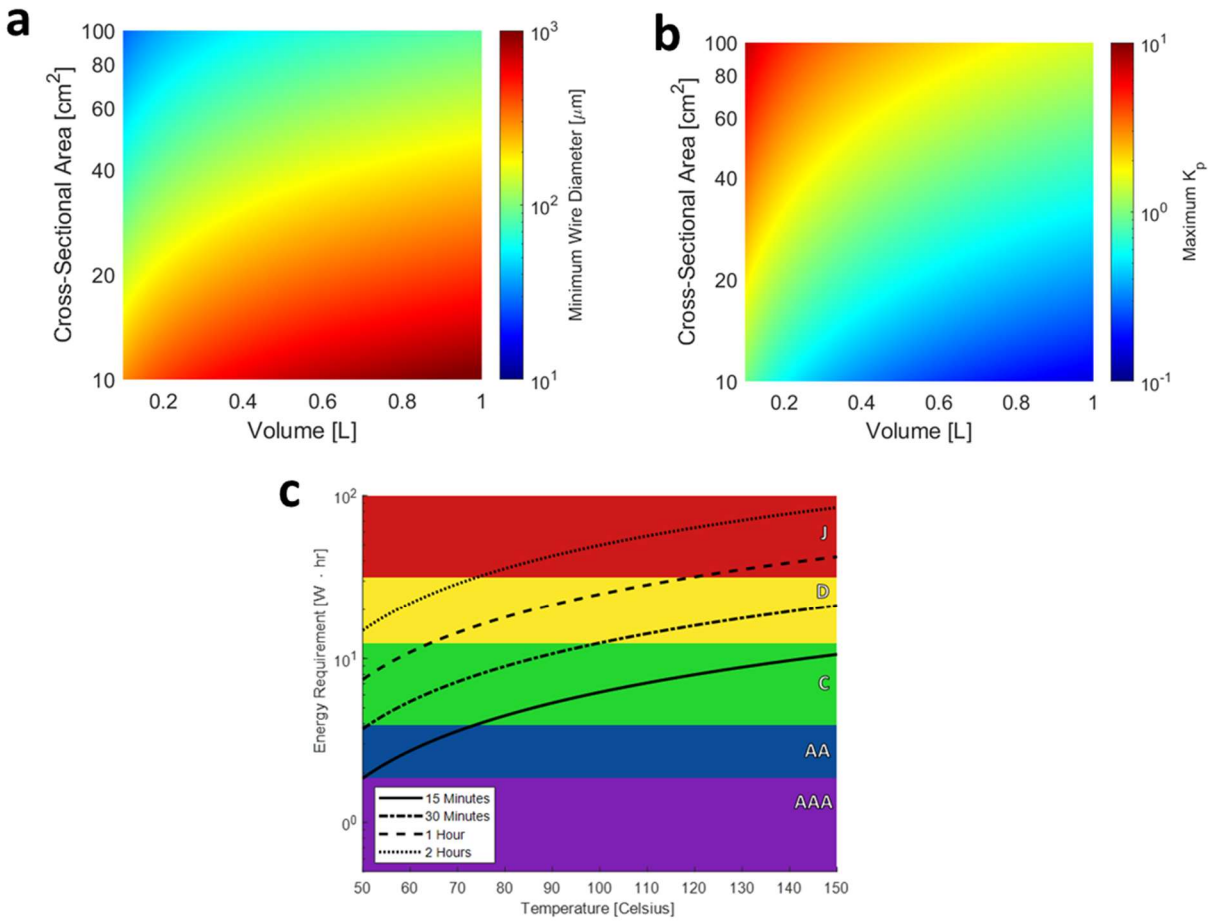

Figure 7-6. (a) Minimum allowable mesh diameter as a function of mask volume and cross-sectional area. The threshold mesh diameter induces a pressure drop of 60 Pa L^{-1} s^{-1} at the maximum breath flow rate of 0.4 liters per second. Mesh solidity is set to 0.1, with wire spacing equal to 3.2 times the wire diameter. Coarser meshes are required in larger masks to obey the pressure drop constraint, while meshes with higher cross-sectional area (and lower aspect ratio) can tolerate finer meshes without exceeding the maximum pressure drop. For the final design case, with a volume of 300 mL and a cross-sectional area of 50 cm^2, a mesh size of 0.1 mm is ideal. (b) Maximum achievable partition coefficient, K_p, as a function of mask volume and cross-sectional area. The partition coefficient is calculated as the ratio of the adsorption rate to the desorption rate, where k_{ads} is calculated from fiber efficiencies while a conservative value of $k_{des} = 1\ s^{-1}$is assumed. It is likely that a mask with a volume of 300 mL and an aspect ratio of 3 can achieve a K_p of 2, allowing for 3-log reduction in SARS-CoV-2 transport. (c) Energy requirement of 300 mL mask versus average temperature. The energy requirement for a given amount of time is compared against the total power supply of standard commercial batteries that have the following power capacities and weights[54]: AAA, 1.87 W hr and 12 grams; AA, 3.9 W hr and 24 grams; C, 12.3 W hr and 65 grams; D, 31.5 W hr and 135 grams; and J, 540 W hr and 272 grams.

With respect to pressure drop, we set an upper bound of 60 Pa L^{-1} s^{-1} at maximum flow, a conservative lower threshold for noticeable inspiratory resistance.[47,48] We take the interior of the mask to be filled with a mesh composed of stacked screens of cross-woven fibers. The mesh is defined by two variables – the fiber diameter, d_w,and fiber spacing, s_w – where the distance between stacked screens is taken to be equal to this fiber spacing, as shown in **Figure 7-S2**. The pressure drop across a single layer of mesh screen under oscillatory flow is predicted from an empirical correlation:[49]

$$\Delta P = \frac{\rho U^2}{2}\frac{\alpha}{(1-\alpha)^2}(17 \cdot Re_d^{-1} + 0.55) \quad [7.20]$$

where ρ is the fluid density, U_{max} the maximum superficial velocity during the oscillatory flow cycle, and Re_d is the Reynolds number based on the wire diameter. The solidity of the screen, α, is defined as the complement of the mesh porosity. For the specified geometry, the solidity of a single screen is equal to:

$$\alpha = \frac{d_w(2s_w+d_w)}{(s_w+d_w)^2} \quad [7.21]$$

The average solidity of the stacked fiber screens is then given as:

$$\alpha' = \alpha\frac{d_w}{s_w+d_w} \quad [7.22]$$

The pressure drop across more than a single mesh – in this case, across the porous interior of a mask—is taken to scale linearly with the number of mesh screens present, and thus scales linearly with length.[50] Given a mesh solidity of 0.1, the minimum wire diameter before the pressure drop constraint is violated for a mask design of some volume and cross-sectional area is shown in **Figure 7-6a**.

Given a wire diameter of 0.1 mm, it is likely that a partition coefficient of $K_p = 2$, which is required to achieve 3-log reduction in virus concentration, can be achieved. The maximum value of the partition coefficient, K_p, is shown as a function of wire diameter and cross-sectional area in **Figure 7-6b**. This predicted value depends on estimates for both the adsorption rate, k_{ads}, and the desorption rate, k_{des}. The adsorption rate can be calculated as shown below:

$$k_{ads} = \eta_f U\frac{4\alpha}{\pi d_w(1-\alpha)} \quad [7.23]$$

where η_f is a single-fiber efficiency. Captured particles are retained by Van der Waals forces,[51] but the mechanism by which they come into contact with the filter medium is dependent on filter and particle geometry. For coronavirus particles, which have a diameter of roughly 100 nm, the dominant mechanism of capture is through Brownian diffusion.[52] The governing parameter for this diffusive mechanism is the Péclet number, defined as the ratio of convective to diffusive transport rates:

$$Pe = \frac{U_0 d_w}{D} \quad [7.24]$$

where d_w is the filter fiber diameter, and D is the diffusion coefficient of the particle. The single fiber efficiency due to diffusion is obtained from an appropriate correlation such as that proposed by Wang et al.[53]:

$$\eta_f = 0.84 \cdot Pe^{-0.43} \quad [7.25]$$

The diffusion coefficient for the particle is obtained from the Stokes-Einstein equation:

$$D = \frac{k_B T C_s}{3\pi\mu d_p} \quad [7.26]$$

where $k_B T$ is the product of the Boltzmann constant and temperature, μ is the fluid dynamic viscosity, d_p the diameter of the particle, and C_s the Cunningham slip correction factor:

$$C_s = 1 + K_n \left[1.207 + 0.44 \cdot exp\ exp\ \left(-\frac{0.78}{Kn}\right)\right] \quad [7.27]$$

where K_n is the Knudsen number of the particle defined as:

$$K_n = \frac{2\lambda}{d_p} \quad [7.28]$$

where λ is the mean free path of a gas molecule in the fluid. For air, and assuming ideality, the mean free path is obtained from the following correlation:

$$\lambda = RT/\sqrt{2}\pi d_{N_2} N_A P \quad [7.29]$$

Where R is the gas constant, d_{N_2} is the diameter of nitrogen, the dominant molecular species in air, N_A is Avogadro's number, and P the pressure.

The desorption rate, by contrast, is less well-known, so we assume a conservative value of $k_{des} = 1\ s^{-1}$ in our calculations. The desorption rate can likely be tuned by various mechanisms. One approach to tailor the desorption rate of captured particles includes making use of the natural oscillatory flow within the mask. Pulsed air flow can effectively cause particle desorption, and is used industrially to clean surfaces from particle debris.[54,55] Mechanical stimulus of the mesh could actively control particle desorption,[56] where optical[57] and pneumatic[58] actuation of these structures is also possible. Applied electric fields can also be used in the same way. By applying an electric field to a conductive mesh, an electrostatic desorption force can be induced.[59] This principle has been applied with success to biological filtration membranes with a continuously applied electrical field,[60] as well with pulsed electric fields to remove microbial surface contamination.[61]

Given these estimates for the adsorption and desorption rate, a partition coefficient K_p of 2 is achievable for a 300 mL mask with a 0.1 mm mesh for a mask cross-sectional area of 50 cm^2, as shown in **Figure 7-6b.** From this analysis of adsorption and desorption rates and mechanisms, then, we see that the necessary viral impedance is likely achievable within the

pressure drop and volume constraints of the design process, even though a cross-sectional area of 50 cm^2 fixes a different aspect ratio (AR=0.85) than the specified aspect ratio of 3. In general, there is a tradeoff between mask volume and achievable viral impedance. The attainable value of K_p is a strong function of the cross-sectional area of the mask. A smaller cross-sectional area produces higher superficial velocities of flow, resulting in a larger value of the adsorption rate constant. However, these higher velocities also induce large pressure drop, and limit the maximum volume of mesh. Thus, at a given temperature, a smaller volume mask with a larger value of K_p may be equally able to achieve a desired viral reduction as a larger mask with a lower value of K_p—where ultimately a smaller mask volume would be the overall preferable option due to lower required energy consumption and smaller profile.

7.3.4 Heating and Safety

Heating the mask requires continuous power input to maintain a set temperature. The incorporation of a power supply within any mask design requires considerations and tradeoff between the duration of power supply and the bulk and weight it adds to the design. **Figure 7-6c** shows the power supply required of a 300 mL mask over a range of set temperatures. This energy requirement is compared against the capacity of standard consumer batteries. For a moderately heated mask of 90 °C, operation for an hour requires 19.5 W-hrs which can be supplied by two C batteries (130 grams total), six AA batteries (120 grams total), or twelve AAA batteries (108 grams total). Because of the substantial battery demands, it is expected that a heated mask could be used during relatively short (<1 hr) periods in particularly crowded situations, though the power requirements could be decreased dramatically with improvements to heat integration within the mask and thermal insulation to ambient air. Furthermore, rechargeable batteries or battery packs could be used instead of single-use batteries to provide a lower cost and long-term way to power the mask.

With respect to mask safety, continuous inhalation of and exposure to heated air and heating elements are matters of concern for the overall comfort and safety of any heated mask design. Appropriate insulation is necessary to limit the surface temperature of the mask—either on the face, or outwards—as well as minimize heat loss. Low-density but high thermally insulating neoprene is one material well-suited out of which the mask may be constructed. Ultra-insulating neoprene with thermal conductivity as low as 0.03 W m^{-1} K^{-1} has recently been constructed, by incorporating noble gases into neoprene foam[62]. Further, neoprene is heat-resistant up to temperatures of 135 °C,[63] making it an ideal material for use in the high-temperature regions of the mask.

Minimizing the temperature of inlet air which is exposed to the face and inhaled is also necessary to provide a safe and comfortable mask. Continual inhalation of air exceeding 125 °F (52 °C) has been shown to be painful for humans.[64] Accordingly, any mask design must incorporate a system to appropriately cool down air before inhalation. The reduction in temperature of inhaled air can be accomplished through incorporation of low thermal diffusivity materials at the inlet and outlet of the heated chamber, while respecting the overall pressure drop constraint for the comfort of the mask wearer. The regions of the mask containing these thermal masses would not be actively heated, but instead retain the thermal energy of the heated air, cooling it down before exiting the mask. This type of thermal design is discussed in the

supplementary information. Notably, for a 300 mL mask heated to an average temperature of 90 °C, the electric power consumption may be able to be reduced from 19.5 W to 8.8 W.

7.3.5 Further Improvements

There are mechanisms beyond thermal viral inactivation that may further improve the mask design. Coating the mesh with a layer of a metal such as copper or iron, which as ions have been shown widely to inactivate viruses and bacteria,[65,66] may improve mask performance. Anti-pathogenic polymeric[67] or non-polymeric[68] coatings may also increase the inactivation rate of adsorbed pathogens. Physical patterning, either on the microscale or nanoscale, could also lead to enhanced rate of inactivation,[69,70] as could the incorporation of UV light[71] with due caution about the hazards of ozone on human health.[72]

The long lifetime of the designed mask relies on its continued ability to inactivate and adsorb viral particles. The use of a small wire spacing within the mesh would minimize the potential of larger particles—such as dust or other debris that can be as large as 100 microns in diameter—to cake or block individual pores on the filter.[73] The cyclic nature of breath, too, presents a natural mechanism of filter clearing. Exhalation, when the flow reverses direction within the mask, would backwash the filter medium, potentially releasing and expelling any particle contaminants present.[74] In general, care must be taken to design a system which is able to retain, inactivate, and then emit that inactivated pathogen of interest without irreversibly capturing other contaminants. In the case where periodic replacement of the mesh material within the mask is necessary, a cheaper and less complex mesh material would be favored. We anticipate that a heated mask will maintain its fit and relative sterility over time, allowing it to be more reusable than an N95 respirator. While an N95 respirator can be reused only a handful of times before the fit deteriorates,[75] a heavier, thicker, and more durable heated mask will likely maintain performance better with repeated use. We anticipate that the flexibility of neoprene would allow a heated mask to maintain its fit better than an N95 ventilator upon donning and doffing. Additionally, a heated mask is less likely to become contaminated between uses, requiring fewer sanitization processes that reduce N95 effectiveness.[76] Experimental validation of a heated neoprene/copper mask would be needed to confirm its continued performance over time.

7.4 Conclusions

We have computationally analyzed the effectiveness of a heated face mask for thermal inactivation of the novel coronavirus, SARS-CoV-2. This constitutes the first quantitative analysis of face mask air purification by thermal inactivation of a pathogen. Relevant design choices for a heated mask include the mask volume, operating temperature, aspect ratio, and the diameter and spacing of fibers within the mask. Parameters which cannot be changed, or which follow from the design choices above, include the tidal volume and frequency of human breath, kinetics of coronavirus inactivation, human comfort and safety limits, power requirements, and the degree to which particles are impeded within the mask, as modelled by the partition coefficient K_p.

We have introduced a framework to consider these factors in mask design optimization, with an optimal mask volume of 300 mL at an operating temperature of 90 °C. This mask can achieve a 3-log reduction in virus concentration with K_p =2, or 6-log reduction in virus concentration with K_p =5. These values of the partition coefficient can likely be achieved without excessive pressure drop in a copper mesh with a wire diameter of roughly 0.6 mm. In general, we note a tradeoff between mask temperature and volume; the dependence of maximum mask volume on mesh material and spacing by the pressure drop constraint; and the presence of different regimes in heated mask design, which we call the plastic bag, straw, and well-mixed limits, on the basis of different dimensionless groups by analogy with reverse-flow chemical reactors. Given physical and safety limits, heated masks are promising options to protect against transmission of COVID-19 if coupled with thermoelectric cooling and thermally insulating liner materials. Future work, including experimental study with heated mask prototypes or more extensive 3D computational fluid dynamics simulations, will shed more light on the exact volume, temperature, and mesh size that are most promising for heated mask design, as well as the materials and battery systems that are most capable of achieving target viral inactivation.

7.5 Notation

A	Frequency factor [1/s]
A_c	Mask flow area [m^2]
c	Specific heat of copper [W m/K]
c_p	Specific heat at constant pressure of the fluid [J/(kg K)]
C	Virus concentration [mol/L]
C_0	Virus concentration in the bulk air [mol/L]
C_s	Cunningham slip correction factor [dimensionless]
d_{N_2}	Diameter of nitrogen [m]
d_p	Diameter of virus particle [m]
d_w	Fiber diameter [m]
D	Diffusion coefficient of the virus particle [m^2/s]
D_e	Dispersion coefficient [m^2/s]
Di	Dispersion number
E_a	Activation energy for virus thermal inactivation [kJ/mol]
F_B	Body force [N]
F_E	Electrostatic force [N]
F_V	Van der Waals force [N]
h_{eff}	Effective heat transfer coefficient [W/m^2/K]
h_f	Free convective heat transfer coefficient for air on the outside surface of the mask [W/(m^2 K)]
k	First-order rate constant for virus thermal inactivation [1/s]
k_{ads}	Virus adsorption rate constant [1/s]
k_B	Boltzmann constant [J/K]
k_{des}	Virus desorption rate constant [1/s]
k_{ins}	Thermal conductivity of insulating material (neoprene) [W/(m K)]
k_m	Effective thermal conductivity [W/(m K)]

K_p	Virus Partition coefficient
K_n	Knudsen number of the particle
L	Mask length [m]
L_{ins}	Thickness of insulating material [m]
$\dot{m}$	Mass flow rate of the fluid [kg/s]
N_A	Avogadro's number
P_m	Mask perimeter [m]
P	Pressure [Pa]
$P\acute{e}$	Péclet number
ΔP	Pressure drop across a single layer of mesh screen under oscillatory flow [Pa]
q	Heat production per unit volume [W/m^3]
r	Virus thermal inactivation rate [mol/(L s)]
R	Gas constant [J/(K mol)]
Re_d	Reynolds number based on the wire diameter
s_w	Fiber spacing [m]
t	Time [s]
T	Temperature [K]
T_{amb}	Ambient temperature [K]
U	Velocity [m/s]
U_0	Superficial velocity of the fluid [m/s]
U_{max}	Maximum air flow velocity within the mask [m/s]
U_{vir}	Effective virus velocity [m/s]
U_p	Particle velocity [m/s]
V_{mask}	Mask volume [L]
V_T	Tidal volume [L]
$\hat{V}$	Reduced volume: ratio of mask volume to tidal volume
W	Imposed electric power [W]
x	Position along the mask [m]
α	Solidity of the screen
α'	Average solidity of the stacked fiber screens
η_f	Single fiber efficiency
φ	Porosity of the mesh
Λ	Filtration efficiency of the porous mesh
λ	Mean free path of a gas molecule in the fluid [m]
μ	Fluid dynamic viscosity [Pa s]
ρ	Fluid density [kg/m^3]
τ	Period of human breath [s]
exh	Exhalation
f	Fluid phase (virus-laden air)
inh	Inhalation
s	Solid phase (copper mesh)

7.6 Supporting Information

1. Proposed Mask Design

Details for the proposed mask design are shown in **Table 7-1.**

Table 7-1. Proposed mask design

Viral reduction	Log-3 (99.9%)
Volume (mL)	300 mL
Temperature	90 °C
K_p	2
Wire diameter	100 μm
Insulation thickness	0.3 cm
Mesh solidity	0.1
Power	19.5 W
Battery requirement	4 9V rechargeable lithium-ion batteries
Battery lifetime	1 hr
Mask mass	350 g
Total mass (mask and battery)	600 g

2. Kinetics of SARS-CoV-2 Thermal Inactivation

Experimental data reported by Yap et al.[1] reaches an upper temperature of 70 °C, while data and model predictions collected by Jiang et al.[2] for coronaviruses including SARS-CoV-1 and MERS-CoV extend to temperatures of 120 °C. These additional data and models confirm that the first-order kinetic model is appropriate at higher temperatures, as shown in **Figure 7-7.** If anything, the experimental degradation rate exceeds first-order kinetics at high temperatures, as shown by the clustering of data points above the line at low inverse temperature.

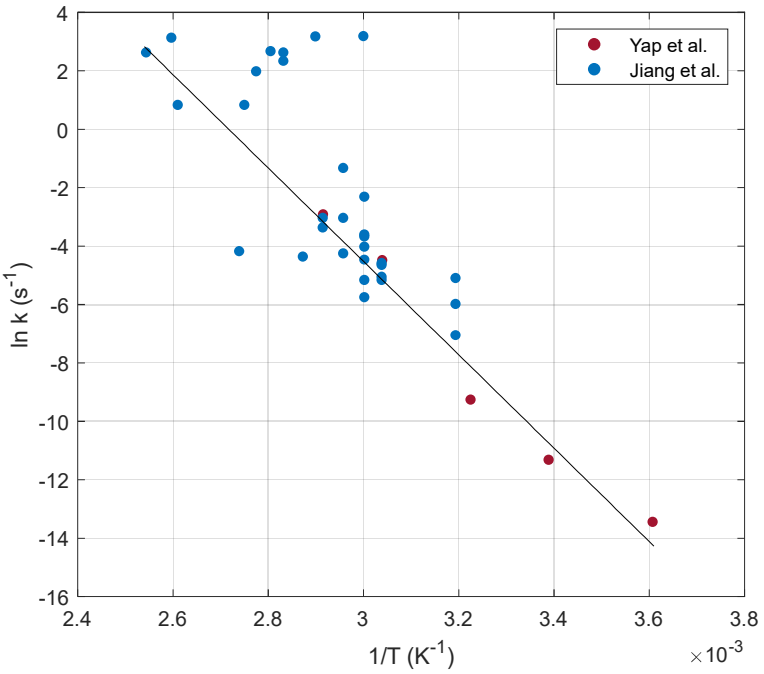

Figure 7-7: First-order kinetics in thermal inactivation of coronaviruses, shown as ln (k) versus 1/T. The experimental data for thermal inactivation of SARS-CoV-2 reported by Yap et al.[1] for temperatures from 4 °C to 70 °C (red) is consistent with experimental data and models of thermal inactivation of various coronaviruses at temperatures from 40 °C to 120 °C, as reported in Jiang et al[2] (blue). The best fit from Yap et al.[1], which is used in this analysis, is shown in black.

3. Comparison with Low Temperature Design

The proposed heated mask functions by a combination of filtration and thermal inactivation. By calculating the ratio of $\log_{10}$ viral reduction to $\log_{10}$ viral reduction at ambient temperature as a function of mask temperature and volume, it is possible to distinguish the effect of thermal inactivation from that of filtration, as shown in **Figure 7-8**. This analysis shows that thermal inactivation is appreciable, as shown by a 10-fold increase in viral reduction, at a temperature around 90 °C, the proposed operating temperature for the final mask design.

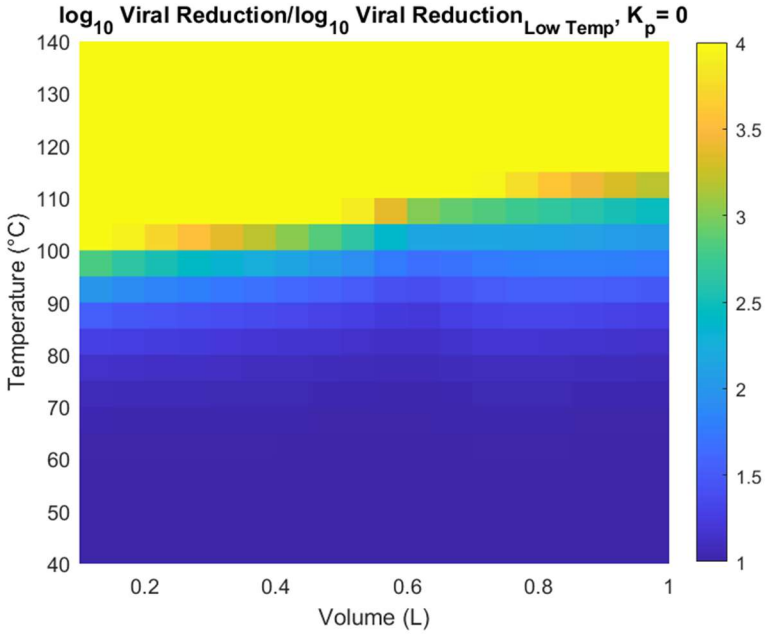

Figure 7-8: Comparison of viral reduction in a heated mask to that in an ambient temperature mask as a function of temperature and volume, with a partition coefficient $K_p = 0$.

4. Thermal Equilibrium Validation

The heat transfer model used in the simulation assumes that temperature difference between the solid part and the fluid is negligible. The assumption is validated by calculating the exact difference in temperature. Relevant dimensionless numbers are computed:

$$\mathrm{Pr} = \frac{\mathrm{c_p}\mu}{k} = 0.7323 \qquad [7.30]$$

$$\mathrm{Re} = \frac{\rho_{air} V_{air} d_w}{\mu_{air}} = 0.843 \qquad [7.31]$$

Heat transfer coefficient is approximated by empirical correlation for the average Nu number for forced convection over circular cylinder in cross flow.[3]

$$\mathrm{Nu} = \frac{\mathrm{hD}}{\mathrm{k_f}} = 0.989 Re^{0.330} Pr^{1/3}, \ 0.4 < R < 4 \qquad [7.32]$$

Result yields that $h = Nu * \frac{k_f}{d_w} = 208 \frac{W}{m^2 K}$. For a 300 mL mask operating at a mean temperature of 90 °C, the averaged heat flux on the mesh surface and temperature difference between copper mesh and air are:

$$\mathrm{q''} = \frac{\mathrm{P}}{A_{mesh\ surface}} = 100.1 \ \frac{W}{m^2} \qquad [7.33]$$

$$\Delta T = \frac{q'}{h} = 0.48 \ K \qquad [7.34]$$

Since the temperature difference is within 0.7% of the temperature change within the mask, the thermal equilibrium approximation is identified as a valid assumption.

5. Regenerative Heating Mask Design

In the preliminary design, the mesh within the mask utilizes homogeneous material, which allows simple fabrication of the mask. However, due to the high thermal diffusivity of the mesh material, copper, the mask requires a high electric power input to maintain at desired temperature. In order to reduce the power requirement, a revised design is proposed: use extra "thermal masses" replaces the copper mesh on both ends of the heating channel. The thermal mass is able to capture more heat within the mass and reduce the heat transferred out of the mask. A low thermal diffusivity (low thermal conductivity, high heat capacity, $\alpha = \frac{k}{\rho c_p}$) in the thermal mass is desired. Low density and low cost are also favored features in our design. Commercial nontoxic wire mesh materials, including aluminum, copper, yellow brass (70% Cu, 30% Zn), bronze (75% Cu, 25% Sn), and stainless steel (eg. T304), are considered as candidates for thermal masses. In addition, glass fiber is evaluated due to its low diffusivity, low density, and low cost. These materials and their relevant physical properties are shown in the table below. A fiberglass is a form of fiber-reinforced plastic where glass fiber is the reinforced plastic. The glass fiber is usually randomly arranged, flattened into a sheet, or woven into a fabric. Data presented is for E-Glass Fiber. Solid volume section presented in the table is obtained for 300 mL mask, with 1/4 of the mask occupied by thermal masses and solidity maintained at 0.1. In **Table S2**., we identify that glass fiber has lowest thermal diffusivity and relatively low cost. The material is also lightweight.

Table S2. Material selection of extra thermal masses.

	k [W/mK]	ρ [g/cm^3]	c_p [J/gC]	ρc_p	α [mm^2/s]	weight [g]
Aluminum	240	2.7	0.9	2.430	98.77	27
Copper	400	8.3	0.386	3.204	124.85	83
Brass	111	8.5	0.38	3.230	34.37	85
Bronze	26	7.2	0.435	3.132	8.30	72
SS T304	16.2	8	0.5	4.000	4.05	80
Glass fiber	1.3	2.6	0.8	2.08	0.625	26

The reduction in power required was found by simulating the temperature distribution in the case of a 300 mL mask, with modified material properties and eliminated heat source within the volume of the mask replaced by the low thermal diffusivity material. The results indicated a significant reduce in required power as shown in **Figure 7-9**: with 1/8 of the total mesh replaced by glass fiber on each side of the channel, the electric power reduced from nearly 19.5 W to 8.8 W, while maintaining the mean temperature at 90°C.

(a) No thermal mass: P = 19.5 W (b) With fiberglass thermal mass: P = 8.8 W

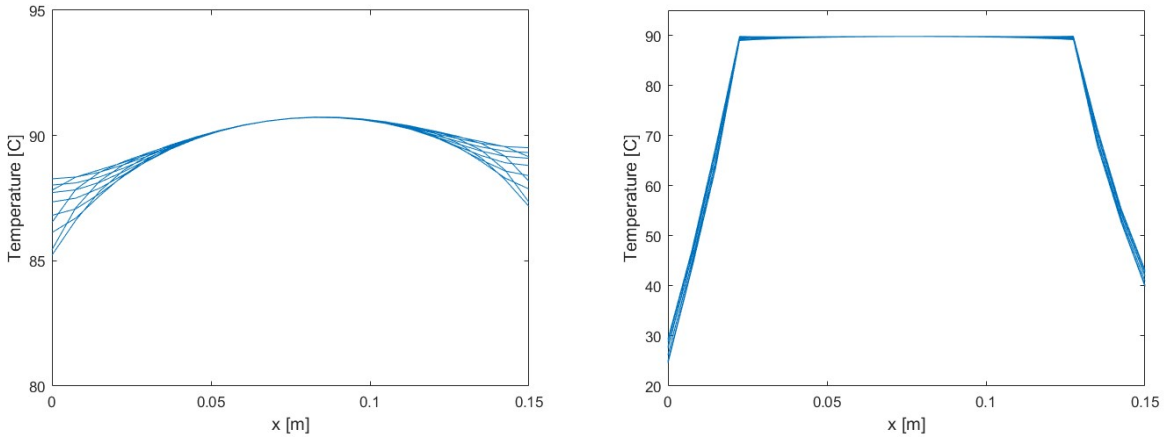

Figure 7-9: Thermal profile of mask containing uniform copper mesh versus low thermal diffusivity fiberglass at the inlet and outlet.

6. 3D Mesh and Electrical Design

The solidity in the simulation represents the 2D mesh design. It is thus important to show how the mesh is packed in 3D. The 3D mesh design is shown in **Figure 7-10**. The solidity of the 3D mesh is 0.13, which is considered close to the 2D mesh setting of 0.1 solidity. The electrical resistant is computed by Ohm's Law:

$$R = V^2/P \quad [7.35]$$

$$P = \rho \frac{l}{A} \quad [7.36]$$

where P is the applied electric power, V is the applied voltage, ρ is the electrical resistivity of copper, l is the length of the specimen, and A is the cross sectional area of the specimen. Current design of 9V rechargeable lithium-ion batteries has capacity of 600mAh and maximum discharge of 1C, i.e., maximum current of 600mA. If 4 batteries were connected in parallel, with copper mesh wire diameter of 0.1mm, the example design with an optimal mask volume of 300 mL at an operating temperature of 90 °C can be powered for 1 hour. A schematic of the mask mesh is shown below in **Figure 7-10**:

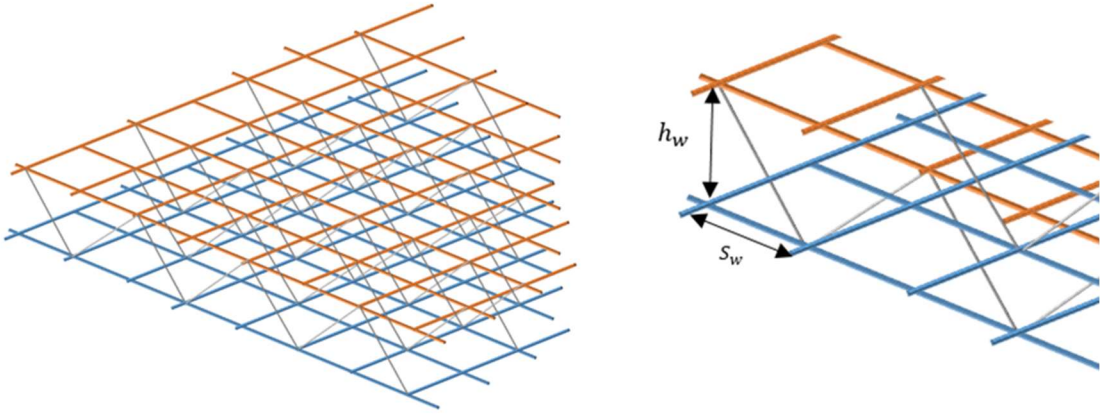

Figure 7-10. 3D mesh packing schematic. 2D mesh are stacked in layers and connected diagonally by zigzag inter-layer wires for supportive purpose. The height between each layer, h_w, is set to be the same as the wire spacing, s_w. The solidity of the 3D mesh is 86%, which is considered close to the 2D mesh.

7.7 References

1. Cheng VCC, Wong SC, Chuang VWM, et al. The role of community-wide wearing of face mask for control of coronavirus disease 2019 (COVID-19) epidemic due to SARS-CoV-2. *J Infect*. 2020;81:107-114. doi:10.1016/j.jinf.2020.04.024
2. Leung NHL, Chu DKW, Shiu EYC, et al. Respiratory virus shedding in exhaled breath and efficacy of face masks. *Nat Med*. 2020;26(5):676-680. doi:10.1038/s41591-020-0843-2
3. Nogee D, Tomassoni A. Concise Communication: Covid-19 and the N95 Respirator Shortage: Closing the Gap. *Infect Control Hosp Epidemiol*. 2020:1-1. doi:10.1017/ice.2020.124
4. Howard J, Huang A, Li Z, et al. An evidence review of face masks against COVID-19. *Proc Natl Acad Sci U S A*. 2021;118(4). doi:10.1073/pnas.2014564118
5. TSI. Mechanisms of Filtration for High Efficiency Fibrous Filters. *TSI Inc*. 2012;041:1-4.
6. Khinast J, Luss D. Mapping regions with different bifurcation diagrams of a reverse-flow reactor. *AIChE J*. 1997;43(8):2034-2047. doi:10.1002/aic.690430812
7. Salinger AG, Eigenberger G. The direct calculation of periodic states of the reverse flow reactor - II. Multiplicity and instability. *Chem Eng Sci*. 1996;51(21):4915-4922. doi:10.1016/0009-2509(96)00327-2
8. A. Viecco G, S. Caram H. The spherical reverse flow reactor. *Chem Eng Sci*. 2002;57(18):4005-4025. doi:10.1016/S0009-2509(02)00310-X
9. Budhi YW. *Reverse Flow Reactor Operation for Control of Catalyst Surface Coverage*.; 2005.
10. Cottrell FG. Purifying gases and apparatus therefor. August 1935. http://www.google.com/patents/US2121733%5Cnhttp://patentimages.storage.googleapis.com/pdfs/US2121733.pdf. Accessed October 13, 2020.

11. Zagoruiko AN. The reverse-flow operation of catalytic reactors : History and prospects. *Curr Top Catal*. 2017;10(May):113-129. https://www.researchgate.net/publication/258208737. Accessed October 13, 2020.
12. Van Sint Annaland M, Nijssen RC. A novel reverse flow reactor coupling endothermic and exothermic reactions: An experimental study. *Chem Eng Sci*. 2002;57(22-23):4967-4985. doi:10.1016/S0009-2509(02)00276-2
13. Abraham JP, Plourde BD, Cheng L. Using heat to kill SARS-CoV-2. *Rev Med Virol*. 2020;30(5). doi:10.1002/rmv.2115
14. Kampf G, Voss A, Scheithauer S. Inactivation of coronaviruses by heat. *J Hosp Infect*. 2020;105:348-349. doi:10.1016/j.jhin.2020.03.025
15. Hessling M, Hoenes K, Lingenfelder C. Selection of parameters for thermal coronavirus inactivation - a data-based recommendation. *GMS Hyg Infect Control*. 2020;15:1-7.
16. Knio ZO, Shelton JA, O'Gara T. Heated Air Delivery by Micro-Sauna: An Experimental Treatment Prototype Concept for Coronavirus Disease 2019. *Cureus*. 2020;12(5). doi:10.7759/cureus.8162
17. Recommended Guidance for Extended Use and Limited Reuse of N95 Filtering Facepiece Respirators in Healthcare Settings | NIOSH | CDC.
18. Strategies for Optimizing the Supply of N95 Respirators: COVID-19 | CDC.
19. Fischer EP, Fischer MC, Grass D, Henrion I, Eric W, Warren SW. Low-cost measurement of facemask efficacy for filtering expelled droplets during speech. *Sci Adv*. 2020;3083:1-11. doi:10.1101/2020.06.19.20132969
20. Cramer A, Tian E, Yu SH, et al. Disposable n95 masks pass qualitative fit-test but have decreased filtration efficiency after cobalt-60 gamma irradiation. *medRxiv*. 2020:10-14. doi:10.1101/2020.03.28.20043471
21. Fisher EM, Shaffer RE. Considerations for recommending extended use and limited reuse of filtering facepiece respirators in health care settings. *J Occup Environ Hyg*. 2014;11(8):115-128. doi:10.1080/15459624.2014.902954
22. Lin TH, Chen CC, Huang SH, Kuo CW, Lai CY, Lin WY. Filter quality of electret masks in filtering 14.6–594 nm aerosol particles: Effects of five decontamination methods. *PLoS One*. 2017;12(10):1-15. doi:10.1371/journal.pone.0186217
23. Livingston E, Desai A, Berkwits M. Sourcing Personal Protective Equipment during the COVID-19 Pandemic. *JAMA - J Am Med Assoc*. 2020;323(19):1912-1914. doi:10.1001/jama.2020.5317
24. Gilbert R, Auchincloss JH, Brodsky J, Boden W. Changes in tidal volume, frequency, and ventilation induced by their measurement. *J Appl Physiol*. 1972;33(2):252-254. doi:10.1152/jappl.1972.33.2.252
25. M. Christopher AMLS. Pressure Drop of Filtering Facepiece Respirators: How Low Should We Go? *Physiol Behav*. 2016;176(1):100–106. doi:10.1016/j.gde.2016.03.011
26. Colby SM, Kabilan S, Jacob RE, Kuprat AP, Einstein DR, Corley RA. Comparison of realistic and idealized breathing patterns in computational models of airflow and vapor dosimetry in the rodent upper respiratory tract. *Inhal Toxicol*. 2016;28(4):192-202. doi:10.3109/08958378.2016.1150367
27. Chin AWH, Chu JTS, Perera MRA, et al. Stability of SARS-CoV-2 in different environmental conditions. *The Lancet Microbe*. 2020;1(1):e10. doi:10.1016/s2666-5247(20)30003-3
28. Yap TF, Liu Z, Shveda RA, Preston DJ. A Predictive Model of the Temperature-

Dependent Inactivation of Coronaviruses. *ChemRxiv*. July 2020. doi:10.26434/chemrxiv.12152970.v4
29. Jiang Y, Zhang H, Wippold JA, et al. Sub-second heat inactivation of coronavirus. *bioRxiv*. October 2020:2020.10.05.327528. doi:10.1101/2020.10.05.327528
30. Deen WM. Analysis of Transport Phenomena 2nd Edition. 2011.
31. Chen BH, Manna BB, Hines JW. Dispersion of liquid in a column packed with screen cylinders. *Ind Eng Chem Process Des Dev*. 1971;10(3):341-346. doi:10.1021/i260039a011
32. Nauman EB, Mallikarjun R. Generalized boundary conditions for the axial dispersion model. *Chem Eng J*. 1983;26(3):231-237. doi:10.1016/0300-9467(83)80018-5
33. Pearson JRA. A note on the " Danckwerts " boundary conditions for continuous flow reactors. *Chem Eng Sci*. 1959;10(4):281-284. doi:10.1016/0009-2509(59)80063-4
34. Nield DA, Bejan A, Nield DA, Bejan A. Heat Transfer Through a Porous Medium. In: *Convection in Porous Media*. Springer International Publishing; 2017:37-55. doi:10.1007/978-3-319-49562-0_2
35. Jegatheesan V, Vigneswaran S. Deep Bed Filtration: Mathematical Models and Observations. *Crit Rev Environ Sci Technol*. 2005;35(6):515-569. doi:10.1080/10643380500326432
36. Bradford SA, Torkzaban S. Colloid Transport and Retention in Unsaturated Porous Media: A Review of Interface-, Collector-, and Pore-Scale Processes and Models. *Vadose Zo J*. 2008;7(2):667-681. doi:10.2136/vzj2007.0092
37. Chiang H-W, Tien C. Dynamics of deep-bed filtration. Part I: Analysis of two limiting situations. *AIChE J*. 1985;31(8):1349-1359. doi:10.1002/aic.690310814
38. Chiang H-W, Tien C. Dynamics of deep-bed filtration. Part II: Experiment. *AIChE J*. 1985;31(8):1360-1371. doi:10.1002/aic.690310815
39. Yuan H, Shapiro AA. Modeling non-Fickian transport and hyperexponential deposition for deep bed filtration. *Chem Eng J*. 2010;162(3):974-988. doi:10.1016/j.cej.2010.07.003
40. Fatt I. The Network Model of Porous Media. *Trans AIME*. 1956;207(01):144-181. doi:10.2118/574-g
41. Bryant SL, King PR, Mellor DW. Network model evaluation of permeability and spatial correlation in a real random sphere packing. *Transp Porous Media*. 1993;11(1):53-70. doi:10.1007/BF00614635
42. Bijeljic B, Muggeridge AH, Blunt MJ. Pore-scale modeling of longitudinal dispersion. *Water Resour Res*. 2004;40(11). doi:10.1029/2004WR003567
43. Joekar-Niasar V, Hassanizadeh SM. Analysis of fundamentals of two-phase flow in porous media using dynamic pore-network models: A review. *Crit Rev Environ Sci Technol*. 2012;42(18):1895-1976. doi:10.1080/10643389.2011.574101
44. Yang H, Balhoff MT. Pore-network modeling of particle retention in porous media. *AIChE J*. 2017;63(7):3118-3131. doi:10.1002/aic.15593
45. OSHA. Carbon Dioxide Health Hazard Information Sheet. *FSIS Environ Saf Heal Gr*. 2010:2-4. https://www.osha.gov/dts/chemicalsampling/data/CH_225400.html. Accessed October 13, 2020.
46. Mosley G. Sterility Assurance Level (SAL): The term and its definition continues to cause confusion in the industry. *Pharm Microbiol Forum Newsl*. 2008;14(5):1-15.
47. Kim JH, Roberge RJ, Powell JB, Shaffer RE, Ylitalo CM, Sebastian JM. Pressure drop of filtering facepiece respirators: How low should we go? *Int J Occup Med Environ Health*.

2015;28(1):71-80. doi:10.13075/ijomeh.1896.00153
48. Electronic code of federal regulations: Fiber definitions. U.S. Government Printing Office. http://www.ecfr.gov. Published 2021.
49. Wakeland RS, Keolian RM. Measurements of Resistance of Individual Square-Mesh Screens to Oscillating Flow at Low and Intermediate Reynolds Numbers. *J Fluids Eng Trans ASME*. 2003;125(5):851-862. doi:10.1115/1.1601254
50. Sun H, Bu S, Luan Y. A high-precision method for calculating the pressure drop across wire mesh filters. *Chem Eng Sci*. 2015;127:143-150. doi:10.1016/j.ces.2015.01.023
51. Kirsh VA. The Effect of van der Waals' Forces on Aerosol Filtration with Fibrous Filters. *Colloid J*. 2000;62(6):714-720. doi:10.1023/A:1026678725025
52. Wang C Sen, Otani Y. Removal of nanoparticles from gas streams by fibrous filters: A review. *Ind Eng Chem Res*. 2013;52(1):5-17. doi:10.1021/ie300574m
53. Wang J, Chen DR, Pui DYH. Modeling of filtration efficiency of nanoparticles in standard filter media. *J Nanoparticle Res*. 2007;9(1):109-115. doi:10.1007/s11051-006-9155-9
54. Ziskind G, Yarin LP, Peles S, Gutfinger C. Experimental investigation of particle removal from surfaces by pulsed air jets. *Aerosol Sci Technol*. 2002;36(5):652-659. doi:10.1080/02786820252883883
55. Soemoto K, Wakimoto T, Katoh K. Removal of fine particles on a wall by high-frequency turbulence added air flow. *Int J Flow Control*. 2013;5(1):47-58. doi:10.1260/1756-8250.5.1.47
56. Zhang S, Zhang S, Zuo P, et al. Anti-Biofouling and Self-Cleaning Surfaces Featured with Magnetic Artificial Cilia. *ACS Appl Mater Interfaces*. 2020;12(24):27726-27736. doi:10.1021/acsami.0c05403
57. Van Oosten CL, Bastiaansen CWM, Broer DJ. Printed artificial cilia from liquid-crystal network actuators modularly driven by light. *Nat Mater*. 2009;8(8):677-682. doi:10.1038/nmat2487
58. Gorissen B, De Volder M, Reynaerts D. Pneumatically-actuated artificial cilia array for biomimetic fluid propulsion. *Lab Chip*. 2015;15(22):4348-4355. doi:10.1039/c5lc00775e
59. Poortinga AT, Smit J, Van Der Mei HC, Busscher HJ. Electric field induced desorption of bacteria from a conditioning film covered substratum. *Biotechnol Bioeng*. 2001;76(4):395-399. doi:10.1002/bit.10129
60. Huang J, Wang Z, Zhang J, Zhang X, Ma J, Wu Z. A novel composite conductive microfiltration membrane and its anti-fouling performance with an external electric field in membrane bioreactors. *Sci Rep*. 2015;5. doi:10.1038/srep09268
61. Feng T, Wu J, Chai K, Yang P. The anti-biofouling behavior of high voltage pulse electric field (HPEF) mediated by carbon fiber composite coating in seawater. *Bioelectrochemistry*. 2018;123:137-144. doi:10.1016/j.bioelechem.2018.04.015
62. Moran JL, Cottrill AL, Benck JD, et al. Noble-gas-infused neoprene closed-cell foams achieving ultra-low thermal conductivity fabrics. *RSC Adv*. 2018;8(38):21389-21398. doi:10.1039/c8ra04037k
63. Shanks RA, Kong I. General Purpose Elastomers: Structure, Chemistry, Physics and Performance. In: *Advanced Structured Materials*. Vol 11. Springer, Berlin, Heidelberg; 2013:11-45. doi:10.1007/978-3-642-20925-3_2
64. Killick EM. Physiological response to breathing hot air. *J Hyg (Lond)*. 1932;32(3):332-339. doi:10.1017/S0022172400018052
65. Sagripanti JL, Routson LB, Lytle CD. Virus inactivation by copper or iron ions alone and

in the presence of peroxide. *Appl Environ Microbiol*. 1993;59(12):4374-4376. doi:10.1128/aem.59.12.4374-4376.1993
66. Grass G, Rensing C, Solioz M. Metallic copper as an antimicrobial surface. *Appl Environ Microbiol*. 2011;77(5):1541-1547. doi:10.1128/AEM.02766-10
67. Haldar J, An D, De Cienfuegos LÁ, Chen J, Klibanov AM. Polymeric coatings that inactivate both influenza virus and pathogenic bacteria. *Proc Natl Acad Sci U S A*. 2006;103(47):17667-17671. doi:10.1073/pnas.0608803103
68. Lin Q, Lim JYC, Xue K, et al. Sanitizing agents for virus inactivation and disinfection. *View*. 2020;1(2). doi:10.1002/viw2.16
69. Mann EE, Manna D, Mettetal MR, et al. Surface micropattern limits bacterial contamination. *Antimicrob Resist Infect Control*. 2014;3(1):1-8. doi:10.1186/2047-2994-3-28
70. Michalska M, Gambacorta F, Divan R, et al. Tuning antimicrobial properties of biomimetic nanopatterned surfaces. *Nanoscale*. 2018;10(14):6639-6650. doi:10.1039/c8nr00439k
71. Buonanno M, Welch D, Shuryak I, Brenner DJ. Far-UVC light (222 nm) efficiently and safely inactivates airborne human coronaviruses. *Sci Rep*. 2020;10(1):1-8. doi:10.1038/s41598-020-67211-2
72. Lippmann M. Health Effects Of Ozone A Critical Review. *J Air Pollut Control Assoc*. 1989;39(5):672-695. doi:10.1080/08940630.1989.10466554
73. Richards T. Particle clogging in porous media: Filtration of a smectite solution. 2010:1-31.
74. Zong Q, Liu Z, Liu H, Yang H. Backwashing performance of self-cleaning screen filters in drip irrigation systems. *PLoS One*. 2019;14(12):1-18. doi:10.1371/journal.pone.0226354
75. Bergman MS, Viscusi DJ, Zhuang Z, Palmiero AJ, Powell JB, Shaffer RE. Impact of multiple consecutive donnings on filtering facepiece respirator fit. *Am J Infect Control*. 2012;40(4):375-380. doi:10.1016/j.ajic.2011.05.003
76. Juang PSC, Tsai P. N95 Respirator Cleaning and Reuse Methods Proposed by the Inventor of the N95 Mask Material. *J Emerg Med*. 2020;58(5):817-820. doi:10.1016/j.jemermed.2020.04.036

8. Conclusions and Future Work

8.1 Conclusions

In this thesis, we studied the behavior of fluids – and particularly the behavior of water – inside isolated carbon nanotubes, with diameters from 0.6 nm to 3 nm that approach molecular length scales. In Chapter 1, we introduced the concept of "single digit nanopores," or nanopores with diameters in the single digits of nanometers. Inside these narrow conduits, there are several critical knowledge gaps in our understanding of fluid dynamics and phase behavior. During the rest of the thesis, we worked to resolve two of these knowledge gaps: enhanced fluid transport under nanoconfinement, and altered phase behavior.

In order to address knowledge gaps in understanding of nanofluidics, my collaborators and I developed experimental platforms that are capable of precise, repeatable nanofluidic measurements. Specifically, we worked on an experimental platform consisting of carbon nanotubes that are (1) isolated, (2) substrate-bound, (3) on marked silicon substrates, and (4) segmented by focused ion beam. While other scientific groups work on different nanofluidic platforms – or even different CNT-based platforms – my thesis work focuses on this platform for several reasons. First, we studied fluid behavior in isolated carbon nanotubes as opposed to multi-pore systems like carbon nanotube membranes or forests. Fluid properties – including phase boundaries, diffusion coefficients, and molecular orientation – depend sensitively and non-monotonically on pore size. Studying one nanoscale pore provides more precise physical insight than studying a multi-pore system, though this comes at the cost of low signal-to-noise ratio and a high rate of device failure. I worked to overcome these obstacles. Second, we studied carbon nanotubes that are substrate-bound, rather than those in solution or free-standing over a trench. Substrate-bound carbon nanotubes do not diffuse or aggregate like those in solution, allowing repeat measurement over long periods of time, and are more robust to subsequent sample processing and laser heating than free-standing tubes. Third, we made custom substrates with lithographic marks. This allowed us to return to the same location on the same carbon nanotube repeatedly, which was essential to observing fluid filling and emptying after humidity and temperature treatments. Fourth, we used a focused ion beam to cut a millimeter-long tube into segments with identical diameter and lengths of roughly 10-100 μm. Segmentation of one ultra-long carbon nanotube into multiple segments of the same diameter tube was invaluable to collecting high-quality data. By producing multiple CNT segments of the same diameter and same length, we turned the stochasticity of nanoscale fluid filling from a liability to an asset: the CNT segments that did not fill with fluid became controls for the segments that filled.

In addition to experimental platform development, another large part of this thesis was the development of improved techniques for fluidic characterization of a single CNT with high temporal and spatial resolution. As described in numerous chapters, we used Raman spectroscopy – and in particular the Raman radial breathing mode (RBM) – as an indicator of a filled, empty, or partly filled nanotube. The fact that we can observe a single nanoscale object on the second time scale using a physical effect as weak and rare as Raman scattering is almost miraculous. It requires the surprising confluence of CNT electronic resonance, and advances in lasers and detectors that allow more precise measurement with less integration time. Much of the

behind-the-scenes work in this thesis involved automation of the Raman instrument to move a motorized stage, focus on the silicon substrate or a carbon nanotube, and collect spectra ever more precisely as a function of position, time, temperature, and humidity.

After the development of precise experimental platforms and means to characterize them by Raman spectroscopy, we were able to address questions about water thermodynamics and dynamics inside carbon nanotubes, as presented in the bulk of this thesis. In Chapter 2, we describe how the change in radial breathing mode, $\Delta\omega_{RBM}$, varies with diameter and how this corresponds to different packing states of fluids in single-file, zigzag, and more complicated arrangements inside the carbon nanotube. In Chapter 3, we develop elastic shell models of radial breathing mode changes in double-walled carbon nanotubes, using these models to explain how double-walled nanotubes, unlike single-walled nanotubes, can distinguish between interior filling and exterior adsorption by RBM shifts alone. In so doing, we introduce the concept of a primary shift (the RBM shift primarily of the shell nearest the fluid) and a sympathetic shift (the RBM shift primarily of the shell farther from the fluid), where the former is larger than the latter. In Chapters 4 and 5, we explore the thermodynamics of water phase transitions inside carbon nanotubes. We developed two slightly different methods to change CNT temperature, with interesting ramifications for system thermodynamics. In the first case (Chapter 4), we change the temperature of the CNT using a bulk temperature stage at low laser power, resulting in the entire sample being heated or cooled with small spatial temperature gradients. This results in an effectively closed thermodynamic system (the "sealed ampoule"), where we observe an equilibrium between a liquid-like state and a vapor-like state that we analyze using a Clausius-Clapeyron-type expression to calculate the enthalpy of phase change as a function of nanotube diameter. In the second case (Chapter 5), we change the temperature of the CNT by changing laser power. This results in local heating of the ~1 μm laser spot, with strong thermal temperature gradients, creating an open thermodynamic system. Rather than the language and modelling of phase equilibria, we analyze this system as an adsorption/desorption process, creating a Langmuir-type model to capture differences in enthalpy of adsorption as a function of nanotube diameter. These two techniques, therefore, are complementary, and prioritize the two different types of interactions that fluids have under extreme confinement: fluid-fluid interactions for the case of the temperature-controlled microscope stage, and fluid-CNT interactions for the case of variable laser heating. Finally, in Chapter 6, we explore dynamics of water filling, showing transitions on the minute time scale among filled, partly filled, and empty states and comparing to Kinetic Monte Carlo simulations to determine parameters including the diffusion coefficient of liquid-like water under conditions of nanotube confinement.

8.2 Future Work

The future of nanofluidics is bright. Advances in nanofabrication at smaller and smaller scales, incorporation of a broader set of 1D and 2D materials, and advances in characterization by electron microscopy, electrical measurements, and spectroscopy will all enable a broad array of nanofluidic platforms to address a broad number of questions in the coming years. Below, five topics for future work in carbon nanotube fluidics and beyond are outlined briefly that build upon the work presented in this thesis.

Filling with non-aqueous fluids: The work in this thesis largely concerns the behavior of water inside carbon nanotubes, but non-aqueous fluids are important for numerous applications in chemical separations and energy storage. The behavior of non-aqueous fluids inside carbon nanotubes would open numerous questions that were addressed for water over the course of this thesis, including questions of packing configuration, dynamics of filling, and thermodynamics of liquid/vapor and adsorption phase transitions. Water is a weak Raman scatterer, but other fluids (e.g. cyclohexane) have strong Raman peaks that do not interfere with CNT vibrational modes, possibly allowing the direct observation of fluid filling in addition to the indirect method of tracking CNT vibrational modes.

Spatial patterning of nanopores: Carbon nanotubes or other nanopores may be able to be spatially patterned using many of the same cleanroom techniques used in sample nanofabrication in this work. Spatial patterning on the micron scale could create regions of greater hydrophobicity and hydrophilicity, encouraging or discouraging fluid nucleation and growth as in Chapter 6 of this work. Spatial patterning on the sub-micron scale, including localization of nanofluidic phenomena to individual crystallographic defects, represents the end point of this sort of work. While this may be many years off, the use of defects in carbon nanotubes for nanofluidic defect fluorescence has already been introduced.

Combined spectroscopy and electron microscopy: Advances in EM capabilities, including *in situ* Raman and fluorescence spectroscopy, open the possibility of combining TEM and Raman to observe nanotube filling and emptying events simultaneously using multiple techniques. The combination of direct imaging and an indirect probe, such as Raman, could help to refine expectations for electron microscope images of nanopores under different fluidic conditions.

Raman observation of non-CNT nanotubes: Achieving a high signal-to-noise ratio requires resonance between the laser excitation and an electronic transition in the nanotube. For carbon nanotubes, electronic transitions occur in the visible, but for boron nitride (and other) nanotubes, these electronic transitions occur in the UV and other less convenient regions of the electromagnetic spectrum for conventional spectroscopy. Notwithstanding these difficulties, boron nitride nanotube and other nanotubes have radial breathing modes that should respond to fluid filling. Given differences in slip flow between CNTs and BNNTs due to quantum effects at the fluid-solid interface, Raman investigation of fluid filling in BNNTs would allow further comparison between two analogous but highly differentiated nanofluidic systems.

In-situ CNT membrane measurement: Carbon nanotube membranes are potentially promising for use in liquid-phase separations. While single-nanotube measurements have key advantages in determining properties of fluids under nanoconfinement, as discussed above, multi-pore systems will likely have greater industrial relevance. Membrane characterization by optical sensing of carbon nanotubes by Raman or fluorescence will allow large-scale transport properties (including permeability and selectivity) to be linked to pore-scale fluid filling state as a function of temperature, humidity, and time.